

ADVANCED READOUT AND CONTROL ELECTRONICS
FOR MEMS GYROSCOPES

A THESIS SUBMITTED TO
THE GRADUATE SCHOOL OF NATURAL AND APPLIED SCIENCES
OF
MIDDLE EAST TECHNICAL UNIVERSITY

BY

YÜKSEL TEMİZ

IN PARTIAL FULFILLMENT OF THE REQUIREMENTS
FOR
THE DEGREE OF MASTER OF SCIENCE
IN
ELECTRICAL AND ELECTRONICS ENGINEERING

AUGUST 2007

Approval of the thesis:

**ADVANCED READOUT AND CONTROL ELECTRONICS
FOR MEMS GYROSCOPES**

submitted by **YÜKSEL TEMİZ** in partial fulfillment of the requirements for the degree of **Master of Science in Electrical and Electronics Engineering Department, Middle East Technical University** by,

Prof. Dr. Canan Özgen
Dean, Graduate School of **Natural and Applied Sciences**

Prof. Dr. İsmet Erkmen
Head of Department, **Electrical and Electronics Engineering**

Prof. Dr. Tayfun Akın
Supervisor, **Electrical and Electronics Engineering Dept., METU**

Examining Committee Members:

Prof. Dr. Cengiz Beşikçi
Electrical and Electronics Engineering Dept., METU

Prof. Dr. Tayfun Akın
Electrical and Electronics Engineering Dept., METU

Asst. Prof. Dr. Haluk Külâh
Electrical and Electronics Engineering Dept., METU

Dr. Said Emre Alper
Technical Vocational School of Higher Education, METU

Dr. Volkan Nalbantoğlu
ASELSAN

Date: 31.08.2007

I hereby declare that all information in this document has been obtained and presented in accordance with academic rules and ethical conduct. I also declare that, as required by these rules and conduct, I have fully cited and referenced all material and results that are not original to this work.

Name, Last Name : Yüksel, Temiz

Signature :

ABSTRACT

ADVANCED READOUT AND CONTROL ELECTRONICS FOR MEMS GYROSCOPES

Temiz, Yüksel

M.Sc., Department of Electrical and Electronics Engineering

Supervisor: Prof. Dr. Tayfun Akın

September 2007, 176 pages

This thesis reports the development of a number of advanced readout and control electronics for various MEMS gyroscopes developed at METU. These gyroscope electronics are separated into three main groups: high-sensitive interface circuits, drive-mode amplitude-controlled self-oscillation feedback loops, and sense-mode phase-sensitive amplitude demodulators. The proposed circuits are first implemented with commercial discrete components for initial tests, and then integrated on CMOS chips that are fabricated in a standard 0.6 μ m CMOS process.

A very compact circuit including a self-oscillation loop with manual amplitude control mechanism and sense-mode signal processing electronics is designed for performance tests of silicon-on-glass (SOG) and silicon-on-insulator (SOI) gyroscopes. This circuit employs a different and superior method for sustaining drive-mode vibrations exactly at the mechanical resonance frequency of the gyroscope. The phase error introduced by the circuit is measured to be lower than 0.5°. Angular rate systems tested with this circuit demonstrate bias instability and angle random walk values as low as 100 °/hr and 2 °/ $\sqrt{\text{hr}}$, respectively.

An improved version of the self-oscillation loop enabling constant amplitude drive-mode vibrations independent of sensor parameters and ambient conditions is developed for SOG gyroscopes. A fully-functional angular rate system, which is constructed by employing this advanced control electronics together with the transresistance amplifier type interfaces and sense-mode electronics, is implemented on a dedicated PCB having 5.4x2.4 cm² area, which is very small for such a complex system. This system demonstrates an impressive performance far better than the best performance achieved by any angular rate system developed at METU. Bias instability and angle random walk values are measured as 14.3 °/hr and 0.126 °/√hr, respectively. The scale factor of the system is found as 22.2 mV/(°/sec) with a nonlinearity of 0.01% and a zero-rate output of 0.1 °/sec, in ±50 °/sec measurement range. In addition, the differential version of the control loop is developed for generating exactly anti-phase driving signals sustaining constant amplitude and balanced vibrations in dual-mass dissolved-wafer process (DWP) gyroscopes. It is verified that the amplitude control mechanism automatically adjusts the level of the sinusoidal differential driving signals in response to variations in system parameters for keeping the oscillation amplitude stable.

CMOS unity-gain buffer (UGB) and transimpedance amplifier (TIA) type resistive and capacitive interfaces are characterized through AC, transient, and noise tests. It is observed that on-chip biasing mechanisms properly DC-bias the high-impedance nodes to 0 V potential. UGB type capacitive interfaces demonstrate superior performance than TIA counterparts due to stability problems associated with TIA interfaces. CMOS differential drive-mode control and sense-mode demodulation electronics give promising results for the future performance tests of the DWP gyroscopes that are still under development.

Keywords: MEMS Gyroscope, Gyroscope Electronics, Interface Circuit, Oscillation Amplitude Control, Amplitude Demodulation, Microelectromechanical Systems (MEMS).

ÖZ

MEMS DÖNÜÖLÇERLER İÇİN İLERİ SEVİYE OKUMA VE KONTROL ELEKTRONİĞİ

Temiz, Yüksel

Yüksek Lisans, Elektrik ve Elektronik Mühendisliği Bölümü

Tez Yöneticisi: Prof. Dr. Tayfun Akın

Eylül 2007, 176 sayfa

Bu tez, ODTÜ’de geliştirilmiş çeşitli MEMS dönüölçerler için tasarlanan ileri okuma ve kontrol elektroniğinin geliştirilmesini anlatmaktadır. Bu dönüölçer devreleri üç ana gruba ayrılmıştır: yüksek hassasiyetli arabirim devreleri, sürüş modu için genlik kontrollü kendiliğinden salınım sağlayan geri-besleme döngüleri, ve algılama modu için faz hassasiyetli genlik kipçözümü devreleri. Öne sürülen devreler başlangıç testleri için ilk olarak ticari ayrık devre bileşenleriyle oluşturulmuş, daha sonra standart 0.6µm CMOS sürecinde üretilen CMOS yongalar üzerinde birleştirilmiştir.

Cam-üzeri-silisyum ve yalıtkan-üzeri-silisyum dönüölçerlerin performans testleri için, elle genlik kontrolü mekanizması ile kendiliğinden salınım sağlayan döngüyü ve algılama modu sinyal işleme elektroniğini içeren ve çok az yer kaplayan bir devre tasarlanmıştır. Bu devre dönüölçerin tam olarak mekanik rezonans frekansında salınım yapmasını sağlayan daha üstün farklı bir yöntem kullanmaktadır. Devrenin kattığı faz hatası 0.5 dereceden daha düşük olarak ölçülmüştür. Bu devre ile test edilen açısal hız sistemleri, sabit kayma kararsızlığı ve açısal rastgele kayması olarak sırasıyla 100 °/saat ve 2 °/√saat değerlerine kadar düşen değerler göstermiştir.

Kendiliğinden salınım döngüsünün duyurga parametrelerinden ve çevre koşullarından bağımsız sabit genlikli sürüş modu titreşimleri sağlayan iyileştirilmiş uyarlaması, SOG dönüölçerler için geliştirilmiştir. Geçiş-direnç yükselteç tipi arabirimleri ve algılama modu devreleriyle birlikte bu ileri kontrol elektroniğinden oluşturulan tamamen işlevsel açısız hız sistemi, böylesine karmaşık bir sistem için çok küçük olan 5.4x2.4 cm² ebadında bir baskı devre plaketi üzerine yerleştirilmiştir. Bu sistem, ODTÜ’de geliştirilmiş açısız hız sistemlerinden elde edilmiş en iyi performanstan çok daha iyi, etkileyici bir performans göstermiştir. Sabit kayma kararsızlığı ve açısız rastgele kayması sırasıyla 14.3 °/saat ve 0.126 °/√saat olarak ölçülmüştür. Sistemin orantı katsayısı, ±50 %/sn ölçüm aralığında %0.01 doğrusallıktan sapma ve 0.1 %/sn sıfır-dönü çıkışıyla birlikte 22.2 mV/(°/sn) olarak bulunmuştur. Bunun yanında, çift kütleli aşındırılmış pul işlemlili dönüölçerlerde sabit genlikli ve dengeli titreşimleri sağlayan tamamen zıt fazlı sürüş sinyallerini üretmek için kontrol döngüsünün tam-farksal uyarlaması geliştirilmiştir. Genlik kontrol mekanizmasının, salınım genliğini sabit tutmak için sistem parametrelerindeki değişimlere tepki olarak sinüs dalgası biçimli tam-farksal sürüş sinyallerini otomatik olarak ayarladığı kanıtlanmıştır.

CMOS kazancı bir olan tampon devre ve geçiş-empedansı yükselteci tipi direnil ve sızgal arabirim devreleri AC, geçici rejim, ve gürültü testleriyle karakterize edilmiştir. Yongayla tümleşik eğilimleme mekanizmalarının yüksek-empedanslı düğümleri gerektiği şekilde 0 V potensiyeline DC olarak eğilimlediği gözlenmiştir. Kazancı bir olan tampon devre tipi sızgal arabirim devreleri, geçiş-empedansı yükselteci tipi benzerlerinde karşılaşılan kararlılık sorunu nedeniyle, geçiş-empedansı yükselteci tipi arabirim devrelerinden daha iyi bir performans göstermiştir. CMOS farksal sürüş modu kontrolü ve algılama modu kipçözümü devreleri, hala geliştirilmekte olan aşındırılmış pul işlemlili dönüölçerlerin gelecekteki performans testleri için umut vaat eden sonuçlar vermiştir.

Anahtar Kelimeler: MEMS Dönüölçer, Dönüölçer Elektroniği, Arabirim Devresi, Salınım Genliği Kontrolü, Genlik Kipçözümü, Mikroelektromekanik Sistemler (MEMS).

To My Dear Mother and Father

And

To My Sweet Sister

ACKNOWLEDGEMENTS

First and foremost, I would like to express my special thanks to my thesis advisor Prof. Dr. Tayfun Akın for his guidance, support, encouragement, and help throughout my graduate studies and the development of this thesis. It is a privilege for me to use exceptional research opportunities provided by him.

I also thank to Dr. Said Emre Alper for being a “paragon” for me with his distinguished knowledge and experience on MEMS gyroscopes, and his friendly attitude. Hardly could I reach my achievements without his guidance and help.

I am particularly grateful to İlker Ender Ocağ for not only coaching me on many equipments but also being an “elder brother” for me. I cannot imagine such a stress-free and motivating research environment without him. I would also like to express my appreciation to Murat Tepegöz for sharing his endless knowledge on circuit design, CADENCE tools, and computer issues, and for answering my numerous questions with a great patience.

I would like to thank to other members of inertial sensors group; Kanber Mithat Silay (currently at EPFL, Switzerland) for sharing his knowledge and experience on design and tests of gyroscope electronics, Kıvanç Azgın for being an excellent colleague and for developing superb gyroscopes enabling me to attend an international conference in JAPAN, Emre Şahin for his helps during the tests, Korhan Şahin for providing FEM simulation results of the MEMS gyroscopes, and Reha Kepenek for not letting me alone at never-ending nights before the CMOS runs.

I would like to express my particular gratitude to my tenderhearted friends and confidants, İpek İstanbulluoğlu (Turhan) and M. Batuhan Dayanık, for supporting and motivating me in every difficulty I have faced. Moreover, I am grateful to all

my dear friends at METU MEMS-VLSI Research group, Fehmi ivitci, Erkan Alpman (currently at CMU, USA), K. afak Demirci (currently at Gatech, USA), Gzde C. Yaşınok (currently at TAI, Ankara), Ercihan İncetürkmen, Kerem Kapucu, Emre Kltrsay, Alperen Toprak, E. Ufuk Temoin (currently at Aselsan, Ankara), H. İbrahim Atasoy, mer Bayraktar, Sertan Sukas, Ata Tuna iftlik, and Alp Oğuz, for providing a pleasant research environment and for their candid friendship. Furthermore, I would also like to express my appreciation to my seniors; M. Yusuf Tanrıkulu, Orhan Akar, Dr. Kağan Topallı, Mehmet nl, and Mustafa Semen not only for their helps but also their friendly attitude. I also express my appreciation to Asuman Yurdakul for her valuable efforts in purchasing issues.

Last but not least, I am very grateful to my mother Aysel Temiz, my father Yusuf Temiz, and my sweet sister Cansel Temiz for their endless support, encouragement, patience, and love.

TABLE OF CONTENTS

ABSTRACT	iv
ÖZ	vi
DEDICATION.....	viii
ACKNOWLEDGEMENTS	ix
TABLE OF CONTENTS	xi
LIST OF TABLES.....	xiv
LIST OF FIGURES	xv
CHAPTERS	
1. INTRODUCTION	1
1.1. Micromachined Vibratory Gyroscopes.....	4
1.2. Overview of Micromachined Vibratory Gyroscopes.....	6
1.3. Overview of Readout and Control Electronics for Vibratory MEMS Gyroscopes.....	15
1.4. Gyroscope Electronics Developed at METU	21
1.5. Research Objectives and Thesis Organization	23
2. THEORY OF VIBRATORY GYROSCOPES	27
2.1. Mechanical Theory of Vibratory Gyroscopes	27
2.1.1. Mechanics of the Drive-Mode Resonator	28
2.1.2. Coriolis Coupling and Mechanics of the Sense-Mode Accelerometer.....	29
2.2. Electrostatic Actuation and Capacitive Sensing Mechanisms	32
2.2.1. Electrostatic Actuation Using Parallel-Plate Capacitors	32
2.2.2. Capacitive Sensing	37
2.2.3. Electrostatic Spring Effect	39
2.3. Electrical Model of Vibratory Gyroscopes	42
2.4. Theory of Vibratory Gyroscope Electronics	45
2.4.1. Capacitive and Resistive Type Interface Electronics	46
2.4.2. Oscillation Criteria and Self-Oscillation Principle.....	50
2.4.3. Automatic Oscillation Amplitude Control Principle	54

2.4.4.	Sense-Mode Rate Output Extraction Electronics	58
2.5.	Summary	61
3.	READOUT AND CONTROL ELECTRONICS DESIGN	62
3.1.	Discrete Readout and Control Electronics	62
3.1.1.	Drive-Mode Self-Resonance Excitation Circuit with Manual Oscillation Amplitude Control	63
3.1.2.	Sense-Mode Open-Loop Rate Sensing Electronics	67
3.1.3.	Transimpedance Amplifier (TIA) Type Resistive Interface	68
3.1.4.	Single-Ended Automatic Amplitude Control Circuit with Open-Loop Rate Sensing Electronics for SOG Gyroscopes	71
3.1.5.	Differential Automatic Amplitude Control Circuit with Open-Loop Rate Sensing Electronics for Dual-Mass Gyroscopes	75
3.2.	CMOS Capacitive and Resistive Interfaces	79
3.2.1.	Unity-Gain Buffer (UGB) Design	79
3.2.2.	UGB Type Resistive Interface	84
3.2.3.	UGB Type Capacitive Interface with Subthreshold Transistor Biasing..	87
3.2.4.	Transimpedance Amplifier (TIA) Type Resistive Interface	91
3.2.5.	Transimpedance Amplifier (TIA) Type Capacitive Interfaces with Controlled-Impedance FET Biasing	94
3.3.	CMOS Drive-Mode Control Electronics	99
3.3.1.	Single-Ended to Differential Convertor	100
3.3.2.	Fully-Differential Self-Resonance Excitation Circuit with Automatic Amplitude Control	101
3.4.	CMOS Sense-Mode Open-Loop Rate Sensing Electronics	115
3.5.	Summary	120
4.	TEST RESULTS	121
4.1.	Test Results of the Discrete Electronics	121
4.1.1.	Readout and Control Electronics with Manual Oscillation Amplitude Control	122
4.1.2.	Readout and Control Electronics with Automatic Oscillation Amplitude Control for SOG Gyroscopes	125
4.1.3.	Differential Readout and Control Electronics with Automatic Oscillation Amplitude Control for DWP Gyroscopes	133

4.2.	Test Results of the CMOS Electronics	141
4.2.1.	Characterization of UGB Type Interfaces	141
4.2.1.1.	UGB type Resistive Interface.....	143
4.2.1.2.	UGB Type Capacitive Interface	147
4.2.2.	Characterization of TIA Type Resistive and Capacitive Interfaces ...	149
4.2.2.1.	TIA Type Resistive Interface	151
4.2.2.2.	TIA Type Capacitive Interface.....	153
4.2.3.	Test Results of CMOS Fully-Differential Control Electronics.....	155
4.2.3.1.	Single-ended to Differential Convertor	155
4.2.3.2.	Fully-Differential Self-Resonance Excitation Circuit with Automatic Amplitude Control	158
4.2.4.	Test Results of CMOS Fully-Differential Open-Loop Rate Sensing Electronics.....	159
4.3.	Summary of the Tests	160
5.	CONCLUSIONS AND FUTURE WORK	164
6.	REFERENCES	170

LIST OF TABLES

Table 1.1: Performance requirements for three different classes of gyroscopes [1]. . . 3	3
Table 2.1: Electrical equivalents of mechanical parameters of a mass-spring-damper system.....42	42
Table 3.1: Expected capacitance values and electromechanical coupling coefficients for drive motor (DM), drive pick-up (DP), and sense pick-up (SP) electrodes.76	76
Table 3.2: Transistor dimensions for the UGB circuit designed for 0.6 μ m n-well CMOS process of XFAB Semiconductor Foundries.80	80
Table 3.3: Transistor dimensions for the VGA circuit designed for a 0.6 μ m standard 5V CMOS process. 106	106
Table 4.1: The best performance values demonstrated by SOG [50] and SOI [51] gyroscopes when the proposed circuit, which is composed of drive-mode self-oscillation loop with manual amplitude control and sense-mode open-loop rate sensing electronics, is employed..... 124	124
Table 4.2: Operation cases for the angular rate system, categorized according to the sense-mode transresistance amplifier (TRA) resistance, the matching mode, the sense-mode instrumentation amplifier (IA) gain, and the vacuum level. 127	127
Table 4.3: Performance test results for the angular rate system operated in four different conditions. 132	132
Table 4.4: Drive-mode circuits tested with different types of gyroscopes..... 161	161
Table 4.5: The best performance results demonstrated by the angular rate systems given in Table 4.4. 161	161

LIST OF FIGURES

Figure 1.1: Behavior of Foucault’s pendulum in response to Earth’s rotation. (a) The pendulum tracks a linear path when the Earth is assumed to be stationary. (b) Path of the pendulum is observed to be elliptical due to Coriolis force induced by Earth’s daily rotation.....	5
Figure 1.2: A moving mass with two degrees-of-freedom (2-DOF), demonstrating the Coriolis based micromachined vibratory gyroscope operation.	6
Figure 1.3: SEM image of Draper’s silicon-on-glass tuning-fork vibratory gyroscope [10].....	7
Figure 1.4: Photograph of the Berkeley’s monolithic dual-axis gyroscope fabricated with Analog Devices’ surface micromachining process [15].	8
Figure 1.5: Die photograph of the iMEMS ADXRS gyroscope, composed of tuning-fork mechanical element and on-chip signal processing electronics [16].	9
Figure 1.6: SEM picture of matched-mode z-axis tuning fork gyroscope fabricated on 50- μm thick SOI substrate [17].	10
Figure 1.7: SEM picture of the DWP gyroscope prototype and the close-up view of the comb fingers [8].....	11
Figure 1.8: SEM photographs of (a) the varying-overlap-area drive fingers and (b) the varying-gap type sense fingers [8].	12
Figure 1.9: Cross-section of the silicon-on-glass (SOG) structure.....	12
Figure 1.10: SEM picture of the fabricated SOG gyroscope showing the drive and sense electrodes, flexures, perforated suspended frames, and anchors [8].	13
Figure 1.11: SEM picture of the SOI dual-mass gyroscope designed at METU and fabricated at MEMSCAP [®] Inc [22].	14
Figure 1.12: Cross-section of the vacuum-packaged DWP structure.....	15
Figure 1.13: Simplified block diagram of the chopper-stabilized ac-bridge preamplifier [27].....	16
Figure 1.14: Circuit schematic of the Analog Devices’ fully-differential transimpedance amplifier designed for high-sensitive capacitance-to-voltage conversion [16].	17

Figure 1.15: Schematic view of a fully-differential switched-capacitor front-end circuit for capacitive sensing applications [32].	18
Figure 1.16: Simplified block diagram of the drive-mode automatic amplitude control and sense-mode open-loop rate sensing electronics designed for micromachined gyroscopes developed at Georgia Institute of Technology [30].	19
Figure 1.17: System-level block diagram of the digital control and readout electronics based on sigma-delta modulation [37].	20
Figure 1.18: Unity-gain buffer (UGB) type capacitive interface developed at METU [8, 20].	21
Figure 1.19: Single-ended source follower biased with subthreshold NMOS transistor [50].	22
Figure 2.1: Typical parallel-plate capacitor configuration that is widely used in transduction mechanisms of micromachined vibratory gyroscopes.	33
Figure 2.2: Driving electrodes for (a) varying-gap and (b) varying-overlap-area type actuation mechanisms.	37
Figure 2.3: Basic electrical model of the capacitive sensing mechanism.	38
Figure 2.4: The effect of DC biasing voltage on the resonance characteristics of (a) the drive-mode and (b) the sense-mode.	41
Figure 2.5: Electrical equivalent model of the drive-mode.	44
Figure 2.6: Generalized electrical model of the overall gyroscope constructed by combining the models of drive and sense modes.	45
Figure 2.7: Generalized view of a basic interface circuit used to convert the charge pumped from the gyroscope to voltage.	47
Figure 2.8: Block diagram of a unity-gain positive feedback system.	50
Figure 2.9: Block diagram of a simple self-oscillation loop together with the bode diagram of the gyroscope drive-mode.	51
Figure 2.10: Pole-zero diagrams and corresponding transient responses of systems having (a) right-half plane poles, (b) imaginary poles, and (c) left-half plane poles.	53
Figure 2.11: Block diagram of the proposed automatic oscillation amplitude control circuit.	55
Figure 2.12: Pole-zero diagram showing the movement of system poles from start-up to steady-state operation.	56

Figure 2.13: Reduced order linearized model of the proposed AGC loop.	57
Figure 2.14: Block diagram of a typical AM demodulation circuit for open-loop rate sensing.....	58
Figure 3.1: Block diagram of the self-resonance excitation circuit with manual amplitude control for CMOS capacitive-type interfaced gyroscopes.....	64
Figure 3.2: Two possible configurations of 90° phase shifters; (a) OPAMP differentiator and (b) OPAMP integrator circuits introducing -90° and 90° phase shifts, respectively.	64
Figure 3.3: Circuit schematic of the self-resonance excitation circuit including differentiator as the phase shifting element.....	65
Figure 3.4: SIMULINK transient response of the interface output when the gain of the attenuator is changed during the simulation.	66
Figure 3.5: Circuit schematic of the open-loop rate sensing circuit used for converting the AM modulated sense-mode output to baseband angular rate related signal.	67
Figure 3.6: Photograph of the PCB including entire sense-mode and drive-mode electronics, fit in a 5.3x2 cm ² area with a dedicated layout design.	68
Figure 3.7: Gyroscope cascaded transresistance amplifier (TRA) structure.....	69
Figure 3.8: Block diagram of the proposed automatic amplitude control mechanism together with the open-loop rate sensing electronics designed for single-mass SOG gyroscopes.	71
Figure 3.9: Circuit schematic of the proposed automatic amplitude control loop and open loop sense-mode electronics.	72
Figure 3.10: SIMULINK transient simulation result for (a) driving signal, and (b) drive-mode interface output, as the quality factor of the gyroscope is changed...73	73
Figure 3.11: (a) General view, (b) Top side, and (c) Bottom side of the PCB, including packaged SOG gyroscope, transresistance amplifiers, open-loop rate sensing electronics, and self-resonance loop with automatic amplitude control.....	74
Figure 3.12: Simplified view of the dual-mass DWP gyroscope.	76
Figure 3.13: Circuit schematic of the differential automatic amplitude control loop designed for DWP gyroscopes and implemented with commercial discrete components.....	77
Figure 3.14: Photographs of six-layer PCBs implemented with (a) dual in line package (DIP) components, and (b) surface mount devices (SMD).	78

Figure 3.15: The schematic view of the UGB circuit, which is the modified version of UGB circuits in [8, 33, 49].....	80
Figure 3.16: Z-parameter analysis result for the input impedance of the UGB circuit.	81
Figure 3.17: Post-layout AC simulation result of the designed UGB when the output is loaded with a 10pF capacitor.	82
Figure 3.18: Noise simulation result for the output referred voltage noise of the UGB.	83
Figure 3.19: Post-layout Monte Carlo simulation result for the output offset of the UGB when transistor mismatches and process variations are modeled as a Gaussian distribution function according to the process parameters provided by XFAB.	84
Figure 3.20: UGB type resistive interface structure designed for DWP gyroscopes.	85
Figure 3.21: Post-layout AC simulation result of the UGB type resistive interface when the circuit is excited with a current source and loaded with a 10 pF capacitor.	86
Figure 3.22: Noise simulation result for the output referred voltage noise of the UGB type resistive interface.	86
Figure 3.23: Layouts of (a) the differential UGB type resistive interface, and (b) the differential UGB type resistive interface cascaded with an on-chip instrumentation amplifier giving single-ended output.	87
Figure 3.24: Circuit schematic of the UGB type capacitive interface, where the high-impedance node is biased with NMOS-PMOS transistor pair operating in subthreshold region.	88
Figure 3.25: Post-layout AC simulation result of the UGB type capacitive interface when the circuit is excited by a current source and the output is loaded with a 10 pF capacitor.	89
Figure 3.26: Transient simulation results for the differential outputs of the UGB type capacitive interface when the circuit is excited with differential current sources having 1 nA of amplitude at 10 kHz.	90
Figure 3.27: Noise simulation result for the output referred voltage noise of the UGB type capacitive interface with NMOS-PMOS biasing transistor pairs having effective channel resistance of 800 M Ω	90
Figure 3.28: Layouts of (a) differential UGB type capacitive interface, and (b) differential UGB type capacitive interface cascaded with on-chip instrumentation amplifier giving single-ended output.	91

Figure 3.29: CMOS TIA type resistive interface circuit designed for drive-mode of the DWP gyroscope.	92
Figure 3.30: Post-layout AC simulation result of the TIA type resistive interface when the circuit is excited with a current source and loaded with a 10 pF capacitor.	93
Figure 3.31: Noise simulation result for the output referred voltage noise of the TIA type resistive interface.	93
Figure 3.32: Circuit schematic of the proposed controlled-impedance FET circuit used for biasing the OPAMP output.	94
Figure 3.33: Circuit schematic of the TIA type capacitive interface employing controlled-impedance FET biasing.	96
Figure 3.34: Post-layout AC simulation result of the TIA type capacitive interface when the circuit is excited by a current source and output is loaded with a 10 pF capacitor.	97
Figure 3.35: Transient response of the differential capacitive TIA circuit when the circuits are excited with differential current sources having 1 nA of amplitude at 10 kHz.	97
Figure 3.36: Noise simulation result for the output referred voltage noise of the TIA type capacitive interface.	98
Figure 3.37: Layouts of (a) differential TIA type capacitive and resistive interfaces combined in a single chip, and (b) interface circuits providing single-ended output by employing on-chip instrumentation amplifiers.	99
Figure 3.38: Circuit schematic of the (a) CMOS instrumentation amplifier, and (b) single-ended to differential converter composed of two unity-gain instrumentation amplifiers.	100
Figure 3.39: Circuit schematic of the CMOS fully-differential self-resonance excitation circuit with automatic amplitude control designed for DWP gyroscopes.	101
Figure 3.40: (a) Basic circuit diagram of the VGA composed of two common-source amplifiers with variable source degeneration resistor connected in common. (b) Circuit schematic of the VGA when current sources and load resistors are replaced with transistors and variable resistor is realized with an NMOS transistor operating in linear region.	103
Figure 3.41: (a) Simplified diagram of the CMFB mechanism used in the proposed VGA. (b) Negative feedback model of the VGA with CMFB for stability analysis.	104
Figure 3.42: Circuit schematic of the fully-differential VGA with CMFB.	106

Figure 3.43: Two cascade-connected VGA circuits operating as one single VGA since common-mode control, V_{CMC} , and gain control, V_{Cont} , voltages of each VGA are shorted.	107
Figure 3.44: Gain versus control voltage simulation result for the proposed VGA circuit, when the control voltage is swept from -2.5V to 2.5V.	108
Figure 3.45: Transient simulation results for (a) the positive output terminal, and (b) the negative output terminal, when the control voltage is swept from 0V to 1V in six steps for the differential input signal having amplitudes of 10 mV.	108
Figure 3.46: SIMULINK block diagram of the reduced order model for the proposed automatic amplitude control loop.	109
Figure 3.47: SIMULINK transient response of the reduced order sensor output for the amplitude set voltage of 100 mV.	110
Figure 3.48: Exact model of the self-oscillation loop with amplitude control constructed in SIMULINK.	110
Figure 3.49: SIMULINK transient response of the sensor cascaded resistive interface output for a step input of amplitude set voltage at 100 mV.	111
Figure 3.50: SIMULINK transient response of the error signal, which is the difference between amplitude detector output and amplitude set voltage.	112
Figure 3.51: SIMULINK transient simulation result of the PI controller output.	112
Figure 3.52: SIMULINK transient simulation results of the sensor output in response to step changes in (a) amplitude set voltage, and (b) mechanical quality factor.	113
Figure 3.53: CADENCE transient simulation results for (a) the instrumentation amplifier output connected to the differential drive-mode interfaces, (b) the generated error signal, and (c) the PI controller output connected to the gain control input of the VGA.	114
Figure 3.54: Block diagram of the proposed AM demodulator circuit based on switching full-wave rectification followed by low-pass filtering.	115
Figure 3.55: Circuit schematic of the fully-differential AM demodulation circuit designed for open-loop rate sensing electronics of DWP gyroscopes operated in mismatched-mode.	116
Figure 3.56: Transient simulation results for the differential full-wave rectifier outputs, when sinusoidal voltages having 100 mV of amplitude at 10 kHz are applied differentially.	117
Figure 3.57: Transient response of the instrumentation amplifier output.	117

Figure 3.58: Transient simulation result of the third-order Sallen-key LPF output for differential sense-mode signals having 100 mV of amplitude.	118
Figure 3.59: Periodic Steady-State (PSS) noise analysis giving output referred voltage noise of the overall demodulator output.	119
Figure 3.60: Layout of the fully-differential automatic amplitude control loop and open-loop rate sensing electronics designed for DWP gyroscopes.	119
Figure 4.1: Photograph of the test setup used for characterization of drive-mode control and sense-mode demodulation electronics.	122
Figure 4.2: a) The measured self-resonance loop output (blue) when a sinusoidal signal with 3 V _{p-p} amplitude and 1 V offset (red) is applied. b) Measured outputs of the sense-mode demodulator (red) and low-pass filter (blue).	123
Figure 4.3: Resonance characteristics for the (a) drive-mode, and the (b) sense-mode of the SOG gyroscope measured with Agilent 4395A network analyzer and Karl Suss micromanipulator probe station at the ambient pressure.	125
Figure 4.4: Photograph of the compact and fully-functional angular rate system placed into the vacuum chamber mounted on Ideal Aerosmith 1280 single-axis rate table.	126
Figure 4.5: Measured responses of the drive-mode interface output for (a) V _{PM} = 20V, P = 5mTorr, (b) V _{PM} = 30V, P = 5mTorr, and (c) V _{PM} = 30V, P = 1500mTorr.	127
Figure 4.6: Measured output response of the angular rate sensor (Case I) when the applied angular rate is swept from zero rate to ±50 deg/sec with 5 deg/sec steps. ..	128
Figure 4.7: Measured response curve giving the scale factor, the zero-rate offset, and the nonlinearity of the overall system.	129
Figure 4.8: Bias drift data collected from the rate output when the system is powered up at zero time, while the sensor is located in the vacuum chamber and kept stationary during the test.	130
Figure 4.9: Allan variance plot generated by the drift data given in Figure 4.8.	131
Figure 4.10: Measured system output in response to a sinusoidal rate at 2Hz.	131
Figure 4.11: Photograph of the test setup used for characterization of control and readout electronics designed for DWP gyroscopes.	133
Figure 4.12: Measured drive-mode resonance characteristics of the vacuum packaged DWP gyroscope when the drive-mode output is read from the motor electrode through a transresistance amplifier with 1 MΩ feedback resistor while the proof mass voltage is set to 15 V.	134

Figure 4.13: Measured driving signal and the drive-mode output generated by the automatic amplitude control loop when the proof mass and the amplitude set voltages are 15 V and 100 mV, respectively.....	135
Figure 4.14: Measured (a) drive-mode output signal, (b) motor signal, (c) amplitude signal, and (d) error signal in response to changes in amplitude set voltage.	138
Figure 4.15: Measured drive-mode (a) output signal, and (b) motor signal when the proof mass voltage is instantaneously changed during the simulation.	138
Figure 4.16: Measured output response of the angular rate system when the applied angular rate is swept from zero rate to ± 50 deg/sec with 5 deg/sec steps.....	139
Figure 4.17: Measured response curve giving the scale factor, the zero-rate offset, and the nonlinearity of the overall system.	140
Figure 4.18: Allan variance plot generated by the drift data collected for two hours.	140
Figure 4.19: Photographs of the CMOS UGB type resistive and capacitive interfaces wire-bonded to the ceramic package.....	142
Figure 4.20: Block diagram of the test setup used in the transient tests of the differential UGB type resistive and capacitive interfaces.....	142
Figure 4.21: Block diagram of the test setup used in the noise tests of the UGB type resistive and capacitive interfaces.	143
Figure 4.22: Measured differential signals at the high-impedance nodes and differential outputs of the UGB type resistive interface when sinusoidal signals having 1 V _{p-p} amplitude and 500 mV offset are applied through coupling capacitors.	144
Figure 4.23: Measured gain and phase characteristics of the differential UGB type resistive interface for the (a) first branch, and the (b) second branch.	145
Figure 4.24: Difference of the differential output nodes of the UGB type resistive interface, illustrating that the output offset is cancelled out after the subtraction operation.....	145
Figure 4.25: Measured noise characteristics of the differential UGB type resistive interface for both differential branches.	146
Figure 4.26: Measured transient response of the differential outputs of the UGB type capacitive interface when ± 500 mV of step functions are applied to the differential inputs of the interface through 10 nF coupling capacitors.....	147

Figure 4.27: Measured differential signals at the capacitive UGB output when differential sinusoidal signals having 1 V _{p-p} amplitude and 500 mV offset are applied through coupling capacitors.	148
Figure 4.28: Measured noise characteristics of the differential UGB type capacitive interface for both differential branches.	149
Figure 4.29: Photograph of the differential TIA type capacitive and resistive interface chip wire-bonded to a ceramic package.....	150
Figure 4.30: Block diagram of the test setup used in the transient tests of the differential TIA type resistive and capacitive interfaces.	151
Figure 4.31: Measured transient response of the TIA type resistive interface when differential signals with 200 mV _{p-p} amplitude are applied through 200 kΩ resistors.	152
Figure 4.32: Gain and phase characteristics of the TIA type resistive interface when the input signal is applied through a 200 kΩ resistor.	153
Figure 4.33: Output response of the test chip, when the 20 mV _{p-p} input signal is applied by the function generator through a 200 kΩ resistor.....	154
Figure 4.34: Photographs of the differential readout electronics and the single-ended to differential convertor wire-bonded to a 24-pin ceramic package.....	156
Figure 4.35: Measured differential output signals generated by the single-ended to differential convertor, when a 500 mV _{p-p} sinusoidal signal is applied by the function generator.....	157
Figure 4.36: Measured gain and phase characteristics of the single-ended to differential convertor for (a) the inverting output and (b) non-inverting output.....	157
Figure 4.37: Photographs of (a) the complete angular rate system, (b) the DWP gyroscope, and (c) the CMOS fully-differential readout and control electronics. ...	158
Figure 4.38: Block diagram of the test setup used in the transient tests of the fully-differential full-wave rectifier.	159
Figure 4.39: Measured differential output signals generated by the fully-differential full-wave rectifier when 1 V _{p-p} differential signals are applied.	160

CHAPTER 1

INTRODUCTION

The 20th century has witnessed numerous innovations bringing an exceptionally modernized life far beyond the marvelous imagination of mankind. Among all these outstanding inventions, it was just a tiny device, the transistor, which initiated the everlasting growth in today's cutting-edge technology and opened the doors of information and communication era. The evolutionary development in transistors soon engendered the integrated circuit (IC) technology, replacing the obsolete bulky systems with fingernail-sized electronic circuits including millions of transistors through miniaturization techniques. Over the past few decades, not only have these techniques provided small, low-cost, efficient, and complex electronic systems, but they have also enabled the fabrication of micro-scale mechanical systems. Based on the highly-developed silicon processing, the micromachining technology has made possible the integration of micromechanics with microelectronics, giving birth to advanced systems entitled as Micro-Electro-Mechanical Systems (MEMS). After years of dedicated research on this remarkable technology, today, MEMS devices are used in vast diversity of fields, involving military, industrial, and consumer applications.

Among many MEMS transducers allowing low-cost, low-power, and compact solutions for expensive and bulky systems, inertial sensors have become one of the most popular devices introduced by the MEMS technology. These sensors aim to monitor the exact position and orientation of a moving object by tracking linear and angular motions. Presently, MEMS inertial transducers are being developed to meet the ever increasing demand in many navigation and stabilization applications, including airplane and submarine navigation, spacecraft and satellite control,

platform stabilization, and guided-missile control, as an alternative for conventional mechanical and optical counterparts. Moreover, this technology has also introduced novel applications of micromachined inertial sensors [1], including automotive safety systems [2-4], handheld camera stabilization, personal navigation, handheld game consoles, and virtual reality systems, where reducing the overall size, cost, and weight of the devices is essential.

Inertial MEMS transducers are categorized into two main branches as accelerometers that sense linear acceleration and gyroscopes that sense angular velocity. Micromachined accelerometers used in automotive applications are already in mass production with a very competitive sales volume in the market [5]. Furthermore, MEMS accelerometers resolving accelerations in the micro-g range, which is required for navigation applications, are reported in the literature [6, 7]. On the other hand, due to more complex mechanical and electrical structures of micromachined gyroscopes, performance of those are still far from the performance values demonstrated by conventional ring laser and fiber-optic gyroscopes currently employed in the advanced navigation systems.

The performance of a gyroscope is determined according to a number of important parameters, including minimum detectable angular rate, or equivalently resolution, bias drift, zero-rate output (ZRO), scale factor, full-scale range, maximum tolerable g-shock, and bandwidth. In the absence of an angular rate input, the output signal of the gyroscope is composed of an offset (ZRO) and a random signal that is the sum of white noise and a slowly varying function. The white noise, which is contributed by both the mechanical-thermal noise of the gyroscope structure and the electrical noise generated by the readout and control electronics, determines the resolution of the overall angular rate system. The resolution per square root of bandwidth is usually expressed in $(\text{deg}/\text{sec})/\sqrt{\text{Hz}}$. Moreover, angle random walk $(\text{deg}/\sqrt{\text{hr}})$ also defines the resolution as the angular error buildup with time as a result of white noise. The slowly varying function at the system output due to a number of random sources causes short or long-term bias drift, which is typically expressed in deg/hr . Then, scale factor is the change in output voltage per unit change in applied angular rate and is expressed in $\text{V}/(\text{deg}/\text{sec})$. Full-scale range is defined as the maximum input

rate that the gyroscope can provide a meaningful output. Moreover, shock survivability of micromachined gyroscopes makes them unique solutions for harsh environment applications. Hence, maximum tolerable g-shock is another important parameter that should be considered while determining the performance grade of the gyroscope. Finally, bandwidth information provides the maximum frequency of the applied angular rate that the gyroscope can response. Based on these parameters, Table 1.1 summarizes the performance requirements for three different classes of gyroscopes: rate-grade, tactical-grade, and inertial-grade [1].

Table 1.1: Performance requirements for three different classes of gyroscopes [1].

Parameter	Rate-Grade	Tactical-Grade	Inertial-Grade
Angle Random Walk (deg/ $\sqrt{\text{hr}}$)	> 0.5	0.5-0.05	< 0.001
Bias Drift (deg/hr)	10-1000	0.1-10	< 0.01
Scale Factor Accuracy (%)	0.1-1	0.01-0.1	< 0.001
Full Scale Range ($^{\circ}/\text{sec}$)	50-1000	> 500	> 400
Max. Shock in 1msec (G)	10^3	10^3 - 10^4	10^3
Bandwidth (Hz)	> 70	~ 100	~ 100

With the outstanding progress in the micromachined gyroscope technology over the past few years, it is now possible to employ micromachined gyroscopes in almost all applications requiring rate-grade performance. Moreover, some of the today's best MEMS gyroscopes demonstrate tactical-grade performances owing to their dedicated mechanical designs, optimized fabrication technologies, high-sensitivity electronics, and high-quality packagings. In the following years, it is expected that batch-fabricated micromachined gyroscopes will replace the bulky optical gyroscopes currently used in tactical-grade applications. However, achieving inertial-grade performance is still a tough challenge for silicon-based micromachined gyroscopes unless new technologies and approaches are introduced.

In order to enhance the performance of today's micromachined angular rate systems, dedicated readout and control electronics are required, as they have dominant effect on the overall performance of the system. Control electronics enable a stable

gyroscope operation, whereas readout electronics convert extremely small displacements in response to applied angular rates to meaningful electrical signals. This thesis proposes advanced electronic circuits designed for boosting the performance of MEMS gyroscopes developed at METU. It is verified that improved angular rate systems developed through this research demonstrate tactical-grade performance levels.

The organization of this chapter is as follows; Section 1.1 gives a brief introduction to micromachined vibratory gyroscopes by explaining their basic operation principles. Section 1.2 summarizes the micromachined vibratory gyroscope structures reported in the literature. Then, Section 1.3 provides an overview of readout and control electronics designed for vibratory MEMS gyroscopes. Section 1.4 introduces the gyroscope electronics developed at METU. Finally, Section 1.5 presents the research objectives and the thesis organization.

1.1. Micromachined Vibratory Gyroscopes

Micromachined vibratory gyroscope operation is based on a fictitious force called Coriolis force, named after Gaspard-Gustave de Coriolis, a French scientist, discovered the apparent deflection of an object from its straight path as the object is observed from a rotating frame of reference. Although the detailed analysis of Coriolis force is beyond the scope of this study, the most explicit example regarding this effect can be illustrated by Foucault's pendulum, which is a swinging pendulum that Leon Foucault, a French physicist, utilized to demonstrate the daily rotation of the Earth in mid-19th century. Figure 1.1 shows the behavior of Foucault's pendulum in response to Earth's rotation. Initially, the pendulum is driven into sustained oscillations along the y-axis. If the Earth is assumed to be stationary, the pendulum continues its linear vibration along the first oscillation mode. On the other hand, as the Earth is rotating about the z-axis, some of the vibration energy is transferred to the second mode along the x-axis due to induced Coriolis force, causing the pendulum to track an elliptical path from the view of an observer on the rotation frame.

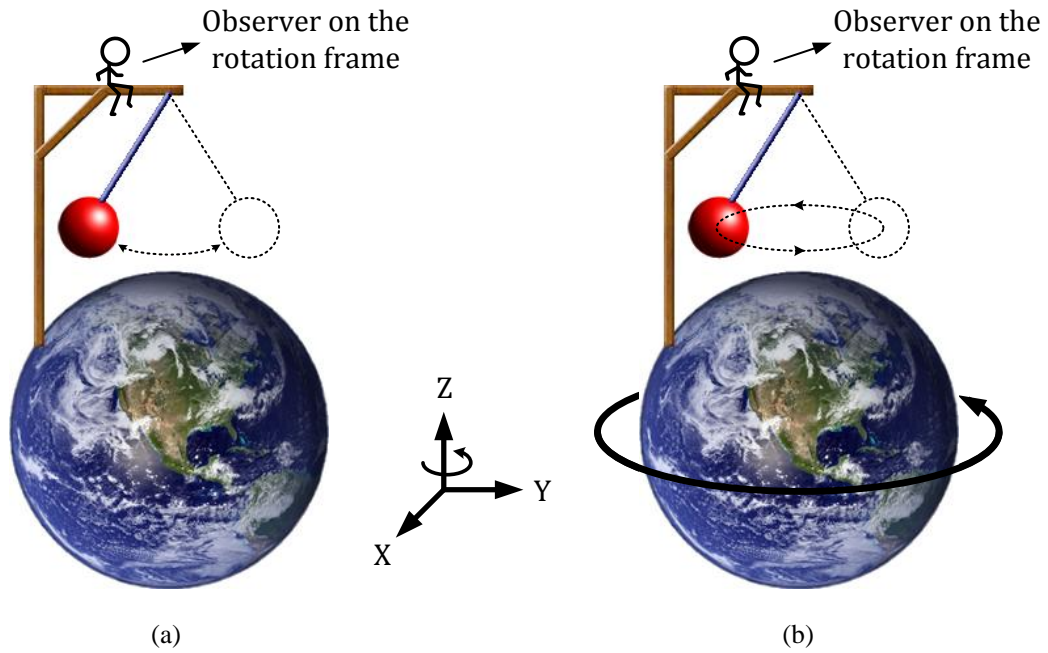


Figure 1.1: Behavior of Foucault's pendulum in response to Earth's rotation. (a) The pendulum tracks a linear path when the Earth is assumed to be stationary. (b) Path of the pendulum is observed to be elliptical due to Coriolis force induced by Earth's daily rotation.

Vibratory MEMS gyroscopes work according to the same principle concerning Foucault's pendulum, except the swinging pendulum is replaced with a vibrating mass attached to rotating frame by springs. Figure 1.2 shows a moving mass with two degrees-of-freedom (2-DOF), demonstrating the Coriolis-based micromachined vibratory gyroscope operation. In this simple gyroscope example, the inertial mass is continuously oscillated along the drive axis. If the gyroscope is rotated about its sensitive axis, which is orthogonal to the drive axis, some portion of the oscillation energy is transferred to the output axis due to Coriolis effect, where the output axis is orthogonal to both the drive axis and the sensitive axis. Since the amplitude of the Coriolis-induced oscillation is proportional to the applied angular rate, it is possible to extract the angular rate information by sensing the deflection along the output axis, which is at the frequency of sustained oscillation. In practical MEMS gyroscopes, the Coriolis-induced deflection in response to an angular rate is much smaller than the drive oscillations, even comparable to the atomic distances, making the design of readout electronics a challenging task.

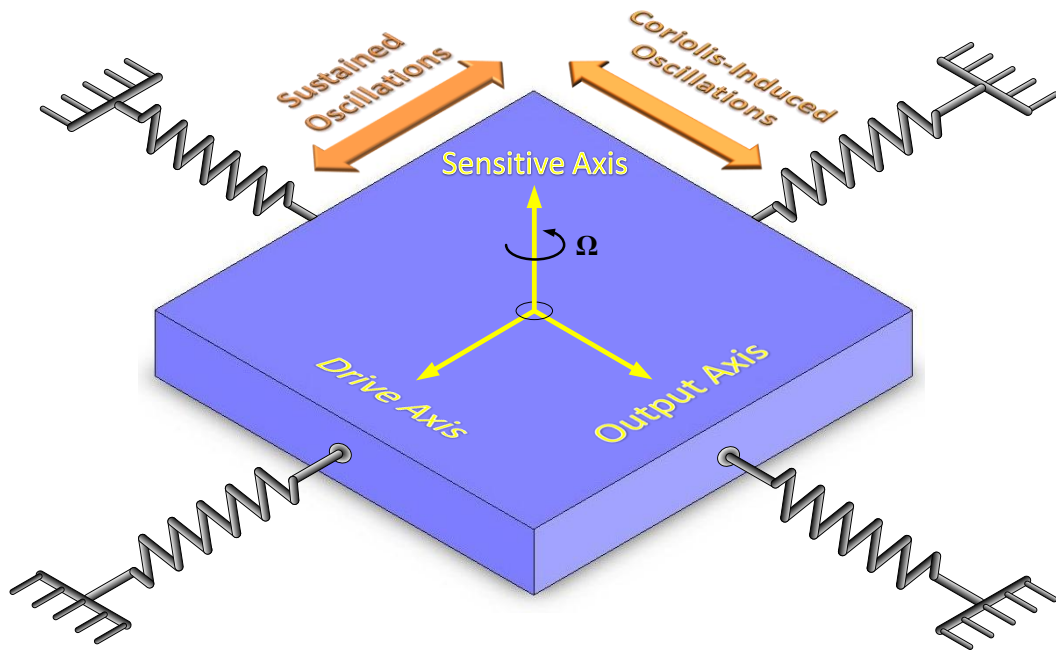


Figure 1.2: A moving mass with two degrees-of-freedom (2-DOF), demonstrating the Coriolis based micromachined vibratory gyroscope operation.

The actuation mechanism used for generating sustained vibrations in microgyroscopes may be electrostatic, electromagnetic, or piezoelectric. Moreover, in order to sense the Coriolis-induced oscillations, capacitive, piezoresistive, or piezoelectric detection mechanisms are commonly used. The micromachined vibratory gyroscopes developed at METU employ electrostatic actuation mechanism in the drive-mode and capacitive sensing in the sense-mode owing to superior performance provided by these mechanisms [8].

1.2. Overview of Micromachined Vibratory Gyroscopes

Many types of silicon-based micromachined vibratory gyroscopes have been demonstrated in the literature since late 1980's [1]. In 1991, The Charles Stark Draper Laboratory introduced one of the first batch-fabricated silicon micromachined vibratory gyroscopes, having a double gimbal structure [9]. The gyroscope has a rotation rate resolution of 4 deg/sec in 1 Hz measurement bandwidth. Due to

problems associated with gimbaled vibratory gyroscopes, later in 1993, Draper reported an improved micromachined tuning-fork vibratory rate gyroscope having 0.19 deg/sec resolution in 1 Hz bandwidth when operated at vacuum [10]. Figure 1.3 shows the SEM image of Draper's silicon-on-glass tuning-fork gyroscope. This gyroscope is electrostatically vibrated by using a set of interdigitated comb-drive fingers enabling vibration amplitudes up to 10 μm . The Coriolis-induced oscillations in response to applied angular rates are capacitively sensed in the sense-mode.

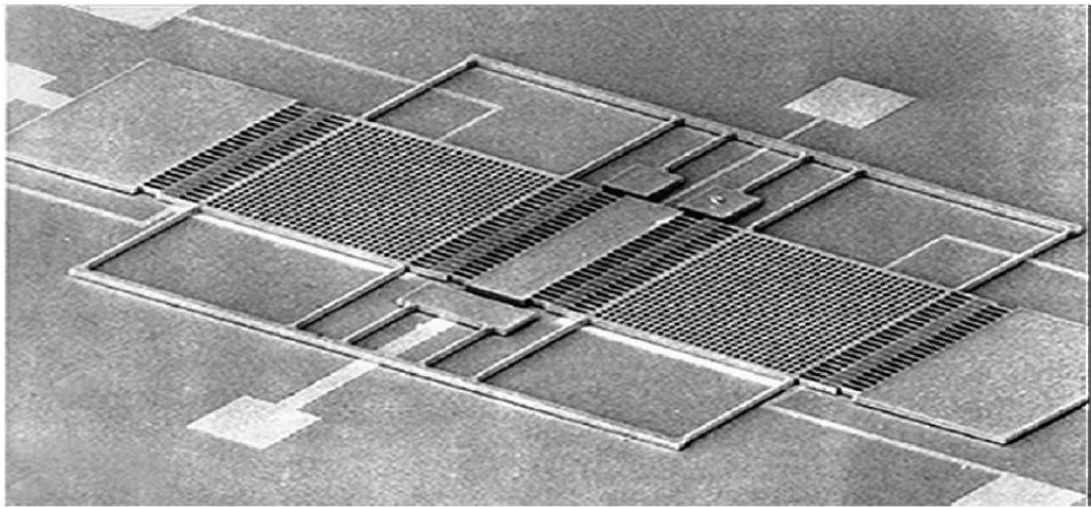


Figure 1.3: SEM image of Draper's silicon-on-glass tuning-fork vibratory gyroscope [10].

Another type of micromachined gyroscope having a symmetrical ring structure is first introduced by the University of Michigan [11]. The ring gyroscope allows the easy matching of the drive and sense modes as well as the electrostatic control of mass imbalances due fabrication tolerances. The improved versions of single-crystal silicon ring gyroscope demonstrate resolutions up to 10 deg/hr [12].

Moreover, there has been extensive research on monolithic gyroscopes enabling the integration of CMOS circuits with mechanical elements on the same die, minimizing the effect of interconnection parasitics. Carnegie Mellon University developed micromachined gyroscopes fabricated with CMOS-MEMS process. This technique involves post-processing of CMOS substrates containing both the mechanical sensor and the supplementary electronics [13, 14]. However, the fabricated devices suffer

from the curling after the releasing process due to the residual stress of the layers deposited in standard CMOS process. These devices demonstrate a resolution of 0.5 deg/sec in 1 Hz bandwidth. Another monolithic angular rate system is reported by University of Berkeley. The proposed system employs a surface-micromachined dual-axis gyroscope composed of 2- μm -thick polysilicon rotor disk [15]. Figure 1.4 shows the photograph of Berkeley's monolithic dual-axis gyroscope fabricated with Analog Devices' surface micromachining process. This symmetric gyroscope has an operation principle based on the rotational resonance of the rotor disk, demonstrating an angle random walk as low as 10 deg/ $\sqrt{\text{hr}}$.

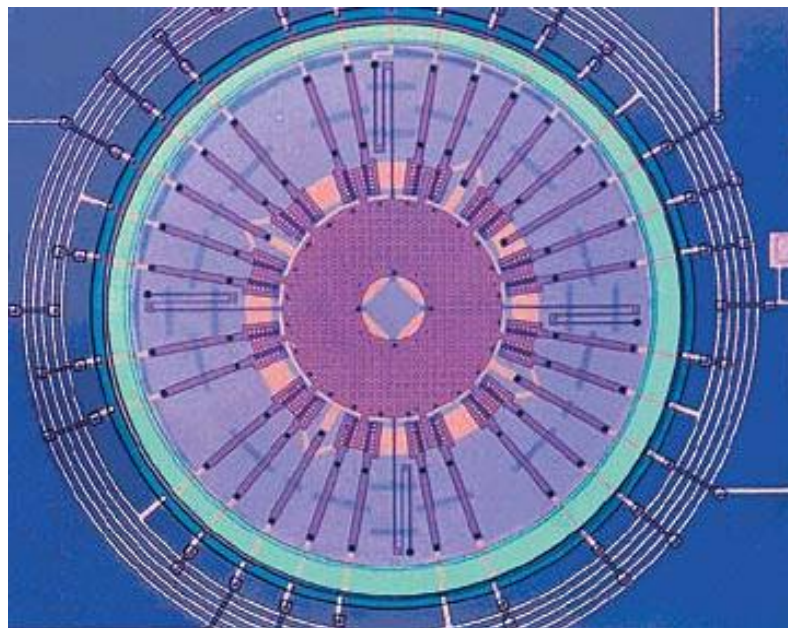


Figure 1.4: Photograph of the Berkeley's monolithic dual-axis gyroscope fabricated with Analog Devices' surface micromachining process [15].

Analog Devices has also developed surface micromachined monolithic gyroscopes using their state-of-the-art iMEMS process [16]. Figure 1.5 shows the die photograph of the iMEMS ADXRS gyroscope, composed of a tuning-fork mechanical element and on-chip signal processing electronics. Although structural thickness of the gyroscope is small compared to those of devices fabricated in bulk micromachining technologies, the sensor gives an impressive noise equivalent rate of

180 deg/hr in 1 Hz bandwidth owing to its high-quality on-chip readout electronics. Moreover, dual-mass tuning-fork structure together with differential readout electronics gives a g-sensitivity of 0.2 deg/sec/g. This device is currently in batch-fabrication to meet the increasing demand for MEMS gyroscopes in automotive, consumer, and industrial applications.

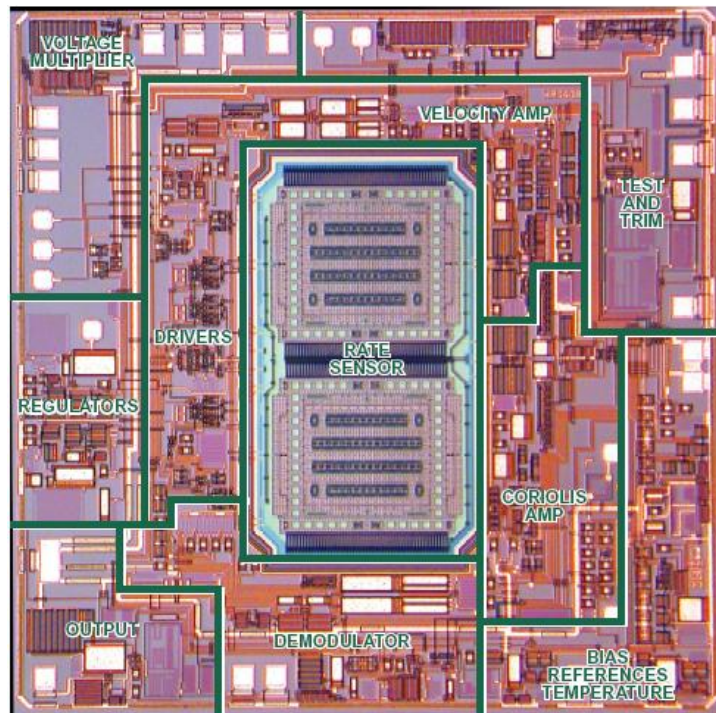


Figure 1.5: Die photograph of the iMEMS ADXRS gyroscope, composed of tuning-fork mechanical element and on-chip signal processing electronics [16].

In addition to monolithic solutions, gyroscope performances can also be increased by operating the gyroscope with matched sense and drive resonant modes. However, this requires closed-loop rate sensing electronics in the sense-mode due to bandwidth concerns. Mode matching also requires more complicated control electronics since the risk of instable operation increases in this mode. Recently, Georgia Institute of Technology reported a matched-mode tuning-fork gyroscope demonstrating an angle random walk of $0.045 \text{ deg}/\sqrt{\text{hr}}$, and a bias instability of 0.96 deg/hr [17]. Figure 1.6 shows the SEM picture of matched-mode z-axis tuning fork gyroscope fabricated on $50\text{-}\mu\text{m}$ thick SOI substrate.

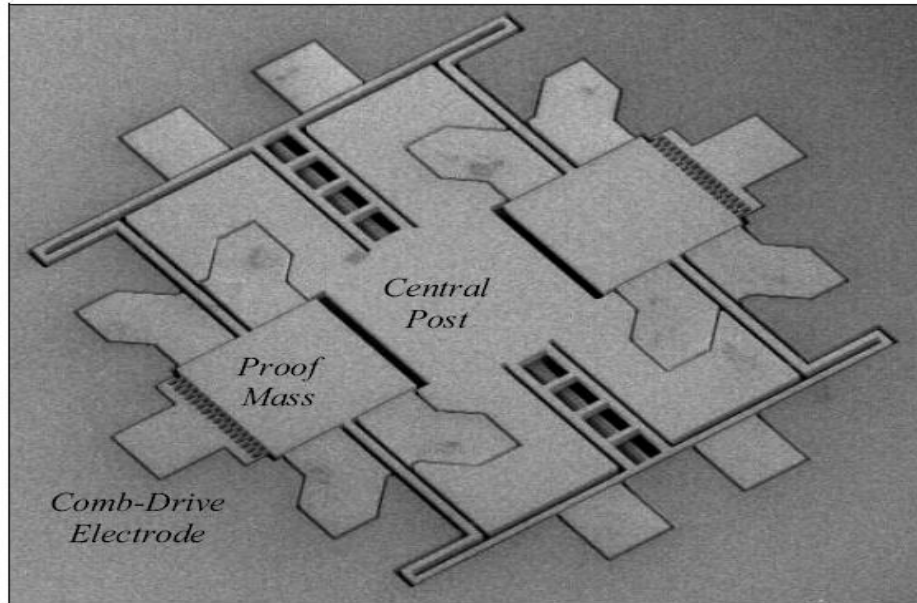


Figure 1.6: SEM picture of matched-mode z-axis tuning fork gyroscope fabricated on 50- μm thick SOI substrate [17].

There has been extensive research on micromachined vibratory gyroscopes also at METU since 1998. Various types of gyroscope structures have been developed using dissolved wafer process (DWP) [8, 18], nickel electroforming [8, 19, 20], silicon-on-insulator (SOI) [21, 22], and silicon-on-glass (SOG) [8, 23] micromachining technologies.

The first prototype of gyroscope fabricated in DWP micromachining process is a symmetrical and decoupled gyroscope employing varying-overlap-area type comb fingers both in the sense and drive modes in order to keep the structure completely symmetric [8]. Thus, the post-process electrostatic tuning for matched-mode operation is not applicable to this gyroscope because of the absence of varying-gap type capacitive comb fingers in the sense-mode. Figure 1.7 shows the SEM picture of the DWP gyroscope prototype and the close-up view of the comb fingers. The thickness of the structure is 12 μm while the measured gap spacing is 1.5 μm . Although the gyroscope is operated in the mismatch-mode at the ambient pressure, it gives rate-grade performance values.

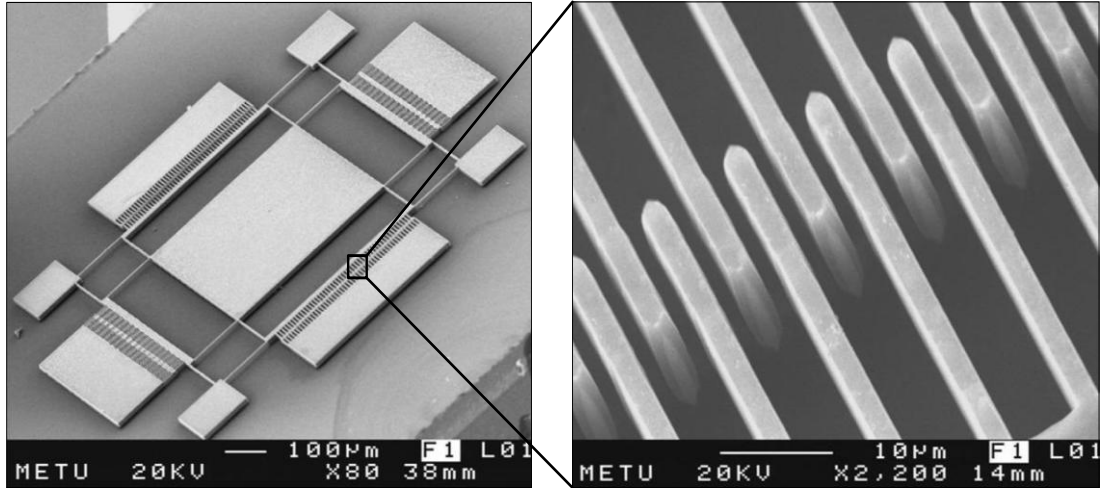
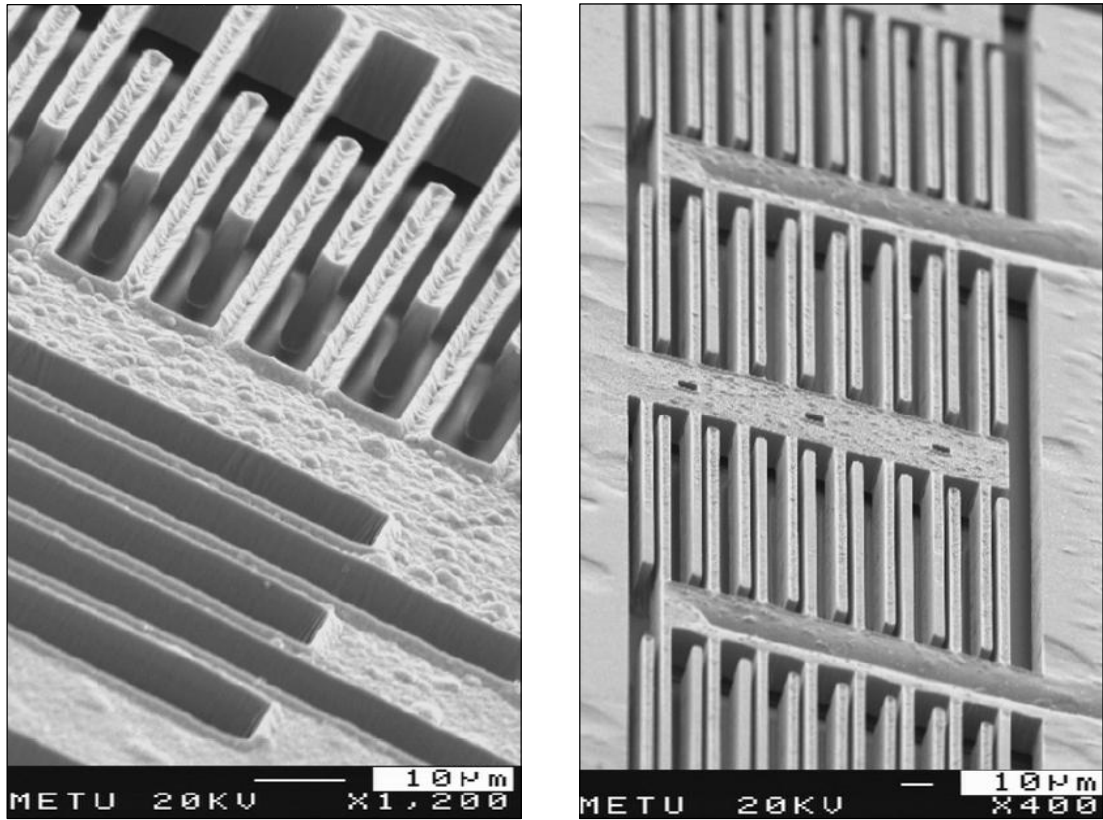


Figure 1.7: SEM picture of the DWP gyroscope prototype and the close-up view of the comb fingers [8].

The improved version of the symmetrical and decoupled gyroscope prototype is then fabricated by using nickel electroforming process [8]. In this process, a high-aspect ratio photoresist is used as the mold material and nickel is electroformed inside the thick photoresist. The gyroscope fabricated with this micromachining process employs varying-overlap-area comb electrodes in the drive mode and varying-gap type electrodes in the sense-mode, enabling electrostatic tuning of the sense-mode resonance frequency for mode matching. Figure 1.8 shows the close-up SEM photographs of the varying-overlap-area drive fingers and the varying-gap type sense fingers.

Then, an advanced symmetrical and decoupled gyroscope prototype is developed by using silicon-on-glass micromachining process [8]. Figure 1.9 shows the cross-section of the silicon-on-glass (SOG) structure. The SOG process starts with the silicon-glass anodic bonding. After patterning the Cr/Au pad metallization, the 100 µm-thick highly-doped single-crystal silicon substrate is anisotropically etched by using deep reactive ion etching (DRIE) until reaching to the glass substrate. Finally, the structure is released by isotropically etching the glass substrate. Thus, a suspended silicon structure anchored to the glass substrate through the anchor regions is obtained.



(a)

(b)

Figure 1.8: SEM photographs of (a) the varying-overlap-area drive fingers and (b) the varying-gap type sense fingers [8].

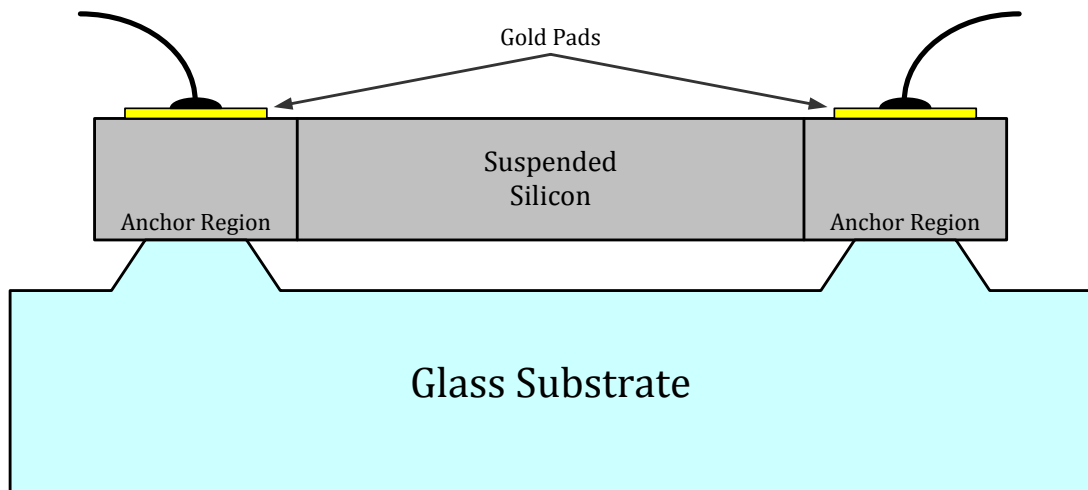


Figure 1.9: Cross-section of the silicon-on-glass (SOG) structure.

Figure 1.10 illustrates the SEM picture of the fabricated SOG gyroscope showing the drive and sense electrodes, flexures, perforated suspended frames, and anchors. This gyroscope structure uses the advantage of large-amplitude linear drive-mode vibrations, high-sensitivity sense electrodes with electrostatic frequency tuning capability, and highly-suppressed mechanical crosstalk between the modes, owing to its single and rigid sense-frame.

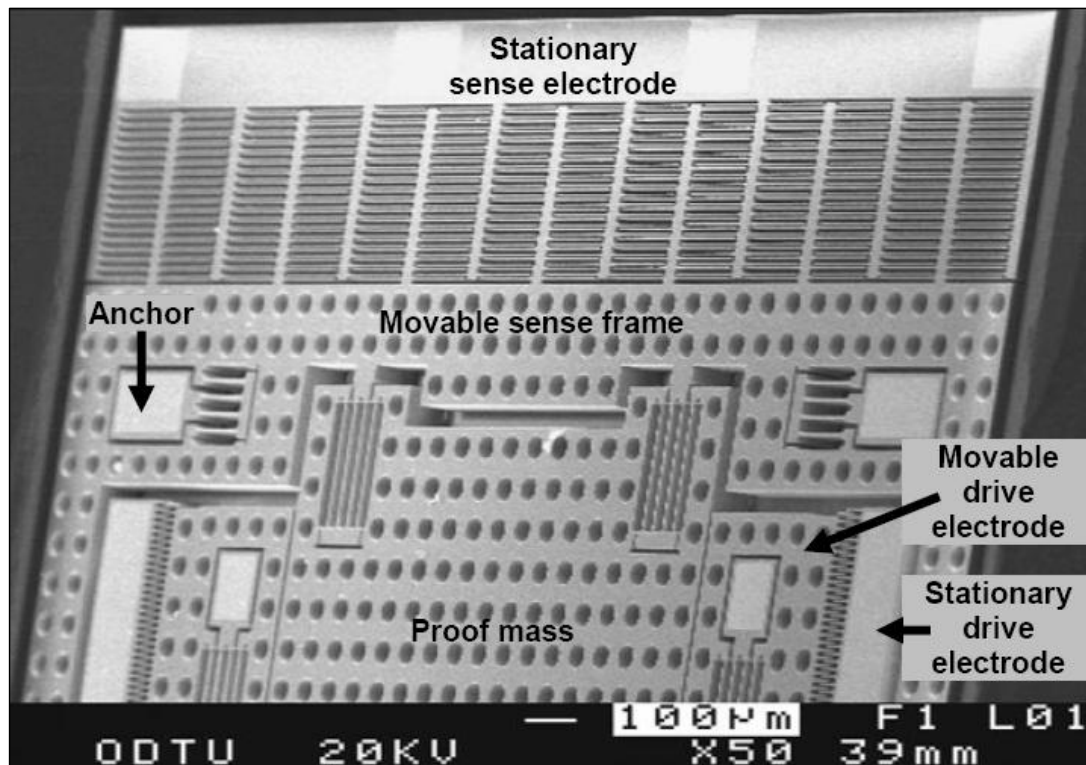


Figure 1.10: SEM picture of the fabricated SOG gyroscope showing the drive and sense electrodes, flexures, perforated suspended frames, and anchors [8].

Besides single-mass gyroscopes, multi-mass gyroscopes providing very low sensitivities against linear accelerations are also developed. The first prototype of the dual-mass gyroscope is fabricated using a commercial SOI-MEMS process of MEMSCAP[®] Inc. The process involves double-sided DRIE of an SOI wafer with 25 µm epitaxial thickness and 400 µm substrate thickness [22]. Figure 1.11 shows the SEM picture of the SOI dual-mass gyroscope designed at METU and fabricated at MEMSCAP[®] Inc.

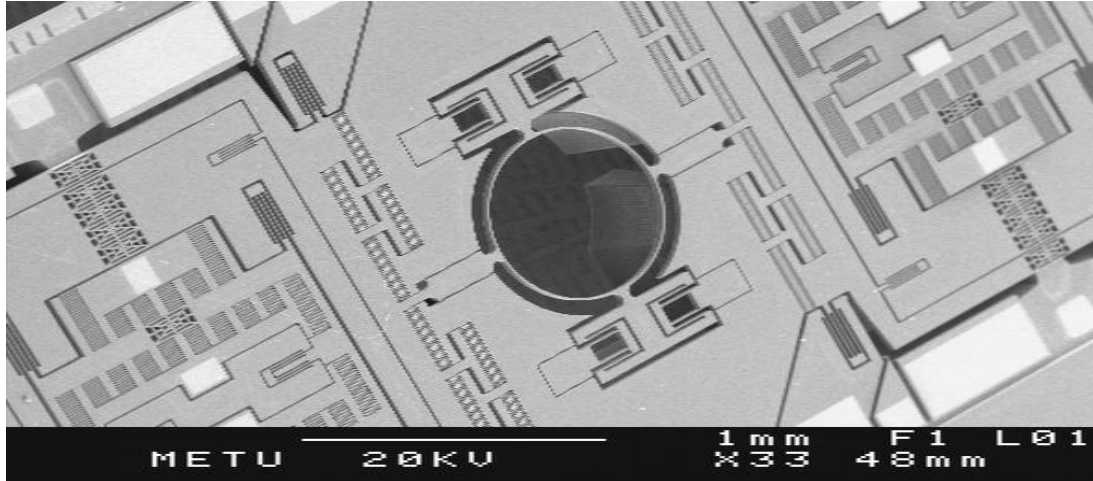


Figure 1.11: SEM picture of the SOI dual-mass gyroscope designed at METU and fabricated at MEMSCAP[®] Inc [22].

In this dual-mass gyroscope, a novel ring-shaped coupling mechanism is used in order to synchronize the movement of individual proof masses. When the gyroscope is driven into oscillation, these two masses oscillate in the opposite directions. Thus, each mass gives in-phase response to the common-mode accelerations and differential response to the angular rates. As the sense-mode output is read differentially, signals generated in response to undesired linear accelerations are suppressed while the rate information is doubled.

Another dual-mass gyroscope is currently under development in dissolved wafer process (DWP) for tactical-grade applications. The aim of this project is to fabricate wafer-level vacuum-packaged gyroscopes with very narrow finger gaps for achieving higher sensitivities. Figure 1.12 shows the cross-section of the vacuum-packaged DWP structure. In this process, silicon substrate having highly p-doped surface region with approximately 15 μm thick is patterned through DRIE. Then, the silicon wafer is bonded to the glass substrate having gold metallization on it. After that, the undoped silicon is dissolved in the ethylenediamine pyrocatechol (EDP) solution, until reaching the highly-doped structural silicon layer, leaving the sensor on the glass substrate. Finally, an anisotropically etched silicon cap is bonded to the structure, providing a constant vacuum ambient.

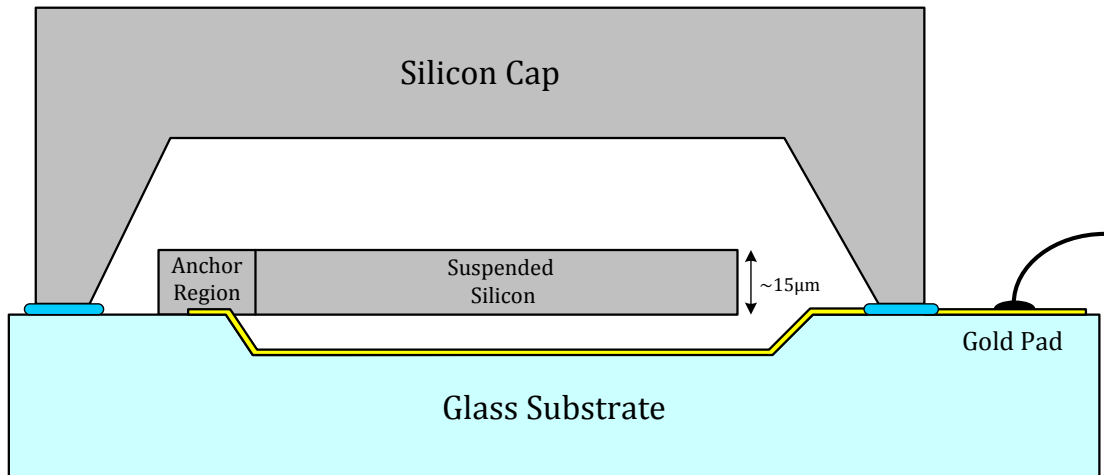


Figure 1.12: Cross-section of the vacuum-packaged DWP structure.

1.3. Overview of Readout and Control Electronics for Vibratory MEMS Gyroscopes

Never can micromachined inertial sensors be complete systems without supplementary electronics. In these systems, readout and control electronics provide a stable gyroscope operation and generate analog or digital signals proportional to the applied angular rate. In general, these electronics can be divided into three main parts: 1) Interface electronics that convert the displacement-induced capacitive variations in the mechanical element to the electrical signals, 2) drive-mode electronics sustaining self-triggered and constant amplitude vibrations in the drive-mode, and 3) sense-mode electronics that process the sense-mode interface output and give an angular rate related baseband signal by using open-loop or closed-loop rate sensing mechanisms. Moreover, additional electronic circuits are also employed in more complex angular rate systems for adaptively cancelling out the quadrature error introduced by fabrication tolerances, generating the necessary voltages to operate the gyroscope in the matched-mode, and compensating the sensitivity variations due to temperature changes.

First of all, high-performance capacitive-based MEMS gyroscopes require low-noise and parasitic-insensitive interface circuits for resolving capacitive changes in the order of zetto-farads. Among various types of capacitive sensor interfaces reported in the literature [24], the most popular ones are ac-bridge with voltage amplifier [25-27], transimpedance amplifier (TIA) [16, 28-30], switched-capacitor circuit [31, 32], and unity-gain buffer [11, 33].

Figure 1.13 shows the simplified block diagram of the chopper-stabilized ac-bridge preamplifier [27]. In this full-bridge configuration, differential sensor capacitances are driven by anti-phase clock signals, and the capacitance change is detected through voltage division. The output of the full-bridge structure is then amplified by a voltage amplifier having DC offset cancellation mechanism. Finally, the amplifier output at the frequency of applied clock signal is converted to a baseband signal by a synchronous demodulator. The main disadvantage of this interface is that it is sensitive to input parasitics, limiting the minimum detectable capacitance change. Thus, this type of capacitive interface is usually employed in monolithic sensors, where the parasitics introduced by interconnections are significantly minimized.

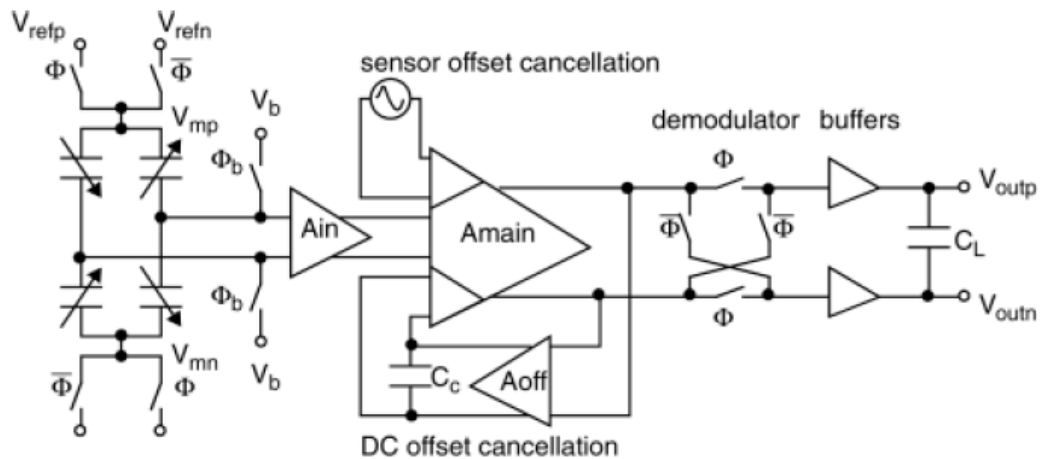


Figure 1.13: Simplified block diagram of the chopper-stabilized ac-bridge preamplifier [27].

Another popular type of capacitive interface is transresistance amplifier that converts the charge pumped by the sensor to the voltage on the impedance of a resistor or

capacitor feedback-connected to the OPAMP. In single-ended transimpedance amplifiers, the high-impedance node of the capacitive sensor is DC-biased through non-inverting terminal of the OPAMP. On the other hand, common-mode feedback (CMFB) mechanism together with feedback resistors biases the differential high-impedance nodes of the sensor in fully-differential interfaces. Figure 1.14 shows the circuit schematic of the Analog Devices' fully-differential transimpedance amplifier designed for high-sensitive capacitance-to-voltage conversion [16]. In this circuit, the switching-type controlled-impedance FET biasing structure provides an effective biasing resistance of $2.5 \text{ G}\Omega$ by switching a long MOSFET with a 1/50 duty-cycle clock. An impressive minimum detectable capacitance change of 12 zF ($1 \text{ zF}=10^{-21}$) is reported with this architecture. Although transimpedance amplifiers provide superior performance owing to their inherent insensitivity to parasitics, dominant poles in the feedback configuration may lead to potential stability problems.

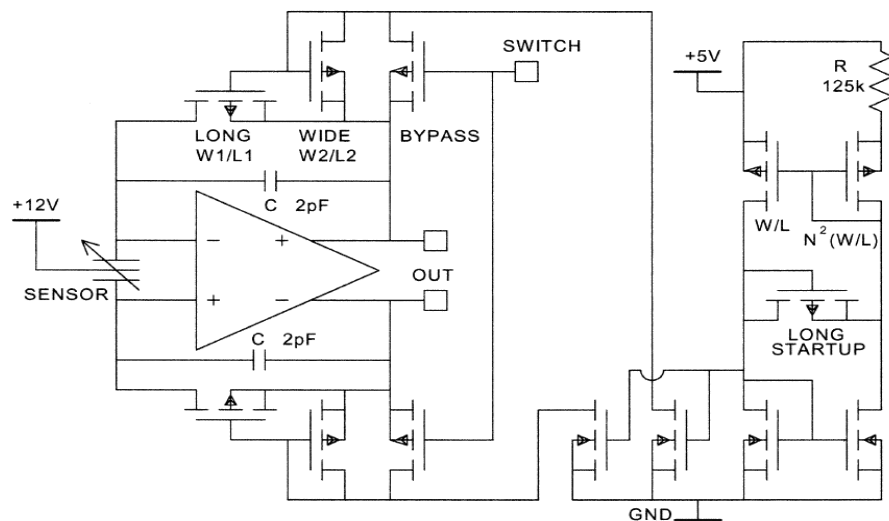


Figure 1.14: Circuit schematic of the Analog Devices' fully-differential transimpedance amplifier designed for high-sensitive capacitance-to-voltage conversion [16].

Furthermore, in switched-capacitor type interfaces, current pumped by the oppositely charged sensor capacitances is integrated on the feedback capacitor, which is reset after each integration cycle. Figure 1.15 shows the schematic view of a

fully-differential switched-capacitor front-end circuit for capacitive sensing applications [32]. This circuit is composed of a fully-differential charge integrator with correlated double sampling mechanism to reduce the offset and noise.

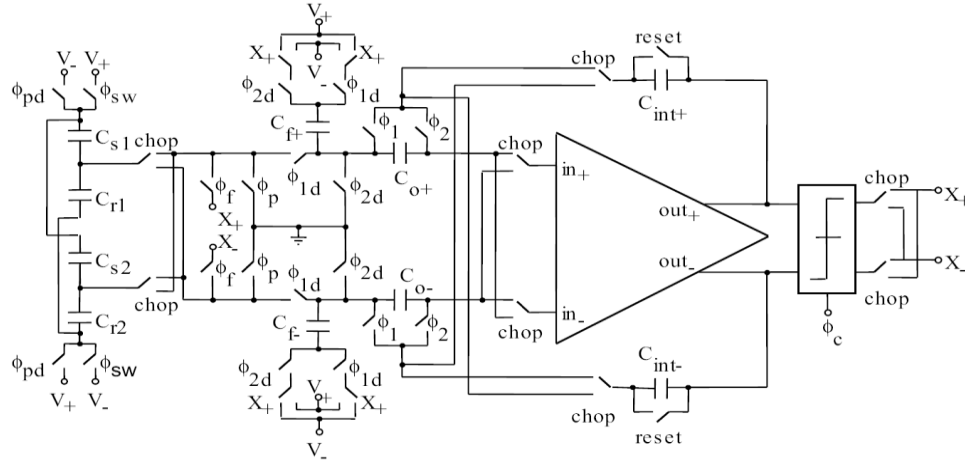


Figure 1.15: Schematic view of a fully-differential switched-capacitor front-end circuit for capacitive sensing applications [32].

The unity-gain buffer (UGB) is another type of interface that is commonly used in micromachined capacitive gyroscopes [11, 33]. UGB circuits provide high SNR values owing to their low input capacitances as the current generated by the sensor is converted to voltage on the input impedance of the buffer. Moreover, these circuits use the advantage of bootstrapping method for minimizing the parasitic capacitances associated with wirebonding pads. However, biasing the high-impedance node of the gyroscope may be problematic as the biasing resistances in the order of gigaohms are required for high-sensitive interfaces.

Besides interface electronics, drive-mode oscillation amplitude control and sense-mode signal processing circuits have dominant effect on the overall performance of an angular rate system. In micromachined gyroscopes employing continuous-time analog electronics, automatic gain control loops sustaining constant-amplitude oscillations in the drive-mode [34-36], and open-loop rate sensing mechanisms in the sense-mode are widely used. Figure 1.16 shows the simplified block diagram of the drive-mode automatic amplitude control and

sense-mode open-loop rate sensing electronics designed for micromachined gyroscopes developed at Georgia Institute of Technology [30].

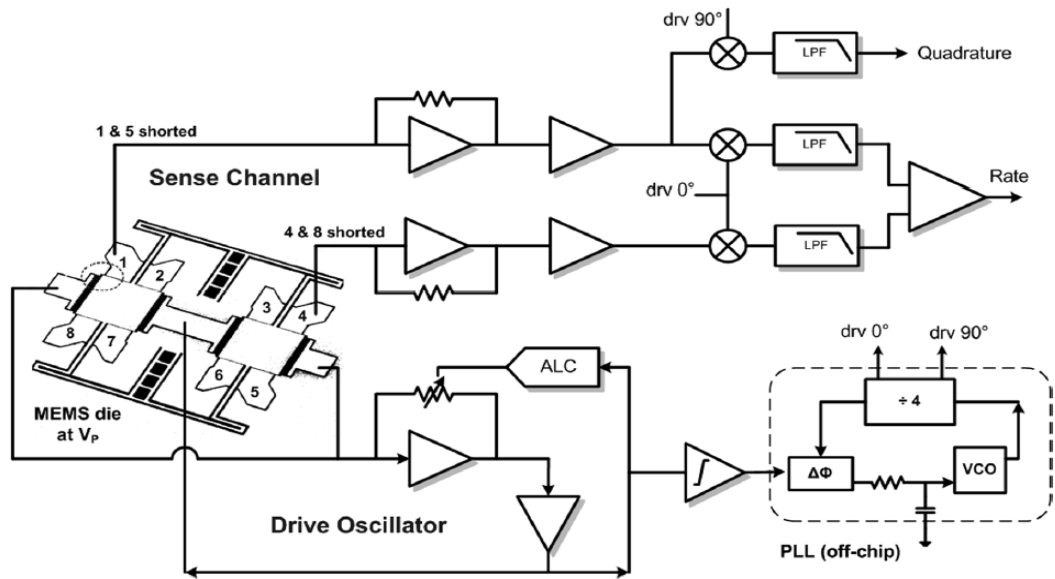


Figure 1.16: Simplified block diagram of the drive-mode automatic amplitude control and sense-mode open-loop rate sensing electronics designed for micromachined gyroscopes developed at Georgia Institute of Technology [30].

In this circuit, the drive-mode oscillation is sensed by a transresistance amplifier, where the feedback resistance is controlled by an automatic level controller (ALC) for constant-amplitude vibrations. Similarly, in the sense-mode, differential transimpedance amplifiers convert the resultant capacitive changes in response to an applied angular rate to voltage for further signal processing operations. Since the sense-mode transimpedance amplifier output is an amplitude-modulated signal at the frequency of drive-mode oscillations, a demodulator circuit composed of a multiplier followed by a low-pass filter transfers the signal to the baseband, where the carrier signal of the demodulator is generated by a PLL circuit connected to the drive-mode oscillator. In addition to analog electronics, there is also dedicated research on digital electronics developed for micromachined vibratory gyroscopes. Figure 1.17 shows the system-level block diagram of the digital control and readout electronics based on sigma-delta modulation [37].

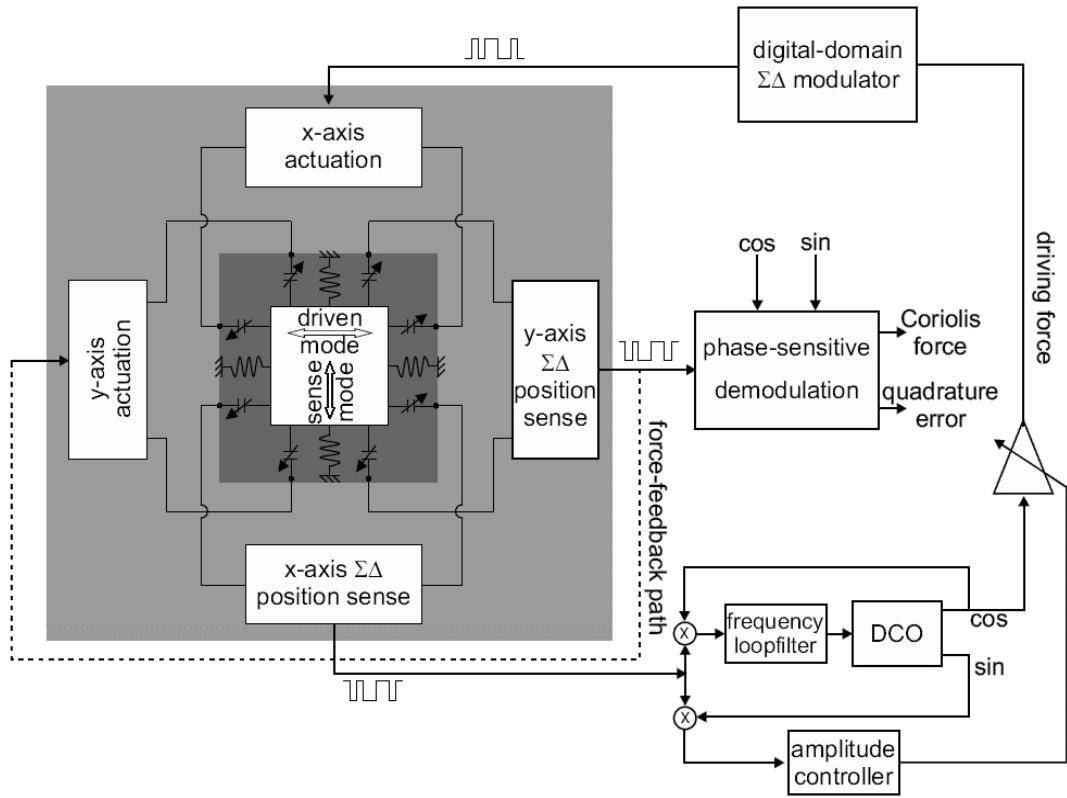


Figure 1.17: System-level block diagram of the digital control and readout electronics based on sigma-delta modulation [37].

In digital closed-loop rate sensing electronics, the force-feedback mechanism generates an electrostatic rebalancing force to damp the displacement of the proof mass in response to an angular rate [37-39]. Although this mechanism requires complicated electronics, it gives more linear response in a higher bandwidth since the sense-mode of the gyroscope is forced to be stationary. Sigma-delta modulators are used also in the drive-mode electronics in order to sustain constant amplitude oscillations by driving the gyroscope with digital pulse trains [37, 40-42]. Moreover, more complex gyroscope adaptive control algorithms enabling error compensation through parameter estimation are developed [43, 44]. Recently, adaptive control mechanisms using Lyapunov approach are also introduced [45-47]. However, these complex algorithms are beyond the scope of this thesis.

1.4. Gyroscope Electronics Developed at METU

At METU, research on gyroscope electronics has been mostly focused on interface electronics. The first capacitive interface prototype developed at METU is a closed-loop ac-bridge with correlated double sampling (CDS) mechanism [48]. The circuit is fabricated in the standard $0.8\ \mu\text{m}$ n-well CMOS process of AMS foundry. Although it cannot be tested with a MEMS gyroscope, it is verified that the proposed circuit has a capacitance change to voltage sensitivity of $45\ \text{mV/fF}$.

The next generation capacitive interface is a unity-gain buffer (UGB), where the high-impedance node of the gyroscope is biased with a MOS transistor operating in cut-off region [8, 20]. Figure 1.18 shows the circuit schematic of the UGB type capacitive interface developed at METU. Although the circuit provides higher sensitivities owing to its very small input capacitance, high-impedance node biasing strategy is problematic since the transistor operating in cut-off region cannot properly bias the sensor node. The improved versions of the UGB structure have been designed [49]. Nevertheless, they also suffer from static discharge and high-impedance node biasing problems causing instabilities in the gyroscope operation.

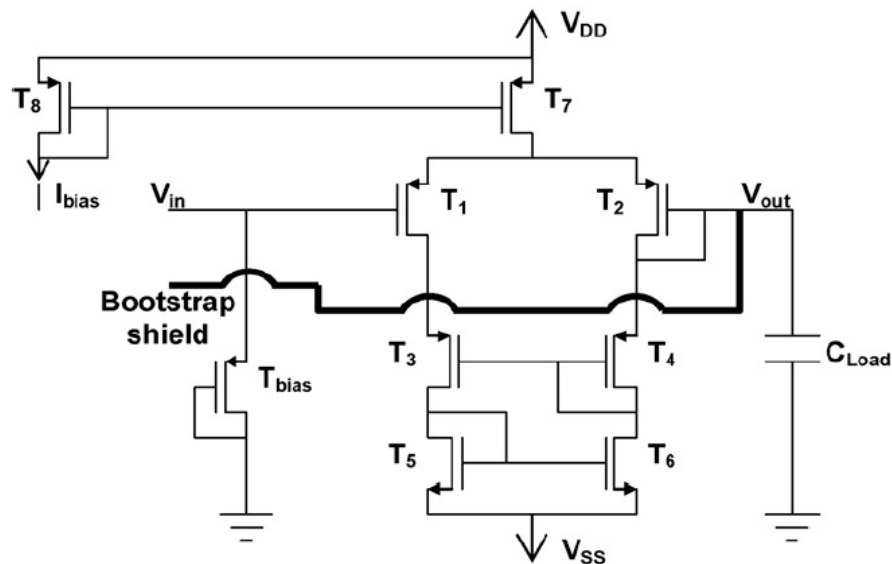


Figure 1.18: Unity-gain buffer (UGB) type capacitive interface developed at METU [8, 20].

After that, single-ended and differential source follower circuits involving stable high-impedance node biasing architectures are introduced [50]. Figure 1.19 shows the circuit schematic of the single-ended source follower biased with subthreshold NMOS transistor. In this design, the channel resistance of the high-impedance node biasing MOS transistor is controlled by an externally applied floating voltage supply. According to the noise tests, it is verified that the proposed interface circuit can resolve 58.3 zF of capacitance change in 1 Hz bandwidth. After hybrid-connecting the circuit to the SOG gyroscope fabricated at METU, bias instability and angle random walk values are found as 124.7 deg/hr and 2.158 deg/ $\sqrt{\text{hr}}$, respectively. On the other hand, this interface introduces some problems as well. First, due to DC voltage drop on the input transistor of the source follower, DC level of the output voltage should be manually controlled by an external bias voltage applied to the source terminal of the biasing transistor. Moreover, it is observed that channel resistance of the subthreshold transistor highly depends on the fabrication tolerances. Finally, according to circuit simulations, the single-ended source follower demonstrates low PSRR because of the high gain from the supply node to the output.

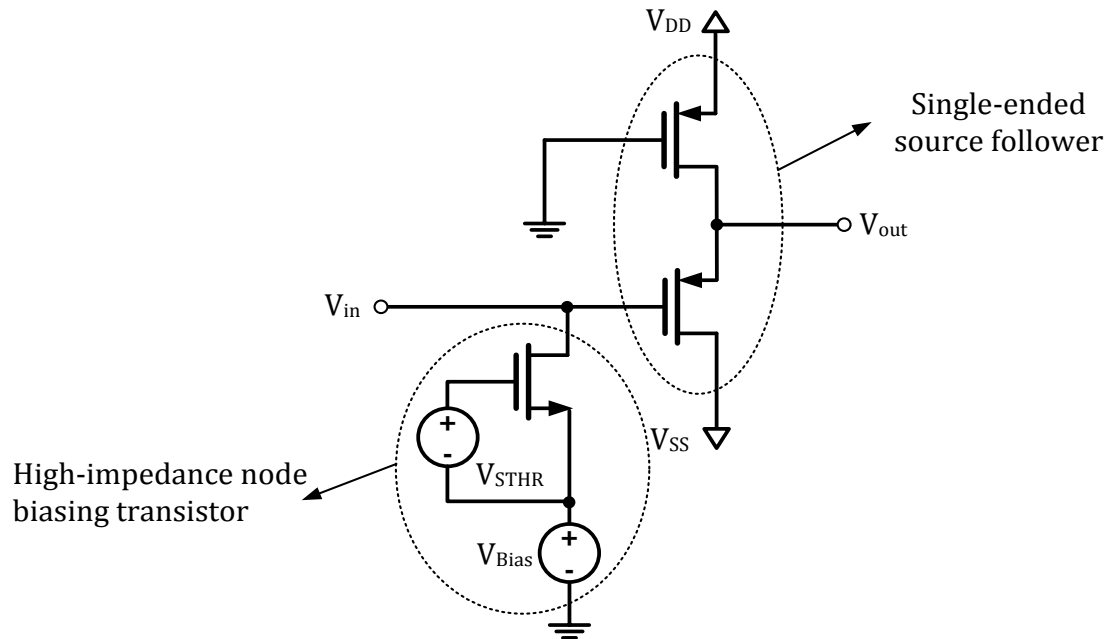


Figure 1.19: Single-ended source follower biased with subthreshold NMOS transistor [50].

In addition to CMOS capacitive interfaces, drive-mode self-resonance circuits and sense-mode rate sensing electronics are also developed for characterization of the fully-functional angular rate systems. Although drive-mode electronics enable sustained oscillations, the absence of an amplitude control mechanism limits the overall performance of the gyroscope at the vacuum, causing large bias instability values. Moreover, the gyroscopes demonstrate high zero-rate offset and low sensitivity values. Thus, it is concluded that fabricated mechanical sensors would give superior performance with more advanced electronics.

1.5. Research Objectives and Thesis Organization

The goal of this research is to develop advanced readout and control electronics for high-performance micromachined angular rate sensors developed at METU. These electronics consist of different types of sensor interfaces, single-ended and differential oscillation control circuits, and high-precision open-loop rate sensing mechanisms, implemented by using both commercial discrete components and the CMOS technology. The specific objectives of this research are listed as follows:

1. Design and implementation of a very compact and reliable printed circuit board (PCB) composed of a single-ended self-resonance loop with manual amplitude control and a single-ended AM demodulator. This PCB should sustain drive-mode vibrations exactly at the mechanical resonance frequency of the gyroscope, and enable manual control on the vibration amplitude. It should also convert the modulated sense-mode output to a baseband signal which is proportional to the applied angular rate. Moreover, it should be adaptable to any type of micromachined vibratory gyroscope for preliminary performance tests.
2. Development of a fully-functional angular rate system for silicon-on-glass (SOG) gyroscopes, implemented with discrete components. The advanced control electronics used in this system should provide self-triggered, constant-amplitude, and stable oscillations independent of sensor parameters

and ambient conditions. It should drive the single-ended SOG gyroscope with an amplitude-controlled sinusoidal signal at the mechanical resonance frequency of the gyroscope in order to get rid of the possible performance-decreasing effects of square-wave driving signals, which are widely used in similar systems. Then, the complete system should be characterized in terms of scale-factor, linearity, dynamic range, angle random walk, bias instability, and zero-rate output.

3. Design of differential readout and control electronics for dual-mass gyroscopes. Whole electronics including the transresistance amplifier type interfaces, the self-resonance circuit with automatic amplitude control mechanism, and the sense-mode phase-sensitive rate signal extraction circuit should be integrated on an extremely small PCB, minimizing the effect of parasitics. Transient characteristics of the differential automatic oscillation amplitude control circuit in response to step changes in the proof mass and the amplitude set voltages should be obtained. Performance tests for the overall system employing the vacuum packaged dual-mass gyroscope as the mechanical element should be carried out.
4. Design of CMOS differential unity-gain buffer (UGB) and transimpedance amplifier (TIA) type capacitive and resistive interfaces. Resistive interfaces should bias the high-impedance nodes of the differential drive-mode outputs through low-doped polysilicon resistors. Moreover, they should convert the charge pumped by the gyroscope to the voltage with a phase error less than 1° . Similarly, high-sensitive capacitive interfaces should bias the high-impedance nodes via MOSFETs operating at subthreshold region, providing channel resistance in the order of gigaohms.
5. Development of CMOS fully-differential automatic oscillation amplitude control circuit for sustaining balanced and controlled vibrations in dual-mass gyroscopes. The complete electronics except the large capacitors should be implemented on-chip. Fully-differential variable gain amplifier (VGA) used

in this loop should generate exactly anti-phase driving signals having common-mode level of 0 V through common-mode feedback (CMFB) mechanism. In addition to this, on-chip single-ended to differential convertor designed for single-ended external drive-mode electronics should generate anti-phase differential signals with minimum phase error from the applied single-ended signal. Moreover, a CMOS single-ended to differential convertor circuit generating exactly anti-phase driving signals should be designed for angular rate systems having single-ended drive-mode external electronics.

6. Design of CMOS fully-differential open-loop rate sensing electronics for dual-mass gyroscopes. This circuit should take differential carrier signals from the drive-mode and transfer the sense-mode interface output at the frequency of drive-mode oscillation to a baseband signal by using a full-wave rectifier followed by a low-pass filter. Finally, CMOS sense-mode and drive-mode electronics should be hybrid-connected to a dual-mass gyroscope, and the overall angular rate system should be characterized.

The organization of this thesis and the summary of the following chapters are presented as follows:

Chapter 2 briefly introduces the theory of micromachined vibratory gyroscopes in the electromechanical domain. Then, it provides the governing equations of gyroscope dynamics and transduction mechanisms in order to construct the generalized electrical equivalent model of the mechanical sensor. This chapter also gives the theory behind the vibratory gyroscope electronics by presenting the capacitive and resistive interface electronics, self-oscillation principle and automatic amplitude control mechanisms, and sense-mode rate output extraction electronics.

Chapter 3 provides the design details and simulations of readout and control electronics for vibratory gyroscopes developed at METU. First, it presents single-ended and differential gyroscope electronics implemented with commercial

discrete components. The operation of the advanced oscillation amplitude control circuit is verified through system-level simulations in SIMULINK. In addition, details of two different types of CMOS interface circuits, fully-differential amplitude-controlled self-oscillation loops, and sense-mode open-loop rate sensing electronics, which are all designed in standard 0.6 μ m CMOS process provided by XFAB, are given in this chapter. It also presents the results of transistor-level simulations of the designed CMOS circuits connected to the equivalent electrical model of the MEMS gyroscope.

Chapter 4 presents the results of the tests performed on discrete and CMOS electronics developed in this research. Performance characteristics demonstrated by fully-functional angular rate systems implemented with commercial discrete components are given in terms of scale factor, linearity, zero-rate offset, angle random walk, and bias instability. Moreover, the results of transient, AC, and noise tests performed on CMOS capacitive and resistive interfaces are presented. This chapter also gives the results of verification tests of CMOS circuits designed for drive-mode oscillation amplitude control and sense-mode signal processing.

Finally, Chapter 5 summarizes this research and gives the conclusions. Moreover, this chapter provides the suggestions for the related studies in the future.

CHAPTER 2

THEORY OF VIBRATORY GYROSCOPES

This chapter presents the basic theory of vibratory gyroscopes in both mechanical and electrical domains. A complete angular rate system powered by an electrical supply and providing analog/digital output proportional to the applied angular rate is composed of mechanical elements and complementary electronics. In this respect, the theory behind the micromachined gyroscope system is required to be studied in an electromechanical design perspective. Section 2.1 briefly explains the mechanics of drive and sense modes by presenting the fundamental equations of the vibratory gyroscope dynamics. Section 2.2 gives the principles of electrostatic actuation and capacitive sensing mechanisms together with the explanation of electrostatic spring effect. Section 2.3 provides the generalized electrical equivalent model of the mechanical element, which is connected to the electronic circuits in SPICE simulators. Section 2.4 describes the basic principles of drive and sense mode electronics. In this section, the theories behind capacitance-to-voltage conversion, self-oscillation and AM demodulation are studied and, in addition, the governing equations of proposed automatic oscillation amplitude control circuit are derived. Finally, Section 2.5 gives a summary of this chapter.

2.1. Mechanical Theory of Vibratory Gyroscopes

The micromachined vibratory gyroscope operation is based on the principle that “while the drive-mode is resonating in one axis, perpendicularly placed sense-mode detects the induced Coriolis acceleration in response to angular rate input, which is orthogonal to both drive-mode and sense-mode axes.” The drive-mode oscillations may also mechanically couple to the sense-mode due to misalignments and

tolerances in the fabrication process, causing unpredictable output offset and the sense-mode electronics to saturate even in the absence of angular rate input. Thus, the gyroscopes used in this research have fully-decoupled and balanced structures to minimize the mechanical crosstalk between the drive and sense modes [8, 51]. Decoupling is achieved by limiting the motion of drive and sense electrodes to one degree-of-freedom (1-DOF) and the proof mass to 2-DOF with the help of flexible beams. In this aspect, dynamics of the mechanically decoupled drive and sense modes are analyzed separately in the following subsections.

2.1.1. Mechanics of the Drive-Mode Resonator

The drive-mode of the gyroscope can be considered as a mechanical resonator whose structure is identical to a second-order mass-spring-damper system with flexible beams, movable drive-mode masses, and the damping of surrounding gas in the ambient. Assuming an ideal second-order system, relation between the applied force and the resulting displacement can be expressed by the transfer function given as

$$\frac{X_D}{F_D}(s) = \frac{1}{m_D \cdot s^2 + b_D \cdot s + k_D} \quad (2.1)$$

where F_D is the force acting along the drive axis, X_D is the resulting deflection, m_D is the total mass, b_D is the damping coefficient, k_D is the total spring constant, and the subscript D denotes the drive-mode. Equation (2.1) can also be expressed in terms of mechanical resonance frequency, ω_D , and quality factor, Q_D , as

$$\frac{X_D}{F_D}(s) = \frac{1/m_D}{s^2 + (\omega_D/Q_D)s + \omega_D^2} \quad (2.2)$$

where,

$$\omega_D = \sqrt{\frac{k_D}{m_D}} \quad (2.3)$$

$$Q_D = \frac{\sqrt{k_D \cdot m_D}}{b_D} \quad (2.4)$$

For $s = j\omega_D$, which means that the gyroscope is driven at the mechanical resonance frequency of the drive-mode, the denominator of Equation (2.2) reaches its minimum value, giving simplified force-deflection relation as

$$\frac{X_D}{F_D}(j\omega_D) = \frac{Q_D}{j \cdot k_D} \quad (2.5)$$

Equation (2.5) corresponds to the maximum achievable deflection with the minimum applied force providing maximum energy efficiency only at the mechanical resonance frequency. This shows that in order to increase the available deflection, quality factor of the system should be increased by either decreasing the damping coefficient or increasing the mass. It can also be concluded that the deflection lags the applied force by 90° at the resonance condition. This resultant phase shift should be considered while constructing the self-resonance loop, which is described in detail in Section 2.4.2.

2.1.2. Coriolis Coupling and Mechanics of the Sense-Mode Accelerometer

As the vibrating proof mass experiences an angular rate along the rotation axis, a self-induced fictitious force, which is due to Coriolis coupling, deflects the proof-mass along the sense-mode axis. This deflection is then sensed by the sense-mode accelerometer composed of capacitive sensing electrodes. Although the detailed derivations of the Coriolis force [8, 51] are beyond the scope of this study,

for the constant angular rate input about the z-axis and drive-mode vibration along the x-axis, the approximated expression for the Coriolis force acting on the proof-mass along the y-axis is given as [8]

$$F_{Coriolis,y}(t) = -2 \cdot m_{pm} \cdot \Omega_z \cdot \dot{x}(t) \quad (2.6)$$

where m_{pm} is mass of the proof-mass, Ω_z is the time-independent angular rate input, and $\dot{x}(t)$ is the velocity of the drive-mode oscillation.

Like drive-mode resonator, sense-mode accelerometer also behaves as a mass-spring-damper system where electrostatic force actuating the drive-mode is replaced by Coriolis force, and drive-mode mechanical parameters are changed with those of sense-mode. Then, the force-deflection relation for the sense-mode is expressed as

$$\frac{Y_S}{F_{Coriolis}}(s) = \frac{1}{m_S \cdot s^2 + b_S \cdot s + k_S} \quad (2.7)$$

where m_S is sum of the mass of sense electrodes and the proof-mass, b_S is the damping acting on the system, and k_S is the total spring constant of the sense-mode.

Furthermore, for time-varying angular rate inputs, which is the case in many practical applications, the analysis of sense-mode dynamics gets more complicated. When a time-varying angular rate input at frequency of ω_z is applied to the gyroscope system about the z-axis, then the Coriolis force, thus the resulting deflection along the sense axis is modulated by the drive-mode resonance frequency. In this case, base-band angular rate input is transferred to higher frequencies, having two components equally separated from the drive-mode in the frequency domain. This fact can be expressed more clearly by inserting the time-dependent version of Equation (2.6) into Equation (2.7), and analyzing each component separately. Then, frequency domain expressions of sense-mode deflection are simplified as follows [8]

$$Y(\omega_D + \omega_z) = \frac{2 \cdot \pi \cdot \Omega_z \cdot x_D \cdot \frac{m_{pm}}{m_S} \cdot \left(\omega_D + \frac{\omega_z}{2}\right)}{(\omega_S^2 - (\omega_D + \omega_z)^2) + j(\omega_D + \omega_z) \cdot \frac{\omega_S}{Q_S}} \quad (2.8)$$

$$Y(\omega_D - \omega_z) = \frac{2 \cdot \pi \cdot \Omega_z \cdot x_D \cdot \frac{m_{pm}}{m_S} \cdot \left(\omega_D - \frac{\omega_z}{2}\right)}{(\omega_S^2 - (\omega_D - \omega_z)^2) + j(\omega_D - \omega_z) \cdot \frac{\omega_S}{Q_S}} \quad (2.9)$$

These equations can be simplified further according to the difference between resonance frequencies of drive and sense modes. If the difference is very small, i.e., $\omega_D \cong \omega_S$, then the operation is called as matched-mode. Assuming that the input rate frequency is much lower than the drive and sense mode resonance frequencies, i.e., $\omega_z \ll \omega_{D,S}$, Equations (2.8) and (2.9) are approximated in single expression given as

$$Y(\omega_D) \approx \frac{2 \cdot \Omega_z \cdot x_D \cdot Q_S}{\omega_D} \cdot \frac{m_{pm}}{m_S} \quad (2.10)$$

On the other hand, in the mismatched-mode of operation, sense-mode resonance frequency is much higher than that of drive-mode, i.e., $\omega_D \ll \omega_S$. With the assumption of small rate input frequency, $\omega_z \ll \omega_{D,S}$, Equations (2.8) and (2.9) are simplified to

$$Y(\omega_D) \approx j \frac{\Omega_z \cdot x_D}{(\omega_S - \omega_D)} \cdot \frac{m_{pm}}{m_S} \quad (2.11)$$

Comparing the Equations (2.10) and (2.11), it is observed that matching of the resonance frequencies boosts the sensitivity considerably, because of the fact that Coriolis motion at the frequency of the drive-mode oscillation is amplified by the mechanical quality factor of the sense-mode. However, as the quality factor of the

sense mode increases, response bandwidth decreases, which is the limiting trade-off for matched-mode operation in gyroscopes having open-loop rate sensing electronics. In practice, slightly mismatch operation is usually preferred for wider bandwidth with sufficient sensitivity. It should also be noted that there is a 90° phase difference between the deflections of matched and mismatched modes. This property should be considered in the phase-sensitive demodulation of the raw sense-mode output in order to reduce the loss in sensitivity due to phase errors.

2.2. Electrostatic Actuation and Capacitive Sensing Mechanisms

Mechanical analysis describing the force-displacement dynamics is not sufficient to predict overall behavior of the vibratory gyroscope. Transduction mechanisms, which are generation of the actuation force for drive-mode vibrations and capacitive sensing of the physical deflections in the sense-mode, should also be analyzed to construct the complete electromechanical model of the gyroscope. This section describes the basic principles behind the electrostatic force generation through parallel-plate capacitors and current injection from a varying capacitance in capacitive sensing mechanism, together with the use of electrostatic spring effect in mode-matching.

2.2.1. Electrostatic Actuation Using Parallel-Plate Capacitors

Electrostatic actuation is based on a basic physics law stating that two charged and isolated conductive plates biased with a potential difference attract each other. As the plates get closer, capacitance between the plates increases, so does the stored energy, inducing more net attraction force. If one of the plates is fixed and the other one is movable, applied electrical energy generates an attractive force which tends to dissipate the stored energy by pulling the moving plate to the stationary plate. Then, Figure 2.1 shows a typical parallel-plate capacitor configuration that is widely used in transduction mechanisms of micromachined vibratory gyroscopes.

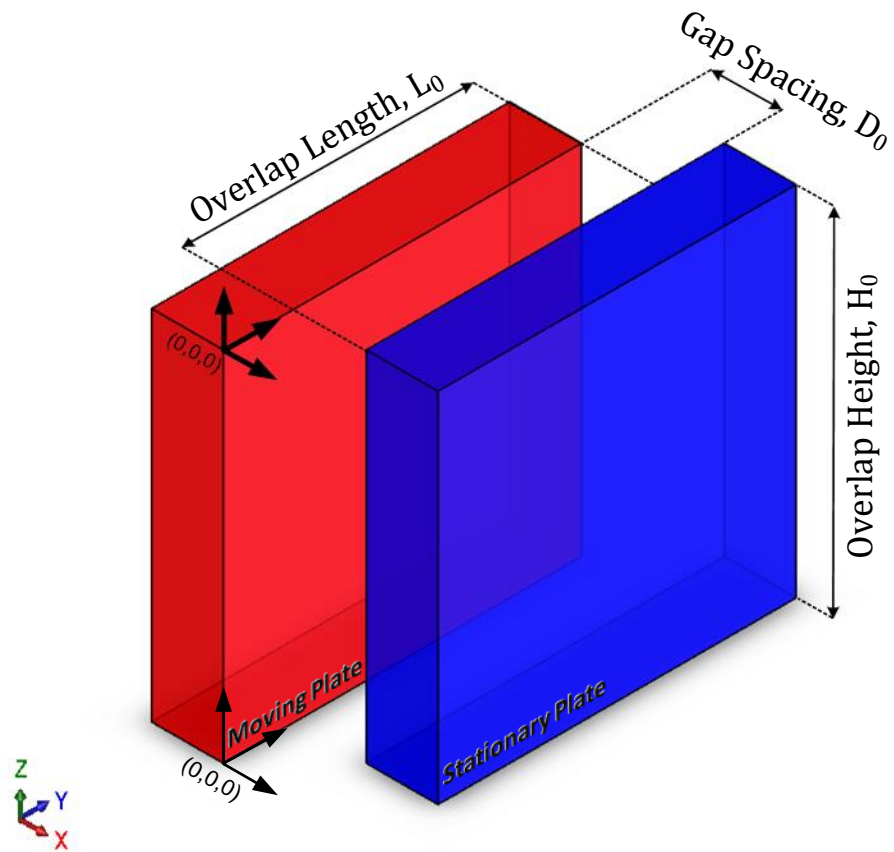


Figure 2.1: Typical parallel-plate capacitor configuration that is widely used in transduction mechanisms of micromachined vibratory gyroscopes.

The position dependent capacitance expression of the parallel-plate capacitor configuration in Figure 2.1 is given as

$$C = \alpha \cdot \epsilon_0 \frac{L(y) \cdot H(z)}{D(x)} \quad (2.12)$$

$$L(y) = L_0 + y \quad (2.13)$$

$$H(z) = H_0 + z \quad (2.14)$$

$$D(x) = D_0 - x \quad (2.15)$$

where α is the correction factor for fringing fields, ϵ_0 is the permittivity of air, $L(y)$ is the overlap length, $H(z)$ is the overlap height, and $D(x)$ is the gap spacing between the plates. The general expression of energy stored in the capacitor is defined as

$$E = \frac{1}{2} \cdot C \cdot V^2 \quad (2.16)$$

where V is the potential difference between the capacitor plates. Because generated electrostatic force is specified as the position gradient of the energy, taking the partial derivatives of energy with respect to x-y-z position vectors yields

$$F_x = \frac{\partial E}{\partial x} = \frac{1}{2} \cdot \frac{\partial C}{\partial D} \cdot \frac{\partial D(x)}{\partial x} \cdot V^2 = \frac{1}{2} \cdot \alpha \cdot \epsilon_0 \cdot \frac{H_0 \cdot L_0}{(D_0 - x)^2} \cdot V^2 \quad (2.17)$$

$$F_y = \frac{\partial E}{\partial y} = \frac{1}{2} \cdot \frac{\partial C}{\partial L} \cdot \frac{\partial L(y)}{\partial y} \cdot V^2 = \frac{1}{2} \cdot \alpha \cdot \epsilon_0 \cdot \frac{H_0}{D_0} \cdot V^2 \quad (2.18)$$

$$F_z = \frac{\partial E}{\partial z} = \frac{1}{2} \cdot \frac{\partial C}{\partial H} \cdot \frac{\partial H(z)}{\partial z} \cdot V^2 = \frac{1}{2} \cdot \alpha \cdot \epsilon_0 \cdot \frac{L_0}{D_0} \cdot V^2 \quad (2.19)$$

where F_x , F_y and F_z are directional components of electrostatic force in x , y , z directions, respectively. In these equations, it is assumed that the applied potential difference across the capacitor plates, V , does not change with the position. Moreover, it is clearly seen that the force components along y and z directions, F_y and F_z , are constant while the force along the x direction, F_x , is position dependent. Although being nonlinear function of displacement, F_x is larger than both F_y and F_z due to the fact that L_0 and H_0 are greater than D_0 for typical micromachined microstructures, including the gyroscopes used in this study.

Equation set (2.17)-(2.19) implies that the electrostatic force is a function of voltage applied across the capacitor plates. Remembering the proper operation of the

vibratory gyroscope, a time-varying excitation voltage, which generates an electrostatic force at the mechanical resonance frequency of the drive-mode resonator, is required for sustaining vibrations. Then, the electrostatic force expression for a purely sinusoidal potential difference is given as

$$F = \frac{\partial E}{\partial r} = \frac{1}{2} \cdot \frac{\partial C}{\partial r} \cdot (V_{ac} \cdot \sin(\omega t))^2 = \frac{\partial C}{\partial r} \left[\underbrace{\frac{V_{ac}^2}{2}}_{DC} - \underbrace{\frac{V_{ac}^2}{2} \cdot \cos(2\omega t)}_{ac \text{ at } 2\omega} \right] \quad (2.20)$$

where V_{ac} is the amplitude of the applied sinusoidal voltage. It is observed that the generated electrostatic force has two frequency components; the first one is a DC causing only static deflection, and the second is an AC at 2ω frequency. This implies that the applied voltage can drive the gyroscope into resonance as long as the frequency of the voltage is half of the mechanical resonance frequency. However, this requires more complex drive-mode electronics, which is not preferred in this research. Another approach can be adding a DC offset to the applied sinusoidal voltage to generate linear electrostatic force at the mechanical resonance frequency of the gyroscope. Rearranging Equation (2.20) for this condition yields

$$F = \frac{\partial E}{\partial r} = \frac{1}{2} \cdot \frac{\partial C}{\partial r} \cdot (V_{DC} + V_{ac} \cdot \sin(\omega t))^2 \quad (2.21)$$

$$= \frac{1}{2} \cdot \frac{\partial C}{\partial r} \left\{ \underbrace{\left[V_{DC}^2 + \frac{V_{ac}^2}{2} \right]}_{DC} + \underbrace{2 \cdot V_{DC} \cdot V_{ac} \cdot \sin(\omega t)}_{ac \text{ at } \omega} - \underbrace{V_{ac}^2 \cdot \cos(2\omega t)}_{ac \text{ at } 2\omega} \right\}$$

Equation (2.21) shows that by adding a DC offset, V_{DC} , electrostatic force component at the frequency of ω can be generated. If this frequency is set to mechanical resonance frequency of the drive-mode resonator, then the gyroscope is vibrated at its resonance frequency with a simpler electronic feedback loop. The frequency component at 2ω would be rejected as the resonator has high-Q band-pass filter characteristics whose center is at the resonance frequency.

In the drive-mode of vibratory gyroscopes, the actuation force can be generated in two basic parallel-plate capacitor configurations, as varying-gap type capacitor and varying-overlap-area type capacitor. Figure 2.2 shows typical driving electrodes for both types of drive-mode actuation mechanisms. In varying-gap type capacitors, electrostatic force generated along the gap direction can be approximated by modifying Equation (2.17) for N number of fingers [8].

$$|F_{y,net}| \approx \frac{1}{2} \cdot N \cdot \alpha \cdot \varepsilon_0 \cdot H_0 \cdot L_0 \cdot \left[\frac{1}{D_0^2} - \frac{1}{D_{anti-gap}^2} \right] \cdot V^2 \quad (2.22)$$

where $D_{anti-gap}$ is the distance between two adjacent moving-stationary conductor pairs, and it is assumed that displacement along the gap direction is much smaller than the stationary gap between the plates, i.e., $x \ll D_0$. For varying-overlap-area capacitors in Figure 2.2b, net force along the direction of oscillation is given as

$$|F_{x,net}| \approx N \cdot \alpha \cdot \varepsilon_0 \cdot \frac{H_0}{D_0} \cdot V^2 \quad (2.23)$$

Comparing Equations (2.22) and (2.23), it is concluded that varying-overlap-area type capacitor provides less electrostatic force than varying-gap type capacitor since the gap spacing is usually designed to be much smaller than other dimensions. However, the former depends on the displacement along the oscillation direction, creating a nonlinear response, which is not desired in drive-mode electronics. In addition, the maximum oscillation amplitude is limited by the gap distance in varying-gap type capacitor actuation mechanisms. Therefore, varying-overlap-area type electrodes, which enable large drive-mode vibration amplitudes for better rate sensitivity, are preferred in the drive-mode actuation mechanisms. On the other hand, unlike drive-mode displacements, those of sense-mode in response to Coriolis force are very small compared to the gap spacing. Thus, varying-gap type electrodes creating much larger injected charge are employed in the sense-mode rate sensing mechanisms without causing significant nonlinearity.

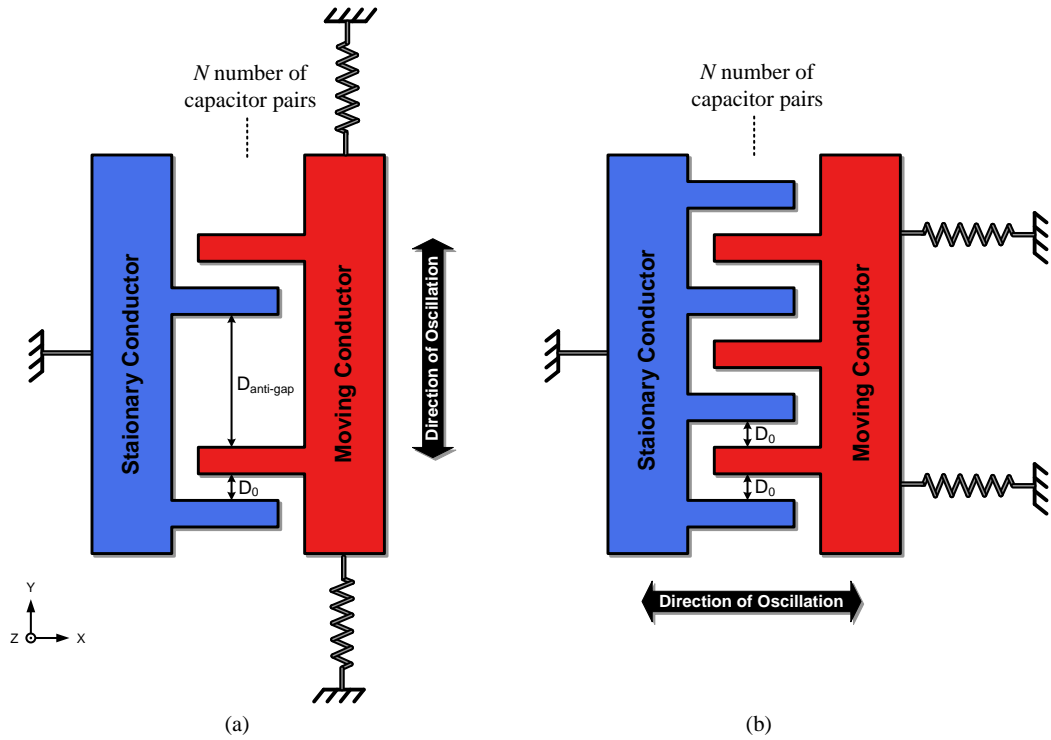


Figure 2.2: Driving electrodes for (a) varying-gap and (b) varying-overlap-area type actuation mechanisms.

2.2.2. Capacitive Sensing

Besides actuating the gyroscope by applying time-varying voltage, physical displacements in response to both electrostatic actuation and Coriolis coupling should be sensed for proper operation of the gyroscope. In this research, capacitive sensing mechanisms are employed to monitor the amplitude of the drive-mode vibrations for constructing a closed-loop self-oscillation circuit and to detect the angular rate related deflections of the sense-mode. The capacitive sensing mechanism is based on the basic voltage-charge relationship given as

$$Q = C \cdot V \tag{2.24}$$

If the capacitance changes, charge on the capacitor also changes as long as the voltage across the variable capacitor is constant. Then, the injected charge is converted to voltage on the effective impedance of the interface electronics. Figure 2.3 illustrates the basic electrical model of the capacitive sensing mechanism, where ac current source symbolizes the generated current at the output node of the capacitor plates biased with a constant potential difference, V_{DC} , and C_o is the stationary sensor capacitance. DC biasing of the capacitor plates is achieved by applying a DC voltage to the proof mass and biasing the stationary electrode to a constant DC potential through interface electronics.

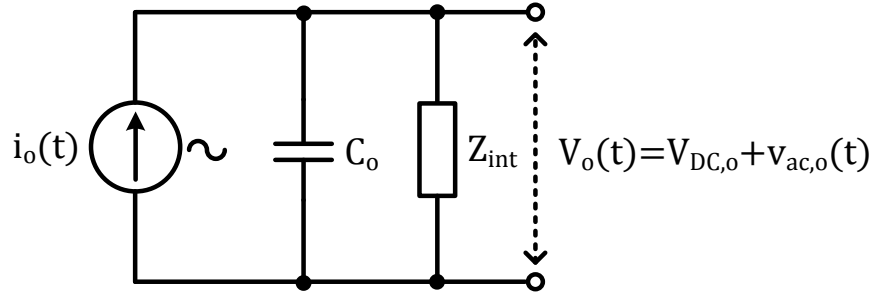


Figure 2.3: Basic electrical model of the capacitive sensing mechanism.

Total time-varying capacitance, which is the summation of the stationary sensor capacitance and the time-dependent capacitance of the oscillating sensor, can be expressed as

$$C_S(t) = C_o + \frac{\partial C}{\partial x} \cdot x(t) \quad (2.25)$$

The current generated from the injected charges due to the displacement of moving plates is then calculated from the time derivative of the total charge as

$$i_o(t) = \frac{\partial Q(t)}{\partial t} = \frac{\partial (C_S(t) \cdot V_o(t))}{\partial t} = C_S(t) \cdot \frac{\partial V_o(t)}{\partial t} + V_o(t) \cdot \frac{\partial C_S(t)}{\partial t} \quad (2.26)$$

Assuming that the DC biasing potential is much larger than the time-varying output voltage, i.e. $V_{DC,o} \gg v_{ac,o}$, so that $V_o(t) \approx V_{DC,o}$, Equation (2.26) can be simplified as

$$i_o(t) = V_{DC,o} \cdot \frac{\partial C_S(t)}{\partial t} \quad (2.27)$$

Inserting Equation (2.25) into Equation (2.27) yields,

$$i_o(t) = V_{DC,o} \cdot \frac{\partial C}{\partial x} \cdot \frac{\partial x}{\partial t} \quad (2.28)$$

or equivalently,

$$I_o(s) = V_{DC,o} \cdot \frac{\partial C}{\partial x} \cdot \underbrace{s \cdot X(s)}_{\text{velocity}} \quad (2.29)$$

Finally, this current is converted to time-varying output voltage on the effective impedance of interface circuit parallel to stationary sensor capacitance as

$$V_{ac,o}(s) = I_o(s) \cdot \left(\frac{1}{sC_o} // Z_{int} \right) \quad (2.30)$$

Equation (2.30) shows that some portion of the generated current flows through the stationary sensor capacitance C_o , and this current is called as feed-through current.

2.2.3. Electrostatic Spring Effect

As mentioned in Section 2.1.2, matching the resonance frequencies of the drive and sense modes increases the sensitivity of the gyroscope considerably, as the mechanical quality factor of the sense-mode amplifies the Coriolis motion, which is

at frequency of drive-mode oscillation. However, due to poor process tolerances of the micromachining technology, it is impossible to match the resonance frequencies in the design phase. Instead, post-process electrostatic tuning can be employed to tune the resonance frequency of the sense-mode formed by varying-gap type electrodes, acting as electrostatic springs. The electrostatic spring constant of varying-gap type capacitors can be found from the classical spring constant calculation defined as the derivative of force with respect to position. Taking the position derivative of the varying-gap-type capacitor force expression given in Equation (2.17) yields,

$$\delta k = \frac{\partial F_x}{\partial x} = \frac{\partial^2}{\partial x^2} = \frac{1}{2} \cdot \frac{\partial^2 C}{\partial x^2} \cdot V^2 = \alpha \cdot \varepsilon_0 \cdot \frac{H_0 \cdot L_0}{(D_0 - x)^3} \cdot V^2 \quad (2.31)$$

Assuming that the potential difference across the capacitor plates is dominated by DC biasing voltage, i.e. $V_{DC} \gg v_{ac}(t)$, so $V \approx V_{DC}$, the electrostatic spring constant expression is then approximated as

$$\delta k \approx \alpha \cdot \varepsilon_0 \cdot \frac{H_0 \cdot L_0}{(D_0 - x)^3} \cdot V_{DC}^2 \quad (2.32)$$

When the electrostatic negative spring effect in Equation (2.32) is considered, the resonance frequency expression in Equation (2.3) can be modified for the sense-mode as

$$\omega_s = \sqrt{\frac{k_s - \delta k}{m_s}} \quad (2.33)$$

Figure 2.4 illustrates the effect of DC biasing voltage on the resonance characteristics of the drive and sense modes assuming that the drive-mode is composed of varying-overlap-area type fingers, and the sense-mode has varying-gap type

capacitive sensing mechanism. As derived in Equations (2.21) and (2.28), the electrostatic force in the actuation mechanism and the generated current in the capacitive sensing are proportional to the biasing voltage, respectively. Hence, both modes give amplified gain responses when the DC voltage is increased. Moreover, resonance frequency of the sense-mode shifts left with the increased voltage because of the electrostatic spring effect expressed in Equation (2.33).

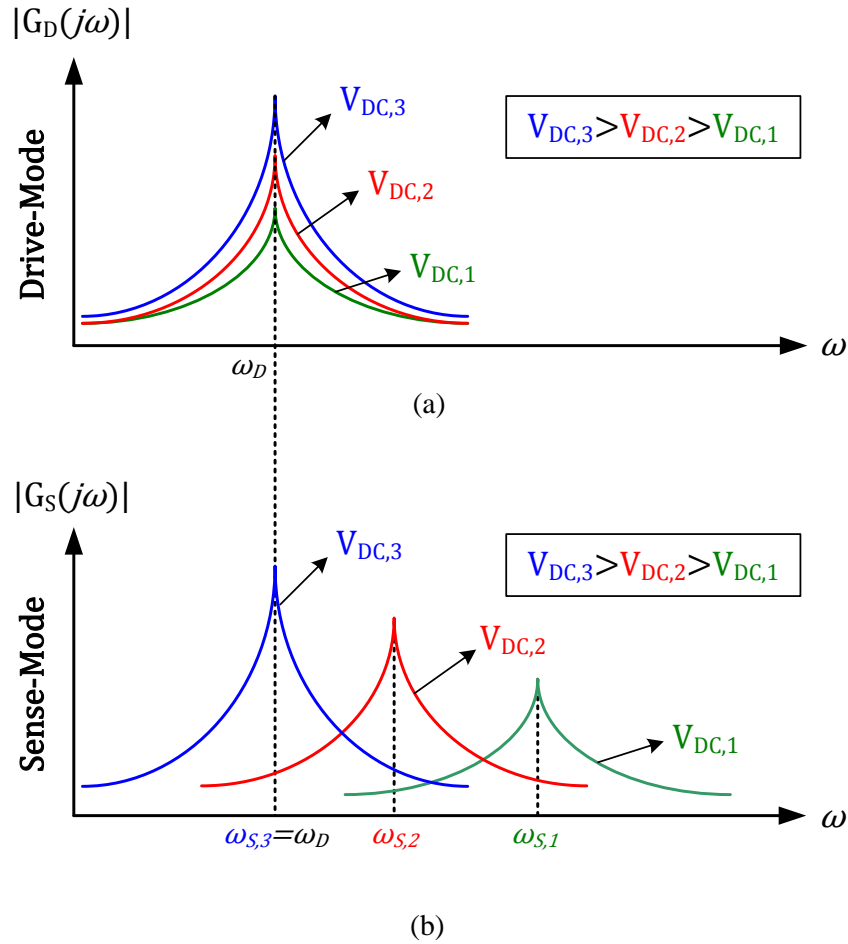


Figure 2.4: The effect of DC biasing voltage on the resonance characteristics of (a) the drive-mode and (b) the sense-mode.

Vibratory gyroscopes used in this study are designed to have mechanical resonance frequencies of sense-mode higher than those of drive-mode. Then, the resonance frequency of the sense-mode is tuned down for the match-mode operation by

adjusting the proof mass DC polarization voltage. However, it is usually not desired to have exactly matched modes in the gyroscopes employing open-loop rate sensing electronics without a special quadrature cancellation mechanism. This is due to the fact that as the modes get very close to each other, effect of the mechanical crosstalk gets more significant, and overall bandwidth of the system degrades. Therefore, despite sacrificing from sensitivity, slightly mismatch modes are preferred for the sake of wider bandwidth and lower output offset.

2.3. Electrical Model of Vibratory Gyroscopes

Modeling the mechanical sensor in electrical domain allows the simulation of the complete electromechanical system in typical SPICE simulators. The electrical model is constructed by using the analogy between the mechanical mass-spring-damper system and the serially connected resistor-inductor-capacitor (RLC) circuit, which are both characterized by identical second-order differential equations. Table 2.1 gives the electrical equivalents of the mechanical parameters of a mass-spring-damper system.

Table 2.1: Electrical equivalents of mechanical parameters of a mass-spring-damper system.

Mechanical Parameter	Electrical Equivalent
Mass (m)	Inductance (L)
Damping Coefficient (b)	Resistance (R)
Spring Constant (k)	Reciprocal of Capacitance (1/C)
Displacement (x)	Charge (Q)
Velocity (v)	Current (I)
Force (F)	Voltage (V)

As mentioned in Section 2.2.1, an actuation voltage applied to the drive-mode electrodes generates an electrostatic force deflecting the drive-mode mass according to the mechanical system parameters. Combining Equation (2.2) and (2.21) in single expression representing the applied AC voltage and generated force relation yields

$$\frac{X_D(s)}{V_{DM}(s)} = \frac{n_{DM}/m_D}{s^2 + (\omega_D/Q_D)s + \omega_D^2} \quad (2.34)$$

where X_D is the drive-mode displacement, V_{DM} is the ac actuation voltage, and n_{DM} is the electromechanical coupling coefficient for drive-motor (DM) electrode. The analytical expression for the electromechanical coupling coefficient is defined as

$$n_{DM} = V_{DC} \cdot \left(\frac{\partial C_{DM}}{\partial x} \right) \quad (2.35)$$

where V_{DC} is the DC biasing voltage across the capacitor plates. Then, at the mechanical resonance frequency of the drive-mode, i.e. $\omega = \omega_D$, Equation (2.34) simplifies to

$$\frac{X_D(j\omega)}{V_{DM}(j\omega)} = \frac{n_{DM} \cdot Q_D}{j \cdot k_D} \quad (2.36)$$

showing that displacement lags the applied voltage by 90° at the resonance.

As described in Section 2.2.2, the generated displacement induces current at the pick-up electrodes. The induced output current expression in Equation (2.29) can be then modified as

$$I_o(j\omega) = j\omega \cdot n_{DP} \cdot X(j\omega) \quad (2.37)$$

where electromechanical coupling coefficient of drive-mode pick-up electrodes, n_{DP} , is defined as

$$n_{DP} = V_{DC} \cdot \frac{\partial C_{DP}}{\partial x} \quad (2.38)$$

By considering Equation set (2.34)-(2.38), electrical equivalent model of the drive-mode can be constructed as shown in Figure 2.5.

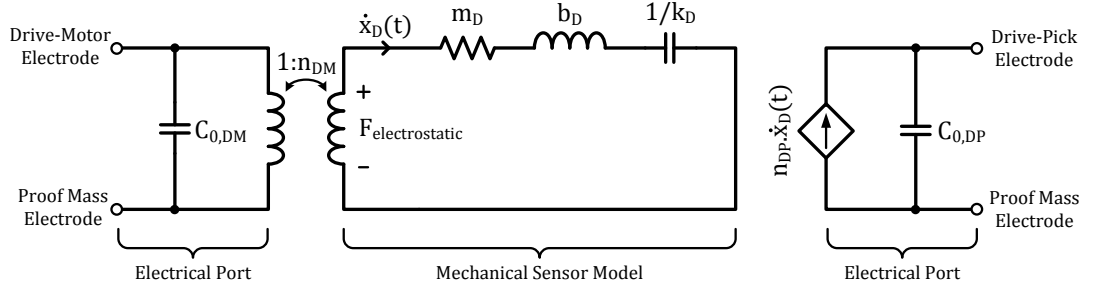


Figure 2.5: Electrical equivalent model of the drive-mode.

Similarly, sense-mode can be modeled in electrical domain by replacing the electrostatic actuation force in the drive-mode with Coriolis force expressed as

$$|F_{Coriolis}(t)| = 2 \cdot m_{PM} \cdot \Omega_Z \cdot \dot{x}_D(t) \quad (2.39)$$

Equation (2.39) implies that Coriolis force depends on the velocity of the drive-mode movement that is modeled as the current flowing through the mechanical part of the electrical equivalent model. Since equivalent of the mechanical force in the electrical domain is potential difference, Coriolis force can be modeled as a current dependent voltage source in the electrical model, where current to voltage conversion coefficient, n_{Cor} , is defined as

$$n_{Cor} = 2 \cdot m_{PM} \cdot \Omega_Z \quad (2.40)$$

Finally, electromechanical coupling coefficient for the sense-mode pick-up electrodes is given as

$$n_{SP} = V_{DC} \cdot \frac{\partial C_{SP}}{\partial y} \quad (2.41)$$

Figure 2.6 illustrates the generalized electrical model of the overall gyroscope constructed by combining the models of drive and sense modes.

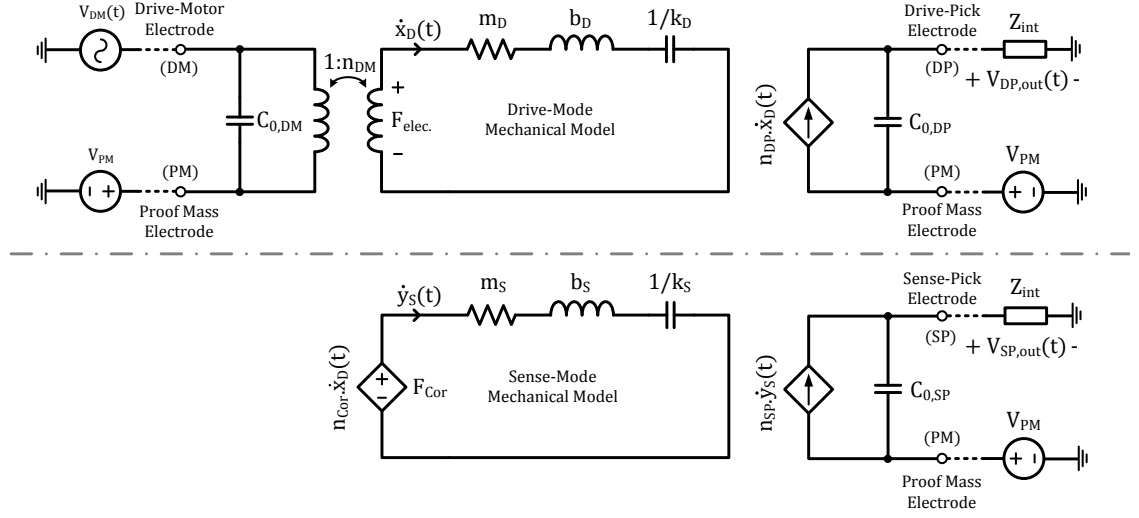


Figure 2.6: Generalized electrical model of the overall gyroscope constructed by combining the models of drive and sense modes.

The schematic in Figure 2.6 provides an electrical model for typical single-ended gyroscopes employing capacitive transduction mechanisms. Silicon-on-glass (SOG) gyroscopes used in this research are single-mass gyroscopes having differential sense-mode, however dual-mass dissolved wafer process (DWP) gyroscopes are differential in both modes. Therefore, input-output electrodes and electromechanical coupling coefficients in the model should be modified for each gyroscope in order to prevent the possible erroneous results during the simulations.

2.4. Theory of Vibratory Gyroscope Electronics

Vibratory gyroscopes only become complete sensor systems with the assistance of dedicated electronic circuits. While converting the physical displacements to electrical signals, circuits also sustain constant-amplitude oscillation in the drive-mode and process the raw sense-mode output in order to get meaningful signals proportional to the applied angular rate. Affecting the overall system

performance significantly, these circuits can be classified in three main categories as interface electronics, drive-mode control electronics, and sense-mode demodulation electronics.

2.4.1. Capacitive and Resistive Type Interface Electronics

Position sensing through capacitance change is the key point in many applications of MEMS structures including micromachined vibratory gyroscopes. For high-performance gyroscopes, it is required to sense capacitance changes in the order of zepto-farads ($1\text{zF} = 10^{-21}\text{F}$) in response to physical displacements much smaller than the diameter of a silicon atom. Such small changes can only be detected by dedicated interface electronics converting the charge at the output of the capacitive gyroscope to a voltage signal. Being the interconnection between mechanical and electrical domains, these interfaces have considerable effect on the overall performance of the gyroscope; therefore, they should meet some challenging requirements. An ideal interface must have very low noise and introduce no phase error while properly biasing the high-impedance node of the gyroscope to a constant DC potential. Figure 2.7 illustrates the generalized view of a basic interface circuit. In this circuit, current injected from the gyroscope is converted to voltage according to basic Ohm's voltage expression given as

$$V_{out}(s) = A_V \left[I_S(s) \left(Z_{in}(s) // \left(\frac{1}{sC_s} \right) // \left(\frac{1}{sC_p} \right) \right) \right] \quad (2.42)$$

where A_V is the voltage gain of the amplifier, I_S is the current pumped by the gyroscope, C_s is the stationary capacitance between the sense electrode and the proof mass, C_p is the total of parasitic capacitances, and Z_{int} is the effective impedance of the interface.

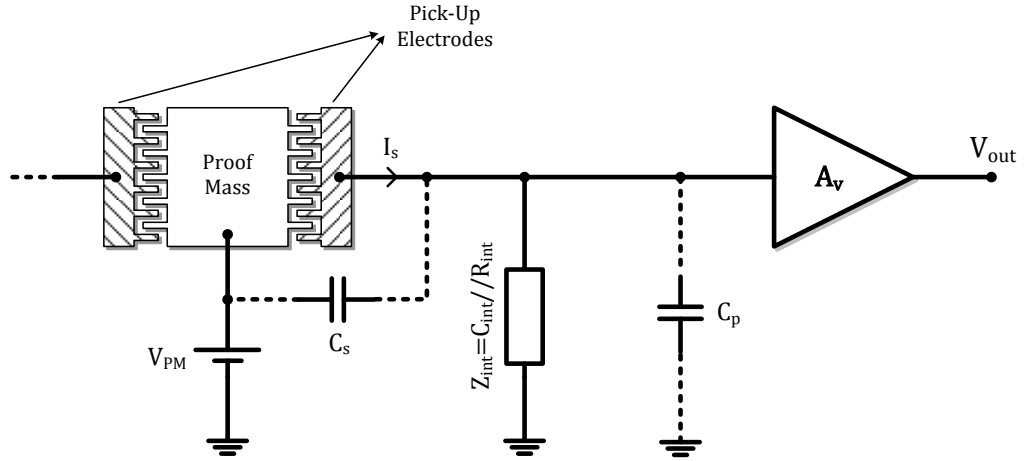


Figure 2.7: Generalized view of a basic interface circuit used to convert the charge pumped from the gyroscope to a voltage.

The interface electronics employed in this research can be classified into two basic categories as resistive-type and capacitive-type according to the type of dominant interface impedance, Z_{int} , on which the generated charge is converted to voltage.

In resistive-type interfaces, the resistance dominates the effective impedance and biases the high-impedance node to a DC potential, which is usually ground. This biasing is quite important in the sense that floating nodes are very susceptible to leakage currents and external noise signals, leading unpredictable behavior at the gyroscope output. For a proper biasing resistor and assuming that the amplifier has infinite input impedance, the equivalent input current noise of the resistive-type interface can be estimated as

$$\frac{\overline{i_n^2}}{\Delta f} = \frac{4kT}{R_{int}} + \frac{\overline{v_i^2}}{R_{int}^2} \quad (2.43)$$

where $\overline{v_i^2}$ is the input-referred voltage noise of the amplifier. From this noise expression, it can be inferred that the interface resistor should be as large as possible to minimize the current noise, so as to maximize the resolution. Nevertheless,

parasitic capacitances would indeed limit the maximum value of the resistor as the total effective impedance of the capacitors should be much larger than that of interface resistor, i.e., $R_{int} \ll [(1/sC_{int}) // (1/sC_S) // (1/sC_P)]$, for almost purely resistive interface impedance. Otherwise, together with the possible large parasitic capacitances, such resistors would introduce phase errors, slow down the circuit and load the resonator.

On the other hand, in the case of capacitive-type interface, biasing resistors are designed to have much larger impedance than that of equivalent interface capacitance, i.e., $R_{int} \gg (1/sC_{int})$, so that the current-to-voltage conversion is achieved on the dominating capacitance, and circuit becomes a current integrator whose current-voltage expression is approximated as

$$V_{out}(j\omega) \approx A_V \cdot \left(\frac{1}{j\omega C_{int}} \right) \cdot I_S(j\omega) \quad (2.44)$$

Obviously, the noise analysis of the capacitive-type interfaces should be carried out in the frequency domain. In this case, white noise spectrum of the resistor thermal noise is shaped by the RC low-pass filter formed by the biasing resistor itself and the charge integration capacitor. Then, the amplifier noise adds up to this noise giving total output referred voltage noise of

$$\frac{\overline{v}_{out}^2}{\Delta f} = A_V^2 \cdot \left(4kTR_{int} \frac{1}{(\omega R_{int} C_{int})^2} + \overline{v}_i^2 \right) \quad (2.45)$$

thus,

$$\frac{\overline{v}_{out}^2}{\Delta f} = A_V^2 \cdot \left(\frac{4kT}{\omega^2 R_{int} C_{int}^2} + \overline{v}_i^2 \right) \quad (2.46)$$

Combining Equation (2.44) and (2.46) yields equivalent input referred current noise given as

$$\frac{\overline{i_n^2}}{\Delta f} = \left(\frac{4kT}{R_{int}} + \omega^2 C_{int}^2 \overline{v_i^2} \right) \quad (2.47)$$

According to Equation (2.47), in order to decrease the current noise and increase the resolution, equivalent capacitance across the high-impedance node and AC ground should be decreased. However, this capacitance is limited by the parasitic capacitances coming from amplifier itself, interconnect metallization and wirebonds. Moreover, as the impedance of the effective capacitance increases, the biasing resistor should also be increased so that the capacitance is the dominant element and phase error is in tolerable ranges. Implementing such large biasing resistors satisfying capacitive interface condition would be problematic due to practical limitations of the CMOS technology. Hence, several approaches other than physical thin-film resistors are developed, like back-to-back diodes, switched capacitors, and MOSFETs operating at sub-threshold region. In this study, MOSFETs providing sufficiently large channel resistances are employed for high-impedance node biasing in capacitive-type interfaces.

Another problematic issue in capacitive-type interfaces is the 90° phase shift introduced inherently by the charge integration. This implies that an additional 90° phase shifting circuit, such as integrator or differentiator, is required in the drive-mode self-oscillation loop, making the overall circuit more complicated. Therefore, resistive-type interfaces, which ideally have either 0° or 180° phase shift, are usually preferred in the drive-mode electronics although capacitive-type interfaces have superior sensitivity performance. In fact, sensitivity performance of the interface is not critical in the drive-mode as long as the oscillation criteria are satisfied. The effect of phase errors and oscillation conditions would be clarified in the following sections introducing self-oscillation principle and phase sensitive demodulation.

2.4.2. Oscillation Criteria and Self-Oscillation Principle

As in the case of typical electronic oscillators, generic oscillator design approaches and oscillation conditions are also valid for vibratory gyroscopes since the drive-mode can be used as the timing element of a high-Q oscillator whose vibration is sustained by electronic feedback circuits. Generally speaking, whether the timing element is mechanical or electrical, oscillation is created by the instability in the circuit. This instability is usually generated by the positive feedback loop designed so that the oscillation frequency is set by the total phase shift in the loop. As the output response of the circuit grows in each cycle of the loop, eventually, nonlinearities or more complicated control electronics limit the output giving constant amplitude vibrations usually at the resonance frequency of the timing element.

Figure 2.8 shows the block diagram of an ideal unity-gain positive feedback circuit involving fundamental oscillation principles. This system has a closed-loop transfer function given as

$$\frac{V_{out}}{V_{in}}(s) = \frac{A(s)}{1 - A(s)} \quad (2.48)$$

where $A(s)$ is the open-loop gain. For $s = j\omega_0$ and $A(j\omega_0) = 1$, the denominator of Equation (2.48) becomes zero, consequently resulting in a closed-loop gain of infinity. When this condition occurs, loop amplifies the signal component at ω_0 indefinitely and the system becomes unstable, giving oscillatory output at this frequency.

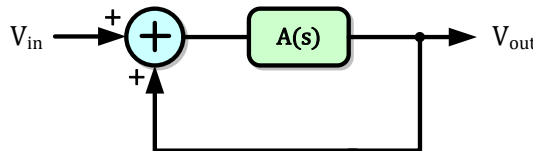


Figure 2.8: Block diagram of a unity-gain positive feedback system.

The necessary oscillation conditions are defined as “Barkhausen Criteria” [52], which states that a positive feedback system oscillates at the frequency where the total open-loop gain is greater or equal to unity, and the total phase shift in the loop is integer multiples of 360° . The interpretation of this definition for vibratory gyroscopes is that the drive-mode vibration never starts as long as the corresponding total loop gain is larger than unity at the frequency where total phase shift is zero degree. However, although Barkhausen criteria give necessary conditions for sustaining oscillation, they are not sufficient to start-up oscillations. Ideally, although a self-oscillation loop guarantees necessary conditions, hardly can oscillation start without a triggering mechanism. In an actual self-oscillation loop without any special start-up circuit, oscillation is triggered by either noise or power-up transitions that have frequency components satisfying gain and phase conditions. At the start-up, noise shaped by the drive-mode transfer characteristics is first phase-shifted and amplified to start oscillations at the desired frequency, then fed back to the sensor, which eventually leads to exponentially growing vibrations.

Figure 2.9 proposes a simple self-oscillation system including gain and phase shifting blocks to satisfy Barkhausen criteria at the resonance frequency of the drive-mode, which is modeled as a second-order mass-spring-damper system.

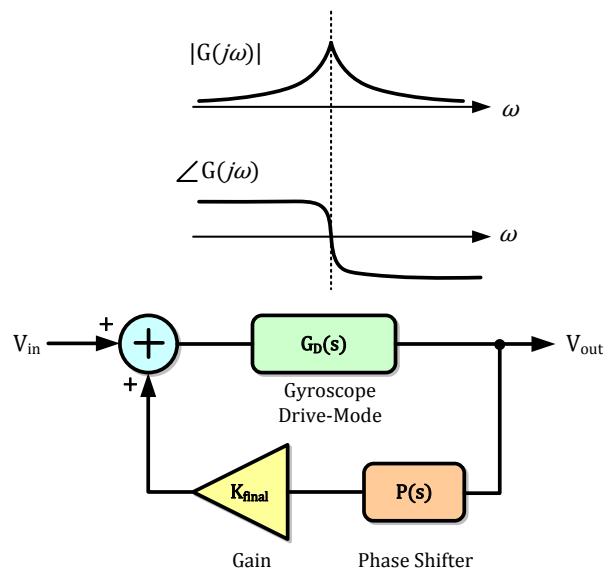


Figure 2.9: Block diagram of a simple self-oscillation loop together with the bode diagram of the gyroscope drive-mode.

The transient response of this system can be completely defined by closed-loop pole-zero diagram extracted from the characteristic equation given as

$$G_D(s) \cdot P(s) \cdot K_{final} - 1 = 0 \quad (2.49)$$

From the generalized electrical model in Figure 2.6, voltage transfer characteristics of the gyroscope drive-mode can be defined as

$$G_D(s) = \frac{V_{DP}}{V_{DM}}(s) = \frac{\left((1/m_D) \cdot n_{DM} \cdot n_{DP} \cdot \left(\frac{1}{sC_{int}} \right) \right) s}{s^2 + \left(\frac{\omega_D}{Q} \right) s + \omega_D^2} \quad (2.50)$$

where it is assumed that the drive-mode output is sensed by a purely capacitive interface. Let the constant terms in the numerator is combined in a gain constant, K_D , then Equation (2.50) simplifies to

$$G_D(s) = \frac{K_D}{s^2 + \left(\frac{\omega_D}{Q} \right) s + \omega_D^2} \quad (2.51)$$

This equation shows that the phase shift is 90° at the resonance since the generated current is converted to voltage by a capacitive-type interface. Therefore, an additional 90° phase shifting block is necessary for the oscillation condition. If a differentiator circuit is employed as the phase shifter, then the characteristic equation becomes

$$s^2 + \left(\frac{\omega_D}{Q_D} - A_{PS} \cdot K_D \cdot K_{final} \right) s + \omega_D^2 = 0 \quad (2.52)$$

where A_{PS} is the phase shifter gain. This system oscillates only if the poles are placed on the right-half plane of the pole-zero diagram. Then, the oscillation condition is given as

$$K_{final} > \frac{\omega_D}{Q_D \cdot A_{PS} \cdot K_D} \quad (2.53)$$

Figure 2.10 illustrates the effect of pole placement on the transient response. If closed-loop poles are located on the right-half plane, which actually corresponds to the Barkhausen gain criterion, then the system becomes unstable and the oscillation grows indefinitely. On the other hand, if poles stay on the left-half plane because of the insufficient loop gain, the oscillation never starts or already sustained oscillations decay and diminish. Therefore, for the proper operation of the vibratory gyroscope, system poles should be on the RHP at the start-up and eventually move to the imaginary axis, where the oscillation amplitude is constant.

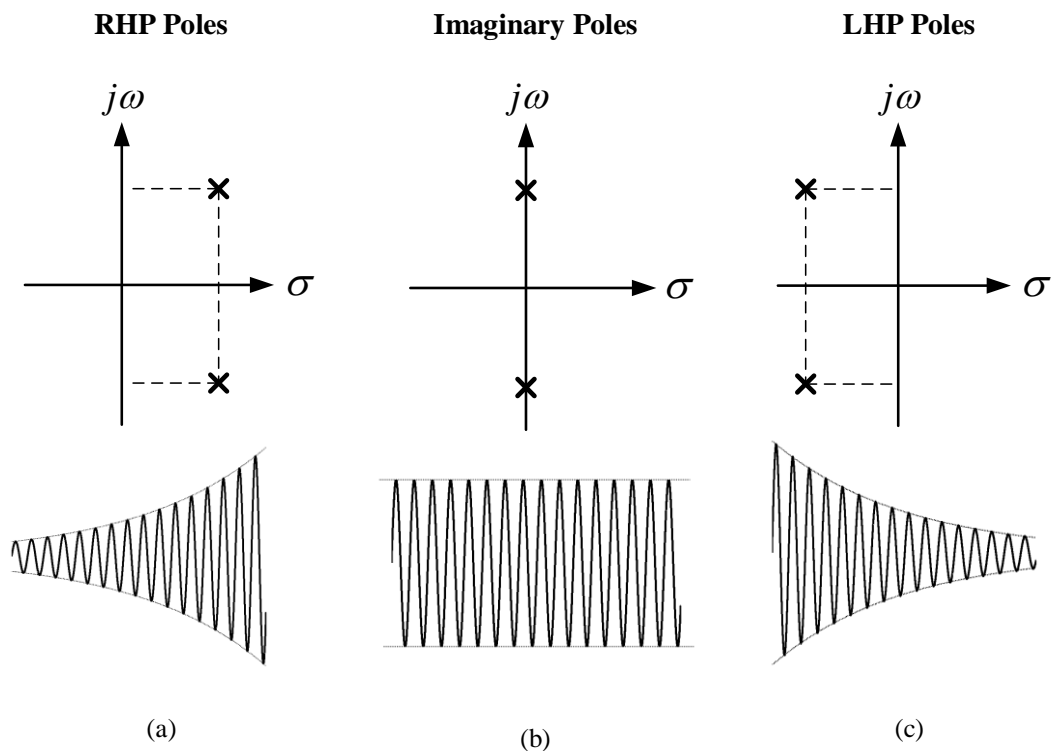


Figure 2.10: Pole-zero diagrams and corresponding transient responses of systems having (a) right-half plane poles, (b) imaginary poles, and (c) left-half plane poles.

Keeping the closed-loop poles on the imaginary axis is not an easy task for linear control systems. In order to sustain constant amplitude vibrations, an additional nonlinearity or an amplitude control mechanism should be introduced. For simple self-oscillation loops as shown in Figure 2.9, the vibration amplitude is limited inherently by the circuit itself. As the oscillation level increases, each stage eventually becomes nonlinear and finally saturates at the supply limits providing a constant amplitude oscillation. In addition to supply limitation, more complex amplitude control circuits should be employed in order to eliminate the dependence of vibration amplitude on supply voltages, temperature, vacuum level, and sensor parameters.

2.4.3. Automatic Oscillation Amplitude Control Principle

Remembering the Coriolis force definition in Section 2.1.2, it can be inferred that sensitivity of the gyroscope is directly related to the drive-mode vibration amplitude. Thus, random deviations in the drive-mode oscillations may cause undesired drift at the gyroscope output, resulting in a bias instability problem. Barely does simple self-resonance circuit shown in Figure 2.9 adapt itself to parameter variations because of the fact that generated oscillations in self-resonance loop completely depend on sensor parameters as well as ambient conditions. The preferred solution for this problem is continuously adjusting the self-resonance loop gain while monitoring the vibration amplitude. Figure 2.11 shows the block diagram of the proposed automatic oscillation amplitude control circuit. This circuit is composed of two nested loops, which are named as self-resonance loop and control loop. The self-resonance loop operates as the oscillation principle described in Section 2.4.2, with the exception of using variable gain amplifier (VGA) instead of constant gain amplifier as the final gain stage. Then, the control loop compares the vibration amplitude to the externally set voltage and generates a gain control signal adjusting the VGA gain, so that the system poles are always on the imaginary axis, providing constant oscillation amplitude. If the vibration amplitude is larger than the predefined value, the gain control signal decreases with the negative error signal, resulting in decaying amplitude due to energy loss, and vice versa. Although this

operation seems to be fairly simple, designing controller parameters and predicting the system transient-response require complicated analysis since the system is nonlinear. Thus, a reduced order linearized system model should be constructed with proper approximations, allowing straightforward controller design methods.

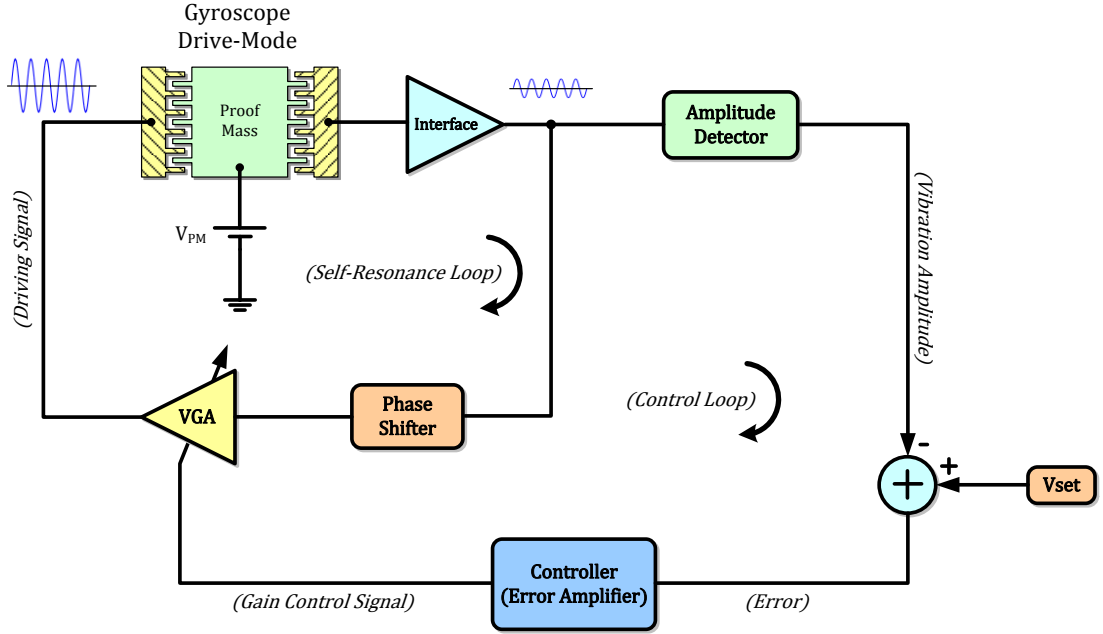


Figure 2.11: Block diagram of the proposed automatic oscillation amplitude control circuit.

Considering the self-resonance loop characteristic equation in Equation (2.52) with the unity-gain phase shifter assumption, i.e. $A_{PS} = 1$, closed-loop system poles can be derived as

$$s_{1,2} = \frac{-\left(\frac{\omega_D}{Q_D} - K_V \cdot K_D\right) \pm \sqrt{\left(\frac{\omega_D}{Q_D} - K_V \cdot K_D\right)^2 - 4\omega_D^2}}{2} \quad (2.54)$$

where K_V is the VGA gain. For the proper operation of automatic gain control (AGC) loop, systems poles should be placed on the RHP at the start-up and move to imaginary axis as the oscillation grows to desired level. Figure 2.12 illustrates the

pole-zero diagram showing the movement of system poles from start-up to steady-state operation.

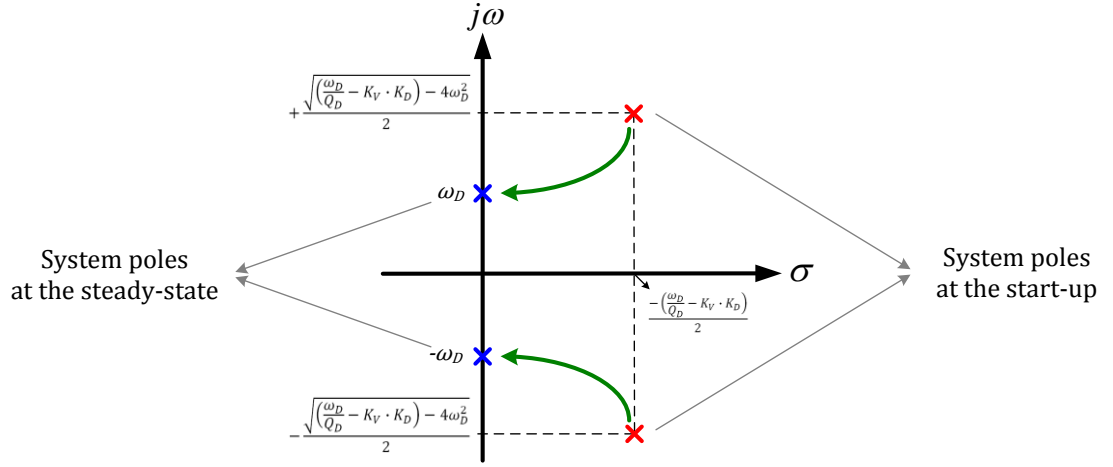


Figure 2.12: Pole-zero diagram showing the movement of system poles from start-up to steady-state operation.

Real parts of the system poles, which describe the transient response of vibration amplitude, are found from the closed-loop system damping factor defined as

$$B(t) = \left(\frac{\omega_D}{Q} - K_V \cdot K_D \right) \quad (2.55)$$

The damping factor expression shows that VGA gain, K_V , can maintain zero damping factor for constant amplitude oscillation by compensating the variations in the resonance frequency, quality factor and drive-mode voltage gain, K_D . On the contrary, non-zero damping factors lead to exponentially increasing or decaying oscillation amplitudes, defined by the expression given as [53, 54]

$$A(t) = A(t_0) \exp \left(-\frac{1}{2} \int_{t_0}^t B(t) dt \right) \quad (2.56)$$

where $A(t_0)$ is the initial value of the amplitude. This equation shows that damping factor and oscillation relation is nonlinear, making the system design complicated. This relation can be linearized assuming that the damping factor is sufficiently small as long as the variations in the system parameters are not very fast. From the Taylor series expansion, Equation (2.56) can be approximated as

$$A(t) \approx -\frac{A(t_0)}{2} \int_{t_0}^t B(t) dt \quad (2.57)$$

or equivalently,

$$A(s) \approx -\frac{A_0 B(s)}{2s} \quad (2.58)$$

Having obtained the linearized relation between the oscillation amplitude and the damping factor, reduced order model of the overall AGC loop given in Figure 2.11 can be constructed, where system inputs are amplitude set voltage, resonance frequency and quality factor. Figure 2.13 shows the reduced order linearized model of the proposed AGC loop.

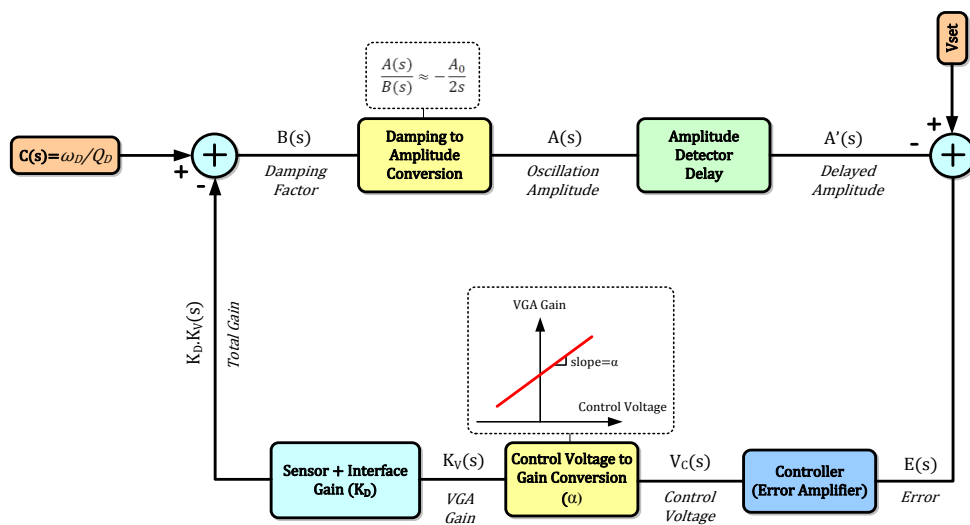


Figure 2.13: Reduced order linearized model of the proposed AGC loop.

In this model, the feedback loop aims to diminish difference between the amplitude set voltage and the oscillation amplitude while keeping the damping factor at zero for sustaining constant amplitude oscillations. Having characterized the sensor, transient response of the system can be defined by controller parameters, amplitude detector delay, and VGA gain, according to the design specifications.

2.4.4. Sense-Mode Rate Output Extraction Electronics

The sense-mode output of the gyroscope is an amplitude-modulated (AM) signal, at the oscillation frequency of the drive-mode. Therefore, this signal should be demodulated to base-band and filtered through a low-pass filter (LPF), giving DC output proportional to the applied angular rate. In fact, there are basically two approaches for rate output extraction: 1) Closed-Loop rate sensing, and 2) Open-Loop rate sensing. In the closed-loop method, sense-mode displacement in response to angular rate is enforced to be zero by applying electrostatic force to the force-feedback electrodes. The voltage required to generate necessary counter force then gives the rate output. In spite of providing more linear response in wider bandwidth, closed-loop rate sensing mechanism needs complex electronics, which is not preferred in this study. On the other hand, open-loop approach uses generic AM demodulation methods that can easily be implemented. Figure 2.14 shows the block diagram of a typical AM demodulation circuit.

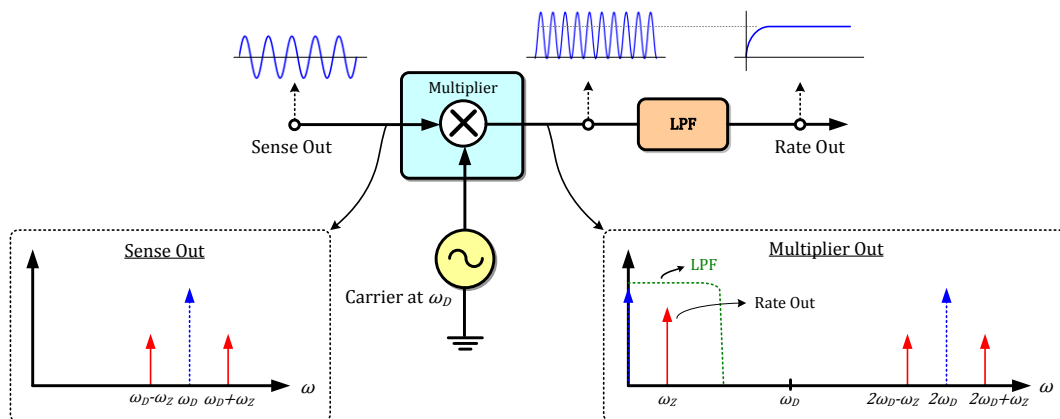


Figure 2.14: Block diagram of a typical AM demodulation circuit for open-loop rate sensing.

For an ideal sense output signal modulated with drive-mode vibration frequency, and assuming that phase errors are zero, time-domain expression of the multiplier output is derived as

$$\begin{aligned}
 M_O(t) &= A_S [\cos((\omega_D + \omega_Z)t) + \cos((\omega_D - \omega_Z)t)] \times A_C \cos(\omega_D t) \\
 &= \frac{A_S \cdot A_C}{2} \left[\underbrace{2\cos(\omega_Z t)}_{\text{Baseband term}} + \underbrace{\cos((2\omega_D + \omega_Z)t) + \cos((2\omega_D - \omega_Z)t)}_{\text{High frequency terms}} \right] \quad (2.59)
 \end{aligned}$$

where A_S and A_C are amplitudes of the sense-mode output and the drive-mode carrier, respectively. This equation shows that signal component at the applied rate frequency, ω_Z , is down converted to baseband while other terms are further transferred to higher frequencies. By employing a low-pass filter having cut-off frequency sufficiently lower than the minimum frequency of undesired signals, i.e. $(2\omega_D - \omega_Z) > \omega_C > \omega_Z$, baseband rate signal is extracted and higher frequency terms are rejected. It should be noted that this filter determines the overall bandwidth of the system assuming that the mechanical bandwidth is wider than the electronic bandwidth. The resultant rate output signal is then expressed as

$$R_O(t) = A_S \cdot A_C \cdot \cos(\omega_Z t) \quad (2.60)$$

Although Equation (2.60) provides an expression for the rate output, it does not consider the non-idealities coming from electronic circuits and mechanical sensor. In fact, there may be a phase difference between modulated and carrier signals due to phase errors introduced by each circuit stage. Moreover, scarcely can fully-decoupled and balanced structure of the gyroscope remove the mechanical crosstalk completely, unless special additional circuits are used. In this research, instead of mechanical crosstalk cancellation circuit, the effect of this non-ideality is minimized by dedicated phase-sensitive demodulation circuits.

As expressed in Equation (2.39), Coriolis based displacement is related to the velocity of drive-mode oscillation. Conversely, displacement produced by the mechanical crosstalk is proportional to the drive-mode displacement. Therefore, there is a 90° phase difference between the signals generated by these two mechanisms. For that reason, error coming through mechanical crosstalk is also called as quadrature error. Then, by including the effects of quadrature and phase errors, the multiplier output expression in Equation (2.59) can be modified as

$$M_o(t) = \underbrace{A_C \cos(\omega_D t + \emptyset)}_{\text{Carrier with phase error}} \left\{ \underbrace{A_Q \sin(\omega_D t)}_{\text{Quadrature error}} + \underbrace{A_S [\cos((\omega_D + \omega_Z)t) + \cos((\omega_D - \omega_Z)t)]}_{\text{Sense output in response to angular rate input}} \right\} \quad (2.61)$$

where \emptyset is the phase error representing the total phase shift between the drive-mode carrier and the sense-mode output signals. Rearranging the terms in Equation (2.61) and applying the signal to a low-pass filter, which rejects the high frequency signals, give the baseband rate output voltage expressed as

$$R_o(t) = \underbrace{\left[-\frac{A_C \cdot A_Q}{2} \right] \sin(\emptyset)}_{\text{Offset}} + \underbrace{[A_S \cdot A_C \cdot \cos(\omega_Z t)] \cos(\emptyset)}_{\text{Rate output}} \quad (2.62)$$

This equation implies that when the quadrature error is demodulated to baseband because of the phase error, there appears an undesired offset even in the absence of angular rate, i.e., $A_S=0$. Since the magnitude of the quadrature error is not predictable, and the drive-mode oscillation amplitude may vary with vacuum level, temperature or sensor parameters, unstable offset at the rate output may lead to critical bias instability problems. As described in Section 2.4.3, an oscillation amplitude control circuit can stabilize the drive-mode vibrations against external variations. In addition to this, the output offset can be minimized with the help of dedicated sense-mode electronics introducing almost zero phase error. Therefore, the effect of quadrature error can be reduced significantly by phase-sensitive

demodulation and vibration amplitude control, as long as the quadrature signal does not saturate the interface electronics.

2.5. Summary

This chapter presented the basic theory behind micromachined vibratory gyroscope mechanics and complementary electronics. First, dynamics of the drive and sense modes are investigated by introducing governing equations of force-displacement relations. Secondly, by examining different types of parallel plate capacitor configurations, the explanations of electrostatic actuation used for actuating the drive-mode, and the capacitive sensing mechanism used for monitoring the drive-mode vibrations and sensing the Coriolis based sense-mode displacements are given. Moreover, the electrostatic spring effect and the mode-matching concept in gyroscopes having varying-gap type electrodes are illustrated. Next, by combining the mechanical properties and transduction mechanisms, the generalized electrical equivalent model of the gyroscope is constructed. Finally, the theory of vibratory gyroscope electronics is presented. The principles of the self-oscillation circuit and the automatic amplitude control loop are given, as well as the amplitude demodulation technique used for the sense-mode rate output extraction.

CHAPTER 3

READOUT AND CONTROL ELECTRONICS DESIGN

This chapter presents design details and simulations of readout and control electronics for silicon-on-glass (SOG), silicon-on-insulator (SOI), and dissolved-wafer-process (DWP) vibratory gyroscopes developed at METU. Section 3.1 gives external gyroscope electronics implemented with commercial discrete components. In this section, besides transresistance amplifier type interfaces, single-ended and differential self-resonance excitation circuits with both manual and automatic oscillation amplitude control mechanisms are introduced. Moreover, the design of open-loop rate sensing electronics involving phase-sensitive AM demodulation is given as well. Section 3.2 explains the design steps of CMOS capacitive and resistive type interfaces implemented in standard 0.6 μ m CMOS process provided by XFAB Semiconductor Foundries. In this section, interfaces are characterized by AC, transient, and noise simulations of CADENCE Analog Artist simulator. Section 3.3 proposes a CMOS fully-differential automatic amplitude control circuit verified by system-level and transistor-level simulations. Section 3.4 presents the design of CMOS open-loop rate-sensing electronics, which is based on full-wave rectification followed by low-pass filtering. Finally, Section 3.5 gives a brief summary of the chapter.

3.1. Discrete Readout and Control Electronics

Although gyroscope electronics implemented with commercial discrete components are known to give inferior performance compared to CMOS counterparts, they provide reliable, low-cost, modifiable, easily implementable, and time-saving solutions for fully-functional angular rate sensor systems. The vast variety of

high-performance discrete components in the market enables the implementation of complete gyroscope electronics on typical printed circuit boards (PCB). Moreover, with the improvements in surface-mount device (SMD) and multi-layer PCB technologies, it is now possible to fit whole electronics in few square centimeters. Hence, in this research, initial functionality and characterization tests are performed with discrete electronics rather than CMOS. Designed drive-mode self-oscillation and sense-mode rate output extraction circuits as well as resistive-type interfaces, which are all implemented with commercial SMDs, are presented in the following sub-sections.

3.1.1. Drive-Mode Self-Resonance Excitation Circuit with Manual Oscillation Amplitude Control

Remembering the proper operation of a vibratory gyroscope, an angular rate input induces Coriolis force in the sense-mode only if the drive-mode is kept in oscillation. Sustaining self-triggered vibrations in the drive-mode requires closed-loop positive feedback circuits satisfying the Barkhausen oscillation criteria, stating that oscillation starts only if the loop gain is greater than unity at the frequency where the total phase shift is zero. Therefore, a simple self-resonance loop is composed of gain and phase compensation blocks for satisfying the oscillation criteria and a vibration amplitude limiter. Figure 3.1 illustrates the proposed self-resonance excitation circuit with manual amplitude control for CMOS capacitive-type interfaced gyroscopes [50]. As explained in Section 2.4.1, capacitive-type interfaces introduce -90° phase shift at the resonance frequency since the generated current is integrated and converted to voltage on the interface capacitor. Then, phase condition for sustaining oscillation at the mechanical resonance frequency is satisfied by a phase shifting circuit introducing additional $\pm 90^\circ$ phase shifts. The resultant signal is applied to a comparator which generates power supply-limited square wave signals at the oscillation frequency. This is the stage where the amplitude of the growing vibrations is limited by a nonlinear operation. Finally, an adjustable-gain attenuator stage is used for determining the amplitude of the driving signal so that the generated vibrations are at the desired level.

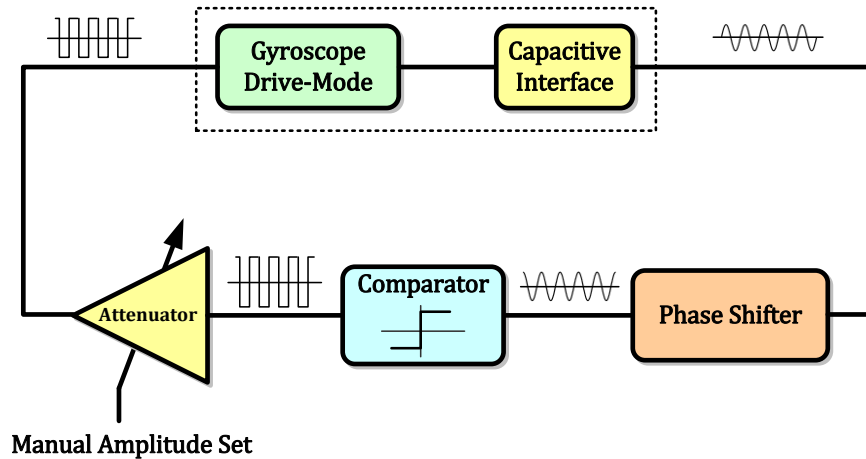


Figure 3.1: Block diagram of the self-resonance excitation circuit with manual amplitude control for CMOS capacitive-type interfaced gyroscopes.

Despite the fact that loop operation is quite simple, realizing phase shifting circuits providing exactly 90° phase shift in a sufficient bandwidth may be challenging due to some disadvantages of these circuits. Figure 3.2 shows two possible configurations of 90° phase shifters: (a) OPAMP differentiator and (b) OPAMP integrator circuits introducing -90° and 90° phase shifts, respectively.

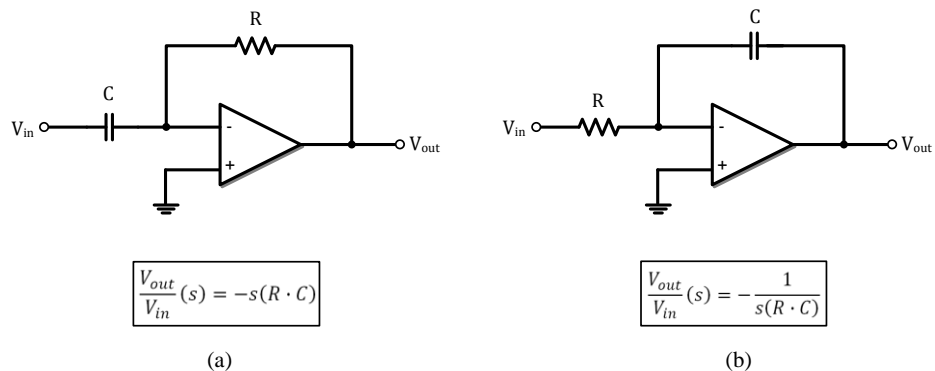


Figure 3.2: Two possible configurations of 90° phase shifters; (a) OPAMP differentiator and (b) OPAMP integrator circuits introducing -90° and 90° phase shifts, respectively.

Giving zero gain at DC, the differentiator cancels out the possible offset coming from the interface circuit while providing almost a 90° phase shift in a sufficiently

wide bandwidth, which is, indeed, limited by the parasitics and OPAMP itself. Since the gain of the differentiator increases as the frequency increases, the amplification of the high-frequency noise and sharp transitions at the differentiator input may cause stability problems in the feedback loop. Alternatively, an ideal OPAMP integrator circuit also introduces 90° phase shift to the incoming signal. However, due to the fact that OPAMP output is not DC-biased through a resistive path, integrator circuit gives saturated output when the input signal has a DC component. In practical applications, an additional output biasing feedback resistor is connected parallel to the integration capacitor. Solving the DC biasing problem, this resistor brings undesired phase errors. Moreover, a high-pass filter circuit is frequently connected to integrator output in order to reject the DC offset. This filter also leads to phase errors, resulting in a vibration frequency that is away from the mechanical resonance frequency of the gyroscope. Comparing the advantages and disadvantages of both phase shifters, it is concluded that the differentiator would give superior performance as long as the electrical coupling of the high-frequency driving signal to the differentiator input is prevented. Figure 3.3 shows the circuit schematic of the proposed self-resonance excitation circuit including differentiator as the phase shifting element.

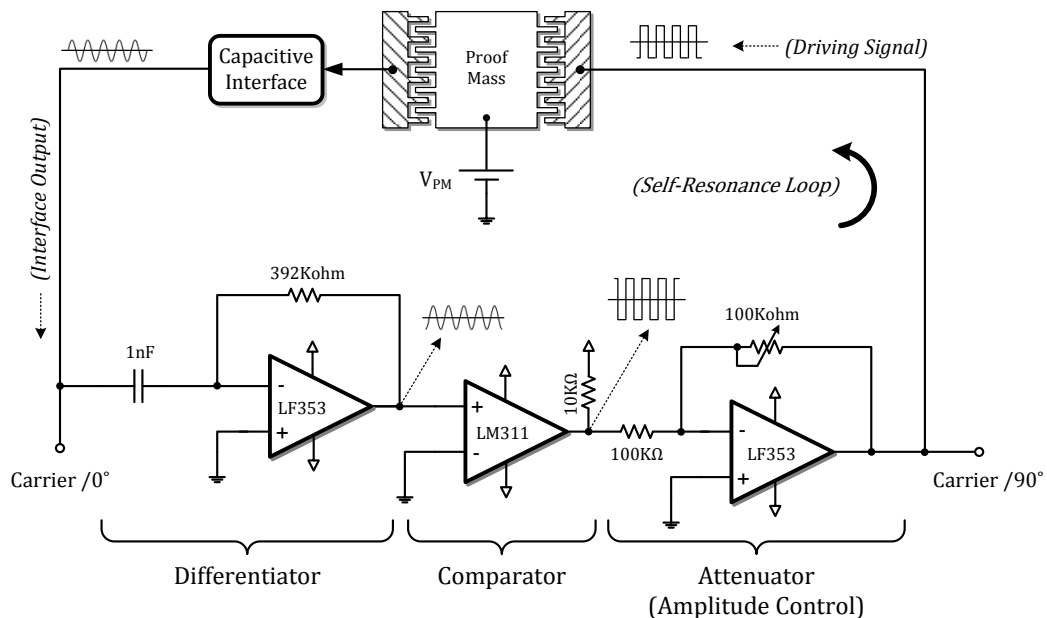


Figure 3.3: Circuit schematic of the self-resonance excitation circuit including differentiator as the phase shifting element.

The transient simulations of the proposed circuit are performed in SIMULINK after constructing the second-order model of the gyroscope cascaded CMOS capacitive-type interface. Figure 3.4 gives the SIMULINK transient response of the interface output when the gain of the attenuator is changed during the simulation. It is observed that vibration level of the drive-mode can be set by manually adjusting the amplitude of the driving signal through the attenuator gain.

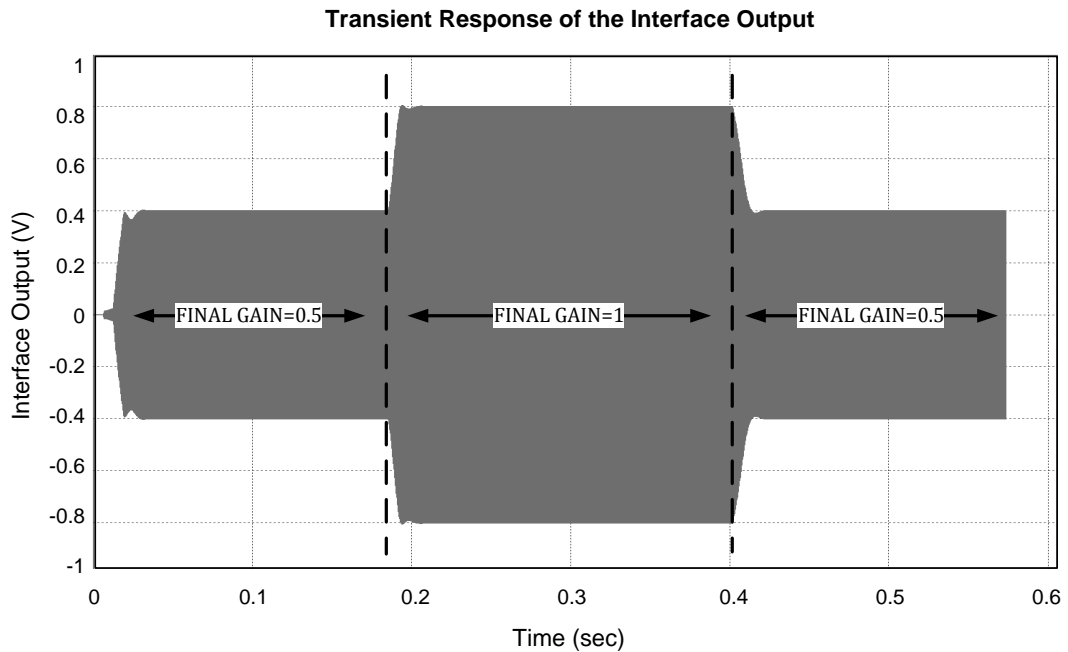


Figure 3.4: SIMULINK transient response of the interface output when the gain of the attenuator is changed during the simulation.

However, self-oscillation loop with manual amplitude control can give constant-amplitude vibrations only if sensor parameters and ambient conditions are constant. As the temperature, vacuum level, supply voltages, or sensor parameters vary, the vibration level of the drive-mode changes, since there is not any adaptive control on the driving signal. Moreover, the gyroscope is driven into resonance with a square wave signal, which may lead to undesired glitches in the circuit and may excite the higher modes of the gyroscope.

3.1.2. Sense-Mode Open-Loop Rate Sensing Electronics

Raw sense-mode output in response to an angular rate is an AM modulated signal at the frequency of drive-mode oscillation. In open-loop rate sensing electronics, this signal is required to be transferred to baseband by a phase sensitive AM demodulator circuit, as theoretically explained in Section 2.4.4. There are several techniques for AM demodulation, usually employing multipliers, switches, half-wave or full-wave rectifiers. In this study, Analog Devices' balanced modulator/demodulator (AD630) integrated circuit [55], providing high precision phase-sensitive demodulation, is used in the sense-mode electronics composed of discrete components. Figure 3.5 shows the complete circuit schematic of the proposed open-loop rate sensing electronics. In this circuit, the sense-mode CMOS capacitive interface output is buffered and applied to demodulator, giving full-wave rectified version of the input signal. The carrier signal of the demodulator is taken from the drive-mode self-resonance circuit given in Figure 3.3. Since the phase difference between sense-mode output and drive-mode oscillation is either 0° or 90° as the gyroscope is operated in matched or mismatched mode, in-phase and 90° phase-shifted versions of the carrier signal are selected by a manual switch according to the operation mode. A third-order Sallen-Key type low-pass filter (LPF) having cut-off frequency of 10Hz then rejects the unwanted high-frequency components in the full-wave rectified signal, giving a baseband angular rate related signal. Finally, LPF output is amplified by a non-inverting gain stage for scale-factor tuning.

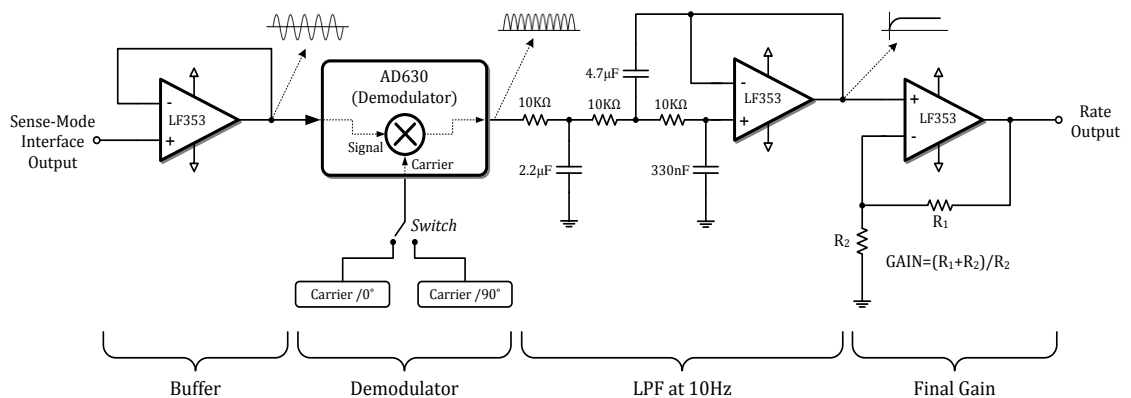


Figure 3.5: Circuit schematic of the open-loop rate sensing circuit used for converting the AM modulated sense-mode output to baseband angular rate related signal.

The proposed sense-mode rate extraction circuit and the self-resonance loop given in Figure 3.3 are implemented with SMD components on a compact printed circuit board (PCB). Figure 3.6 shows the photograph of the PCB including entire drive-mode and sense-mode electronics, fit in a 5.3×2 cm² area with a dedicated layout design.

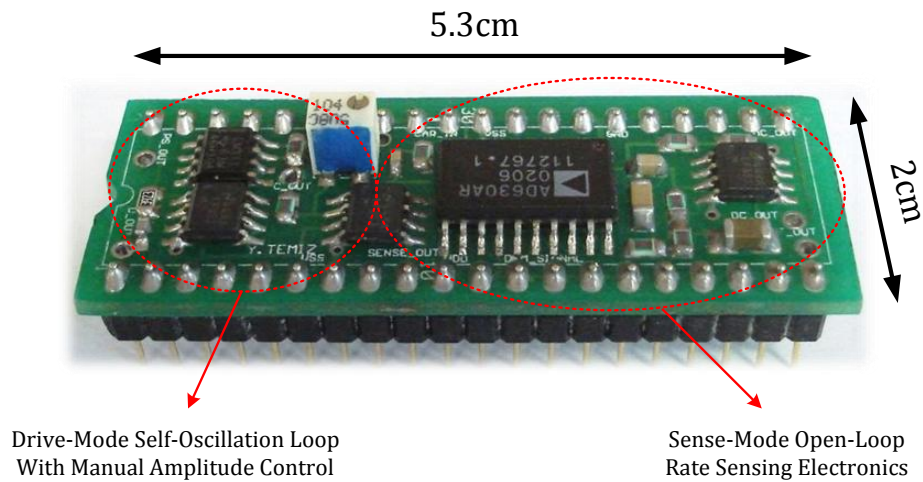


Figure 3.6: Photograph of the PCB including entire sense-mode and drive-mode electronics, fit in a 5.3×2 cm² area with a dedicated layout design.

3.1.3. Transimpedance Amplifier (TIA) Type Resistive Interface

Interface circuits play an important role in the overall performance of the micromachined gyroscopes, as they convert atomic scale displacements to meaningful electrical signals. In the drive-mode of the gyroscope, these circuits are used for monitoring the vibration amplitude in order to construct a positive-feedback loop for self-oscillation. Furthermore, displacements in response to applied angular rates are sensed by more sensitive interfaces in the sense-mode. Because of the fact that generated currents due to these physical displacements are extremely small, proximity of the interface to the mechanical sensor is one of the major parameters that limit the performance of the system. In an angular rate sensor system where the MEMS gyroscope and electronic interface cannot be placed on the same die due to

process limitations, parasitics coming from interconnections degrade the sensitivity of the gyroscope significantly. Therefore, either parasitic capacitances should be minimized or interface electronics eliminating the effect of parasitics should be employed. The former is usually not practical for the interface electronics implemented with commercial discrete components. Therefore, a transimpedance amplifier type resistive interface, which is also called as transresistance amplifier (TRA), is preferred since it minimizes the effect of parasitic capacitances. As mentioned in Section 2.4.1, capacitive-type interfaces provide higher sensitivity; thus, they are usually employed in the sense-mode. However, the difficulty of implementing sufficiently large biasing resistors prevents the realization of capacitive-type interfaces with discrete components. Hence, in the discrete electronics involving automatic amplitude control mechanism, resistive-type interfaces are preferred for not only the drive-mode but also the sense-mode of the gyroscope. Figure 2.1 illustrates a gyroscope cascaded TRA structure, where C_S is the capacitance between the stationary electrode and the proof mass, C_P is the total of parasitic capacitances coming from interconnections and OPAMP input capacitance, and I_S is the current generated by the sensor.

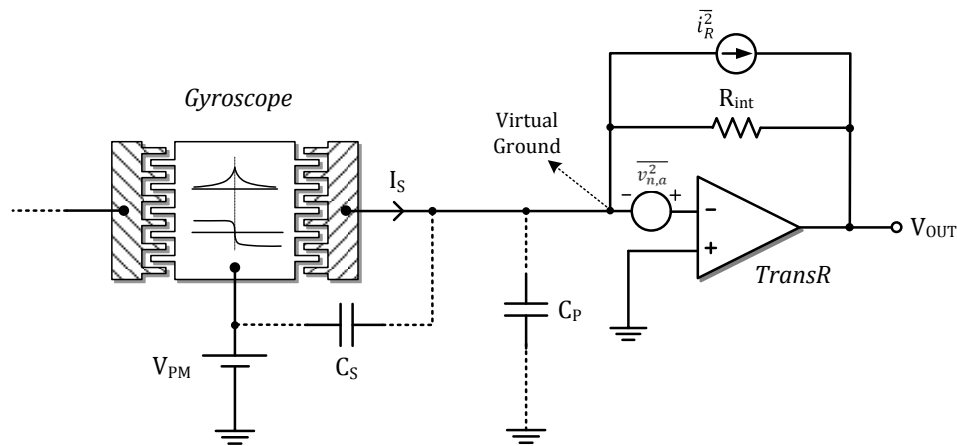


Figure 3.7: Gyroscope cascaded transresistance amplifier (TRA) structure.

In the normal operation of the feedback connected OPAMP, the difference between the OPAMP input terminals is almost zero due to very high open-loop gain of the

OPAMP. Since the non-inverting terminal is directly connected to ground, inverting terminal is also at ground potential, which is called as virtual ground. Therefore, the high-impedance node of the gyroscope is DC-biased to ground through non-inverting terminal. In addition, the OPAMP output is also DC-biased to ground via feedback resistor, R_{int} , connected between the high-impedance node and OPAMP output. If the current source and effective impedance of the capacitances parallel to the current source is converted to their Thevenin equivalent circuit, it is observed that the effect of capacitances across high-impedance node and ground diminishes, leading to output voltage expression given as

$$V_{OUT} = -(R_{int} \cdot I_S) \quad (3.1)$$

Therefore, output voltage is only proportional to the generated current and interface resistor, implying that TRA theoretically minimizes the phase error and gain loss due to the parasitic capacitances and the stationary capacitance of the gyroscope.

In addition to phase shift and gain characteristics, electronic noise contribution from the interface is also quite important in determining the overall gyroscope performance. The electronic noise of the TRA interface is composed of the noise of the OPAMP and the thermal noise of the interface resistor. Then, equivalent input-referred current noise is expressed as

$$\frac{\overline{i_{n,in}^2}}{\Delta f} = \frac{4kT}{R_{int}} + \frac{\overline{v_{n,a}^2}}{R_{int}^2} \quad (3.2)$$

which indicates that the interface resistor should be as large as possible to decrease the current noise. However, resistances of commercial thin-film SMD resistors are limited. Moreover, error tolerance and parasitic capacitance of the resistor highly depend on its value. Then, interface resistors in the range of 1-10M Ω are used in the sense-mode and maximum of 1M Ω in the drive-mode because of the fact that drive-mode does not require as high sensitivities as the sense-mode.

3.1.4. Single-Ended Automatic Amplitude Control Circuit with Open-Loop Rate Sensing Electronics for SOG Gyroscopes

Although the self-oscillation loop explained in Section 3.1.1 provides constant amplitude vibrations, it cannot adjust driving signal according to variations in sensor parameters, supply voltages, temperature, and vacuum level. Moreover, driving voltage is a square wave signal which may excite the high frequency modes of the gyroscope and result in glitches in the circuit due to electrical coupling. Therefore, more complicated drive-mode electronics employing continuous adaptive amplitude control mechanism is required to obtain superior sensor performance. Figure 3.8 shows the block diagram of the proposed automatic amplitude control mechanism together with the open-loop rate sensing electronics designed for single-mass silicon-on-glass (SOG) gyroscopes [8] developed at METU. This loop aims to adjust the loop gain through variable gain amplifier (VGA) according to the difference between the amplitude set voltage and the monitored drive-mode vibration amplitude so that the system poles are always on the imaginary axis. Thus, it sustains constant amplitude vibrations independent of the sensor parameters and ambient conditions.

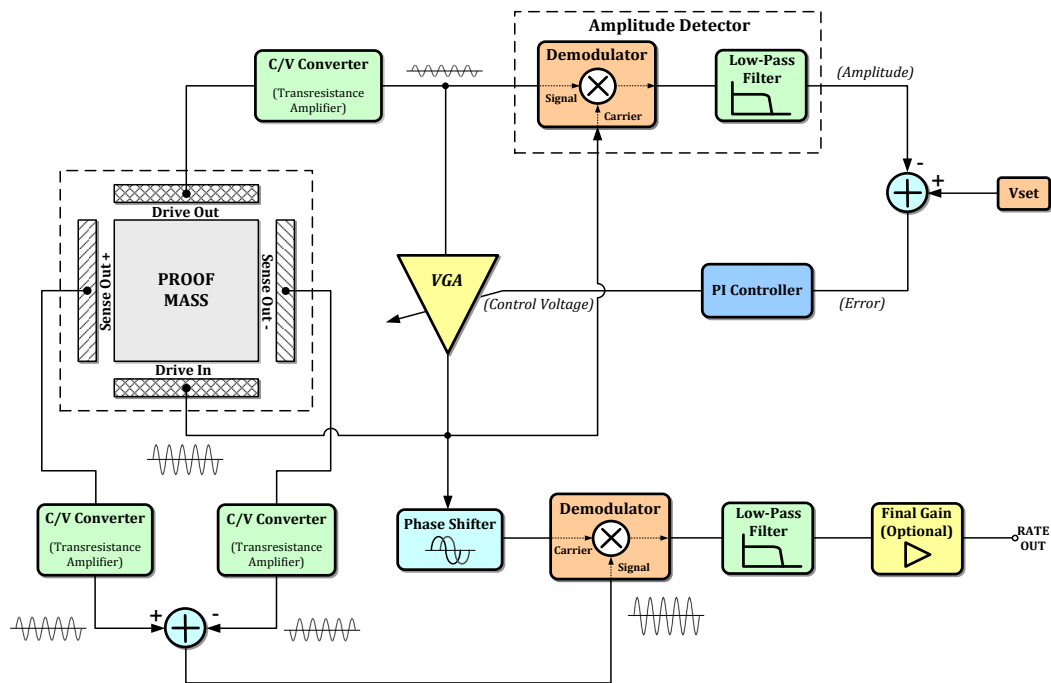


Figure 3.8: Block diagram of the proposed automatic amplitude control mechanism together with the open-loop rate sensing electronics designed for single-mass SOG gyroscopes.

Figure 3.9 shows the circuit schematic of the proposed automatic amplitude control loop and open loop sense-mode electronics. In this circuit, both differential sense-mode electrodes and single-ended drive-mode electrode are sensed by transresistance amplifiers. In the drive-mode, a constant gain inverting amplifier inverts the transresistance amplifier output, satisfying the phase condition of oscillation. The vibration amplitude information is then extracted by a demodulator followed by a first-order low-pass filter. After the comparison of amplitude voltage to predefined set value, the resultant error signal is applied to the PI controller, which generates the necessary control voltage for the VGA gain adjustment. The Analog Devices' variable gain amplifier, AD602 [56], providing dB linear gain between -10dB and +30dB, is preferred as the final gain stage of the loop. In the sense-mode, differential outputs are converted to a single-ended signal and transferred to baseband by AD630 demodulator followed by third-order LPF having cut-off frequency at 10Hz. Either in-phase or 90° shifted versions of the driving signal is applied to the demodulator carrier input according to the matched or mismatched operation of the gyroscope.

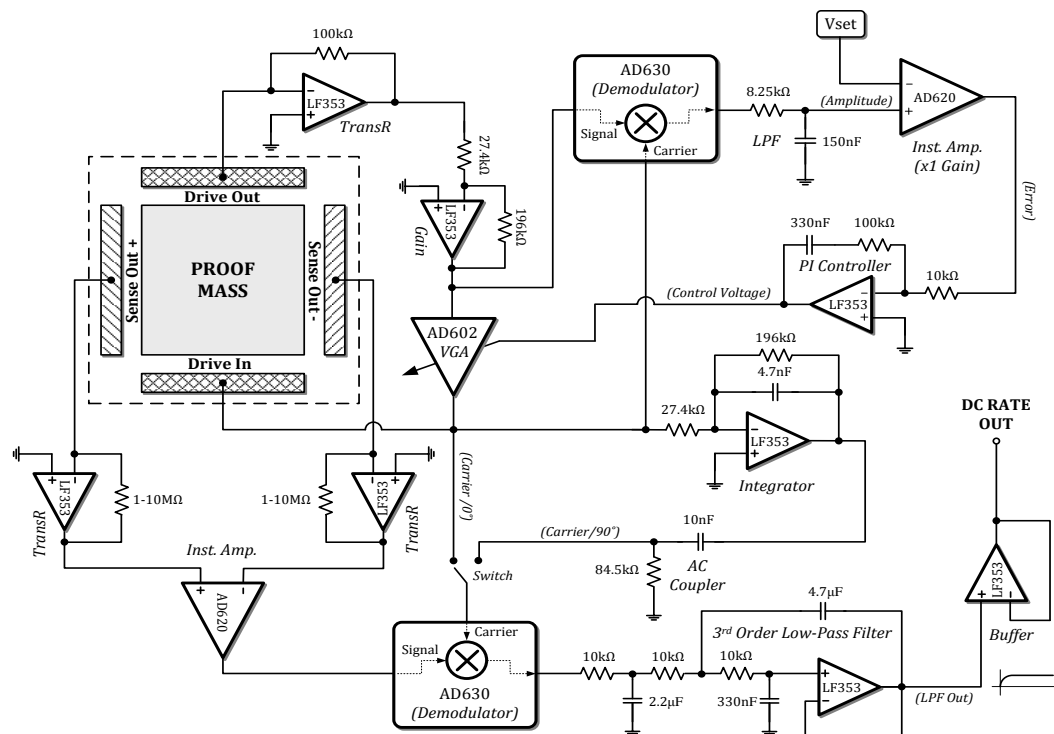


Figure 3.9: Circuit schematic of the proposed automatic amplitude control loop and open loop sense-mode electronics.

After obtaining the transfer characteristics of the mechanical sensor, the overall system is modeled in SIMULINK for system-level transient simulations. Figure 3.10 gives the transient simulation results for the driving signal and drive-mode interface output, as the quality factor of the gyroscope is changed during the simulation. At the start-up, system has an overshoot response since the PI controller gives saturated output, resulting in a maximum VGA gain. As the PI controller output stabilizes, both the driving signal and the interface output reach to the desired levels, giving constant amplitude oscillation at the mechanical resonance frequency. Furthermore, when the quality factor is increased instantaneously, system automatically senses the increase in the vibration amplitude and decreases the driving signal, and vice versa. Besides variations in the quality factor, it is verified that the circuit can adjust the driving signal for constant amplitude oscillation when the sensor gain, resonance frequency, and supply voltages are also changed.

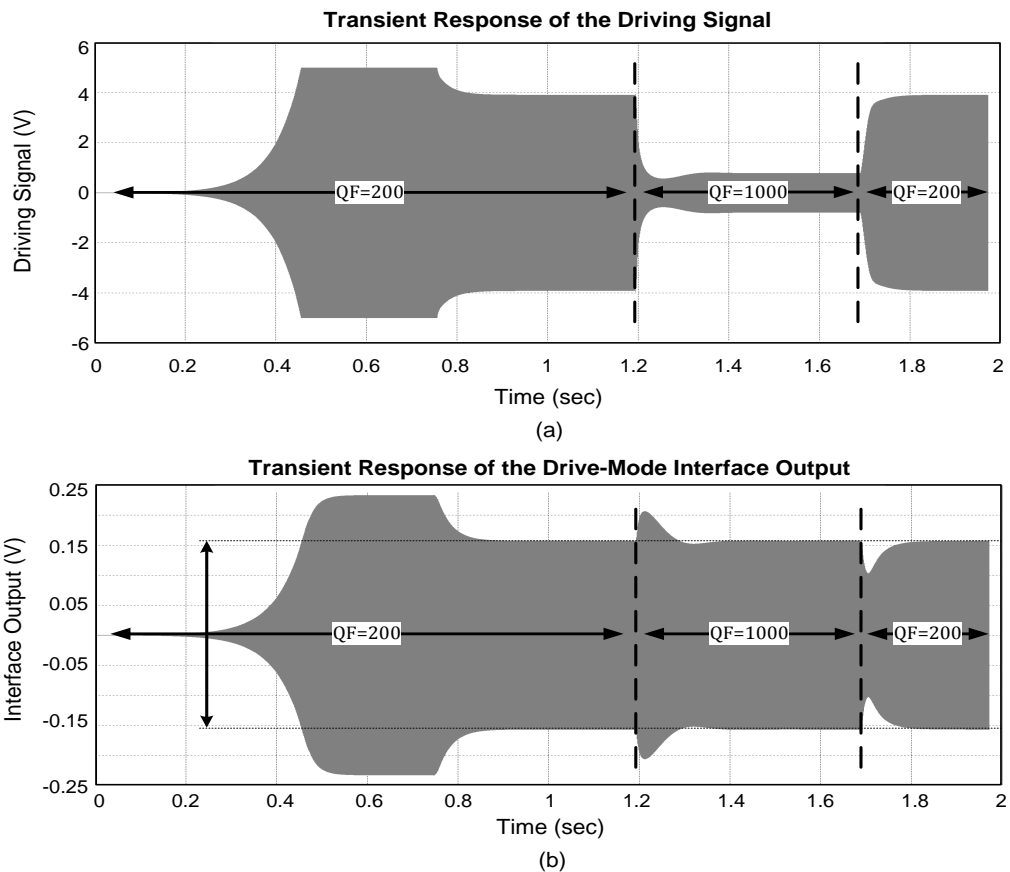


Figure 3.10: SIMULINK transient simulation result for (a) driving signal, and (b) drive-mode interface output, as the quality factor of the gyroscope is changed.

After verifying that the proposed circuit operates properly, it is implemented with SMD components on a compact PCB having $5.4 \times 2.4 \text{ cm}^2$ area. Figure 3.11 shows the top and bottom sides of the PCB including packaged SOG gyroscope, transresistance amplifiers, open-loop rate sensing electronics, and self-resonance loop with automatic amplitude control.

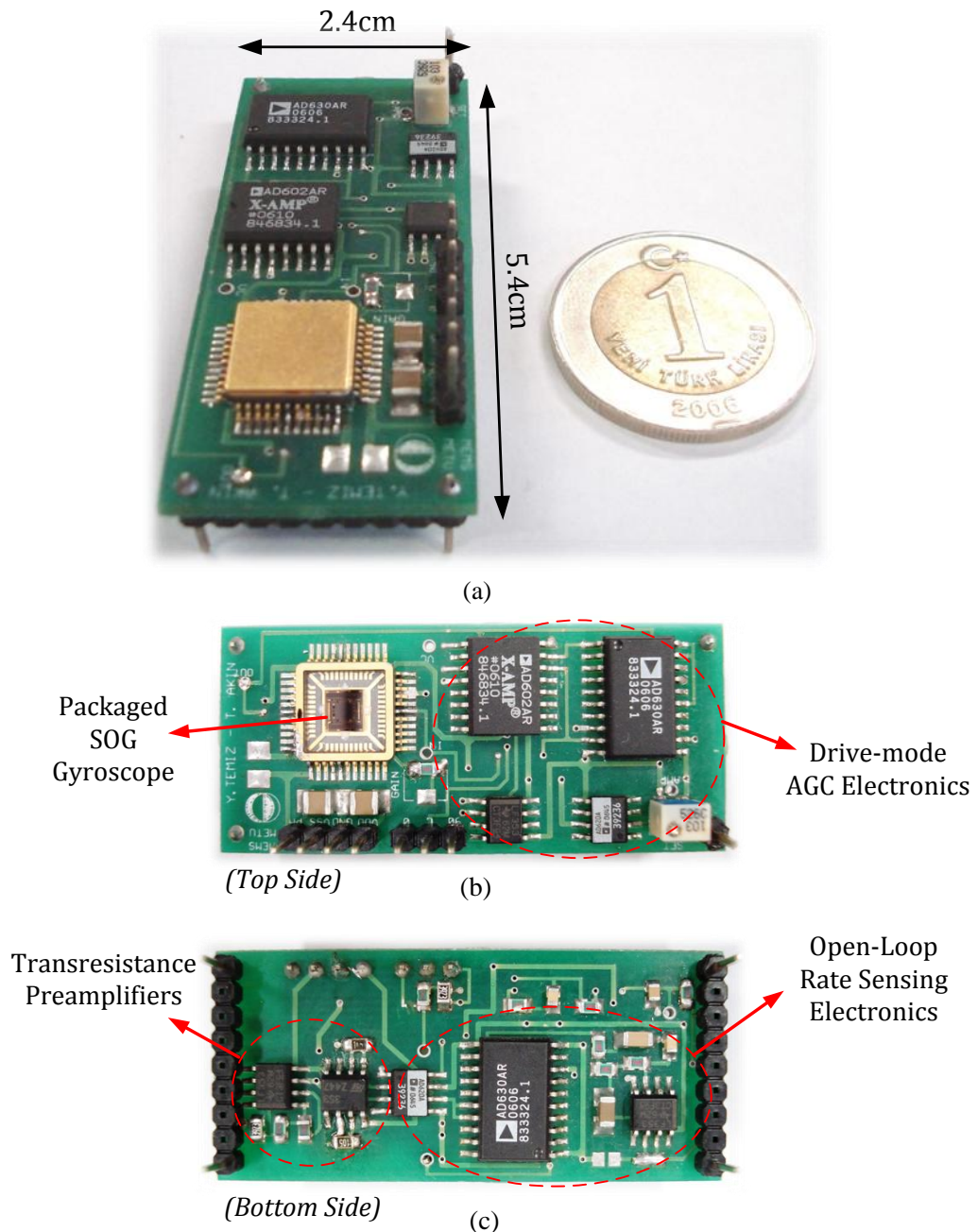


Figure 3.11: (a) General view, (b) Top side, and (c) Bottom side of the PCB, including packaged SOG gyroscope, transresistance amplifiers, open-loop rate sensing electronics, and self-resonance loop with automatic amplitude control.

In this PCB, both the drive-mode and sense-mode transresistance amplifiers are located just under the sensor, which is the closest placement that can be achieved without sacrificing the symmetry of the differential sense-mode signals. Packaged SOG gyroscope and most of the drive-mode electronics are placed on the top side where sense-mode circuits are on the bottom side of the double-layer PCB. Moreover, the sinusoidal driving signal generated by the self-resonance loop is isolated from the sense-mode signals in order to prevent the possible electrical coupling resulting in an output offset in the phase-sensitive demodulation.

3.1.5. Differential Automatic Amplitude Control Circuit with Open-Loop Rate Sensing Electronics for Dual-Mass Gyroscopes

Sensitivity to linear and rotational accelerations is one of the major problems of MEMS gyroscopes. Ideally, a gyroscope should detect the Coriolis acceleration while rejecting the possible linear or rotational accelerations along the sensitive axis. These accelerations deflect the sense-mode moving electrodes, causing nonlinearity in the scale-factor and a DC shift in the output bias [51]. The most preferred solution for the acceleration sensitivity problem is utilizing multi-mass gyroscopes sensed by differential readout electronics. Thus, unlike SOG gyroscopes, dissolved-wafer process (DWP) gyroscopes developed at METU are dual-mass gyroscopes, where each mass is vibrated in opposite directions in the drive-mode. Owing to this mechanism, the gyroscope gives anti-phase responses to the Coriolis action, and in-phase responses to other common accelerations. When the sense-mode outputs are read differentially, common-mode signals diminish whereas the angular rate related signal doubles after differential outputs are converted to a single-ended signal by a subtraction operation. Figure 3.12 illustrates the simplified view of the dual-mass DWP gyroscope whose design and fabrication details are beyond the scope of this thesis. In this gyroscope, drive-mode motor electrodes (DM) are connected so that each proof mass resonates in opposite directions when differential driving signals are applied. The vibration amplitude information of resonating drive-mode is extracted through differential drive-mode pick-up electrodes (DP). The sense-mode pick-up electrodes (SP) are cross-connected since the deflections in

response to angular rates are in opposite directions for each mass. These electrical connections enable two mechanically-coupled gyroscopes behave as a single gyroscope operating differentially in both modes.

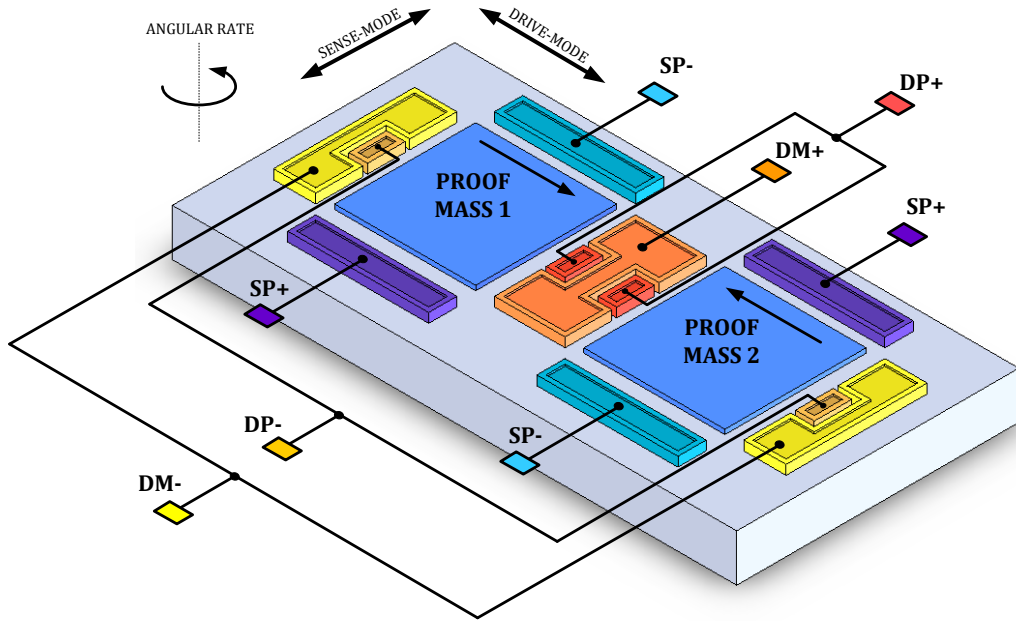


Figure 3.12: Simplified view of the dual-mass DWP gyroscope.

Table 1.1 provides the expected capacitance values and electromechanical coupling coefficients for drive motor (DM), drive pick-up (DP), and sense pick-up (SP) electrodes. It should be noted that stationary capacitance values are given as half of the total since each mechanism has two differential electrodes.

Table 3.1: Expected capacitance values and electromechanical coupling coefficients for drive motor (DM), drive pick-up (DP), and sense pick-up (SP) electrodes.

Parameter	Definition	Value
C_{DM}	Drive-mode motor (DM) capacitance (Half of total)	2.1 pF
n_{DM}	Current-to-velocity coefficient for drive motor	2.02×10^{-6}
C_{DP}	Drive-mode pick-up (DP) capacitance (Half of total)	0.32 pF
n_{DP}	Velocity-to-current coefficient for drive pick-up	3.08×10^{-7}
C_{SP}	Sense-mode pick-up (SP) capacitance (Half of total)	3.04 pF
n_{SP}	Velocity-to-current coefficient for drive pick-up	5.08×10^{-5}

In differential gyroscopes, balanced operation in the drive-mode is achieved with the generation of perfectly anti-phase excitation signals applied at both sides of the drive-mode resonators. One possible solution for differential signal generation may be inverting the single-ended signal in the self-oscillation loop. However, inverting amplifiers inevitably introduce phase errors which lead to imbalanced driving and deviation from the mechanical resonance frequency. An alternative and superior way of obtaining differential excitation signals is constructing two self-oscillation loops having totally symmetric structures. Figure 3.13 shows the circuit schematic of the proposed differential automatic amplitude control loop designed for DWP gyroscopes and implemented with commercial discrete components. In this circuit, there are two self-oscillation loops constructed by two VGAs packaged in one single chip, minimizing the mismatches between the loops. Drive-mode oscillations are sensed by TRAs connected to the pick-up electrodes placed on the same side with the motor electrodes as shown in in Figure 3.12. Since the phase difference between driving and pick-up signals is 180° at the resonance, an additional 180° phase shift introduced by the TRA is sufficient for the phase condition of oscillation. Then, the gain criterion is satisfied by the VGA gain, where gain control voltage is generated by the PI controller according to the difference between the vibration amplitude and the amplitude set voltage.

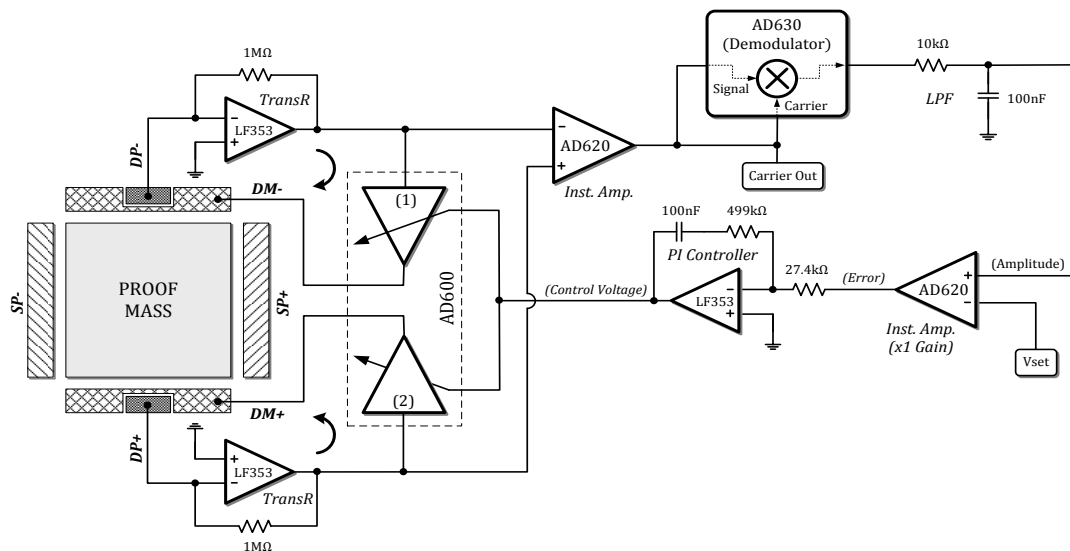


Figure 3.13: Circuit schematic of the differential automatic amplitude control loop designed for DWP gyroscopes and implemented with commercial discrete components.

The proposed loop together with differential open loop rate sensing electronics, which is similar to the one given in Figure 3.9, is implemented with commercial discrete components on very compact PCBs. Figure 3.14 shows the photographs of six-layer PCBs implemented with (a) dual in line package (DIP) components, and (b) surface mount devices (SMD). With a dedicated layout design, complete electronics is fit in a $2.1 \times 4.4 \text{ cm}^2$ area, which is extremely small for such a complex circuit. In this system, the DWP gyroscope and the transresistance preamplifiers are placed on a separate gold-plated PCB having $2.1 \times 1.9 \text{ cm}^2$ area.

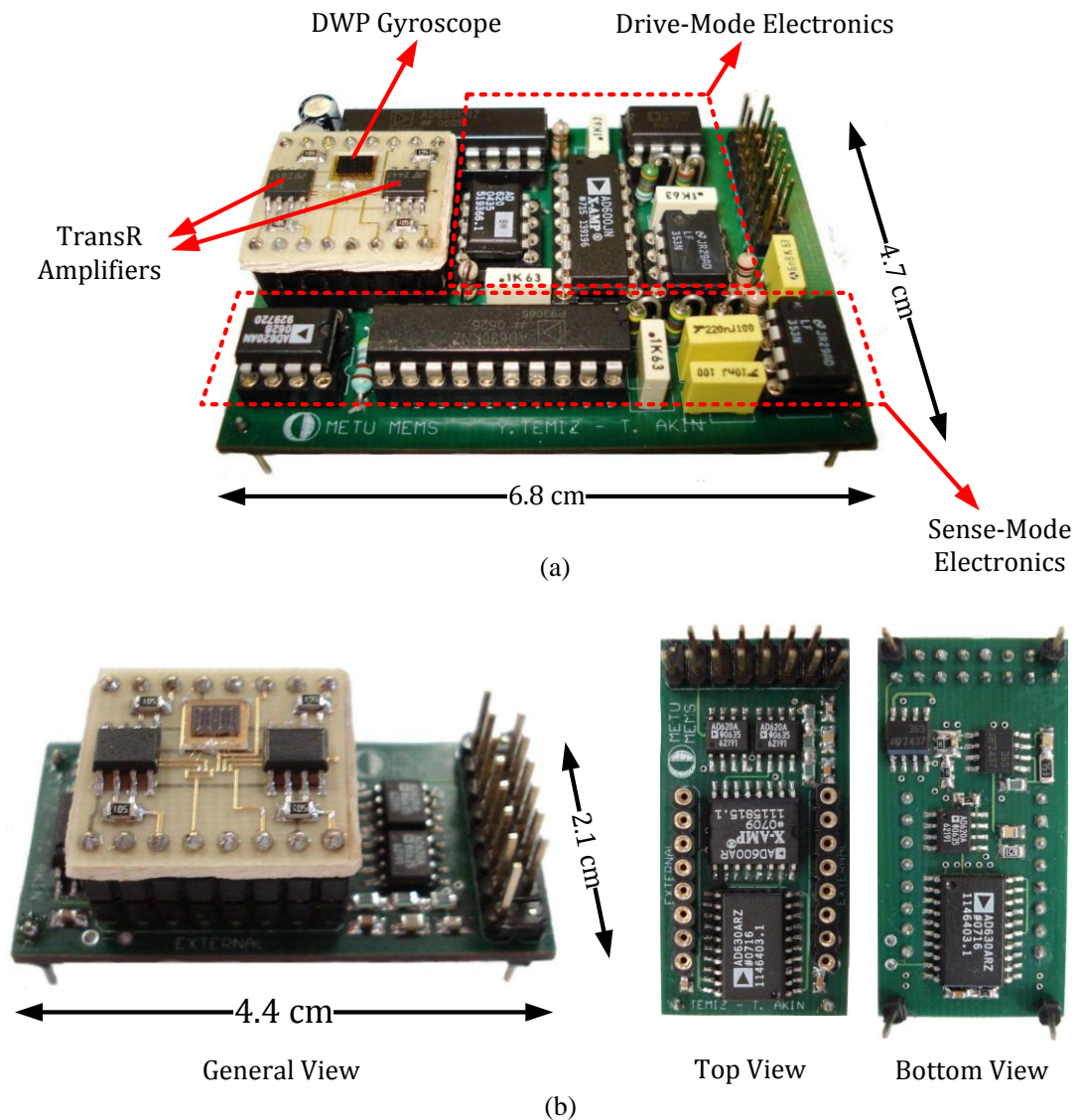


Figure 3.14: Photographs of six-layer PCBs implemented with (a) dual in line package (DIP) components, and (b) surface mount devices (SMD).

3.2. CMOS Capacitive and Resistive Interfaces

Gyroscope electronics implemented with commercial discrete components have large parasitic capacitances coming from wirebonds, packages, and PCBs. Moreover, difficulties in fabricating sufficiently large biasing resistors with small error tolerances in SMD technology limit the maximum achievable sensitivity of an angular rate sensor system. Therefore, dedicated CMOS electronics, which minimize the parasitic capacitances and provide several approaches for realizing biasing resistors in the order of gigaohms [8, 51], are required in high-performance micromachined vibratory gyroscopes. In this study, CMOS unity-gain buffer (UGB) and transimpedance amplifier (TIA) type capacitive and resistive interfaces are designed for high-SNR capacitance to voltage conversion in DWP gyroscopes.

3.2.1. Unity-Gain Buffer (UGB) Design

The input capacitance of an interface circuit adds directly to the overall parasitic capacitance across the high-impedance node and ground. Therefore, it is desired to design interface circuits having very small input capacitances for higher sensitivities. This requirement can be met by UGB circuits due to a phenomenon called Miller effect [52]. According to Miller's theorem, effective capacitance between two nodes can be separated into two grounded capacitances whose values approach to zero as the voltage gain between the nodes gets closer to unity. Based on this effect, input capacitance of a differential amplifier having moderate gain reduces significantly when the amplifier is buffer-connected. Figure 3.15 shows the schematic view of the proposed UGB circuit, which is the modified version of UGB circuits in [8, 33, 49], and Table 2.1 gives the transistor dimensions of the circuit designed for 0.6 μ m n-well CMOS process.

The open-loop circuit is actually a moderate-gain single-stage differential amplifier. The buffer connection is achieved by connecting the negative input terminal to the amplifier output. All transistors are designed to operate in the saturation region and a 100 μ A of tail current is generated by the M7 transistor biased by a bandgap

referenced bias cell producing 1.03 V. Input capacitance of the circuit is dominated by gate-to-source, gate-to-drain, and gate-to-bulk capacitances of the input transistor, M1. Because of the buffer connection and the current mirrors, drain and source terminals of the input transistor directly track the input ac voltage, giving gate-to-drain and gate-to-source gains very close to unity. Moreover, for an n-well process, bulk terminal of the PMOS input transistor is connected to its source. Then, all parasitic capacitances associated with the input transistor minimizes due to the Miller effect, resulting in a very low input capacitance for the UGB circuit.

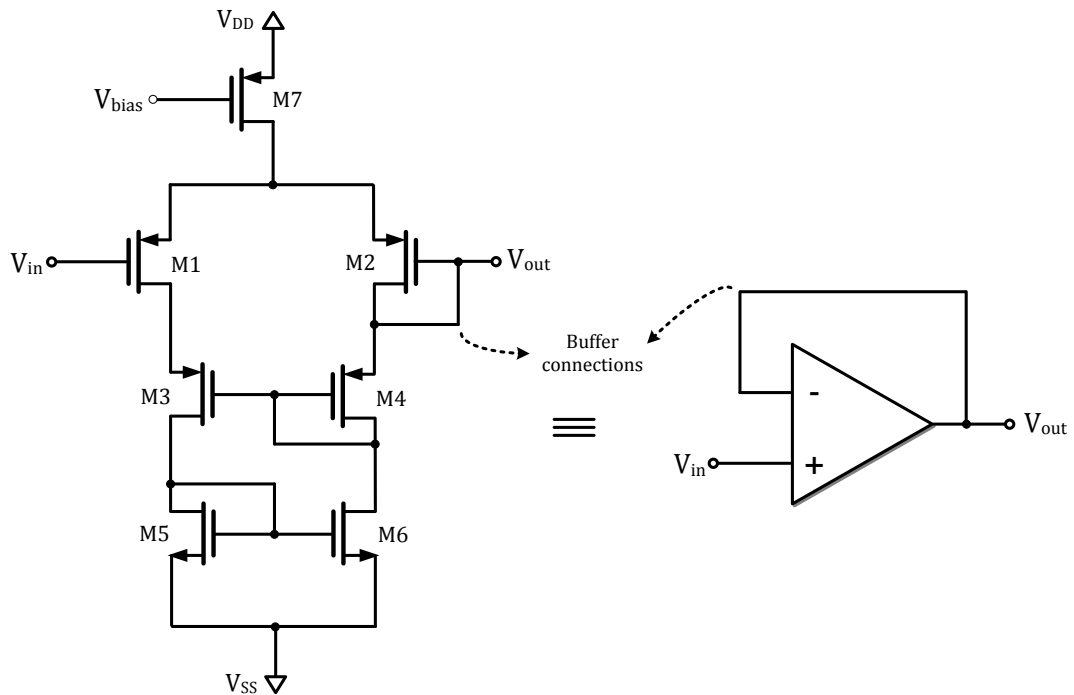


Figure 3.15: The schematic view of the UGB circuit, which is the modified version of UGB circuits in [8, 33, 49].

Table 3.2: Transistor dimensions for the UGB circuit designed for 0.6 μm n-well CMOS process of XFAB Semiconductor Foundries.

	M1	M2	M3	M4	M5	M6	M7
Width (W)	80 μm	80 μm	40 μm	40 μm	40 μm	40 μm	72 μm
Length (L)	4 μm	4 μm	4 μm	4 μm	8 μm	8 μm	4 μm

According to DC operating point simulations of the circuit, the nput transistor has total gate capacitance of 604 fF. However, this is not the actual input capacitance of the circuit because of the unity-gain feedback connection. Figure 3.16 shows the Z-parameter analysis result for the input impedance of the UGB circuit. According to this simulation, input capacitance is found as 2.71 fF, which is much smaller than the total gate capacitance of the input transistor since the unity-gain connection reduces the effective parasitic capacitance across the high-impedance node and ground.

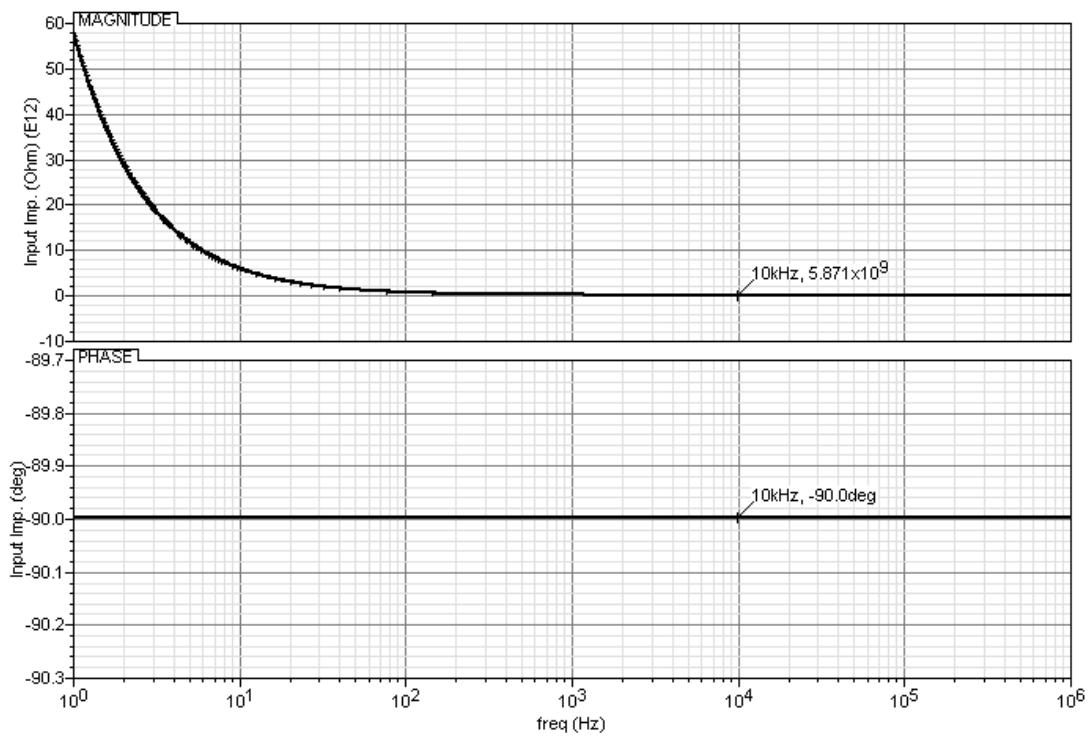


Figure 3.16: Z-parameter analysis result for the input impedance of the UGB circuit.

Moreover, parasitic capacitances associated with CMOS pads can also be minimized by using bootstrapping method [11, 33]. In this method, an electrically conductive shield layer is inserted between the top pad metal, where the high-impedance node is connected, and the substrate of the CMOS chip. By connecting the shield layer to UGB output, it is achieved that shield layer tracks the voltage at the high-impedance node. As the UGB gain approaches to unity, the parasitic capacitance between the

top metal pad and the shield layer diminishes according to the Miller effect, suppressing the total effective parasitic capacitance coming from wirebonding pads. Thus, gain of the UGB is quite important in determining the effective parasitic capacitances. Figure 3.17 shows the post-layout AC simulation result of the designed UGB when the output is loaded with a 10pF capacitor. The UGB voltage gain and phase error are found as 0.999 V/V (-8.581 mdB) and -28.44 mdeg, respectively. This analysis shows that UGB circuit provides almost perfect gain and phase characteristics.

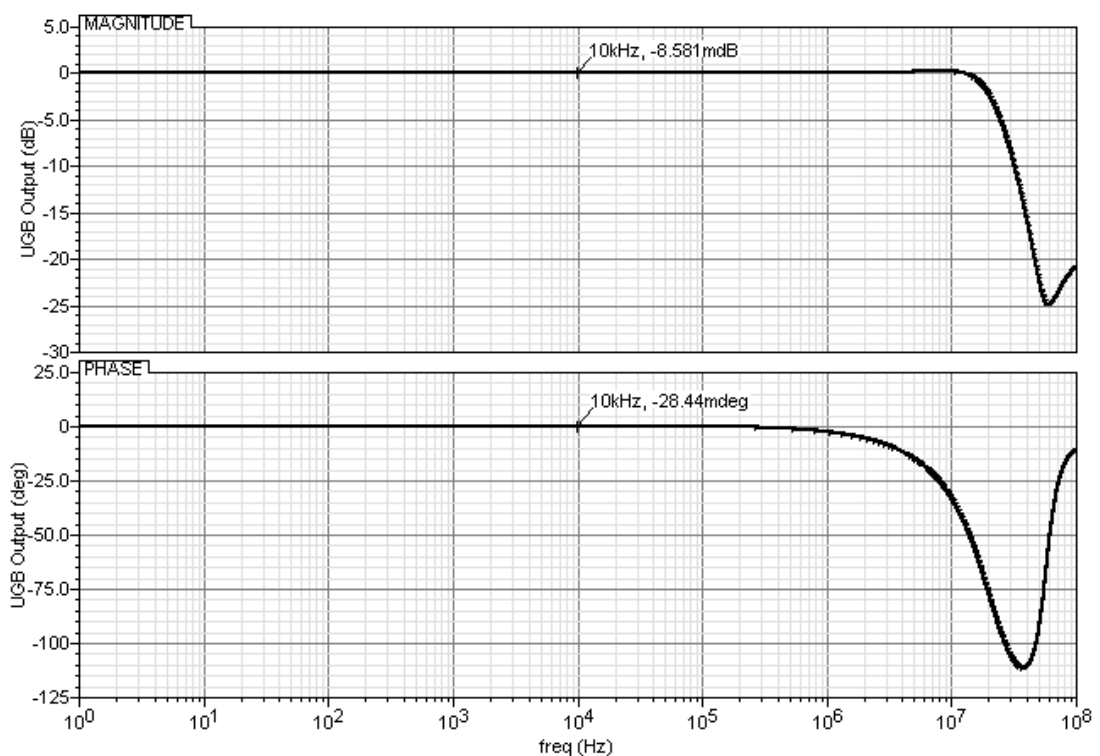


Figure 3.17: Post-layout AC simulation result of the designed UGB when the output is loaded with a 10pF capacitor.

Figure 3.18 shows the noise simulation result for the output referred voltage noise of the UGB. The spot noise at 10 kHz is $13.83 \text{ nV}/\sqrt{\text{Hz}}$, which is dominated by thermal noise contributions of load transistors, M5 and M6, and input transistors, M1 and M2. In addition to this, the flicker noise at the low frequencies is again dominated by input and load transistors.

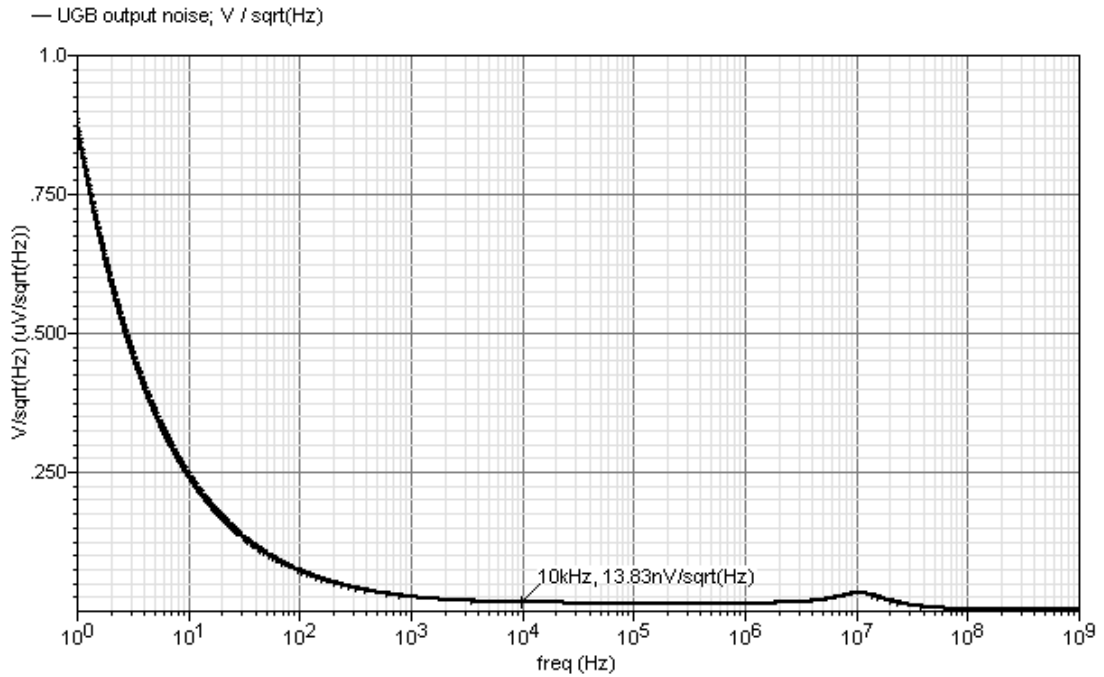


Figure 3.18: Noise simulation result for the output referred voltage noise of the UGB.

Another important parameter for the UGB circuit is the output offset. Ideally, the UGB output is DC biased to ground through unity-gain feedback connection since the positive input terminal is DC-biased by a high-impedance node biasing resistor. However, due to transistor mismatches and process variations, there would be an unpredictable offset at the output of the fabricated chip. Figure 3.19 gives the post-layout Monte Carlo simulation result for the output offset of the UGB when transistor mismatches and process variations are modeled as a Gaussian distribution function according to the process parameters provided by XFAB. In this simulation, offset is calculated many times for randomly selected mismatch and process variations. Monte Carlo simulation histogram for a hundred trials shows that output offset is within ± 3 mV range with 1.23 mV standard deviation, where the mean value is 203 μ V, and the most probable output offset voltage is 900 μ V. Although expected offset values are in tolerable ranges, it is possible to further cancel out the common-mode offset by employing a differential UGB circuit with a dedicated layout.

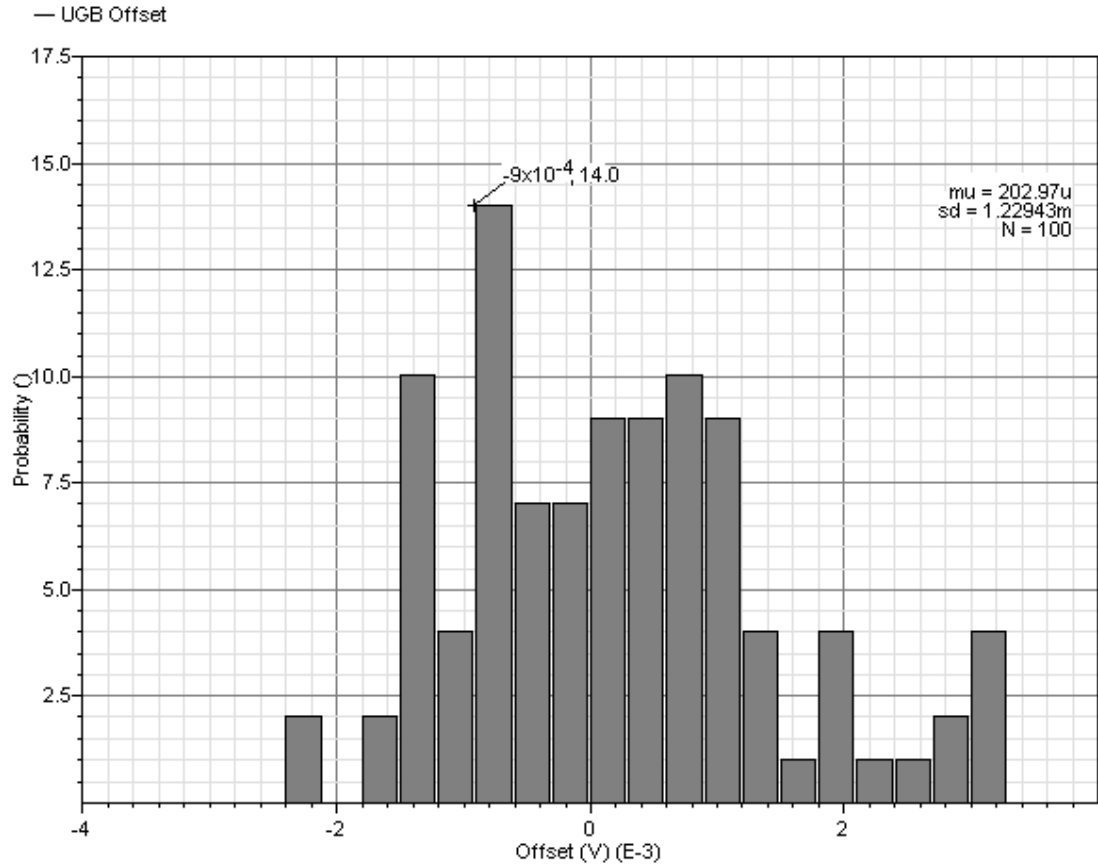


Figure 3.19: Post-layout Monte Carlo simulation result for the output offset of the UGB when transistor mismatches and process variations are modeled as a Gaussian distribution function according to the process parameters provided by XFAB.

According to post-layout simulations, the proposed UGB circuit has very small input capacitance with a very low output noise, thus, providing high SNR. Moreover, it has a voltage gain of almost unity, eliminating the parasitics coming from wirebonding pads by the bootstrapping method. Thus, it is verified that the differential version of the UGB circuit can be used in the resistive and capacitive type interfaces designed for DWP gyroscopes.

3.2.2. UGB Type Resistive Interface

UGB type resistive interfaces are mostly employed in the drive-mode electronics because the drive-mode does not require as high sensitivities as the sense-mode.

Furthermore, the phase shift introduced by the resistive interfaces is ideally 0° , which removes the necessity of additional phase shifting blocks in the self-oscillation loop. Figure 3.20 shows the UGB type resistive interface structure designed for DWP gyroscopes. In this circuit, high-impedance node of the gyroscope is DC-biased to the ground potential through an interface resistor. Then, the current generated by the gyroscope is converted to voltage on the interface resistor as long as the resistor has much smaller impedance than that of parasitic capacitances. Since the UGB circuit has very high input impedance, it is possible to employ sufficiently large interface resistors without causing unacceptable phase errors.

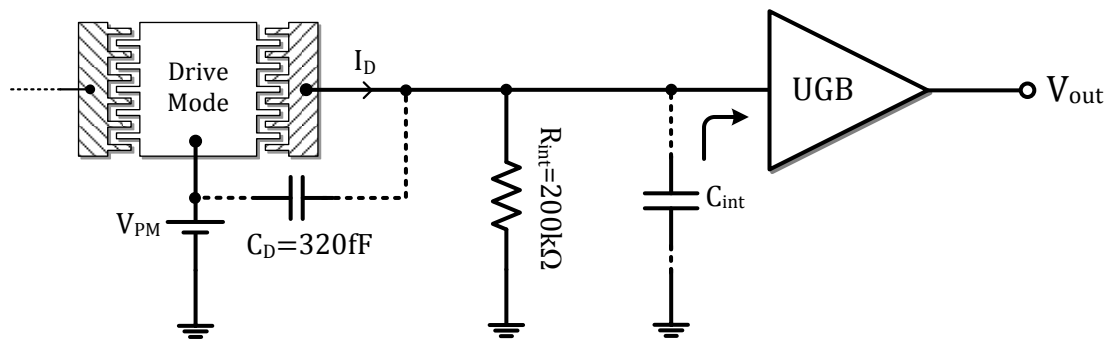


Figure 3.20: UGB type resistive interface structure designed for DWP gyroscopes.

Figure 3.21 shows the post-layout AC simulation of the UGB type resistive interface when the circuit is excited with a current source. Magnitude of the current-to-voltage gain is found as $197.3\text{ k}\Omega$ with a phase error of -438.4 mdeg for $200\text{ k}\Omega$ of interface resistor and 10 pF of load capacitance. It should be noted that this minor phase error comes from the stationary sensor capacitance, C_D , since the input capacitance of the interface, C_{int} , is negligible.

Figure 3.22 shows the simulation result for the output referred voltage noise of the UGB type resistive interface. According to the noise simulation, the circuit has $58.92\text{ nV}/\sqrt{\text{Hz}}$ of output voltage noise at 10 kHz . Comparing the resistive type interface noise characteristics with the UGB noise given in Figure 3.18, it is concluded that while the flicker noise remains the same, thermal noise increases due to the noise contribution of the interface resistor.

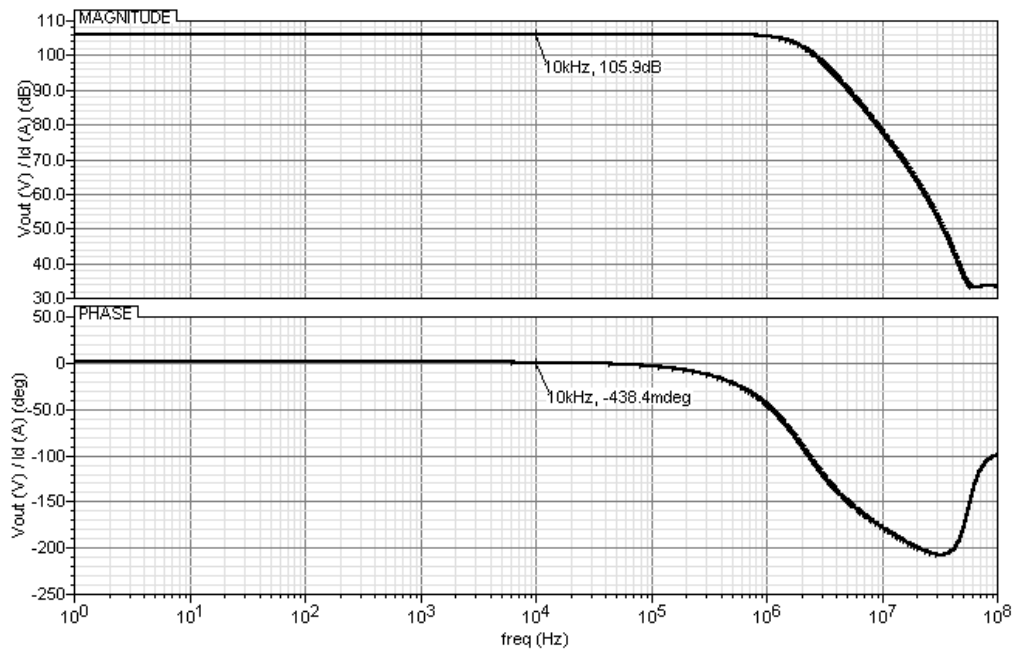


Figure 3.21: Post-layout AC simulation result of the UGB type resistive interface when the circuit is excited with a current source and loaded with a 10 pF capacitor.

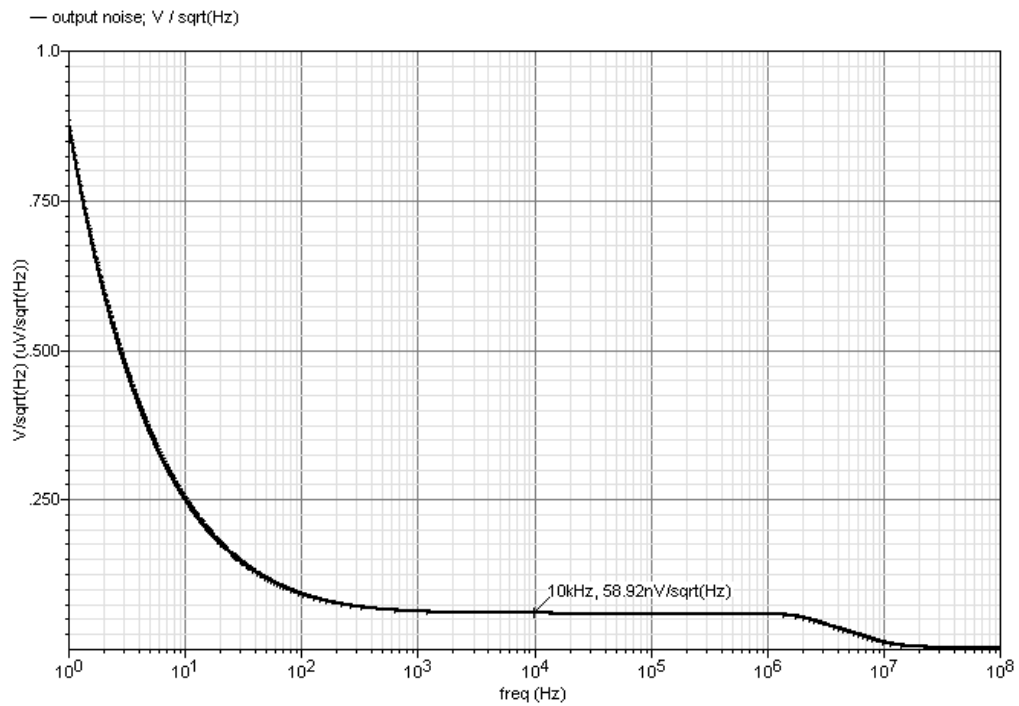


Figure 3.22: Noise simulation result for the output referred voltage noise of the UGB type resistive interface.

After verifying the circuit operation through a number of simulations, two of the UGB type resistive interface circuits given in Figure 3.20 are combined in a single chip with a dedicated layout minimizing the mismatches between interfaces. Figure 3.23(a) shows the layout of the differential UGB type resistive interface and Figure 3.23(b) shows the layout of differential UGB type resistive interface cascaded with an on-chip instrumentation amplifier giving single-ended output. Moreover, the chip shown in Figure 3.23(b) includes a single-ended to differential converter for generating differential drive-mode motor signals, which is explained in Section 3.3.1.

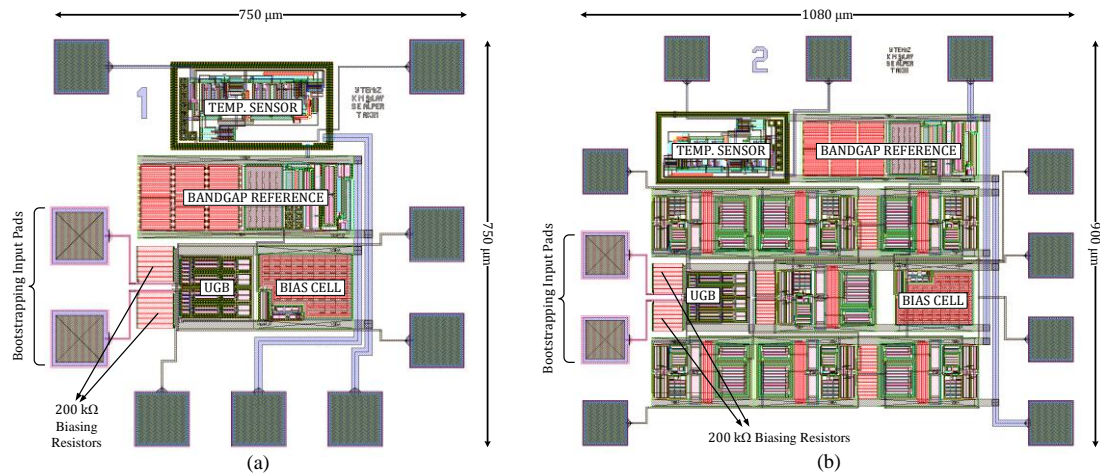


Figure 3.23: Layouts of (a) the differential UGB type resistive interface, and (b) the differential UGB type resistive interface cascaded with an on-chip instrumentation amplifier giving single-ended output.

3.2.3. UGB Type Capacitive Interface with Subthreshold Transistor Biasing

Remembering the capacitive-type interface condition explained in Section 2.4.1, the high-impedance node of the gyroscope should be DC-biased with a resistor having much larger impedance than that of interface capacitor, i.e., $R_{int} \gg (1/sC_{int})$. When this condition is satisfied, the pumped charge is converted to voltage on the interface capacitor which should be as small as possible for higher sensitivities. However, this requires high-impedance node biasing resistors in the order of

gigaohms, which is not practical to implement with physical resistors due to area constraints. On the other hand, biasing resistors much larger than few gigaohms lead to large time constants, decreasing the response time of the system. Therefore, among several approaches, a MOSFET operating in its subthreshold region is preferred for realizing controllable channel resistances in the order of few gigaohms.

Figure 3.24 shows the circuit schematic of the UGB type capacitive interface, where the high-impedance node is biased with NMOS-PMOS transistor pair operating in the subthreshold region. Compared to single transistor biasing [50], this biasing strategy is less dependent to the polarity of the AC signal appeared at the high-impedance node. Gate voltages of the biasing transistors are adjusted so that the channel resistance of each transistor is $1.6 \text{ G}\Omega$, giving effective biasing resistance of $800 \text{ M}\Omega$. Considering that the operation frequency of the DWP gyroscope is around 10 kHz , impedance of the stationary sense-mode capacitance, C_S , is $5.235 \text{ M}\Omega$. Therefore, a biasing resistance of $800 \text{ M}\Omega$ is sufficient for the capacitive-type interface condition.

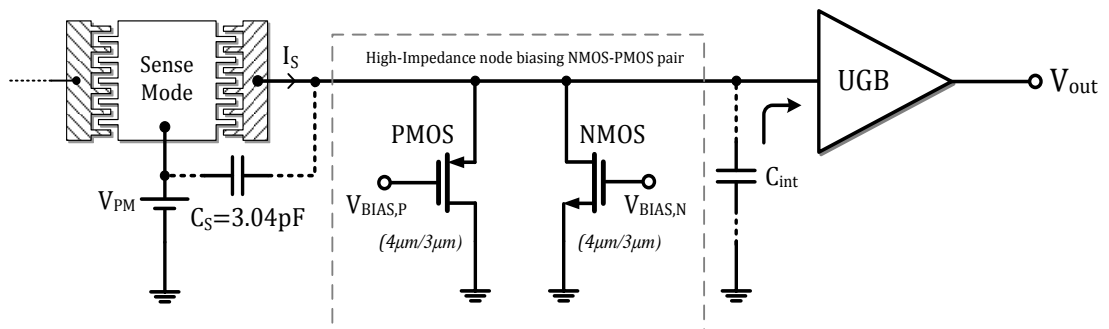


Figure 3.24: Circuit schematic of the UGB type capacitive interface, where the high-impedance node is biased with NMOS-PMOS transistor pair operating in subthreshold region.

Figure 3.25 shows the post-layout AC simulation result of the UGB type capacitive interface when the circuit is excited by a current source and the output is loaded with a 10 pF capacitor. The phase shift introduced by the circuit is found as -89.79 deg , meaning that interface is almost purely capacitive. Moreover, 134.3 dB of current-to-voltage gain at 10 kHz corresponds to $5.188 \text{ M}\Omega$ of effective impedance,

which implies that the current is converted to a voltage on the stationary sense-mode capacitance of the gyroscope.

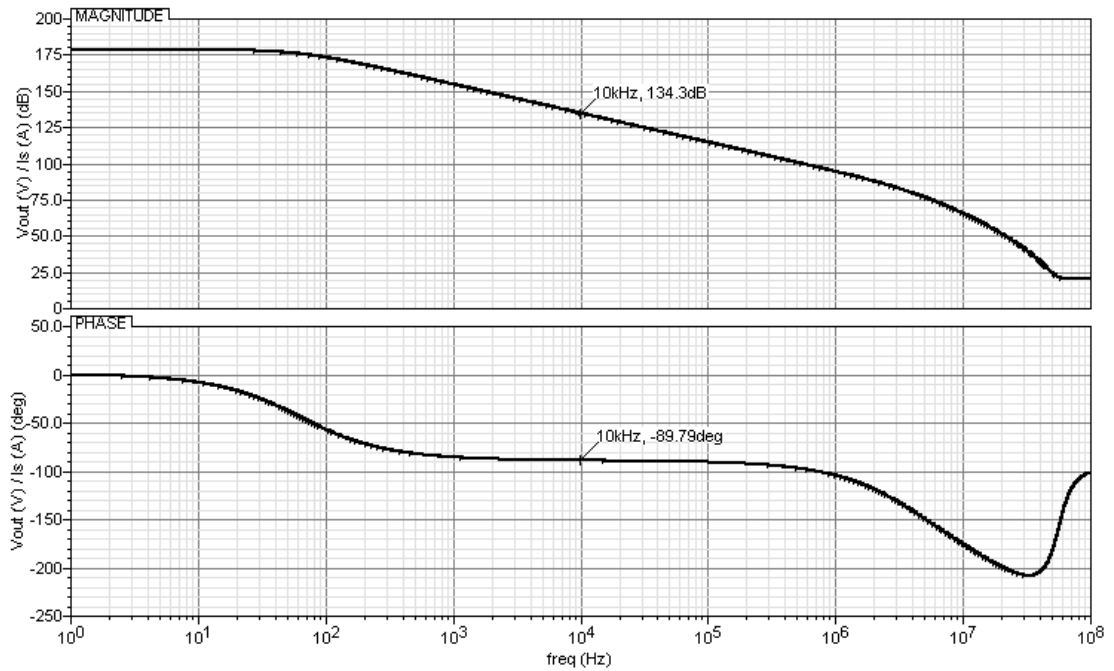


Figure 3.25: Post-layout AC simulation result of the UGB type capacitive interface when the circuit is excited by a current source and the output is loaded with a 10 pF capacitor.

It is already mentioned that large biasing resistors increase the circuit time-constant, and thus, decrease the system response. Figure 3.26 shows the transient simulation results for the differential outputs of the UGB type capacitive interface when the circuit is excited with differential current sources having 1 nA of amplitude at 10 kHz. According to the simulation, high-impedance node biasing transistor pair DC-biases the gyroscope output to ground within 10 ms, which is in tolerable ranges.

Figure 3.27 shows the noise simulation result for the output referred voltage noise of the UGB type capacitive interface biased with NMOS-PMOS biasing transistor pairs having an effective channel resistance of 800 M Ω . The circuit has an output voltage noise of 23.56 nV/ $\sqrt{\text{Hz}}$, which is smaller than that of the resistive interface due to the smaller thermal noise contribution of MOS transistors. However, the flicker noise is increased because of the flicker noise generated by the transistors.

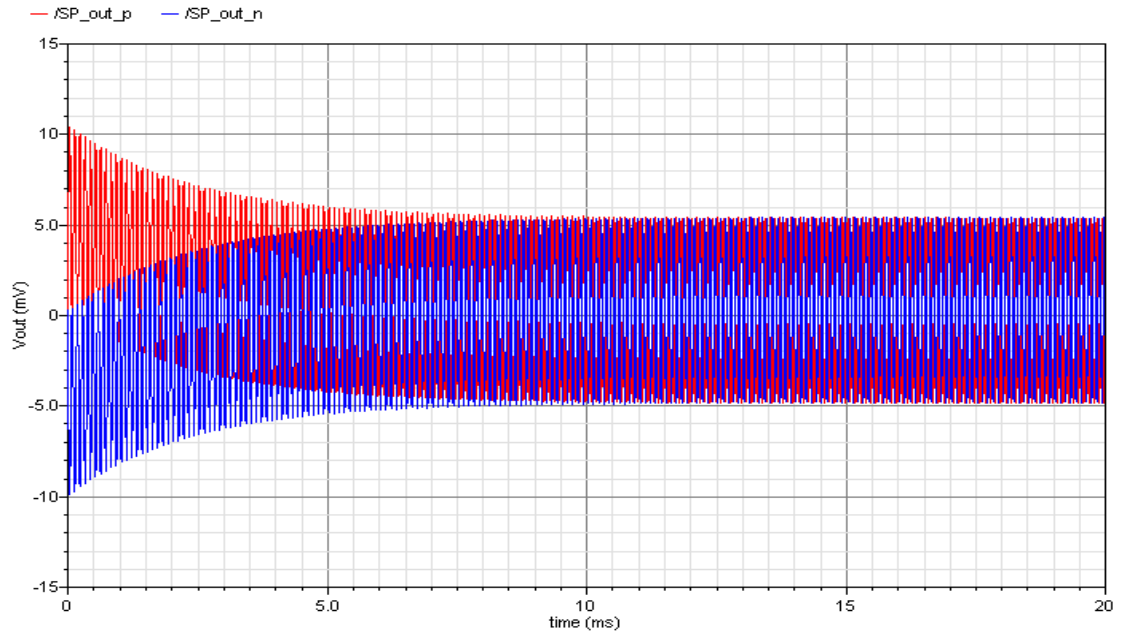


Figure 3.26: Transient simulation results for the differential outputs of the UGB type capacitive interface when the circuit is excited with differential current sources having 1 nA of amplitude at 10 kHz.

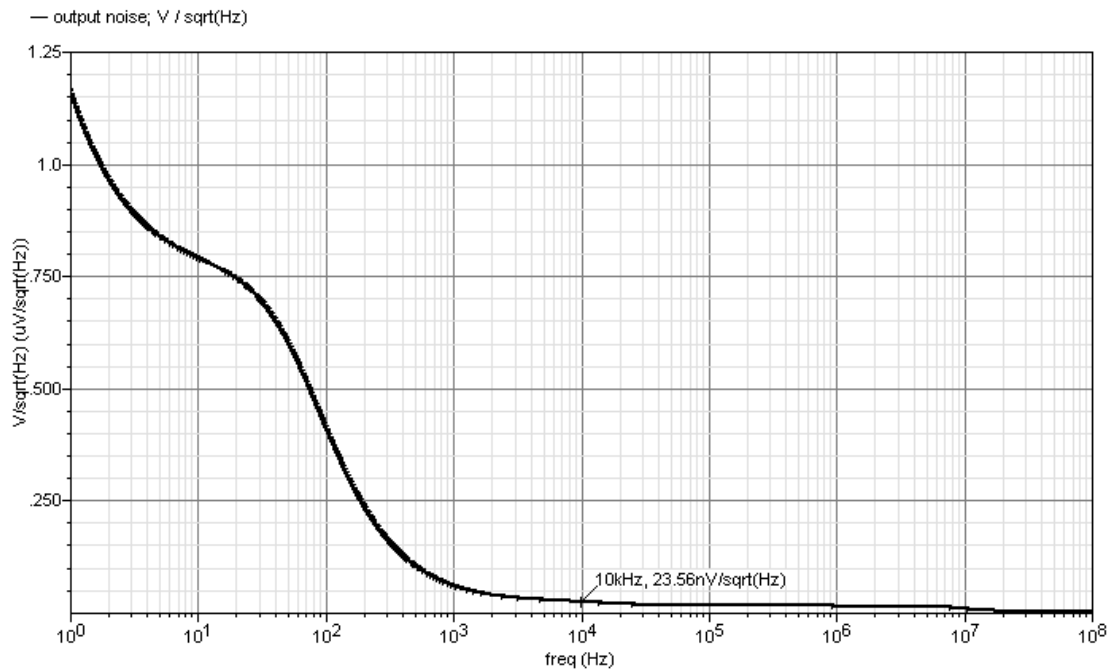


Figure 3.27: Noise simulation result for the output referred voltage noise of the UGB type capacitive interface with NMOS-PMOS biasing transistor pairs having effective channel resistance of 800 M Ω .

Figure 3.28(a) shows the layout of the designed differential UGB type capacitive interface circuit, and Figure 3.28(b) shows layout of the instrumentation amplifier cascaded version of the circuit.

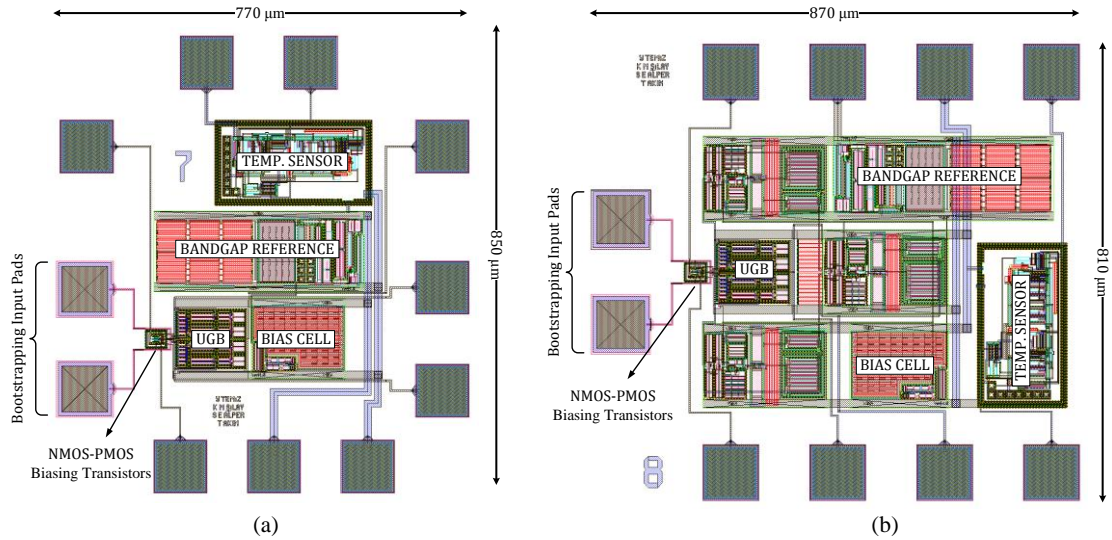


Figure 3.28: Layouts of (a) differential UGB type capacitive interface, and (b) differential UGB type capacitive interface cascaded with on-chip instrumentation amplifier giving single-ended output.

3.2.4. Transimpedance Amplifier (TIA) Type Resistive Interface

Although UGB type interfaces have very low input capacitances, output voltages are dependent to the stationary capacitance of the sensor, which limits the maximum achievable sensitivity of the gyroscope. As explained in Section 3.1.3, TIA type interfaces eliminate the effect of parasitics at the high-impedance node, providing higher sensitivities with minimum phase error. Thus, in the drive-mode of DWP gyroscopes, TIA type resistive interfaces, in other words transresistance amplifiers, are preferred for current-to-voltage conversion. Figure 3.29 shows the CMOS TIA type resistive interface circuit designed for drive-mode of the DWP gyroscope. In this circuit, 1 MΩ of interface resistor is implemented with low-doped polysilicon occupying much less area compared to other types of resistors.

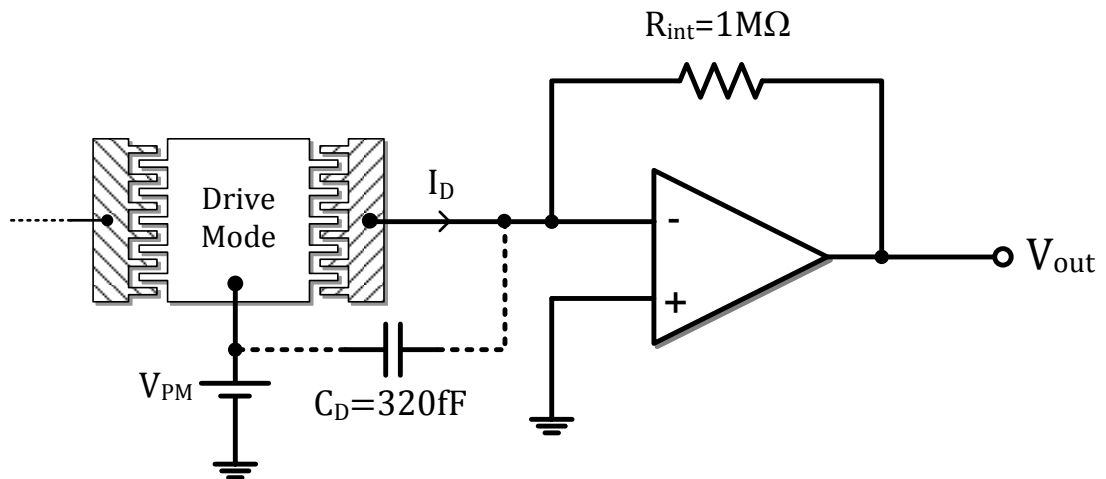


Figure 3.29: CMOS TIA type resistive interface circuit designed for drive-mode of the DWP gyroscope.

Figure 3.30 shows the post-layout AC simulation result of the TIA type resistive interface when the circuit is excited with a current source and loaded with a 10 pF capacitor. It is observed that the circuit has inverting characteristics since the current-to-voltage conversion is achieved on the feedback resistor. Moreover, the phase error is less than 100 mdeg, indicating that the interface is almost purely resistive despite the fact that 1 MΩ of interface resistor is larger than that of the UGB type resistive interface. Therefore, this simulation verifies that the TIA type interface enables higher sensitivities through larger interface resistors without increasing the phase error significantly.

Figure 3.31 shows the noise simulation result for the output referred voltage noise of the TIA type resistive interface. The circuit has output referred voltage noise of 129.2 nV/√Hz at 10 KHz, which is larger than the noise of the UGB type resistive interface because of the fact that OPAMP and 1MΩ resistor contribute much more thermal noise than the UGB circuit. On the other hand, in the drive-mode self-oscillation loop, output noise is not as important as the phase error if the noise is in tolerable ranges.

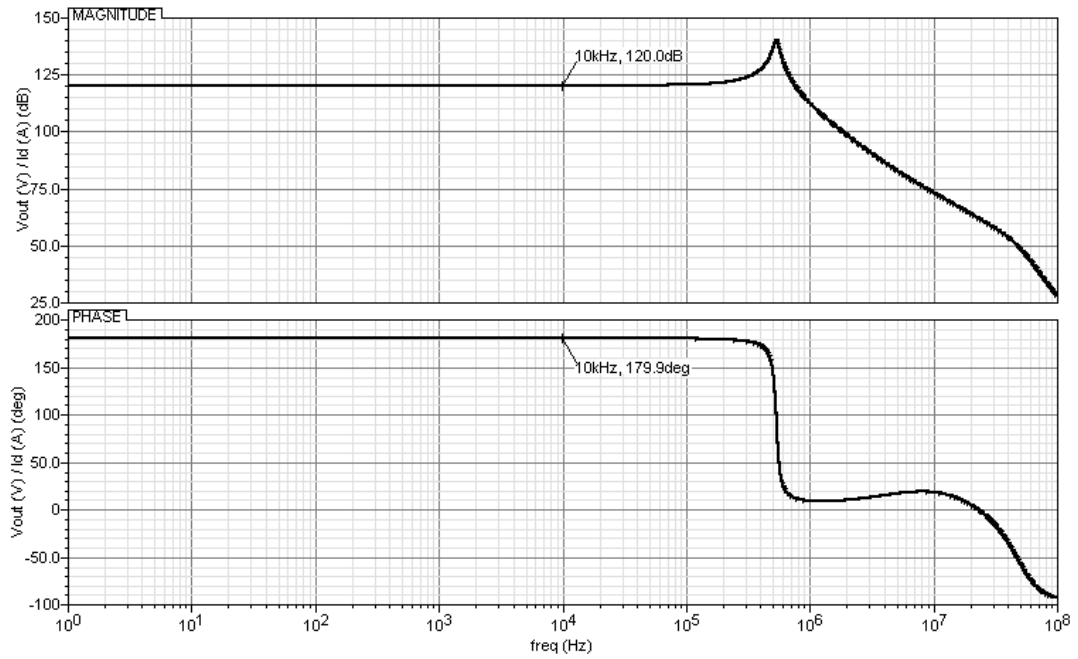


Figure 3.30: Post-layout AC simulation result of the TIA type resistive interface when the circuit is excited with a current source and loaded with a 10 pF capacitor.

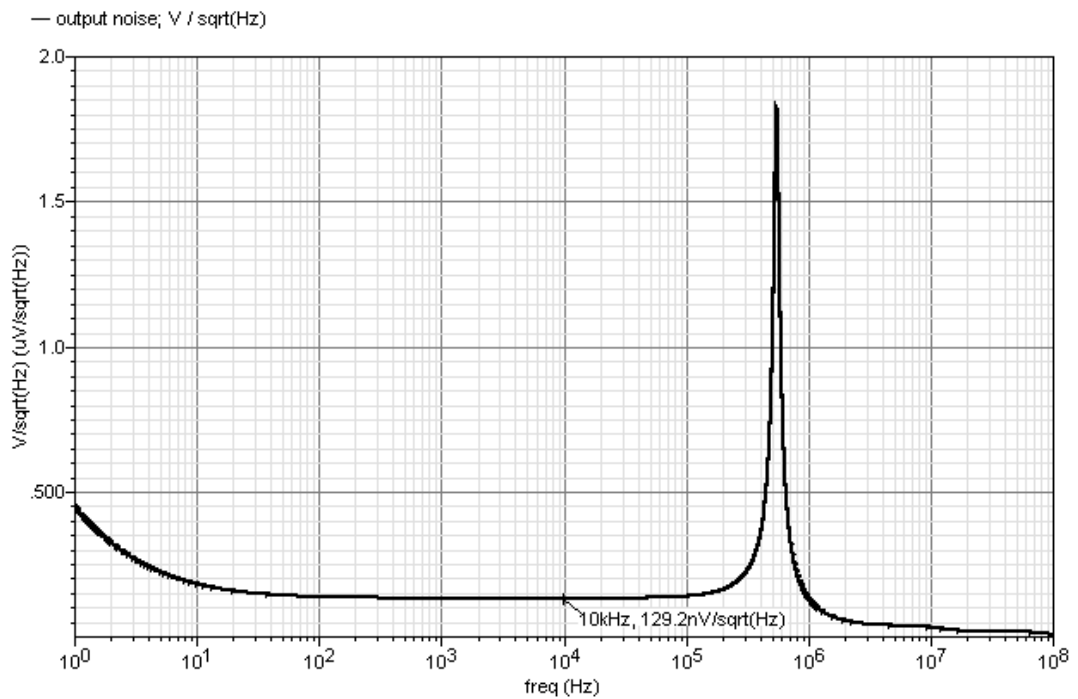


Figure 3.31: Noise simulation result for the output referred voltage noise of the TIA type resistive interface.

3.2.5. Transimpedance Amplifier (TIA) Type Capacitive Interfaces with Controlled-Impedance FET Biasing

The TIA structure can also be used as capacitive type interface if sufficiently large resistors can be implemented for biasing the output node of the OPAMP. Remembering the UGB type capacitive interfaces explained in Section 3.2.3, high-impedance node of the gyroscope is biased by NMOS-PMOS transistor pair operating in sub-threshold region. However, the channel resistance of a transistor having weak inversion layer highly depends on the applied gate voltage and the transistor parameters. As the transistor goes into deep subthreshold region, even few millivolts of gate voltage variations may lead to resistance changes in the order of megaohms. Therefore, in TIA type interfaces, large resistors are realized by controlled-impedance MOSFETs [16] operating in edge of linear region. Figure 3.32 shows the circuit schematic of the proposed controlled-impedance FET circuit used for biasing the OPAMP output. In this circuit, the resistance across a-b nodes is controlled by changing the channel resistance of M1 through DC current generated by M3. It should be noted that the channel resistance is independent of the AC voltage across the transistor since the gate-to-source voltage is kept constant by the current source.

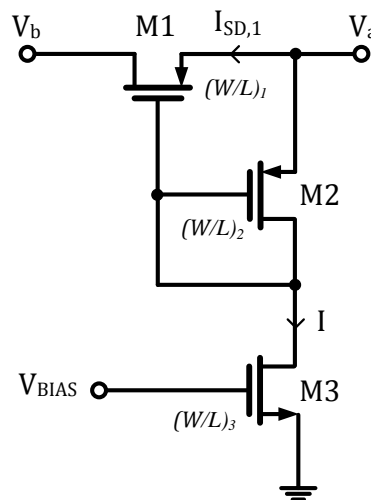


Figure 3.32: Circuit schematic of the proposed controlled-impedance FET circuit used for biasing the OPAMP output.

Assuming that M1 is a long transistor operating in linear region and its source-to-drain voltage is sufficiently small, i.e., $V_{SD,1} \ll (V_{SG,1} + V_{TP})$, then the channel transconductance is approximated as

$$G_{ab} = G_{SD,1} \approx K_P \cdot (W/L)_1 \cdot (V_{SG,1} + V_{TP}) \quad (3.3)$$

Due to the parallel connection of M1 and M2, both transistors have the same gate-to-source voltage, i.e. $V_{SG,1} = V_{SG,2}$, where M2 transistor is forced to operate in saturation region by the diode-connection. Considering the saturated M3 transistor generating constant DC current, gate-to-source voltage of M1 transistor is defined as

$$V_{SG,1} = V_{SG,2} = \sqrt{\frac{K_N \cdot (W/L)_3}{K_P \cdot (W/L)_2}} \cdot (V_{BIAS} - V_{TN} - V_{TP}) \quad (3.4)$$

Inserting Equation (3.4) into Equation (3.3) yields the transconductance expression given as

$$G_{DS,1} = \frac{1}{R_{DS,1}} = K_P \cdot (W/L)_1 \cdot \left[\sqrt{\frac{K_N \cdot (W/L)_3}{K_P \cdot (W/L)_2}} \cdot (V_{BIAS} - V_{TN} - V_{TP}) + V_{TP} \right] \quad (3.5)$$

This equation shows that it is possible to obtain a floating resistor having sufficiently large resistance by implementing M1 and M2 as very long and very wide transistors, respectively.

Figure 3.33 shows the circuit schematic of the TIA type capacitive interface employing controlled-impedance FET biasing. According to the DC operating point simulations, the M1 transistor has channel resistance of 1.2 G Ω , when M3 transistor is biased with -1.565 V supplied by an on-chip bandgap referenced bias cell. The generated channel resistance is verified to be sufficient for the capacitive interface

condition as the impedance of 2 pF interface capacitance at the operation frequency of the gyroscope is around 8 M Ω .

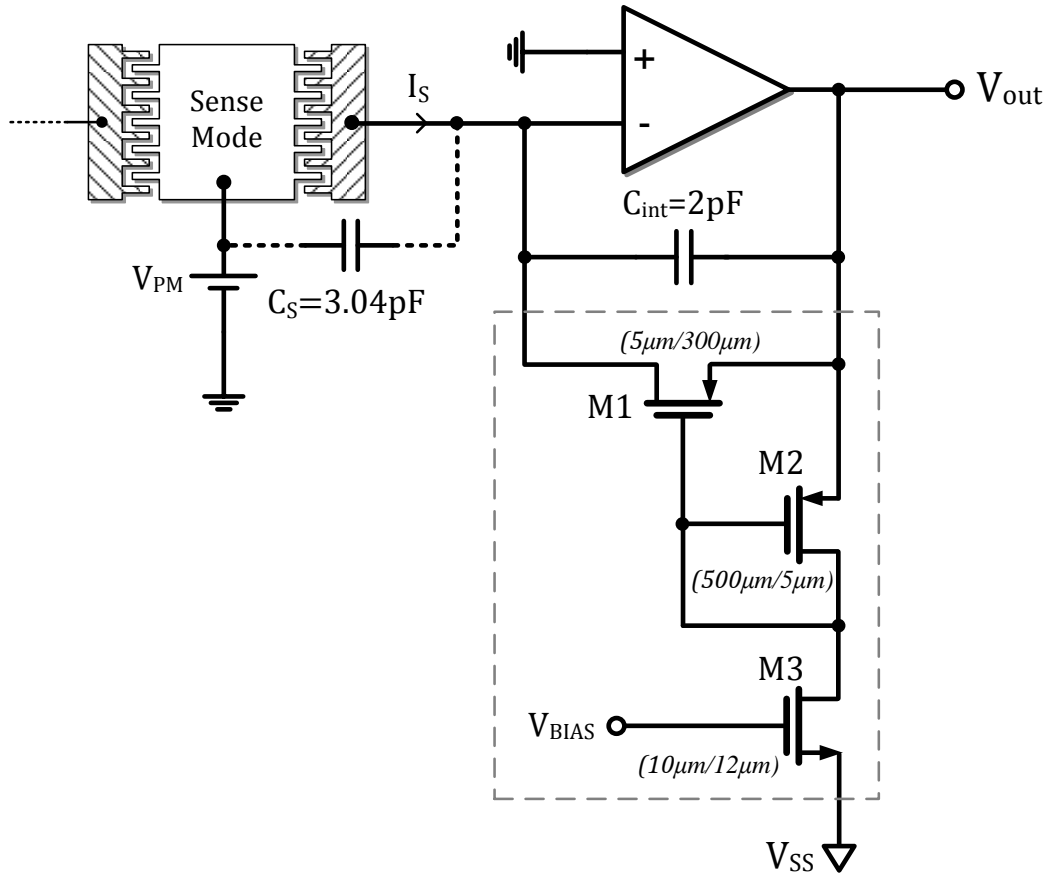


Figure 3.33: Circuit schematic of the TIA type capacitive interface employing controlled-impedance FET biasing.

Figure 3.34 shows the post-layout AC simulation result of the TIA type capacitive interface when the circuit is excited by a current source and output is loaded with a 10 pF capacitor. The current-to-voltage gain at 10 kHz is 7.852×10^6 (137.9 dB), which is exactly equal to the impedance of 2 pF interface capacitor at 10 kHz.

Figure 3.35 shows the transient response of the differential capacitive TIA circuit when the circuits are excited with differential current sources having 1 nA of amplitude at 10 kHz. It is observed that controlled-impedance FET circuit DC-biases the output of the OPAMP to ground potential within 15 ms.

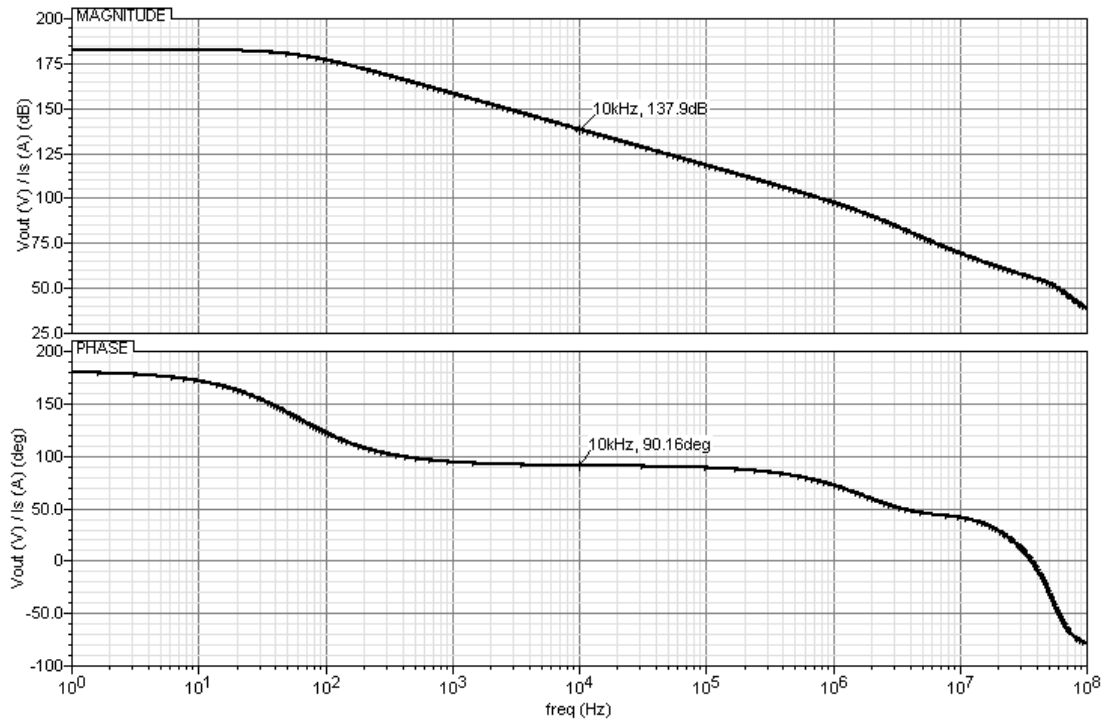


Figure 3.34: Post-layout AC simulation result of the TIA type capacitive interface when the circuit is excited by a current source and output is loaded with a 10 pF capacitor.

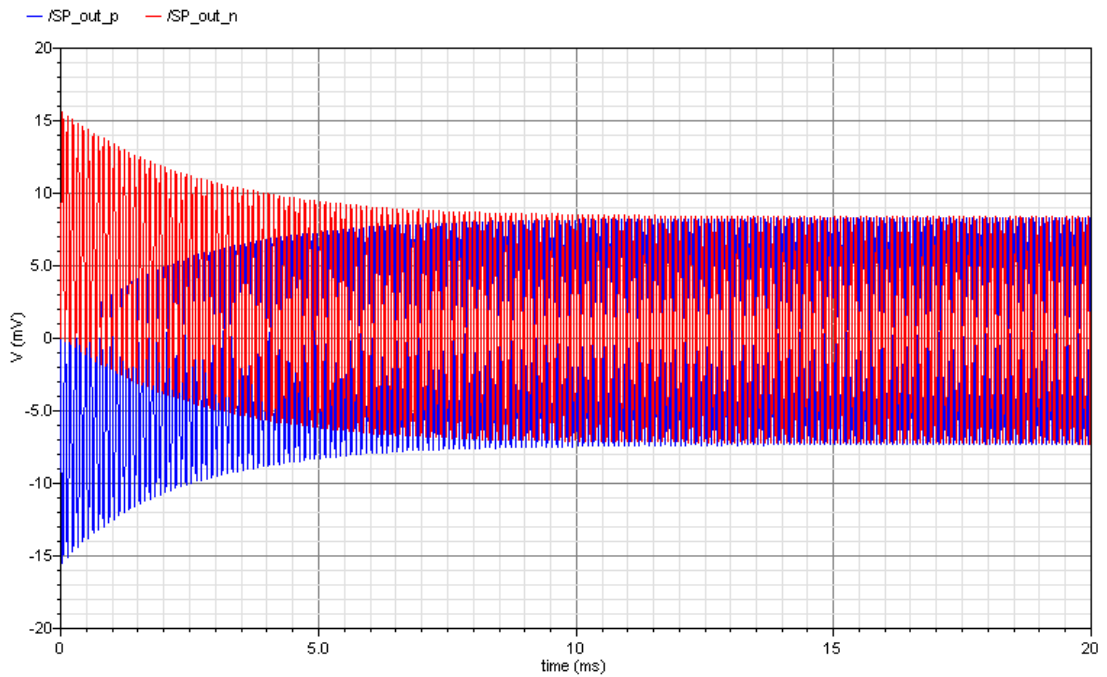


Figure 3.35: Transient response of the differential capacitive TIA circuit when the circuits are excited with differential current sources having 1 nA of amplitude at 10 kHz.

Since the proposed capacitive interface is designed to be used in the sense-mode, noise contribution of the interface circuit is quite important in determining the resolution of the gyroscope. Figure 3.36 shows the noise simulation result for the output referred voltage noise of the TIA type capacitive interface. The circuit has output voltage noise of $32.38 \text{ nV}/\sqrt{\text{Hz}}$ at 10 kHz . This value is smaller than the noise of TIA type resistive interface having $1 \text{ M}\Omega$ of interface resistor. However, the capacitive interface has larger flicker noise due to the flicker noise contributed by MOS transistors.

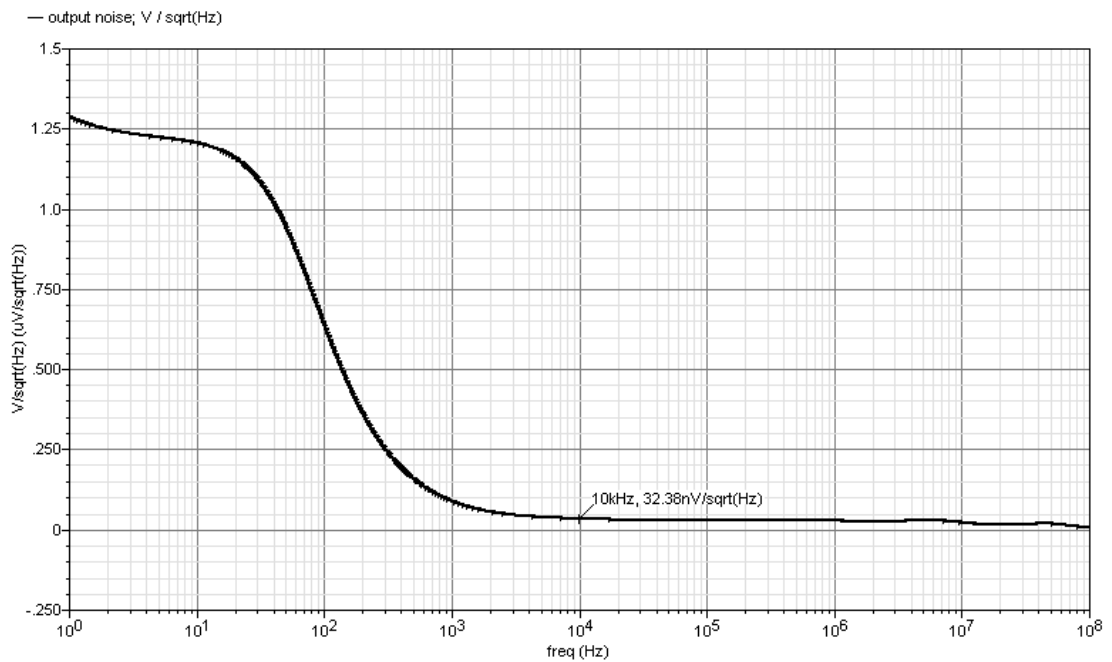


Figure 3.36: Noise simulation result for the output referred voltage noise of the TIA type capacitive interface.

In this study, differential capacitive and resistive TIA interfaces are combined in a single chip having pad distribution arranged according to the DWP gyroscope. Figure 3.37(a) shows the layout of the differential interfaces, and Figure 3.37(b) gives the layout of the interface circuits providing single-ended output by employing on-chip instrumentation amplifiers. In addition, the chip shown in Figure 3.37(b) involves a single-ended to differential converter for generating exactly anti-phase drive motor signals, which is explained in Section 3.3.1.

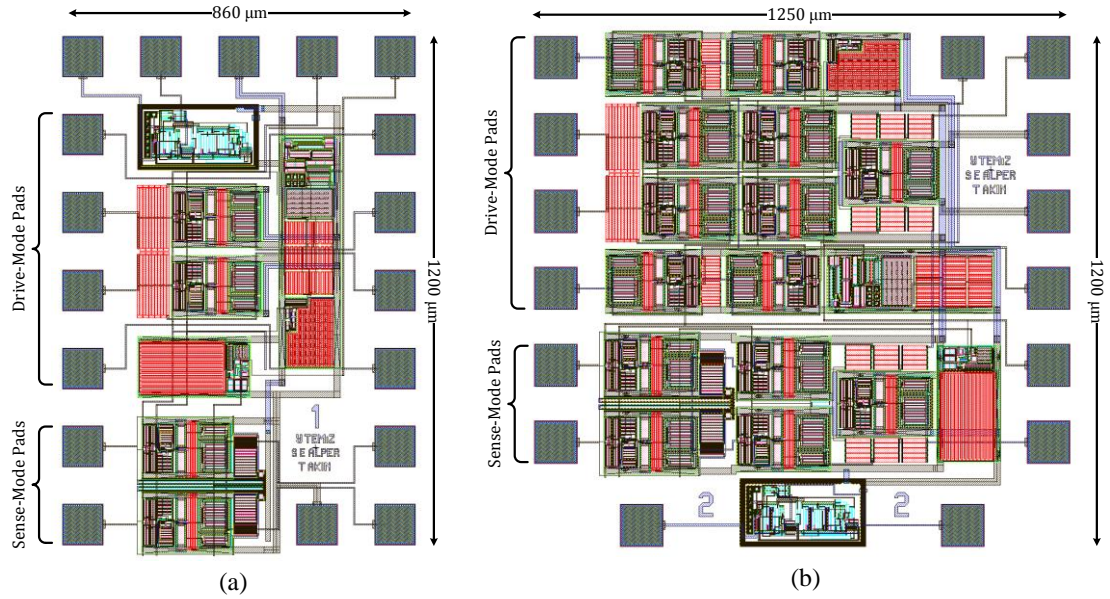


Figure 3.37: Layouts of (a) differential TIA type capacitive and resistive interfaces combined in a single chip, and (b) interface circuits providing single-ended output by employing on-chip instrumentation amplifiers.

CMOS chips given in Figure 3.37 are designed to be used with external drive-mode and sense-mode electronics implemented with commercial discrete components. On the other hand, it is possible to combine whole electronics in a single chip, boosting the overall gyroscope performance and reducing the total sensor area. Following sections explain CMOS control and rate sensing electronics having TIA type capacitive and resistive interfaces, designed for DWP gyroscopes.

3.3. CMOS Drive-Mode Control Electronics

It is required to generate anti-phase driving signals for obtaining balanced vibrations in the drive-mode of dual-mass DWP gyroscopes. Hardly can discrete electronics produce exactly anti-phase signals due to unpredictable parasitics, mismatches and asymmetries coming from PCBs and components. Therefore, CMOS single-ended to differential convertors and fully-differential automatic amplitude control loops are developed to minimize the phase errors between drive motor signals.

3.3.1. Single-Ended to Differential Convertor

The CMOS single-ended to differential convertor circuit aims to convert applied sinusoidal signal to two anti-phase signals having phase difference of exactly 180°. This is achieved by using a simple approach involving subtraction property of the instrumentation amplifier. Figure 3.38(a) shows the CMOS instrumentation amplifier circuit schematic designed for differential to single-ended conversion of signals generated by CMOS interfaces used in the drive and sense modes. Figure 3.38(b) shows the proposed single-ended to differential convertor circuit composed of two unity-gain instrumentation amplifiers, where the input terminals are cross-connected and one of these connections is grounded.

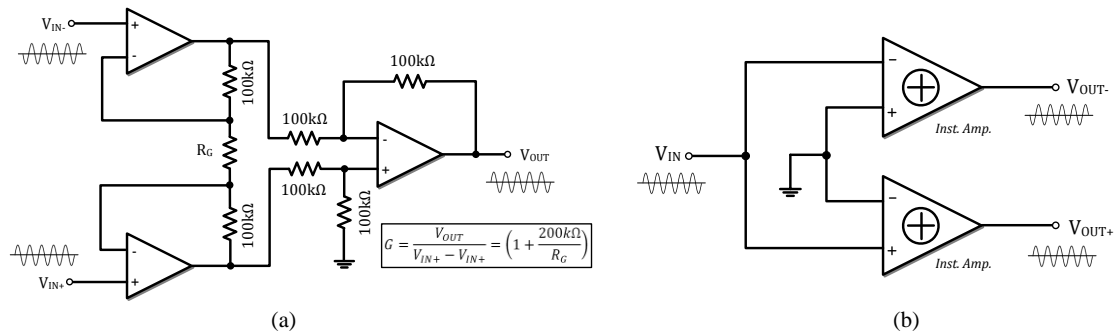


Figure 3.38: Circuit schematic of the (a) CMOS instrumentation amplifier, and (b) single-ended to differential convertor composed of two unity-gain instrumentation amplifiers.

Since the applied signal sees approximately same parasitics through two branches, generated sinusoids are expected to have exactly 180° phase difference as long as the circuit layout is symmetric and process mismatches are ignored. Post-layout AC simulations show that the phase difference between the applied signal and the non-inverting output is 196.7 mdeg. Moreover, the phase error between inverting and non-inverting output signals is simulated to be less than 5 mdeg, verifying that generated signals are almost perfectly anti-phase. Thus, this circuit can be used in the single-ended self-oscillation loops for driving the gyroscope with exactly anti-phase motor signals.

3.3.2. Fully-Differential Self-Resonance Excitation Circuit with Automatic Amplitude Control

Differential automatic amplitude control circuit composed of discrete components is already discussed in Section 3.1.5. On the other hand, unlike discrete electronics, application specific integrated circuit (ASIC) technology enables the realization of fully-differential components, minimizing the possible mismatches between the differential signals. Figure 3.39 shows the circuit schematic of the CMOS fully-differential self-resonance excitation circuit with automatic amplitude control designed for DWP gyroscopes.

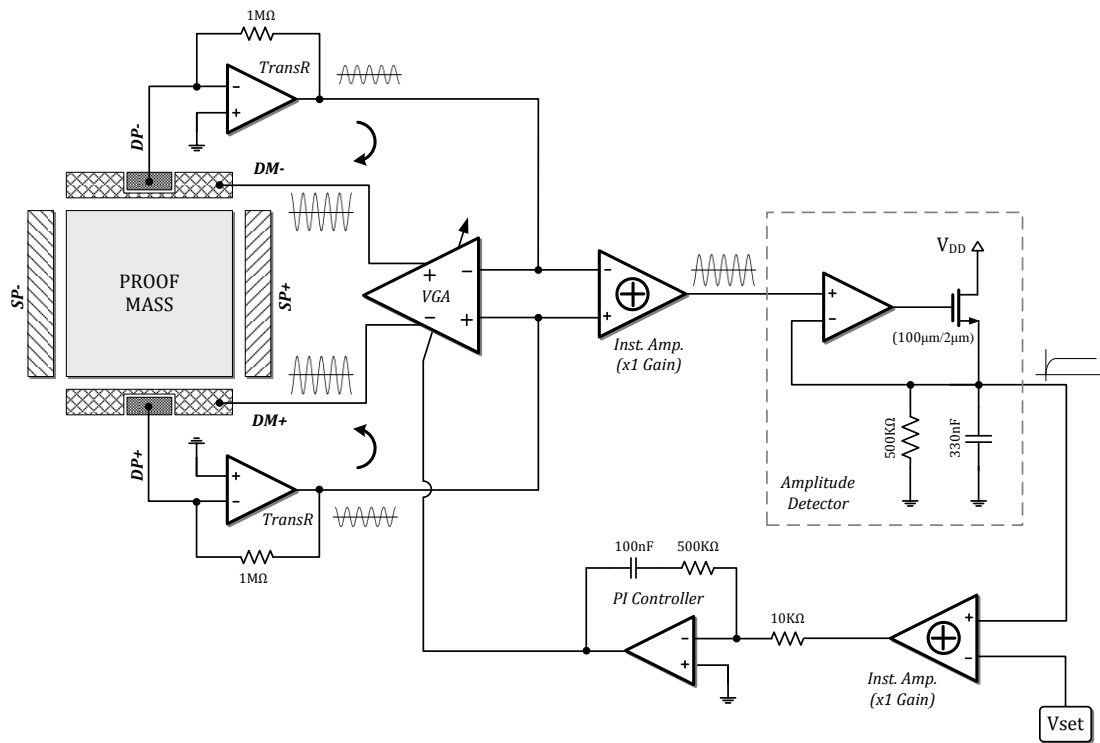


Figure 3.39: Circuit schematic of the CMOS fully-differential self-resonance excitation circuit with automatic amplitude control designed for DWP gyroscopes.

In this circuit, drive-mode vibrations are sensed by TIA type resistive interfaces, which are explained in Section 3.2.4. A fully-differential CMOS variable gain amplifier (VGA), whose gain is controlled so that the vibration amplitude is constant,

generates exactly anti-phase sinusoidal drive-mode motor signals. Vibration amplitude information is extracted by an amplitude detector circuit composed of an OPAMP comparator, an NMOS transistor, and a capacitor-resistor pair. If the comparator detects an increase in the oscillation amplitude, the transistor charges up the capacitor, giving DC signal proportional to the vibration amplitude. In the opposite case, resistor parallel to the capacitor discharges the capacitor, tracking the decrease in the amplitude since the transistor is in cut-off region at this condition. Thus, in the steady-state, the proposed amplitude detector circuit provides baseband signals following the slow variations in the oscillation amplitude since the time-constant of the circuit is set so that the circuit does not give response to signals at the oscillation frequency. The amplitude voltage is then compared to the set voltage. The resultant error signal is amplified by the PI controller generating the necessary gain control voltage for sustaining oscillation at the desired level.

The most important component of the proposed loop is fully-differential VGA [57]. Figure 3.40(a) shows the basic circuit diagram of the VGA composed of two common-source amplifiers with variable source degeneration resistor connected in common. Assuming that each branch has components having identical parameters, it can be stated that the control resistor draws no DC current since the potential across the resistor is zero. Thus, transconductances of input transistors can be expressed as

$$g_{m_{1,2}} = \sqrt{2\mu_n C_{ox} \left(\frac{W}{L}\right)_{1,2} \cdot I_{bias}} \quad (3.6)$$

From the small-signal model of the circuit, the voltage gain expression is given as

$$A_v = \frac{\Delta V_{out}}{\Delta V_{in}} = -\frac{g_{m_{1,2}} R_D}{1 + g_{m_{1,2}} \frac{R_{cont}}{2}} = -\frac{2g_{m_{1,2}} R_D}{2 + g_{m_{1,2}} R_{cont}} \quad (3.7)$$

which shows that the voltage gain of a common-source amplifier can be controlled by changing the value of the source degeneration resistor.

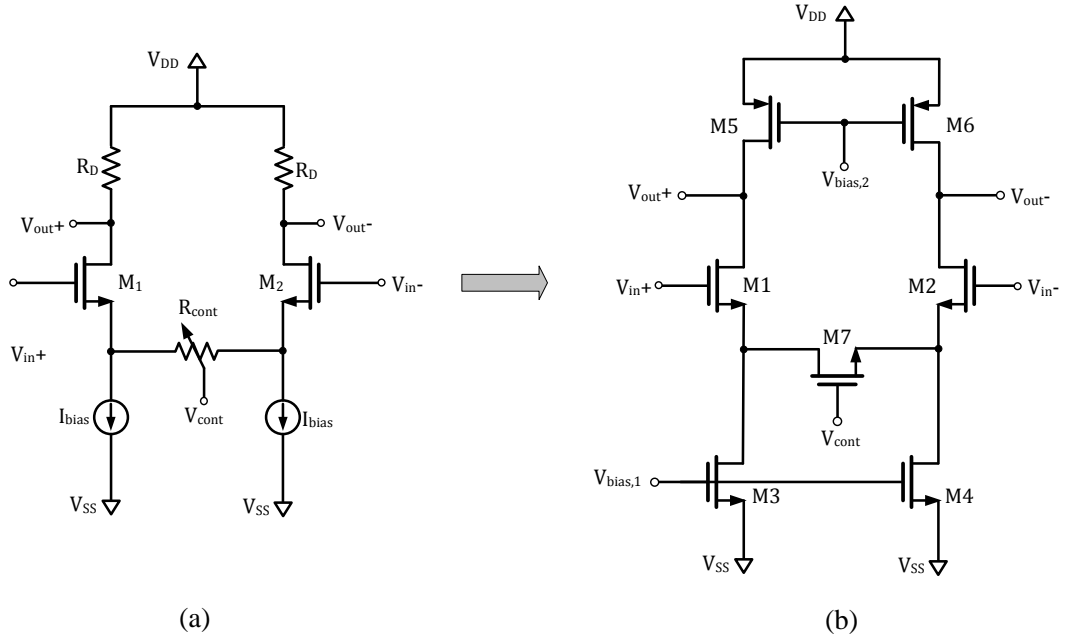


Figure 3.40: (a) Basic circuit diagram of the VGA composed of two common-source amplifiers with variable source degeneration resistor connected in common. (b) Circuit schematic of the VGA when current sources and load resistors are replaced with transistors and variable resistor is realized with an NMOS transistor operating in linear region.

Figure 3.40(b) shows the circuit schematic of the VGA when current sources and load resistors are replaced with saturated transistors and the variable resistor is realized with an NMOS transistor operating in its linear region. Modifying Equation (3.7) for this circuit yields

$$A_v = -\frac{2g_{m_{1,2}}(r_{o_{5,6}}//R_L)}{2 + g_{m_{1,2}}\left(\frac{1}{G_7}\right)} \quad (3.8)$$

where r_o is the output resistance of the load transistors, R_L is the resistance of the external load and G_7 is the transconductance of M_7 , which is expressed as

$$G_7 = \mu_n C_{ox} \left(\frac{W}{L}\right)_7 (V_{GS7} - V_{TN}) \quad (3.9)$$

For $g_{m_{1,2}} \gg 2G_7$, Equation (3.8) can be approximated as

$$A_v = -2G_7(r_{o_{5,6}}//R_L) = 2\mu_n C_{ox} \left(\frac{W}{L}\right)_7 (V_{GS7} - V_{TN})(r_{o_{5,6}}//R_L) \quad (3.10)$$

showing that the gain of the circuit can be controlled by the gate-to-source voltage of M7, which is directly related to the control voltage applied to the gate of M7.

Another important issue in fully-differential VGA design is the common-mode DC level of the output nodes, which is determined by source-to-drain voltages of saturated PMOS load transistors, M5 and M6. By considering the channel-length modulation effect, a voltage-current expression for the saturated load transistors is provided as

$$I_{bias} = \frac{1}{2} \mu_p C_{ox} \left(\frac{W}{L}\right)_{5,6} (V_{DD} - V_{bias2} - V_{TP})^2 (1 + \lambda V_{SD_{5,6}}) \quad (3.11)$$

which implies that source-to-drain voltage, thus output DC level, is determined by process parameters if the biasing current, I_{bias} , and biasing voltage, V_{bias2} , are constant. Dependency of output common-mode level to process parameters leads to unpredictable offsets at the output node. Therefore, a common-mode feedback (CMFB) circuit is employed to adaptively set the DC level to the desired value.

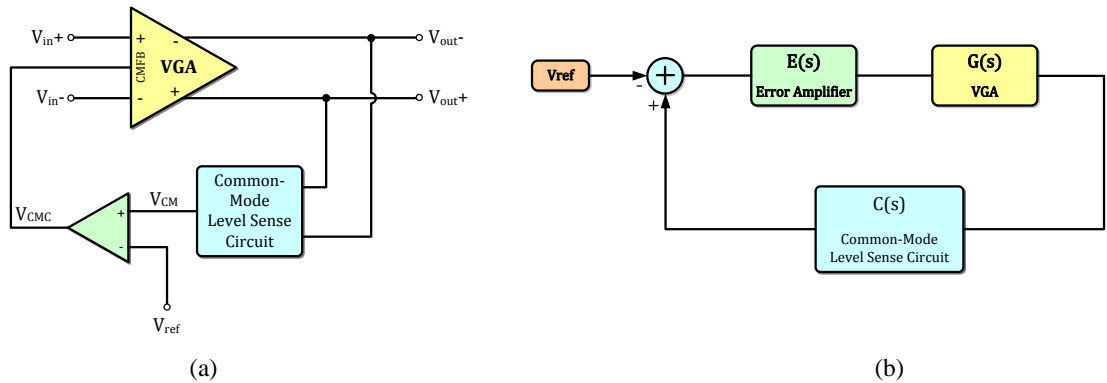


Figure 3.41: (a) Simplified diagram of the CMFB mechanism used in the proposed VGA. (b) Negative feedback model of the VGA with CMFB for stability analysis.

Figure 3.41(a) shows the simplified diagram of the CMFB mechanism used in the proposed fully-differential VGA. In this diagram, the common-mode level sense circuit finds the common DC level by taking the average of differential outputs. Then, the common-mode voltage is compared to the reference value, and the control voltage is generated by the error amplifier, which is actually an OPAMP operated in the open-loop configuration. From Equation (3.11), since the control voltage is connected to the gate terminals of load transistors, the output DC level is directly determined by the negative feedback. However, it is possible to obtain an unstable output if the closed-loop system poles are on the right-half plane. Then, Figure 3.41(b) shows the negative feedback model of the VGA with CMFB for stability analysis. The characteristic equation derived from this model is given as

$$1 + E(s)G(s)C(s) = 0 \quad (3.12)$$

where $E(s)$ is the open-loop gain of the OPAMP, which is used as an error amplifier, $G(s)$ is the control voltage to common-mode level transfer function, and $C(s)$ is the transfer function of the common-mode level sensing circuit. As a rule of thumb, phase margin derived from the characteristic equation should be larger than 45° for a sufficiently safe operation.

Figure 3.42 shows the circuit schematic of the fully-differential VGA with CMFB, and Table 3.3 gives the transistor dimensions of the circuit designed for a standard $0.6\mu\text{m}$ CMOS process. In this circuit, the resistor division network connected between the differential outputs provide the common-mode level as

$$V_{CM} = V_{out+} - \frac{V_{out+} - V_{out-}}{2R} R = \frac{V_{out+} + V_{out-}}{2} \quad (3.13)$$

It should be noted that capacitors parallel to the common-mode level sensing resistors are placed for increasing the phase margin of the CMFB due to stability concerns.

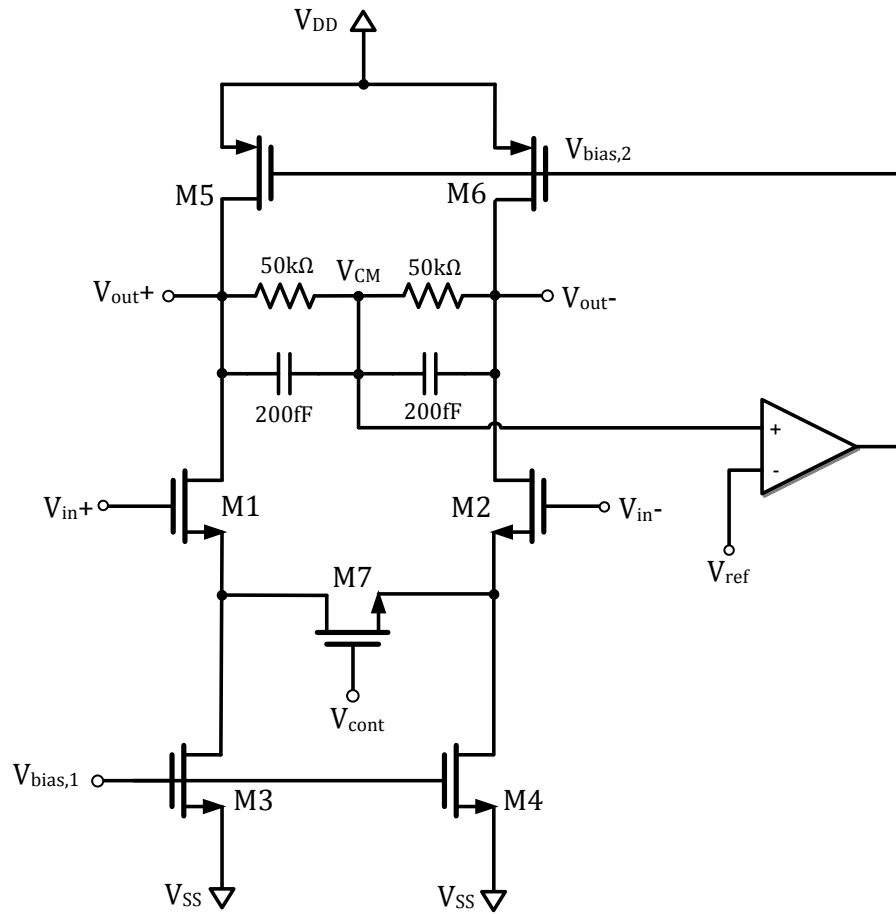


Figure 3.42: Circuit schematic of the fully-differential VGA with CMFB.

Table 3.3: Transistor dimensions for the VGA circuit designed for a $0.6\mu\text{m}$ standard 5V CMOS process.

	M1	M2	M3	M4	M5	M6	M7
Width (W)	$100\mu\text{m}$	$100\mu\text{m}$	$50\mu\text{m}$	$50\mu\text{m}$	$30\mu\text{m}$	$30\mu\text{m}$	$5\mu\text{m}$
Length (L)	$4\mu\text{m}$	$4\mu\text{m}$	$2\mu\text{m}$	$2\mu\text{m}$	$4\mu\text{m}$	$4\mu\text{m}$	$5\mu\text{m}$

On the other hand, it is concluded that the single-stage VGA given in Figure 3.42 cannot provide sufficient gain for the self-oscillation condition because the common-mode level sensing resistors limit the maximum load resistance, thus maximum gain. Moreover, as the single-stage gain increases, the gain versus the

control voltage relation becomes highly non-linear. Therefore, it is proposed to connect two moderate gain VGA circuits in series for increasing the overall VGA gain, being linearly dependent to the control voltage. Figure 3.43 shows two cascade-connected VGA circuits operating as one single VGA since common-mode control, V_{CMC} , and gain control, V_{Cont} , voltages of each VGA are shorted.

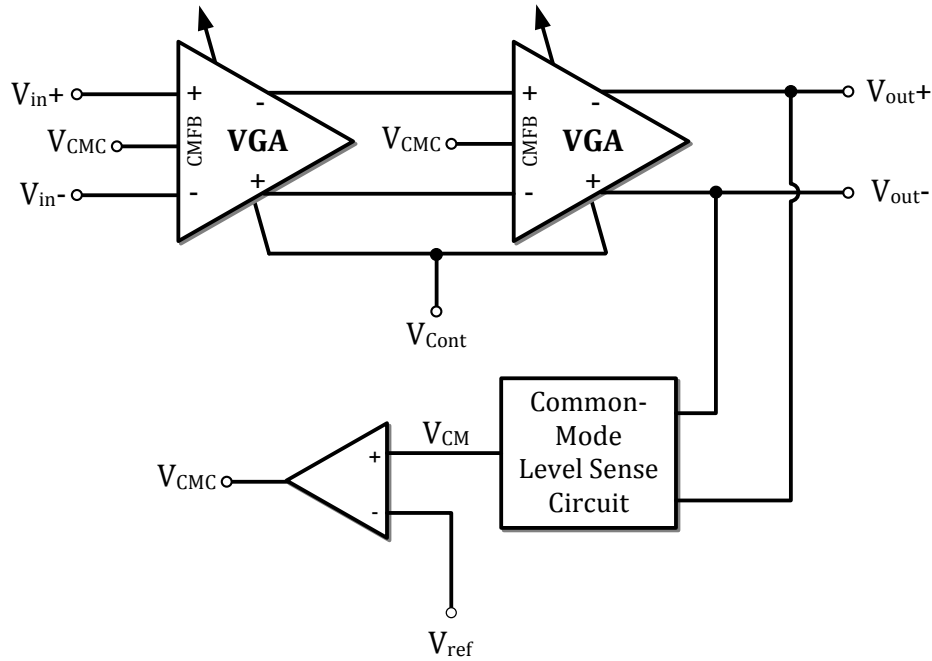


Figure 3.43: Two cascade-connected VGA circuits operating as one single VGA since common-mode control, V_{CMC} , and gain control, V_{Cont} , voltages of each VGA are shorted.

Figure 3.44 gives the gain versus control voltage simulation result for the proposed VGA circuit, when the control voltage is swept from -2.5V to 2.5V. For negative values of the control voltage, the gain control transistor M7 is in cut-off region, hence the circuit provides almost zero gain. When the control voltage is increased so that the M7 starts to conduct in linear region, gain increases because of the decrease in channel resistance. In the linear portion of the gain versus control voltage characteristics, the slope is approximately 57, and the maximum achievable gain is 124. As the control voltage gets closer to supply limits, gain starts to saturate; however, this does not cause any major problem in the automatic amplitude control loop operation.

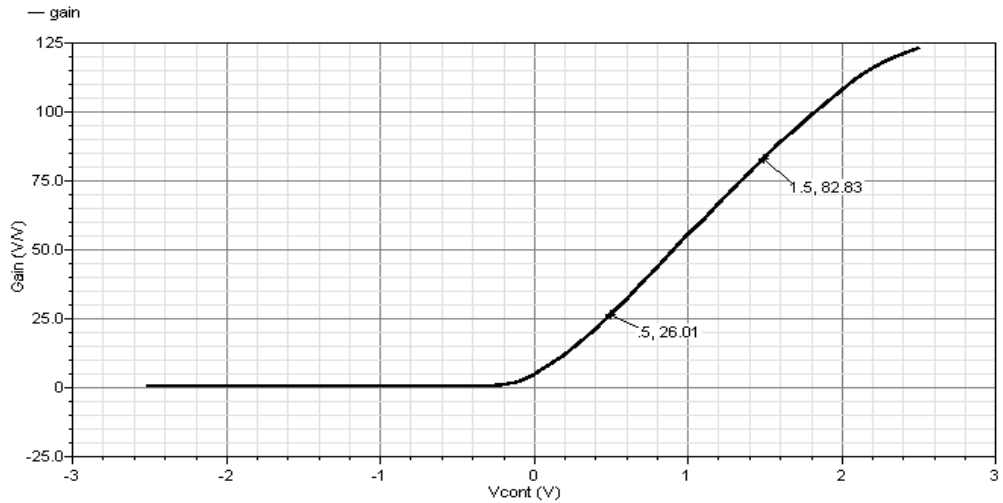


Figure 3.44: Gain versus control voltage simulation result for the proposed VGA circuit, when the control voltage is swept from -2.5V to 2.5V.

Figure 3.45 shows the transient simulation results for the positive and negative output terminals, when the control voltage is swept from 0V to 1V in six steps for the differential input signals having amplitudes of 10 mV. It is observed that common-mode level is at ground potential, indicating that CMFB circuit operates properly.

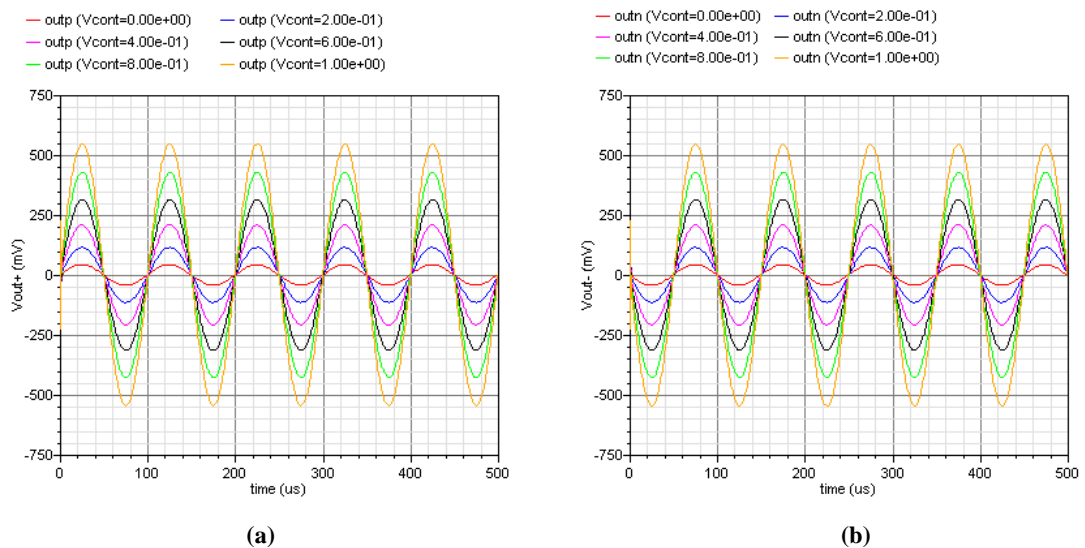


Figure 3.45: Transient simulation results for (a) the positive output terminal, and (b) the negative output terminal, when the control voltage is swept from 0V to 1V in six steps for the differential input signal having amplitudes of 10 mV.

After designing the CMOS circuits, PI controller parameters are defined according to the sensor characteristics. However, it is not an easy task for a non-linear feedback system, like the automatic amplitude control loop proposed in this research. Thus, linearized and reduced order model of the loop should be constructed first in order to calculate the unknown PI controller parameters. Figure 3.46 shows the SIMULINK block diagram of the reduced order loop model constructed according to the linearization and order reduction theory explained in Section 2.4.3. In this model, PI controller parameters are calculated by SIMULINK Parameter Optimization Tool, which is a powerful tool optimizing the desired parameters according to the design specifications. For the optimization operation, a signal constraint block is connected to the sensor output node, which actually represents the sensor cascaded resistive interface output. After the desired system response to step input is entered to the simulator, optimization tool finds the unknown parameters in several iterations by also considering the possible error tolerances coming from the mechanical sensor.

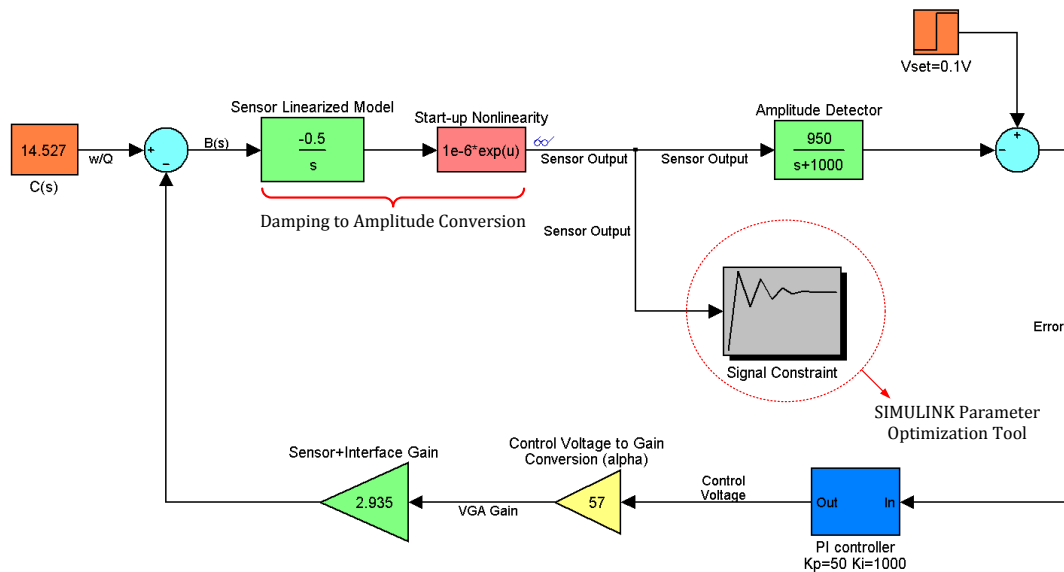


Figure 3.46: SIMULINK block diagram of the reduced order model for the proposed automatic amplitude control loop.

Figure 3.47 shows the SIMULINK transient response of the reduced order sensor output for the amplitude set voltage of 100 mV. It is observed that the sensor output

reaches to its steady-state value within 0.3 seconds. Moreover, there is a minor difference between final value of the sensor output and the amplitude set voltage, which is due to the attenuation introduced by the amplitude detector.

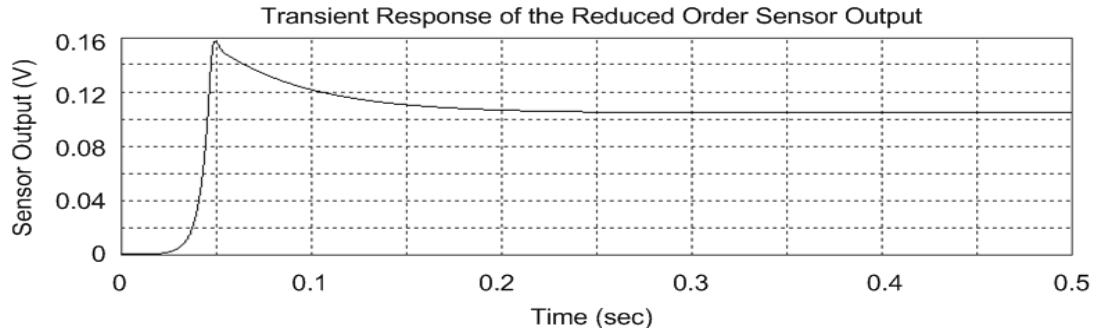


Figure 3.47: SIMULINK transient response of the reduced order sensor output for the amplitude set voltage of 100 mV.

After calculating the system parameters, system-level simulations are performed with the actual higher-order non-linear model of the loop. Figure 3.48 shows the exact model of the self-oscillation loop with amplitude control constructed in SIMULINK. Amplitude detector and VGA blocks are modeled according to the CADENCE simulations, and sensor is modeled theoretically from the mechanical parameters of DWP gyroscopes.

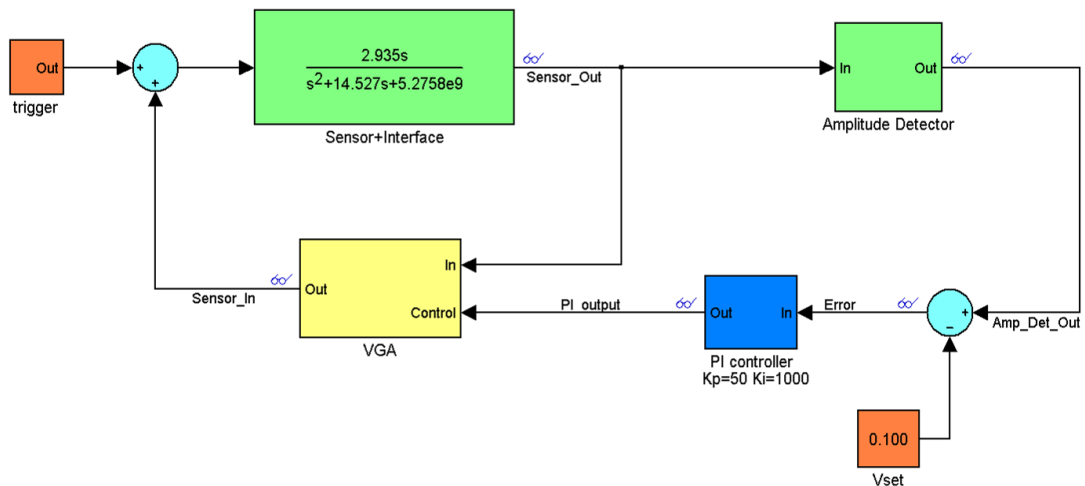


Figure 3.48: Exact model of the self-oscillation loop with amplitude control constructed in SIMULINK.

Figure 3.49 shows the SIMULINK transient response of the sensor cascaded resistive interface output for a step input of amplitude set voltage at 100 mV. Comparing the responses given in Figure 3.47 and Figure 3.49, it is observed that reduced order model provides very close estimation for the step response of the sensor output.

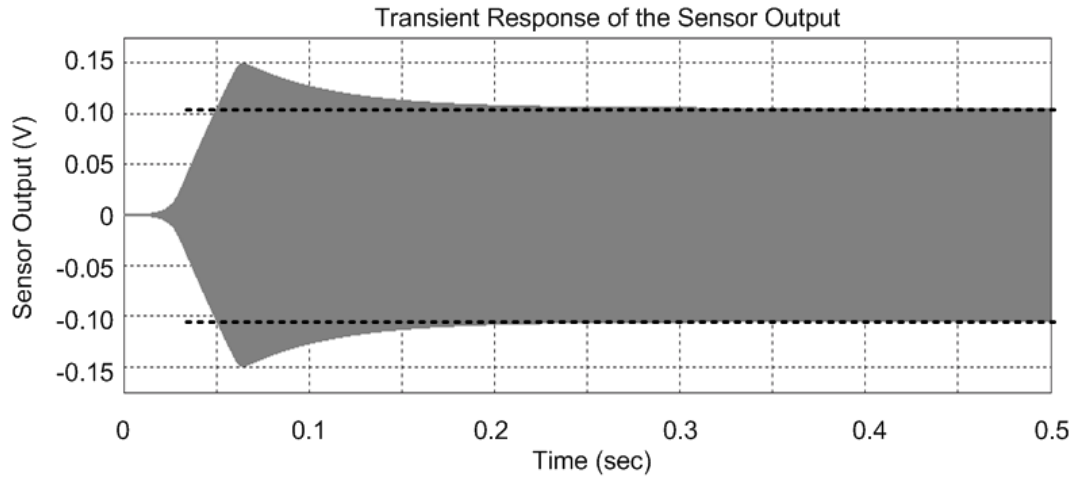


Figure 3.49: SIMULINK transient response of the sensor cascaded resistive interface output for a step input of amplitude set voltage at 100 mV.

Figure 3.50 shows the SIMULINK transient response of the error signal, which is the difference between the amplitude detector output and the amplitude set voltage. At the start-up, error signal is -100 mV since the gyroscope is stationary. As the increasing amplitude vibrations are sustained, error decreases until the loop gain stabilizes for constant amplitude oscillations. At the steady-state, error signal is zero indicating that drive-mode is vibrating exactly at the desired level.

Figure 3.51 shows the SIMULINK transient simulation result of the PI controller output. Remembering the inverting PI controller circuit given in Figure 3.39, output of the OPAMP is not DC-biased because of the integrating capacitor in the feedback path. Therefore, PI controller gives a saturated output at the start-up, providing maximum VGA gain. As the polarity of the error signal changes with the increasing oscillation amplitude, PI controller output converges to the level at which the VGA gain keeps the system poles on the imaginary axis for the constant amplitude oscillation.

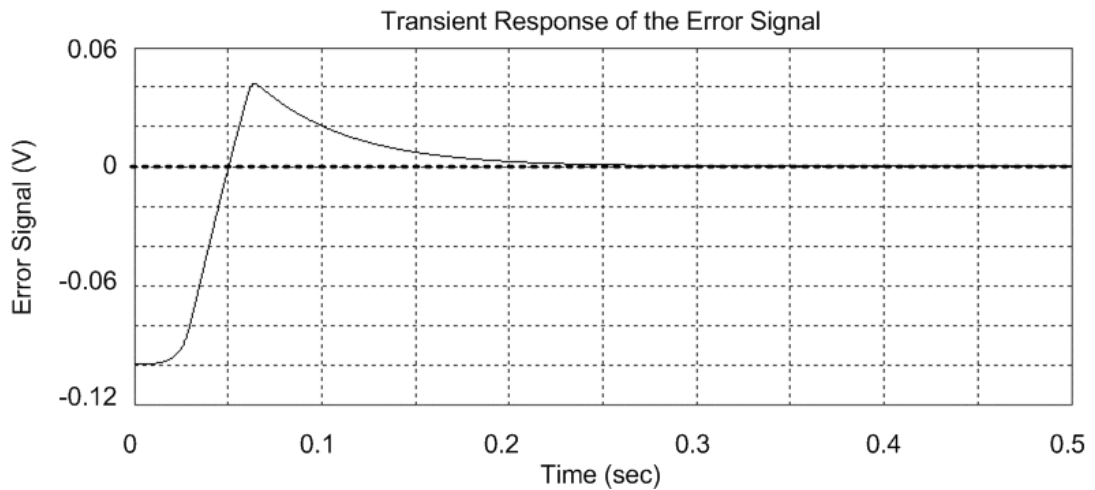


Figure 3.50: SIMULINK transient response of the error signal, which is the difference between amplitude detector output and amplitude set voltage.

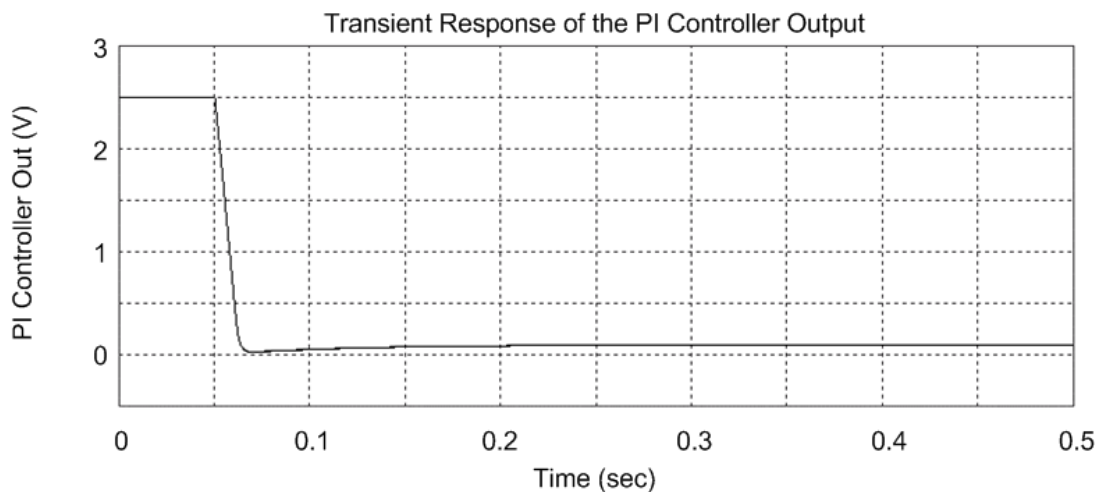


Figure 3.51: SIMULINK transient simulation result of the PI controller output.

The proposed loop is also simulated for the variations in sensor parameters and ambient conditions. Figure 3.52(a) shows the transient response of the sensor output in response to step changes in amplitude set voltage when the mechanical quality factor of the drive-mode is constant at 10000. When the amplitude set voltage changes, the amplitude control loop, which monitors the error signal continuously, adjusts the VGA gain so that the gyroscope vibrates at the set value. Figure 3.52(b)

gives the transient response of the sensor output when the step changes in the quality factor are simulated. Although sharp transitions in vacuum level are not expected during the normal operation of the gyroscope, it is verified that the amplitude control loop adapts itself to new conditions and provides constant amplitude vibrations at the mechanical resonance frequency of the gyroscope.

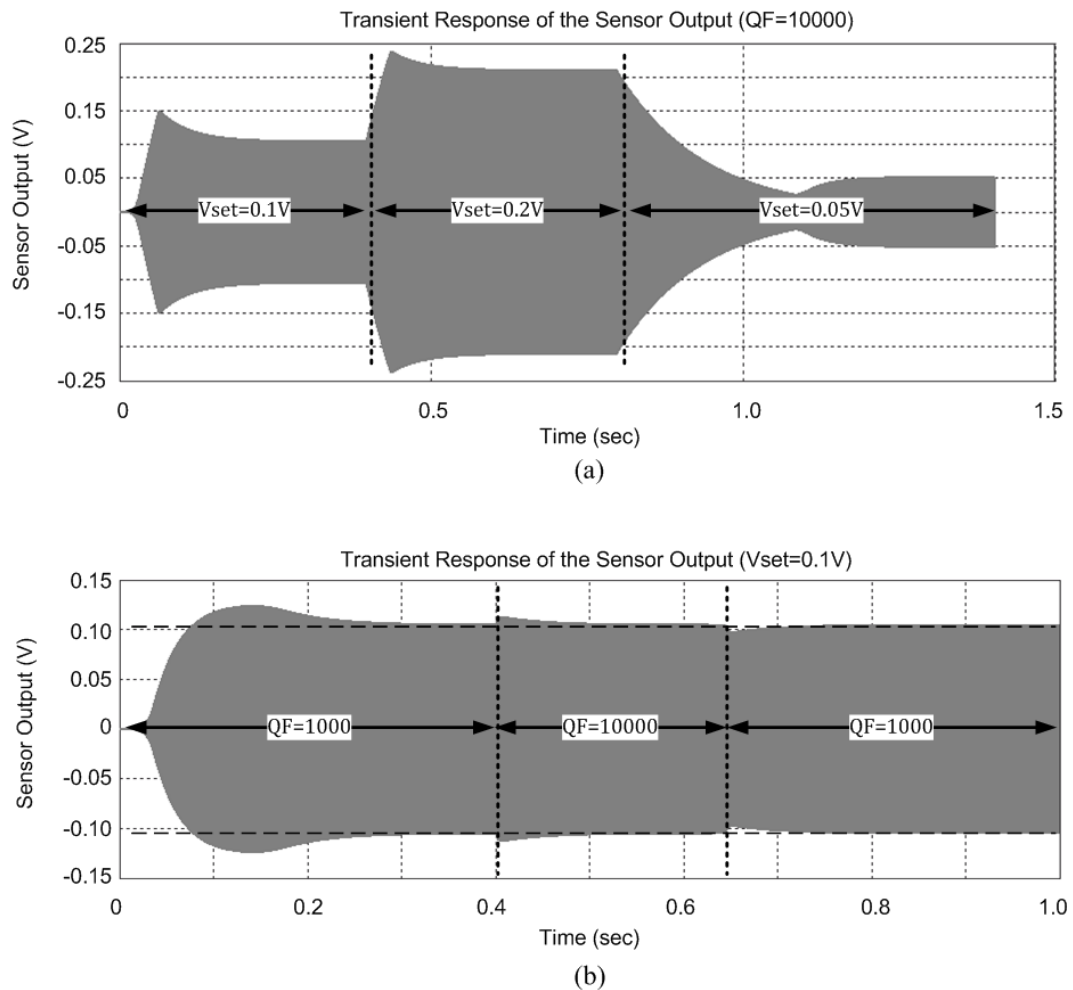


Figure 3.52: SIMULINK transient simulation results of the sensor output in response to step changes in (a) amplitude set voltage, and (b) mechanical quality factor.

After finalizing the system level design in SIMULINK, transistor-level circuit simulations of the amplitude controlled self-oscillation circuit given in Figure 3.39 are performed in CADENCE analog environment. Figure 3.53 shows the CADENCE transient simulation results for (a) instrumentation amplifier output

connected to the differential drive-mode interfaces, (b) generated error signal, and (c) PI controller output connected to the VGA gain control input. Comparing these simulation results with SIMULINK transient responses given in Figure 3.49, Figure 3.50, and Figure 3.51, it is concluded that CADENCE and SIMULINK provide almost identical results. Therefore, SIMULINK can be preferred to predict circuit response since CADENCE simulations usually last in several hours.

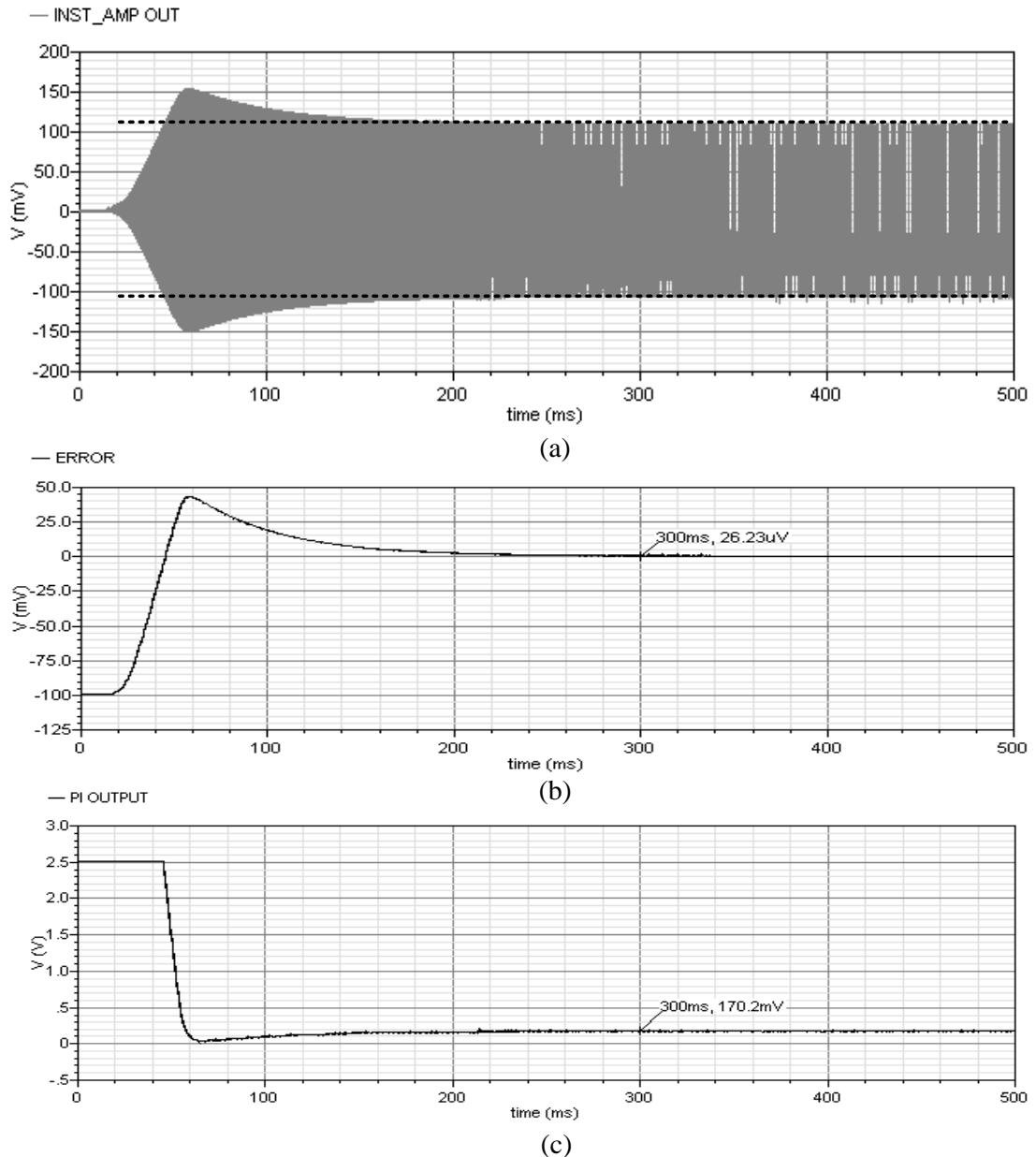


Figure 3.53: CADENCE transient simulation results for (a) the instrumentation amplifier output connected to the differential drive-mode interfaces, (b) the generated error signal, and (c) the PI controller output connected to the gain control input of the VGA.

3.4. CMOS Sense-Mode Open-Loop Rate Sensing Electronics

Remembering the Coriolis force definition in Section 2.1.2, the output of the sense-mode in response to an applied angular rate is an amplitude modulated signal at the vibration frequency of the drive-mode. Thus, CMOS open-loop rate sensing electronics aims to demodulate the differential sense-mode output signals to the baseband. The most important issue in this demodulation operation is the phase difference between the sense-mode output and the carrier signal. Such phase errors lead to undesired offset due to demodulation of quadrature signal at the sense-mode output. The detailed theory behind the phase-sensitive AM demodulation and the effect of phase errors are given in Section 2.4.4.

Figure 3.54 shows the block diagram of the proposed AM demodulator circuit based on switching full-wave rectification followed by low-pass filtering. In this technique, CMOS switch, which is controlled by a square-wave signal at the frequency of drive-mode oscillation, passes either positive or negative cycles of the differential sense-mode outputs. The resultant full-wave rectified signal is then filtered by a LPF, which rejects the high frequency components and gives an angular rate related DC signal.

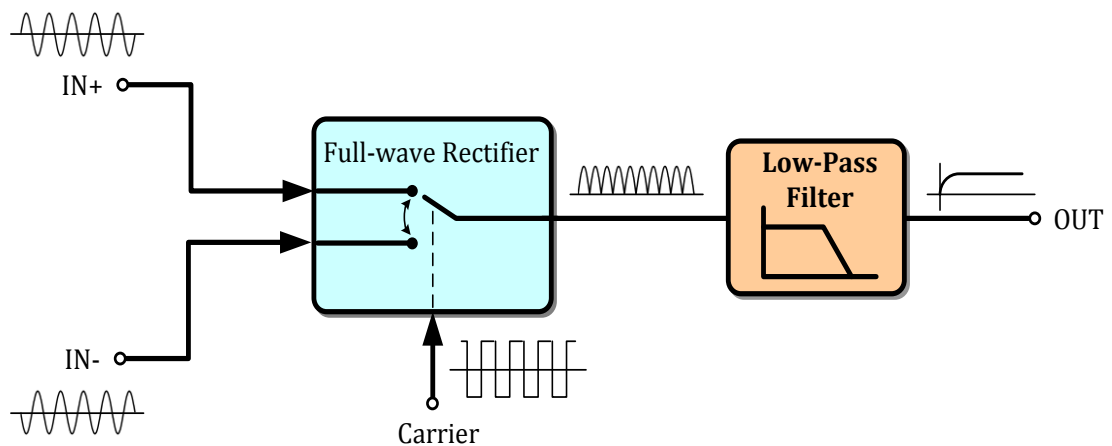


Figure 3.54: Block diagram of the proposed AM demodulator circuit based on switching full-wave rectification followed by low-pass filtering.

Figure 3.55 shows the circuit schematic of the fully-differential AM demodulation circuit designed for open-loop rate sensing electronics of DWP gyroscopes operated in mismatched-mode. In this mode, phase difference between the drive-mode resistive interface and the sense-mode capacitive interface outputs is ideally zero. Therefore, an additional 90° phase shifting block, which increases the complexity of the circuit, is not required for this configuration. Differential full-wave rectified signals are generated by switching the sense-mode outputs, where generic complementary CMOS switches with dummy transistors [58] are employed as the switching elements in order to minimize the charge injection problem. These CMOS switches are controlled by two analog comparators converting the drive-mode sinusoidal outputs to rail-to-rail square wave signals with minimum phase error. Then, differential full-wave rectified signals are applied to an instrumentation amplifier providing a glitch-free signal at the LPF input. A Sallen-Key type third-order LPF having cut-off frequency of 100 Hz then gives the baseband angular rate output by rejecting the undesired signal components. Because the capacitors of the LPF have impractical values to be implemented in CMOS technology, they are connected externally through the pads.

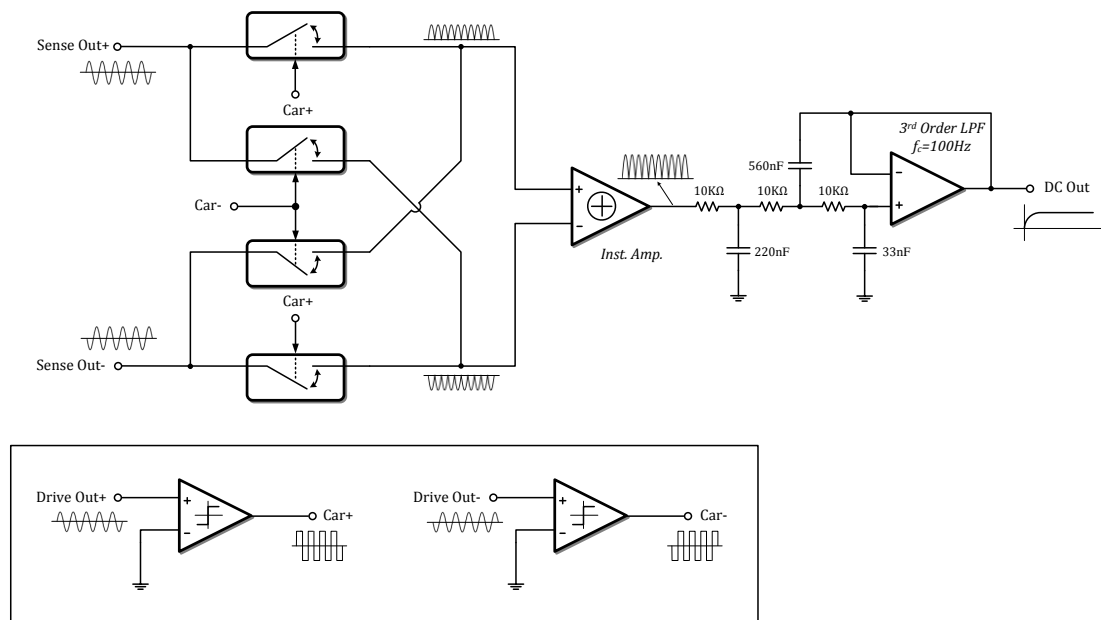


Figure 3.55: Circuit schematic of the fully-differential AM demodulation circuit designed for open-loop rate sensing electronics of DWP gyroscopes operated in mismatched-mode.

The post-layout simulations of the proposed circuit are performed in CADENCE analog environment. Figure 3.56 gives the transient simulation results for the differential full-wave rectifier outputs, when sinusoidal voltages having 100 mV of amplitude at 10 kHz are applied differentially.

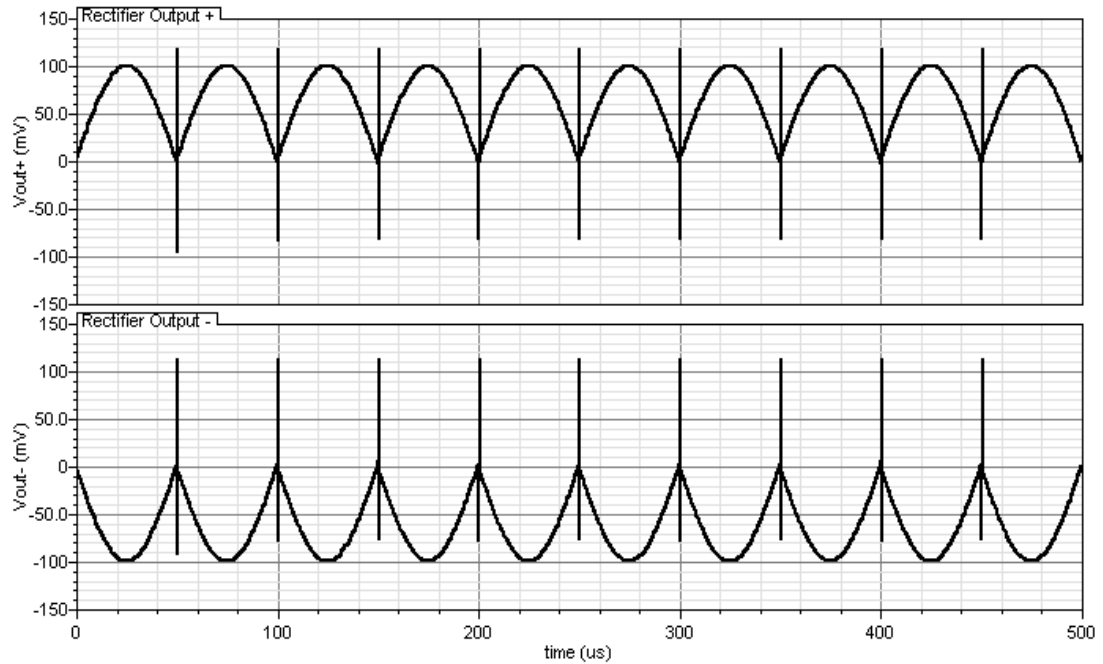


Figure 3.56: Transient simulation results for the differential full-wave rectifier outputs, when sinusoidal voltages having 100 mV of amplitude at 10 kHz are applied differentially.

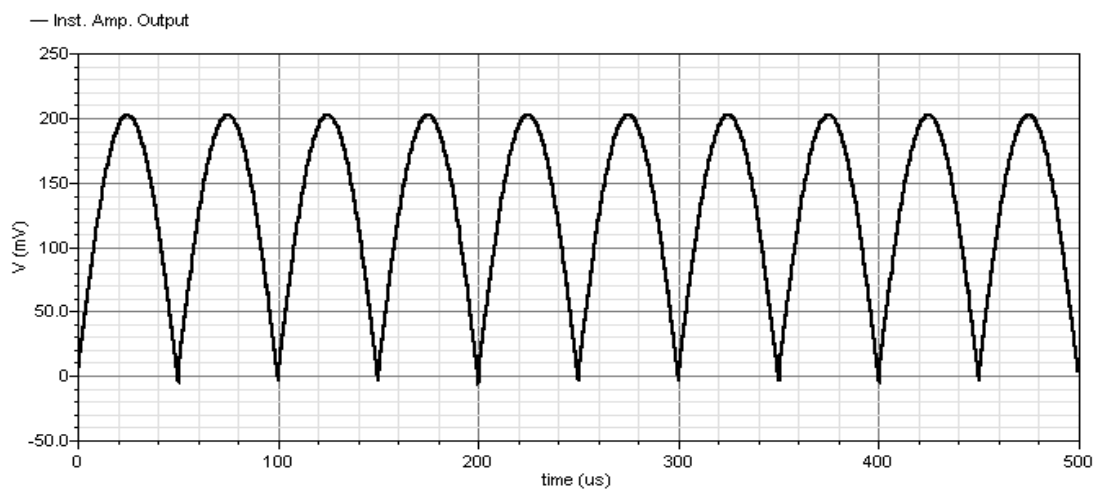


Figure 3.57: Transient response of the instrumentation amplifier output.

Although CMOS switches rectify the incoming signals properly, glitches appear at the differential outputs due to the sharp switching transitions. Since these glitches are common in both branches, they would be suppressed after the subtraction operation. Figure 3.57 gives the transient response of the instrumentation amplifier output, showing that glitches are rejected.

Figure 3.58 shows the transient simulation result of the third-order Sallen-key LPF output for differential sense-mode signals having 100 mV of amplitude. It is a well known fact that the DC level of a full-wave rectified sinusoidal signal is $2/\pi$ of the signal amplitude. Then, it is observed that the LPF output converges to 125 mV, which corresponds to the theoretical DC level of the instrumentation amplifier output.

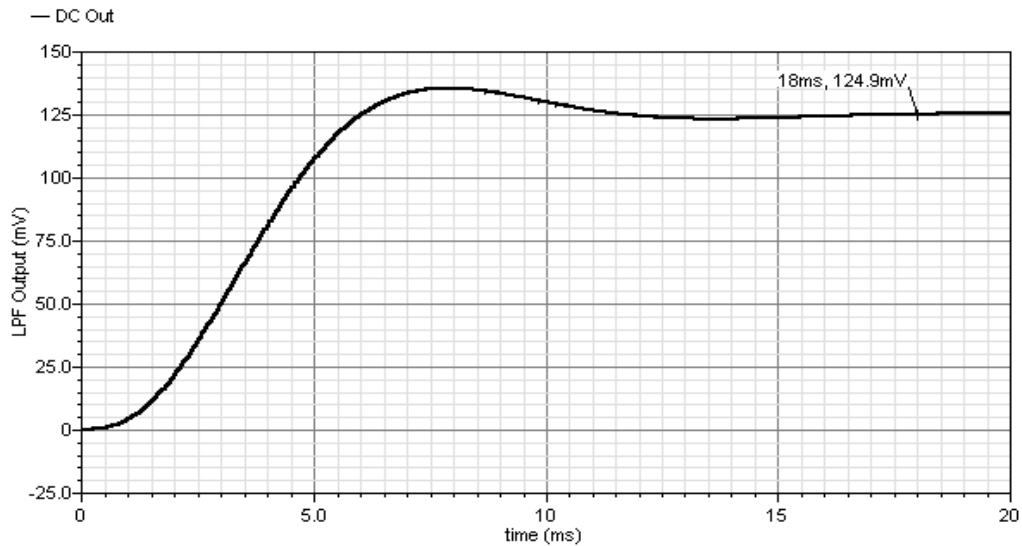


Figure 3.58: Transient simulation result of the third-order Sallen-key LPF output for differential sense-mode signals having 100 mV of amplitude.

Because the proposed demodulator circuit is a switching rectifier, continuous-time noise analysis leads to erroneous results. Hence, periodic steady state (PSS) noise analysis, which finds a proper operating point according to the switch conditions, should be performed. Figure 3.59 shows the Periodic Steady-State (PSS) noise analysis giving output referred voltage noise of the overall demodulator output.

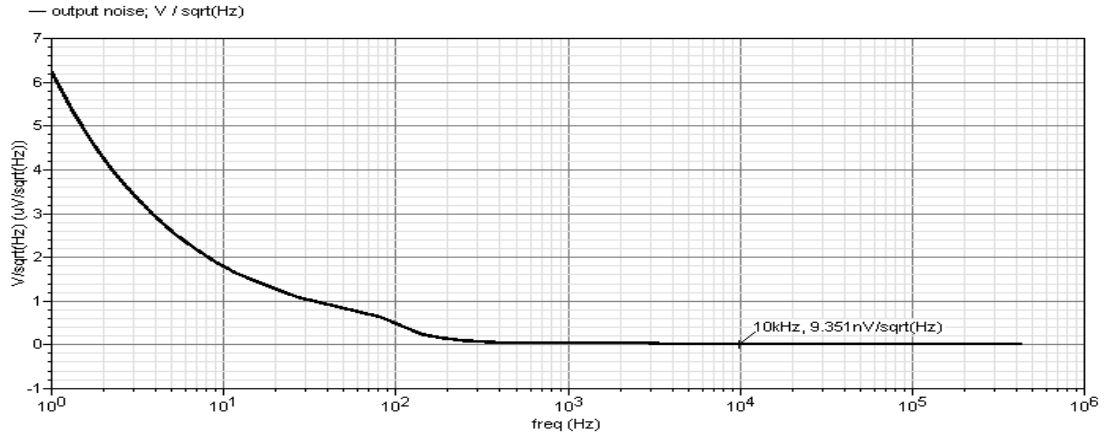


Figure 3.59: Periodic Steady-State (PSS) noise analysis giving output referred voltage noise of the overall demodulator output.

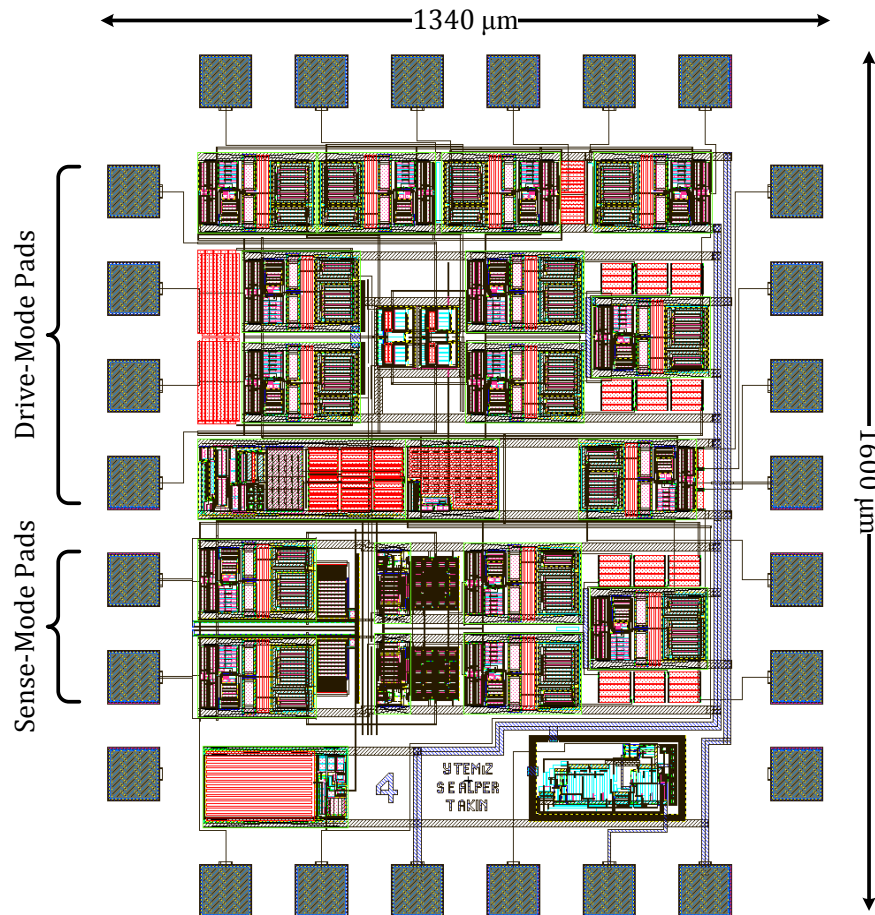


Figure 3.60: Layout of the fully-differential automatic amplitude control loop and open-loop rate sensing electronics designed for DWP gyroscopes.

CMOS demodulator circuit and fully-differential automatic amplitude control loop given in Figure 3.39 are combined in a single chip according to the pad distribution of DWP gyroscopes. Figure 3.60 shows the layout of the CMOS chip including complete readout and control electronics necessary for a proper gyroscope operation.

3.5. Summary

This chapter provides the details of readout and control electronics implemented with both discrete components and the CMOS technology. First, the drive-mode self-oscillation loop with manual amplitude control and the sense-mode open-loop rate sensing electronics, which are realized with SMD components for SOG and SOI gyroscopes, are introduced. In the basic self-oscillation loop, it is observed that the oscillation amplitude depends on the sensor parameters and ambient conditions. Then, an improved automatic amplitude control loop idea sustaining constant amplitude vibrations in the drive-mode is proposed. Together with the SOG gyroscope, TIA type resistive interfaces, and the sense-mode rate sensing electronics, the proposed loop is implemented on a compact PCB having $5.4 \times 2.4 \text{ cm}^2$ area. After that, the differential version of the automatic amplitude control circuit is designed for dual-mass DWP gyroscopes, where whole circuit is implemented with commercial SMD components. Next, high-performance CMOS capacitive and resistive interfaces are presented. Unity-gain buffer and transimpedance amplifier type interfaces are investigated separately by providing the transistor-level simulation results. High-impedance node biasing structures enabling the realization of resistances in the order of gigaohms through the channel resistance of MOS transistors are proposed as well. Then, fully-differential CMOS drive-mode electronics for dual-mass gyroscopes are introduced. The circuit operation is verified by system-level and transistor-level simulations performed in SIMULINK and CADENCE. Finally, a CMOS demodulator circuit based on the switching type full-wave rectification followed by the low-pass filtering is proposed.

CHAPTER 4

TEST RESULTS

This chapter presents the test results of both discrete and CMOS electronics designed for silicon-on-glass (SOG), silicon-on-insulator (SOI), and dissolved-wafer process (DWP) gyroscopes developed at METU. Section 4.1 gives the results of performance tests performed on the complete angular rate systems composed of micromachined vibratory gyroscopes and discrete electronics implemented with commercial components. The results are demonstrated in terms of scale factor, linearity, zero-rate output, dynamic range, angle random walk, and bias instability. Then, Section 0 presents the AC, transient, and noise test results of CMOS capacitive and resistive interfaces. Results of the characterization tests performed on the fully-differential automatic oscillation amplitude control circuit and the sense-mode demodulation electronics designed for DWP gyroscopes are also given in this section. Finally, Section 4.3 summarizes the tests and discusses the results.

4.1. Test Results of the Discrete Electronics

In this section, test results are illustrated for three main types of discrete electronics:

- 1) readout and control electronics with manual oscillation amplitude control designed for gyroscopes interfaced with CMOS capacitive-type source followers,
- 2) readout and control electronics with automatic oscillation amplitude control designed for SOG gyroscopes interfaced with off-chip transresistance amplifiers, and
- 3) differential readout and control electronics with automatic oscillation amplitude control designed for DWP gyroscopes.

4.1.1. Readout and Control Electronics with Manual Oscillation Amplitude Control

The circuit tested in this section is composed of the drive-mode self-resonance loop circuit with manual oscillation amplitude control and the sense-mode open-loop rate sensing electronics, which are explained in Section 3.1.1 and Section 3.1.2, respectively. Figure 4.1 shows the photograph of the test setup used for characterization of the drive-mode control and the sense-mode demodulation electronics. Preliminary tests are performed by applying sinusoidal signals by a function generator (Agilent 33120A), and observing the output signals generated by the circuit through an oscilloscope (Agilent Infinium 54815A).

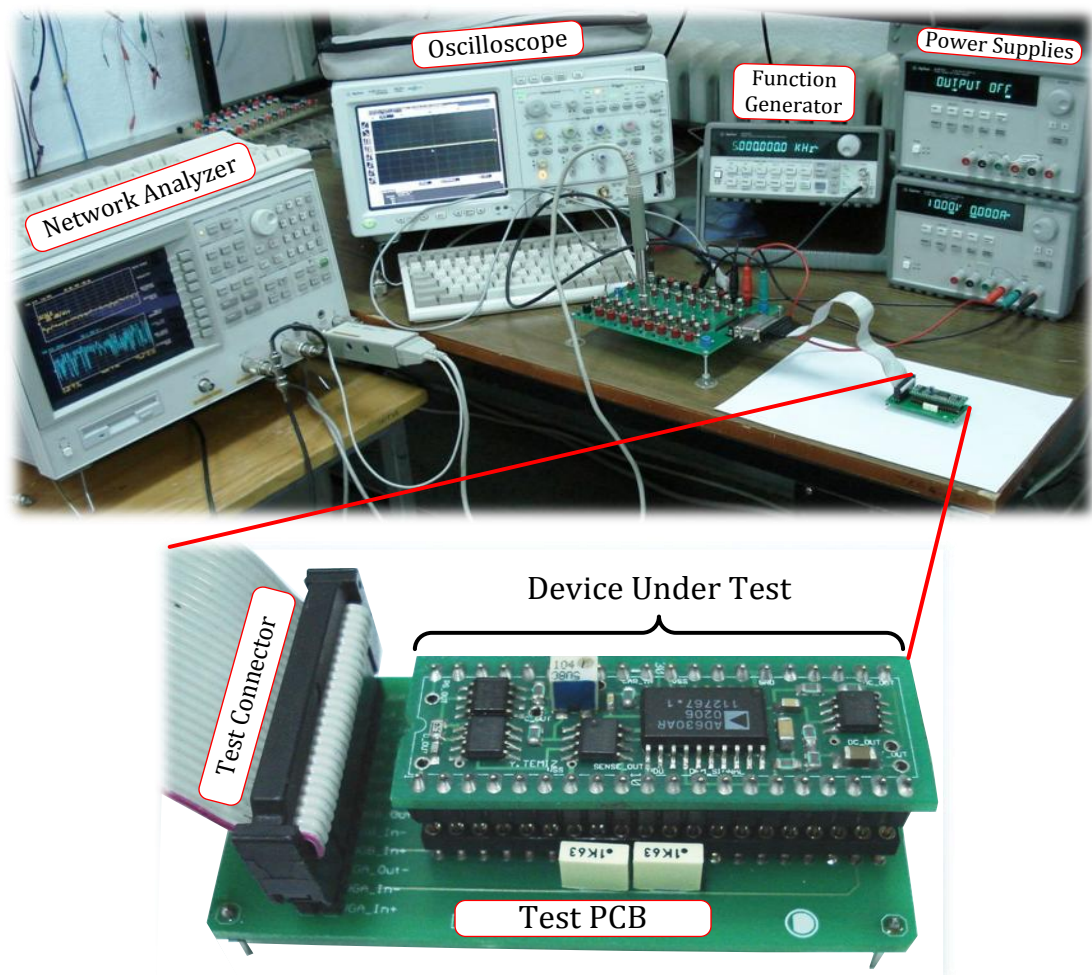
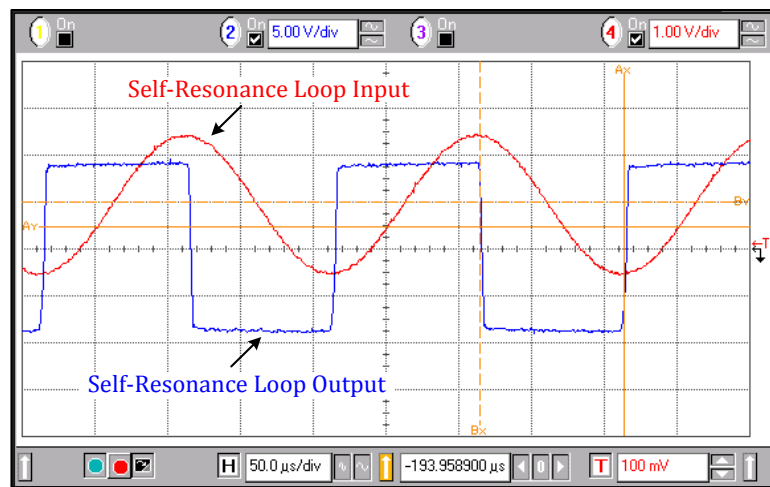
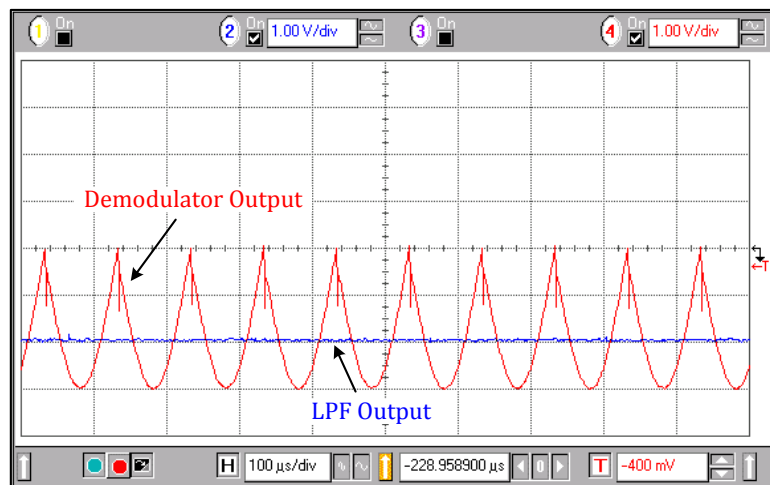


Figure 4.1: Photograph of the test setup used for characterization of drive-mode control and sense-mode demodulation electronics.

Figure 3.3(a) shows the self-resonance loop output when a sinusoidal signal with $3 V_{p-p}$ amplitude and 1 V offset is applied. While introducing 90° phase shift to the incoming signal, the differentiator circuit in the self-resonance loop totally rejects the DC offset, making the loop insensitive to the undesired offset at the interface output. According to the transfer characteristics measured by the network analyzer (Agilent 4395A), the differentiator phase error is below 0.5° in a 10 kHz bandwidth. Moreover, it is verified that the amplitude of the self-resonance loop output can be easily controlled by a potentiometer for sustaining drive-mode vibrations at the desired level.



(a)



(b)

Figure 4.2: a) The measured self-resonance loop output (blue) when a sinusoidal signal with $3 V_{p-p}$ amplitude and 1 V offset (red) is applied. b) Measured outputs of the sense-mode demodulator (red) and low-pass filter (blue).

Figure 3.3(b) shows the measured outputs of the sense-mode demodulator and the low-pass filter (LPF). The demodulator circuit generates the full-wave rectified version of the applied sinusoid, and the third-order LPF finds the DC level of the generated signal by rejecting high-frequency components. When a sinusoidal signal having $3 V_{\text{peak}}$ amplitude is applied to the demodulator input, the LPF gives a DC signal having 1.9 V of amplitude, which is exactly $2/\pi$ of the peak value. It is also observed that the proposed demodulator circuit rejects the DC offset at the sense-mode interface output.

After verifying that this compact circuit gives superior performance compared to the previous gyroscope electronics developed at METU, it is used in the characterization tests of SOG gyroscopes interfaced with CMOS single-ended source-followers [50] and SOI gyroscopes interfaced with discrete buffers [22, 51]. Table 1.1 summarizes the best performance values demonstrated by SOG [50] and SOI [51] gyroscopes when the proposed circuit is used in the drive and sense-mode electronics.

Table 4.1: The best performance values demonstrated by SOG [50] and SOI [51] gyroscopes when the proposed circuit, which is composed of drive-mode self-oscillation loop with manual amplitude control and sense-mode open-loop rate sensing electronics, is employed.

Parameter	SOG Gyroscope [50]	SOI Gyroscope [51]
Scale Factor (mV/(deg/sec))	1.97	8.9
R ² Nonlinearity (%)	0.001	0.04
Angle Random Walk (deg/ $\sqrt{\text{hr}}$)	2.16	4.8
Bias Instability (deg/hr)	124.7	106

Although the circuit gives very satisfactory results in the characterization tests, it is concluded that the circuit is not suitable for systems required to have tactical-grade performance due to some drawbacks introduced by the circuit. First, because of the absence of an automatic amplitude control mechanism, the vibration amplitude highly depends on the sensor parameters and the ambient conditions. In addition to this, the driving signal is a square wave that may excite the higher modes of the gyroscope and cause glitches due to the electrical coupling. Thus, more complicated electronics are essential to achieve superior performances.

4.1.2. Readout and Control Electronics with Automatic Oscillation Amplitude Control for SOG Gyroscopes

In this section, performance test results of the complete angular rate system employing an SOG gyroscope as the mechanical sensing element are illustrated. In this system, drive and sense modes of the gyroscope are sensed by discrete transresistance amplifier type interfaces. The drive-mode vibrations are sustained through a self-oscillation loop with automatic amplitude control mechanism. Then, the sense-mode output is demodulated to baseband by open-loop rate sensing electronics. The design details and the system-level simulations of the proposed circuit are given in Section 3.1.4.

Figure 4.3 shows the resonance characteristics for the drive and the sense modes of the SOG gyroscope measured with Agilent 4395A network analyzer and Karl Suss micromanipulator probe station at the ambient pressure. The resonance frequencies are measured to be matched at about 4.06 kHz for a DC polarization voltage of 31 V applied to the proof mass. The quality factors of the gyroscope for the drive and the sense modes at the atmospheric pressure are found as 241 and 2.3, respectively. The measured resonance characteristics are then used in the SIMULINK model to estimate the unknown parameters of the self-oscillation loop.

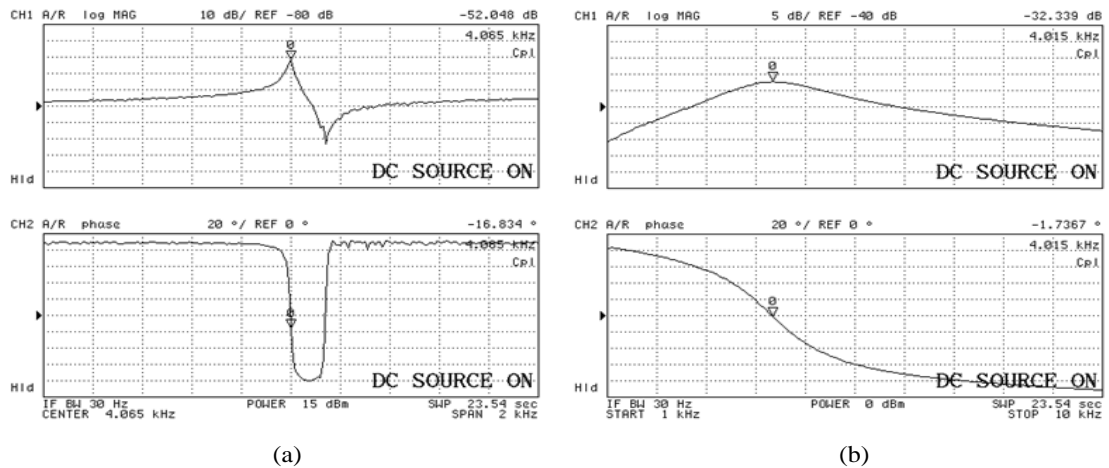


Figure 4.3: Resonance characteristics for the (a) drive-mode, and the (b) sense-mode of the SOG gyroscope measured with Agilent 4395A network analyzer and Karl Suss micromanipulator probe station at the ambient pressure.

The proposed automatic oscillation amplitude control loop and the complete angular rate system are tested in a vacuum chamber providing at most 5 mTorr of vacuum level by using a mechanical pump. Figure 4.4 shows the photograph of the compact and fully-functional angular rate system placed into the vacuum chamber mounted on Ideal Aerosmith 1280 single-axis rate table.

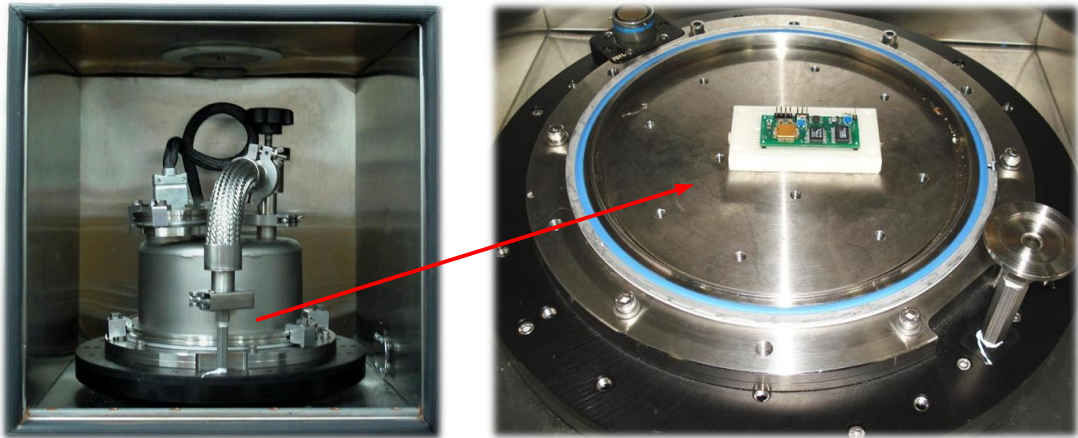


Figure 4.4: Photograph of the compact and fully-functional angular rate system placed into the vacuum chamber mounted on Ideal Aerosmith 1280 single-axis rate table.

The drive-mode self-oscillation loop is tested for various combinations of proof mass voltage (V_{PM}) and pressure level (P). Figure 4.5 shows the measured responses of the drive-mode interface output for (a) $V_{PM} = 20V$, $P = 5mTorr$, (b) $V_{PM} = 30V$, $P = 5mTorr$, and (c) $V_{PM} = 30V$, $P = 1500mTorr$. It is a well-known fact that the gain of the gyroscope highly depends on the proof mass voltage and the vacuum level. Therefore, the vibration amplitude of an angular rate system employing self-resonance loop without any automatic amplitude control mechanism would change according to the applied proof mass voltage and the vacuum level. On the other hand, the proposed loop provides constant amplitude oscillations by adapting itself to wide range of deviations in the system parameters and the ambient condition. Moreover, comparing the gyroscope resonance characteristics given in Figure 4.3 to output responses in Figure 4.5, it is verified that the loop sustains oscillations exactly at the mechanical resonance frequency of the drive-mode.

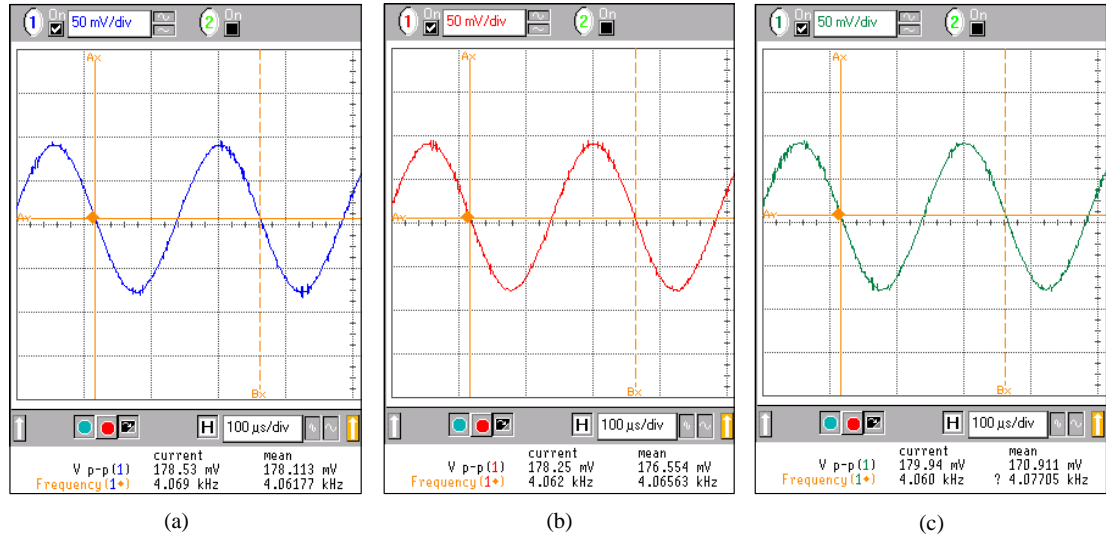


Figure 4.5: Measured responses of the drive-mode interface output for (a) $V_{PM} = 20V$, $P = 5mTorr$, (b) $V_{PM} = 30V$, $P = 5mTorr$, and (c) $V_{PM} = 30V$, $P = 1500mTorr$.

After verifying that the amplitude control loop provides very stable and self-triggered drive-mode oscillations by driving the gyroscope with a sinusoidal signal exactly at the mechanical resonance frequency of the drive-mode, system characterization tests are performed for scale factor, linearity, zero-rate output, dynamic range, bias instability, and angle random walk. In these test, the system is operated for four different cases. Table 4.2 gives the operation cases for the angular rate system, categorized according to the sense-mode transresistance amplifier (TRA) resistance, the matching mode, the sense-mode instrumentation amplifier (IA) gain, and the vacuum level.

Table 4.2: Operation cases for the angular rate system, categorized according to the sense-mode transresistance amplifier (TRA) resistance, the matching mode, the sense-mode instrumentation amplifier (IA) gain, and the vacuum level.

	Sense-Mode TRA Resistance	Matching Mode	Sense-Mode IA Gain	Vacuum Level
Case I	10 M Ω	Near-Match	4	5 mTorr
Case II	10 M Ω	Mismatch	4	5 mTorr
Case III	1 M Ω	Near-Match	6	5 mTorr
Case IV	1 M Ω	Mismatch	6	5 mTorr

In this section, test results of only Case I are illustrated graphically, and those of other cases are given numerically. Figure 4.6 shows the measured output response of the angular rate sensor (Case I) when the applied angular rate is swept from zero rate to ± 50 deg/sec with 5 deg/sec steps.

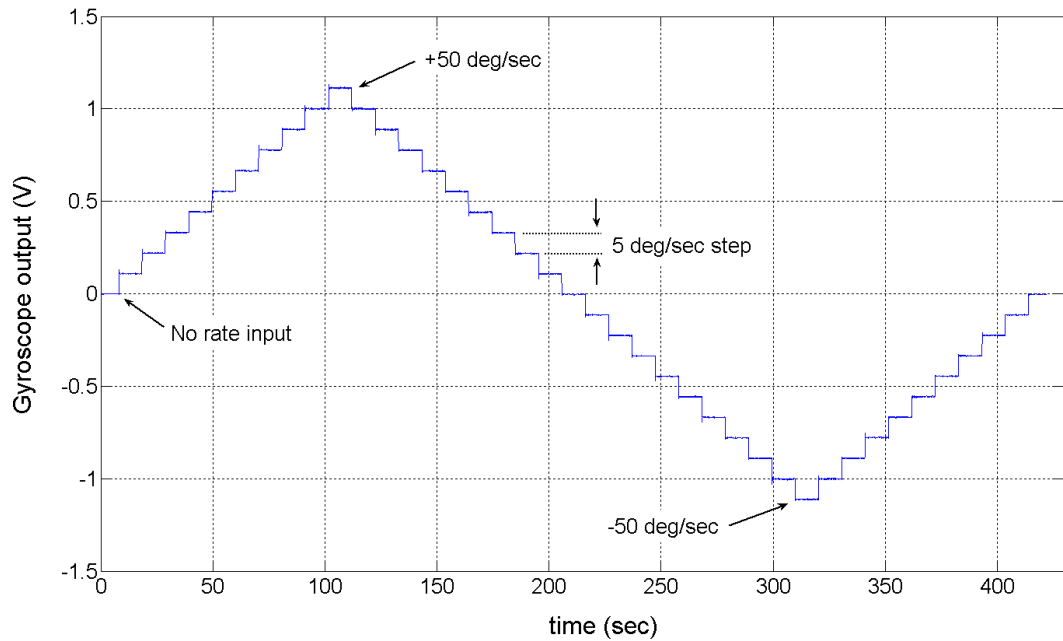


Figure 4.6: Measured output response of the angular rate sensor (Case I) when the applied angular rate is swept from zero rate to ± 50 deg/sec with 5 deg/sec steps.

The data obtained from this test is then used to construct the output voltage versus applied angular rate characteristics of the sensor. Figure 4.7 shows the measured response curve giving the scale factor, the zero-rate offset, and the nonlinearity of the overall system. The sensor has a scale-factor of 22.2mV with a zero-rate offset of 2.2mV, corresponding to 0.1deg/sec. The offset is quite small owing to very small phase error introduced by the electronics, precise phase-sensitive demodulation, and the small mechanical coupling between the drive and sense modes of the SOG gyroscope. Moreover, the R^2 -nonlinearity of the response curve is measured to be less than $\pm 0.01\%$, whereas the composite nonlinearity of the scale factor, including hysteresis, systematic nonlinearity, and other uncertainties in the measurement, is measured to be as low as $\pm 0.6\%$. The dynamic range of the angular rate sensor

system is limited to $\pm 50\text{deg/sec}$, above which the scale-factor nonlinearity increases due to open-loop rate sensing.

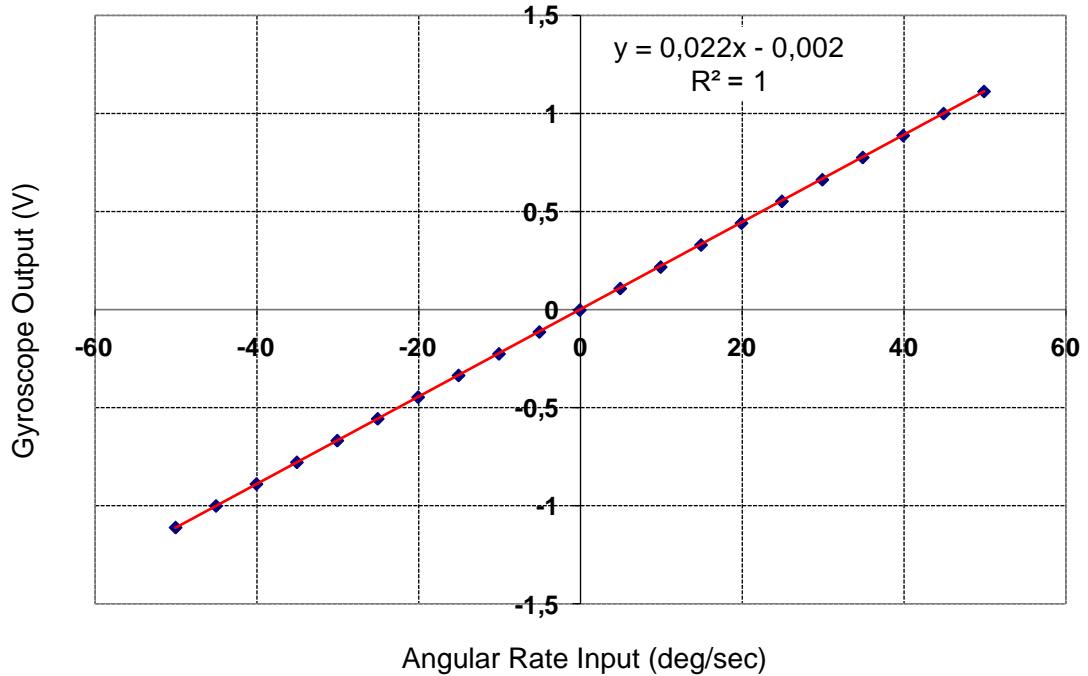


Figure 4.7: Measured response curve giving the scale factor, the zero-rate offset, and the nonlinearity of the overall system.

The bias instability and the angle random walk values demonstrated by the angular rate system are determined by Allan Variance analysis. The output of the sensor is collected for a period of time more than $1\frac{1}{2}$ hours by using a multimeter (Agilent 34401A) and HPVVEE software. Figure 4.8 gives the bias drift data collected from the rate output when the system is powered up at zero time, while the sensor is located in the vacuum chamber and kept stationary during the test. In the short-term, system output makes an overshoot due to temperature increase, as the circuit cannot easily remove the heat in the vacuum ambient. Then, in the long-term, system gives a decreasing response that eventually saturates. The reason for this decrease is found to be the slight change in the vacuum level during the test, because the output voltage drifts in the opposite direction when the vacuum is released. The amplitude

controlled self-oscillation loop provides vacuum-independent drive-mode vibrations. However, demodulation of the quadrature error due to very small phase errors causes a vacuum-dependent zero-rate output since the quadrature error increases with the vacuum level.

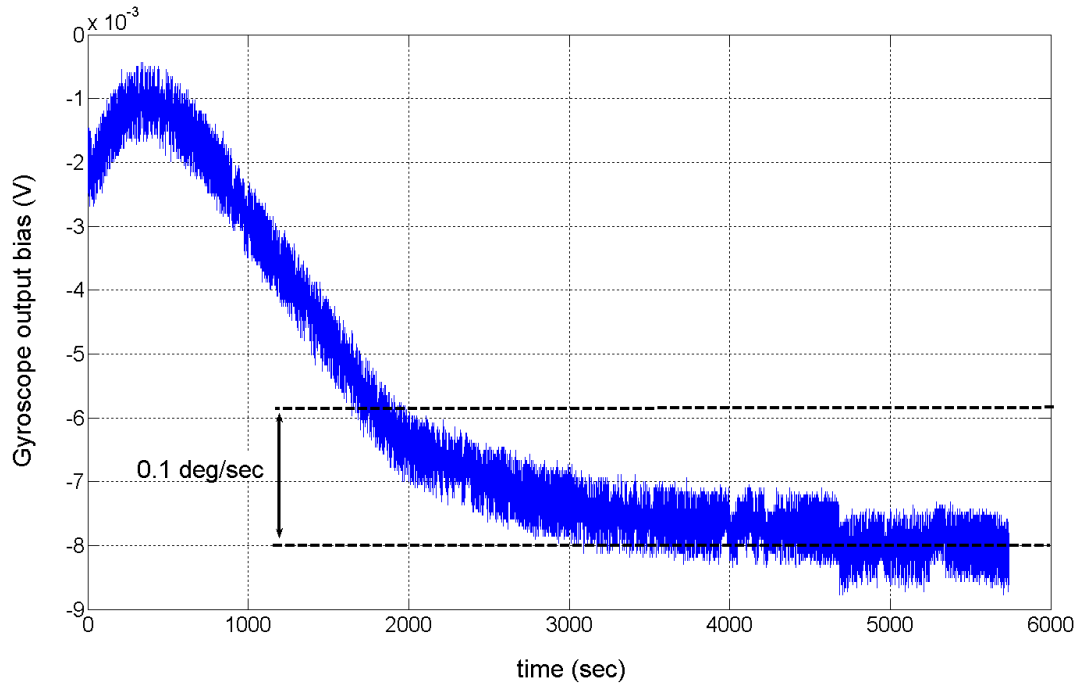


Figure 4.8: Bias drift data collected from the rate output when the system is powered up at zero time, while the sensor is located in the vacuum chamber and kept stationary during the test.

Figure 4.9 shows the Allan variance plot generated by the drift data. The bias instability of the sensor is determined by dividing the measured dip-level of the Allan variance plot by the factor of 0.664 as described in [59]. The bias instability of the angular rate sensor system is found to be 14.3 deg/hr, which is sufficient for several tactical-grade applications. In fact, this value can be further improved by using a controllable vacuum chamber providing precisely controlled vacuum level, or a vacuum-packaged gyroscope. Moreover, the developed system demonstrates an angle random walk of 0.126 deg/ $\sqrt{\text{hr}}$, or an equivalent white noise density of 7.56 (deg/hr)/ $\sqrt{\text{Hz}}$. The measured noise density is impressively low recognizing that the whole electronics are constructed by discrete components.

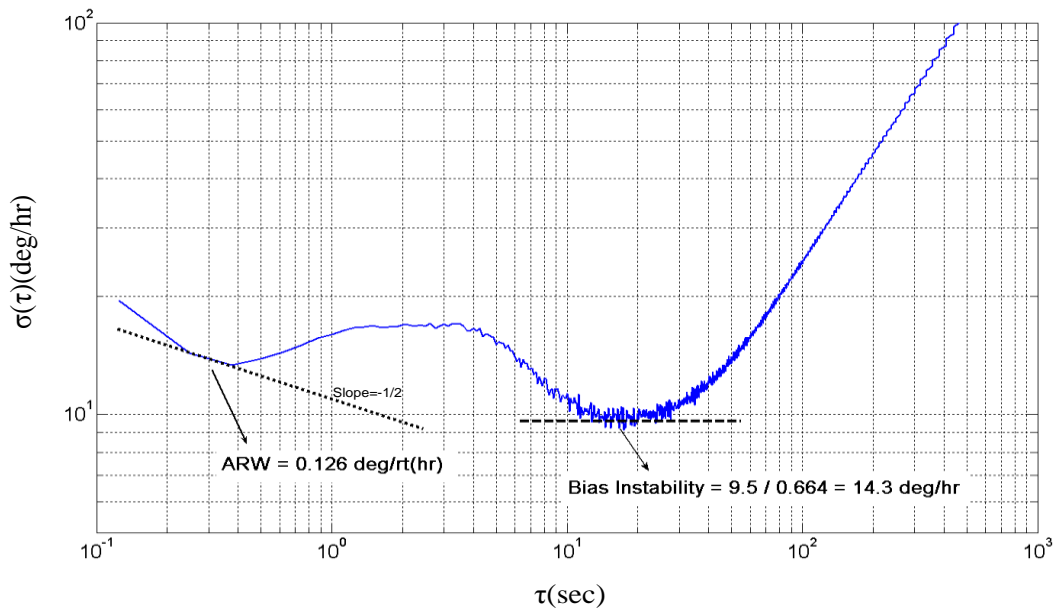


Figure 4.9: Allan variance plot generated by the drift data given in Figure 4.8.

The angular rate system is also tested for time-varying angular rates. Figure 4.10 shows the measured system output in response to a sinusoidal rate at 2 Hz. It is verified that the system has bandwidth of 10 Hz, which is limited by the LPF circuit used in the open-loop rate sensing electronics.

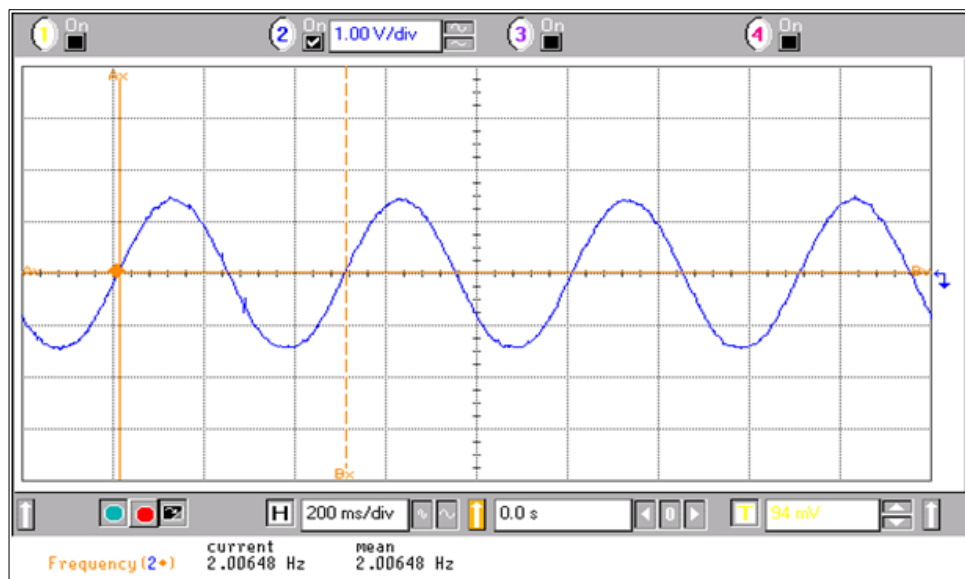


Figure 4.10: Measured system output in response to a sinusoidal rate at 2Hz.

In order to compare the effects of critical parameters on the overall performance of the system, similar performance tests are also performed for other cases given in Table 4.2. Table 4.3 summarizes the performance test results for the angular rate system operated in four different conditions. It is verified that the performance of the system significantly improves by using larger TIA resistance in the sense-mode. However, as the electronic gain increases by increasing the TIA resistance, circuit stages start to become nonlinear for higher angular rates, limiting the dynamic range. In addition, operating the gyroscope closer to the matched-mode also boosts the sensitivity. However, in this mode, the deflection of the sense-mode in response an angular rate increases, causing mechanical nonlinearity and possible pull-in. In fact, the proposed system is also tested for exactly matched-mode condition. Although it demonstrates exceptional performance with a scale factor higher than 100 mV/(deg/sec) and bias instability lower than 10 deg/hr, the dynamic range is just limited to ± 10 (deg/sec) due to open-loop sense electronics. Therefore, it is concluded that it is possible to obtain far better performance by supporting the proposed amplitude control loop with close-loop electronics employing force-feedback mechanism to keep the proof mass stationary.

Table 4.3: Performance test results for the angular rate system operated in four different conditions.

Parameter	Case I	Case II	Case III	Case IV
Scale Factor (mV/(deg/sec))	22.2	16.8	9.8	7.3
R² Nonlinearity (%)	0.01	0.01	0.35	0.06
Dynamic Range (deg/sec)	± 50	± 50	± 100	± 100
Zero Rate Output (deg/sec)	-0.1	+3.45	+0.35	+0.8
Bias Instability (deg/hr)	14.3	12.2	30	30
Angle Random Walk (deg/ $\sqrt{\text{hr}}$)	0.126	0.176	0.247	0.412

Although implemented with discrete components, the developed angular rate sensor system demonstrates an impressive performance by integrating a MEMS gyroscope with advanced electronics generating amplitude-controlled and stable drive-mode oscillations and extracting the rate signal by phase-sensitive detection.

4.1.3. Differential Readout and Control Electronics with Automatic Oscillation Amplitude Control for DWP Gyroscopes

This section presents the test results of discrete readout and control electronics designed for dual-mass DWP gyroscopes. The proposed circuit is composed of drive and sense mode transresistance amplifiers, the differential automatic amplitude control loop that sustains constant-amplitude oscillations, and the differential open-loop rate sensing electronics that transfers the sense-mode output to a baseband signal proportional to the applied rate. The design details of the circuit are given in Section 3.1.5. Figure 4.11 shows the photograph of the test setup used for characterization of the circuit.

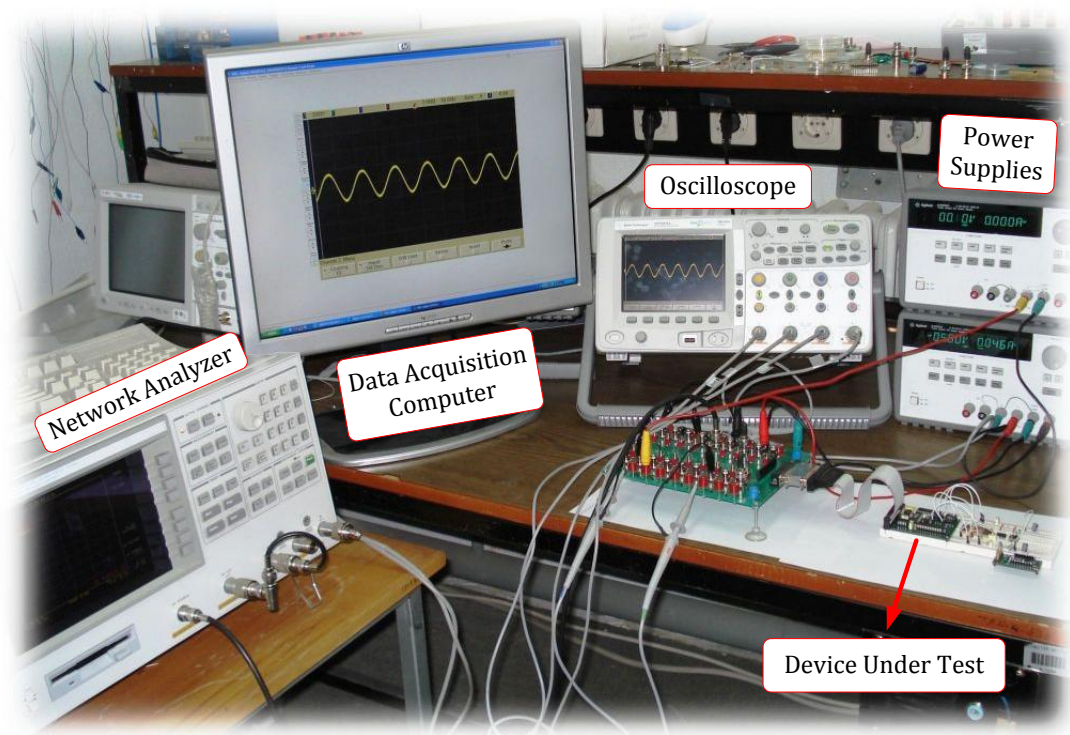


Figure 4.11: Photograph of the test setup used for characterization of control and readout electronics designed for DWP gyroscopes.

The preliminary tests are performed on a vacuum-packaged DWP gyroscope prototype in order to obtain the electromechanical model parameters. Figure 4.12 shows the measured drive-mode resonance characteristics of the vacuum packaged

DWP gyroscope when the drive-mode output is read from the motor electrode through a transresistance amplifier with a 1 M Ω feedback resistor while the proof mass voltage is set to 15 V. The quality factor of the drive-mode is found as 1238, which is actually lower than what is expected, possibly due to internal outgassing after vacuum packaging. According to the gain characteristics, the measured resonance frequency is 12.62 kHz, where the corresponding gain is -15 dB. This implies that a VGA gain of 15 dB is required for keeping the system poles on the imaginary axis.

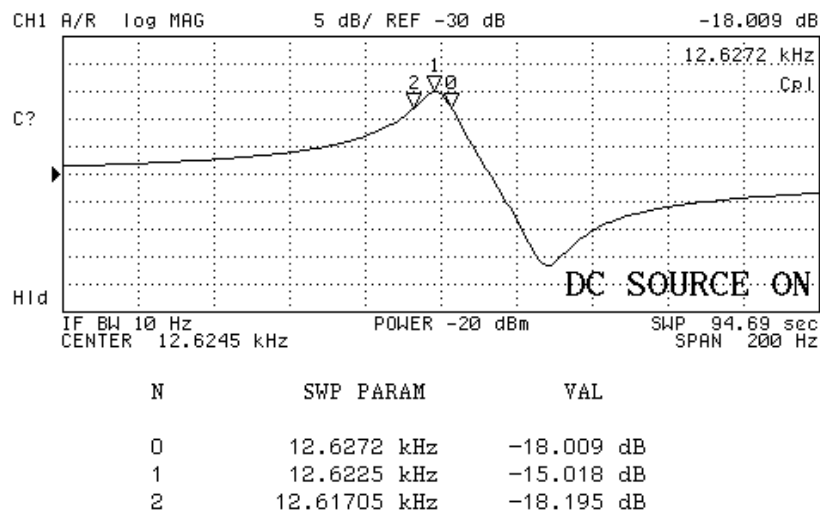


Figure 4.12: Measured drive-mode resonance characteristics of the vacuum packaged DWP gyroscope when the drive-mode output is read from the motor electrode through a transresistance amplifier with 1 M Ω feedback resistor while the proof mass voltage is set to 15 V.

After modifying the loop parameters according to the gyroscope resonance characteristics, the gyroscope is driven into oscillation by the proposed control loop. Figure 4.13 shows the measured driving signal and the drive-mode output generated by the automatic amplitude control loop when the proof mass and the amplitude set voltages are set to 15 V and 100 mV, respectively. It is observed that the frequency of the sustained oscillations is very close to the drive-mode resonance frequency. The peak level of the sustained oscillations is found as 159 mV, which seems to be inconsistent with 100 mV of amplitude set voltage at the first glance. In fact, the

proposed loop compares the DC level of the output signal to the amplitude set voltage. Since the DC level of a full-wave rectified sinusoid is $2/\pi$ of its peak level, it is verified that the system provides oscillations exactly at the desired level. Moreover, the driving signal is a sinusoidal signal, showing that VGA keeps the system poles precisely on the imaginary axis without letting any stage to saturate. It should be noted that driving the gyroscope with a sinusoidal signal is quite important since square signals generated in generic self-oscillation loops may lead to stability problems and also cause glitches due to the electrical coupling.

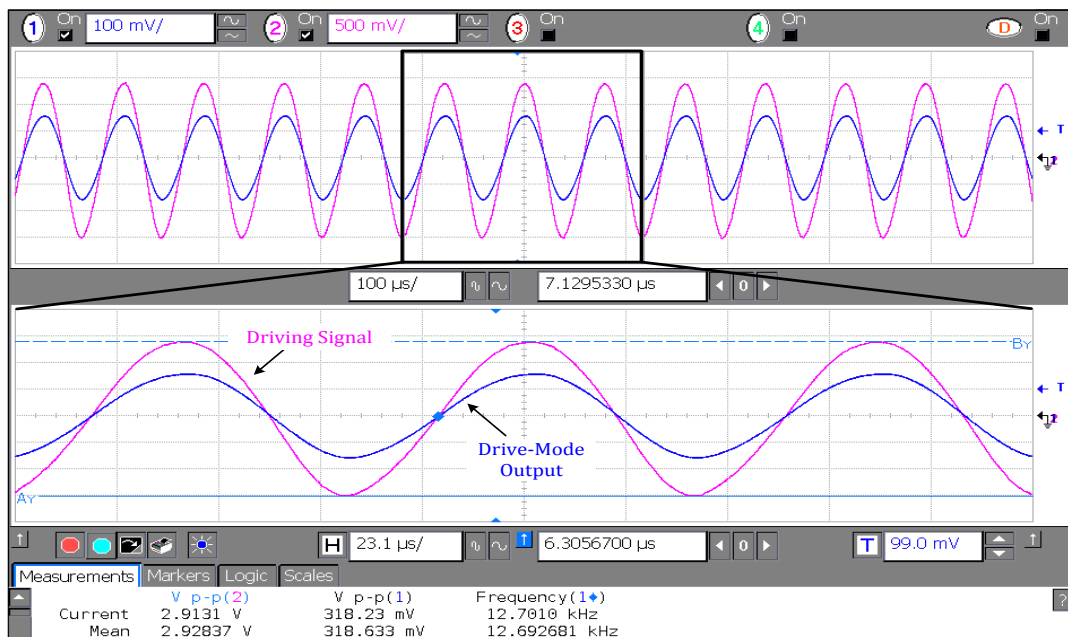
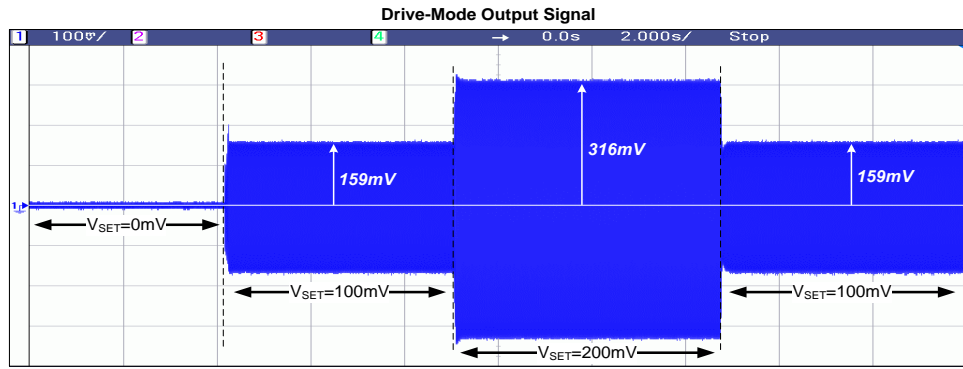
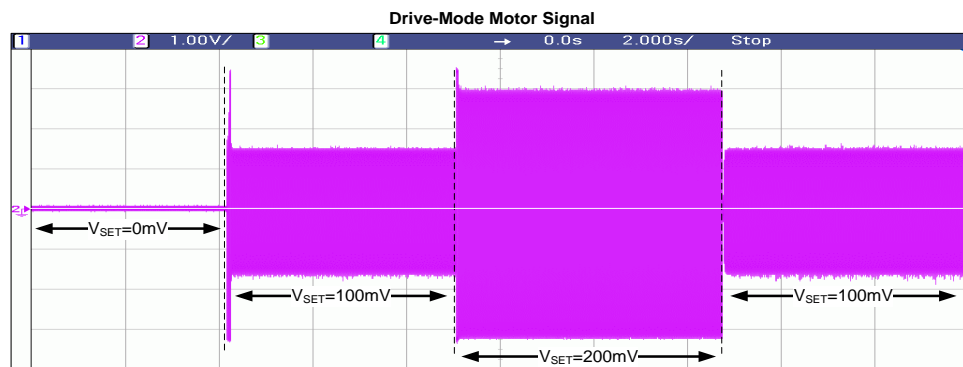


Figure 4.13: Measured driving signal and the drive-mode output generated by the automatic amplitude control loop when the proof mass and the amplitude set voltages are 15 V and 100 mV, respectively.

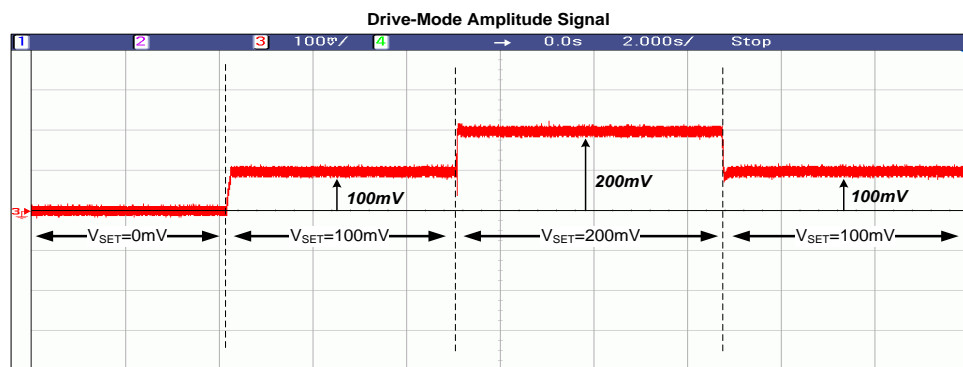
In addition to the steady-state measurements, the response of the loop to variations in system parameters should also be determined. However, typical oscilloscopes cannot catch the sudden changes when the time scale is too large. Then, “roll” mode of the Infiniium MSO6034A oscilloscope, which is a special mode that displays the signals by shifting them from right to left, is used for this purpose. Figure 4.14 shows the measured (a) drive-mode output signal, (b) motor signal, (c) amplitude signal, and (d) error signal in response to changes in the amplitude set voltage.



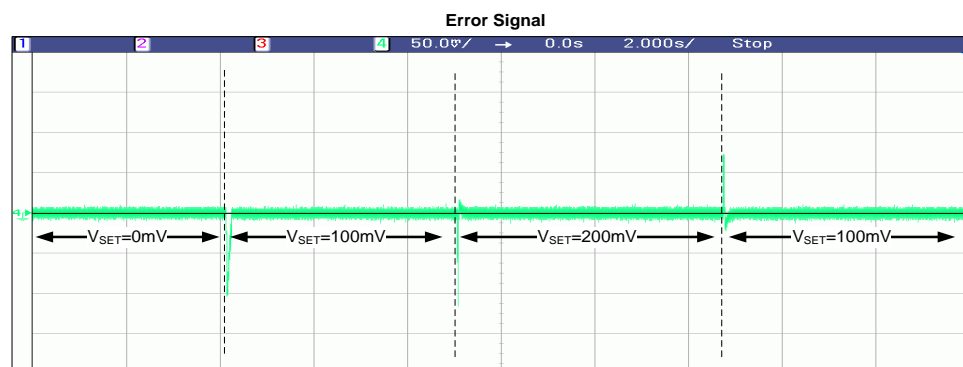
(a)



(b)



(c)



(d)

Figure 4.14: Measured (a) drive-mode output signal, (b) motor signal, (c) amplitude signal, and (d) error signal in response to changes in amplitude set voltage.

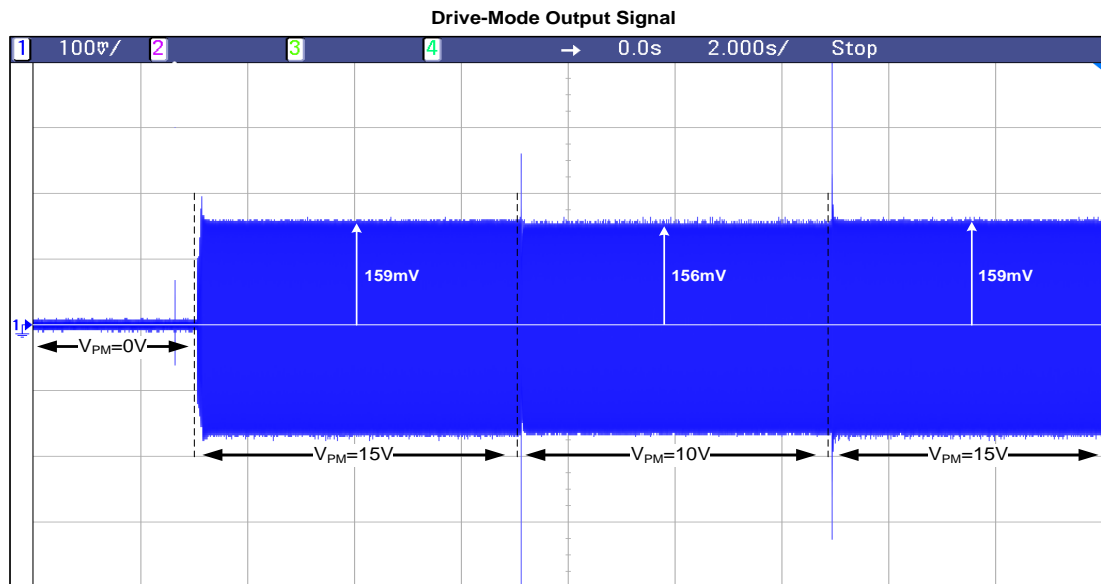
During the test, a 100 mV of amplitude set voltage is applied at the start-up, then it is increased to 200 mV, and finally set back to 100 mV again. The gyroscope output signal given in Figure 4.14(a) makes a slight overshoot due to the instantaneous change in the amplitude set voltage. This overshoot is, in fact, in tolerable ranges and consistent with the simulation results. Moreover, the error signal is always at zero-level, implying that the oscillation amplitude continuously tracks the amplitude set voltage. Therefore, it is verified that the control loop monitors the changes in the amplitude set voltage and adjusts the system gain until the oscillation amplitude stabilizes at the desired level.

Moreover, the proposed loop is also tested for the variations in the proof mass voltage. Remembering that the DC polarization voltage applied to the proof mass directly affects the sensor gain, a generic self-oscillation loop without any amplitude control mechanism gives varying oscillation amplitudes in response to changes in the proof mass voltage. On the other hand, it is expected that the proposed loop adaptively adjusts the amplitude of the driving signal in order to keep the oscillation level constant independent of the proof mass voltage.

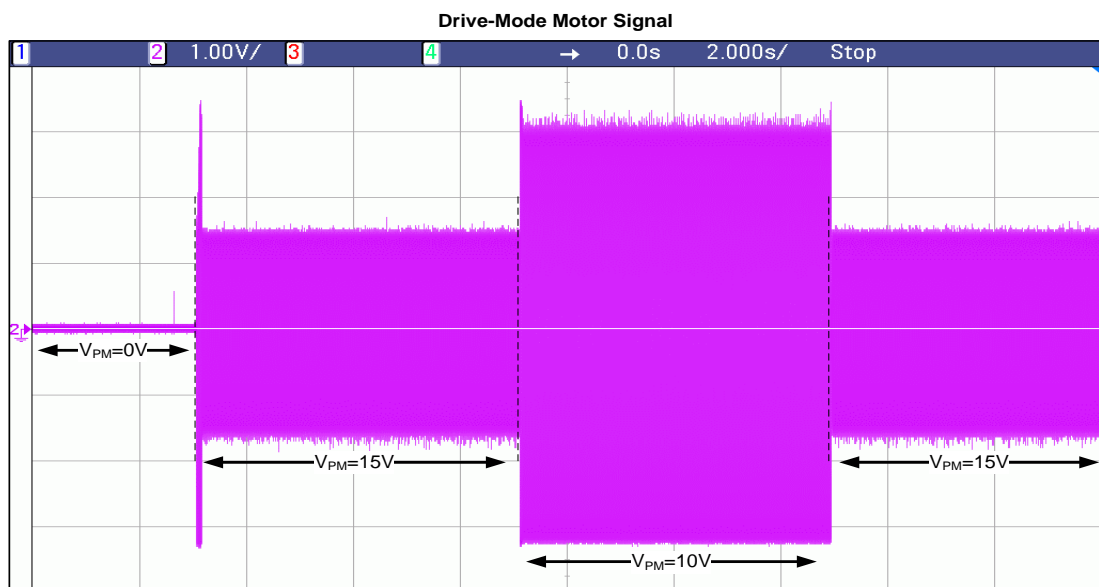
Figure 4.15 shows the measured drive-mode (a) output signal, and (b) motor signal when the proof mass voltage is instantaneously changed during the simulation. When the proof mass voltage is decreased from 15 V to 10 V, gain of the sensor also decreases. Then, the loop senses the sudden decrease in the sensor gain and automatically increases the VGA gain. The resultant increase in the motor signal can be clearly seen in Figure 4.15(b). Oppositely, when the proof mass voltage is increased, the control loop again adjusts the amplitude of the driving signal.

It is verified that the amplitude controlled differential self-resonance loop operates properly. Nevertheless, a problem associated with the sense-mode of the DWP gyroscope prototype is observed. Because of the thermal stress that appears during the wafer bonding of the silicon wafer to the glass wafer in the fabrication process, the gyroscope is stretched and the distance between the outermost sense fingers gets closer from the design value of 1 μm . Thus, when the proof mass voltage is applied to the sensor, electrical shorts occur between the moving and the stationary sense

electrodes, causing permanent damages in the interface electronics and the sensor itself. Solutions for this sensor fabrication problem are still under investigation. After solving this problem, it is expected that DWP gyroscopes demonstrate tactical-grade performances with the help of advanced electronics designed throughout this research.



(a)



(b)

Figure 4.15: Measured drive-mode (a) output signal, and (b) motor signal when the proof mass voltage is instantaneously changed during the simulation.

Then, the same circuit is tested with SOI gyroscopes having differential drive and sense mode electrodes [51]. First, it is verified that the amplitude control loop sustains constant amplitude oscillations by differentially driving the gyroscope at its mechanical resonance frequency. After that, performance tests are done for overall angular rate system operated in 5 mTorr vacuum level. Figure 4.16 shows the measured output response of the angular rate system when the applied angular rate is swept from zero rate to ± 50 deg/sec with 5 deg/sec steps.

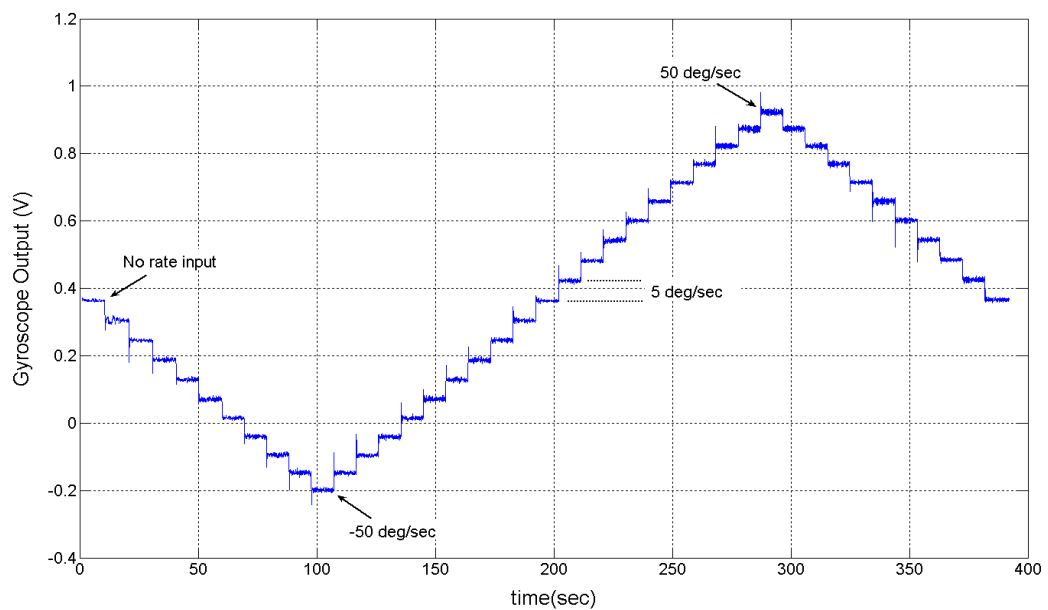


Figure 4.16: Measured output response of the angular rate system when the applied angular rate is swept from zero rate to ± 50 deg/sec with 5 deg/sec steps.

Figure 4.17 shows the measured response curve giving the scale factor, the zero-rate offset, and the nonlinearity of the overall system. The scale-factor of the angular rate sensor is measured as 11.4 mV/(deg/sec) with 0.03% nonlinearity and 363.5 mV zero-rate output. Then, the output of the gyroscope is sampled with the Agilent multimeter and HPVEE software. Figure 4.18 shows the Allan variance plot generated by the drift data collected for two hours. The bias instability and angle random walk values are measured as 102.4 deg/hr and 2.19 deg/ $\sqrt{\text{hr}}$, respectively, where the system bandwidth is 100 Hz, which is limited by the third-order LPF in the sense-mode demodulator stage.

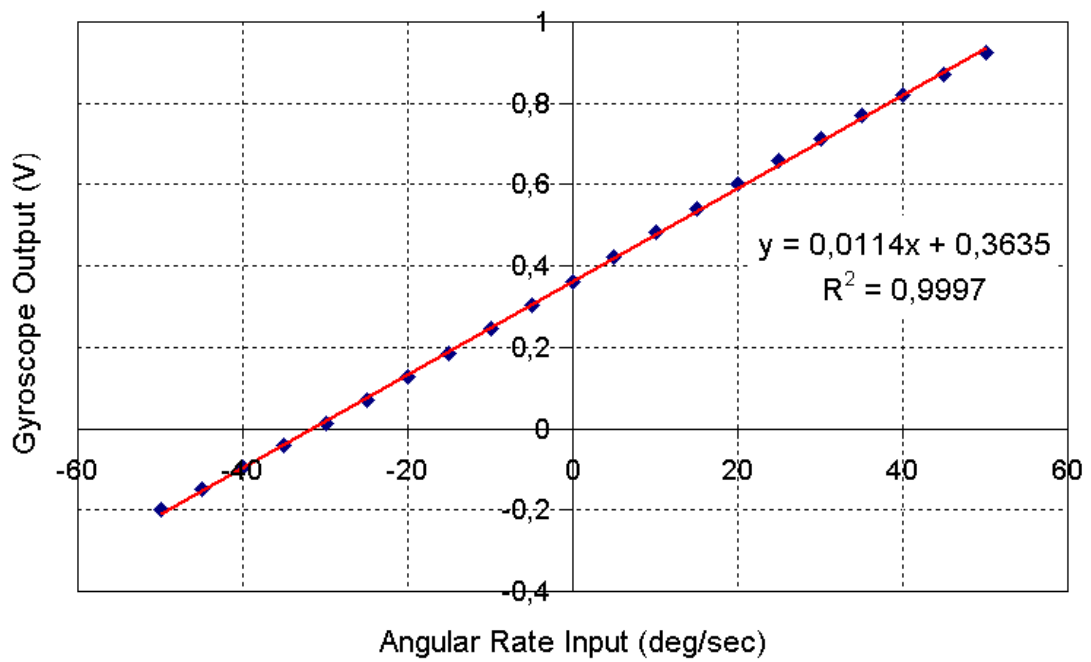


Figure 4.17: Measured response curve giving the scale factor, the zero-rate offset, and the nonlinearity of the overall system.

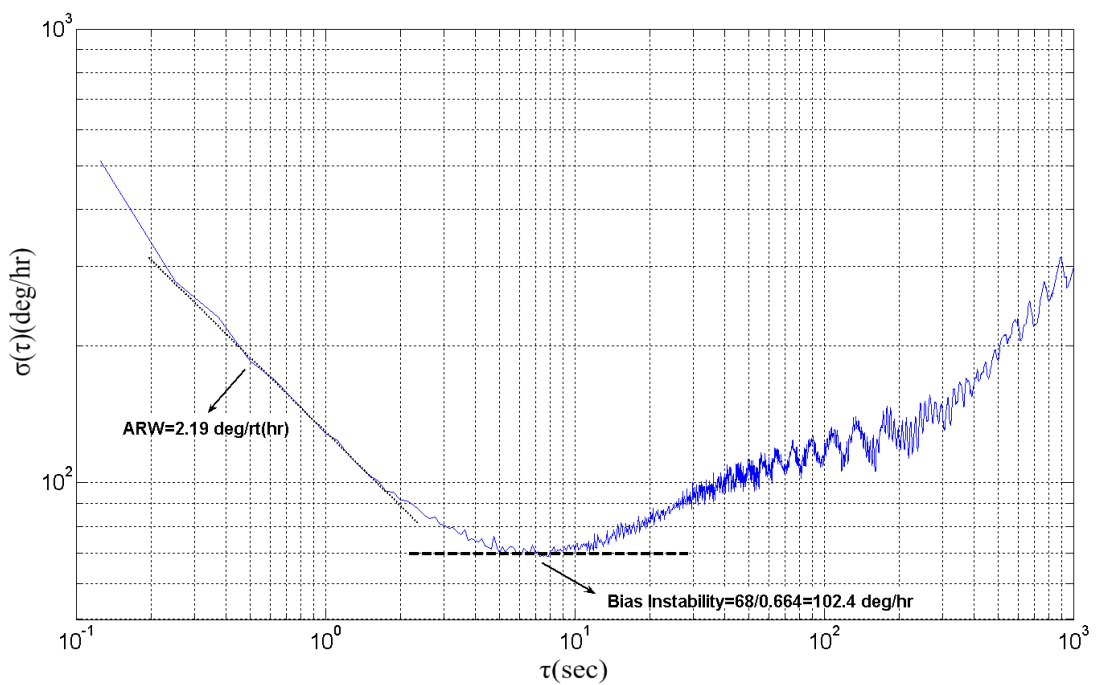


Figure 4.18: Allan variance plot generated by the drift data collected for two hours.

The angular rate system employing the SOI gyroscope and the differential drive and sense mode electronics designed in this research demonstrates the best performance obtained in SOI gyroscopes developed at METU.

4.2. Test Results of the CMOS Electronics

In this section, results of the characterization tests performed on the CMOS electronics are presented. First, CMOS resistive and capacitive interfaces are characterized with AC, transient, and noise tests, where the design details and post-layout transistor-level simulations of these interfaces are given in Section 3.2. Then, the test results of the drive-mode control electronics, including the single-ended to differential converter and the fully-differential automatic amplitude control circuit are presented. The design details of these circuits are available in Section 3.3. Finally, results of the transient tests performed on the fully-differential open loop rate sensing electronics explained in Section 3.4 are demonstrated.

4.2.1. Characterization of UGB Type Interfaces

UGB type interfaces fabricated in 0.6 μ m standard CMOS process are wire-bonded to a 24-pin ceramic package for the characterization tests. Figure 4.19 shows the photographs of the CMOS UGB type resistive and capacitive interfaces wire-bonded to the ceramic package. Figure 4.20 shows the block diagram of the test setup used in the transient tests of the differential UGB type resistive and capacitive interfaces. In this setup, exactly anti-phase differential signals are generated by a single-ended to differential convertor circuit implemented with discrete components. External coupling capacitors are connected between outputs of the convertor and inputs of the interface circuits in order to prevent the convertor to DC-bias the input nodes of the UGB. Thus, biasing effect of polysilicon resistors in resistive interfaces and subthreshold MOSFETs in capacitive interfaces can be observed. Moreover, AC tests providing gain and phase characteristics of the interfaces are performed by the network analyzer (Agilent 4395A) with a similar test setup given in Figure 4.20.

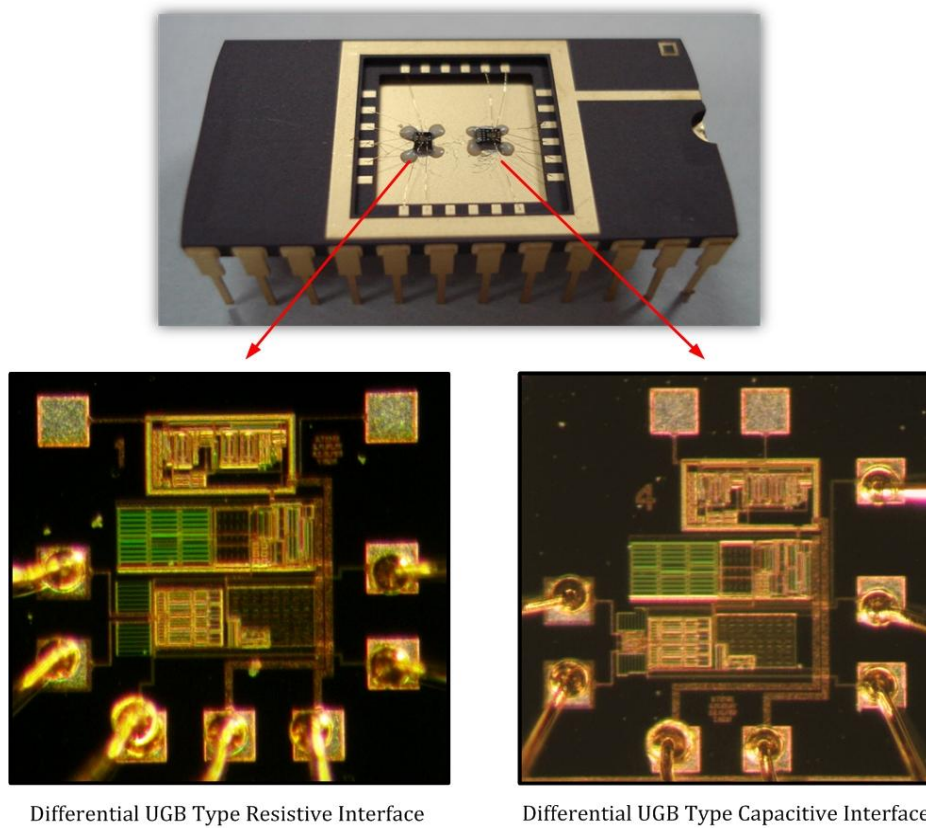


Figure 4.19: Photographs of the CMOS UGB type resistive and capacitive interfaces wire-bonded to the ceramic package.

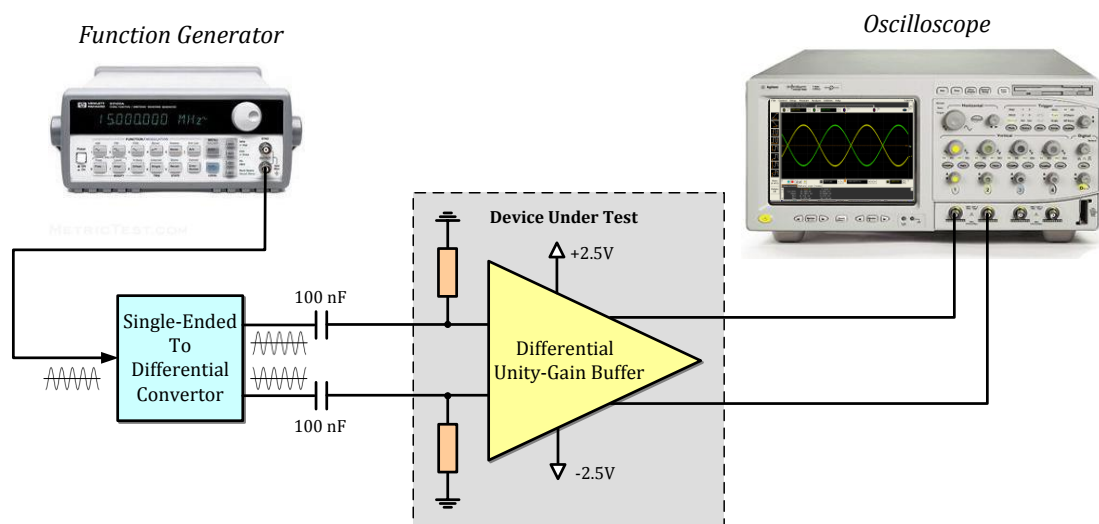


Figure 4.20: Block diagram of the test setup used in the transient tests of the differential UGB type resistive and capacitive interfaces.

Figure 4.21 shows the block diagram of the test setup used in the noise tests of the UGB type resistive and capacitive interfaces. The output noise generated by the interface circuit is DC-filtered and amplified through cascaded AC coupler and gain stages. Then, the spectrum of the resultant signal is plotted by a dynamic signal analyzer (Agilent 35670A). It should be noted that, input terminals of the interfaces are kept floating during the tests in order to let the biasing mechanisms to DC-bias the high-impedance nodes to ground potential.

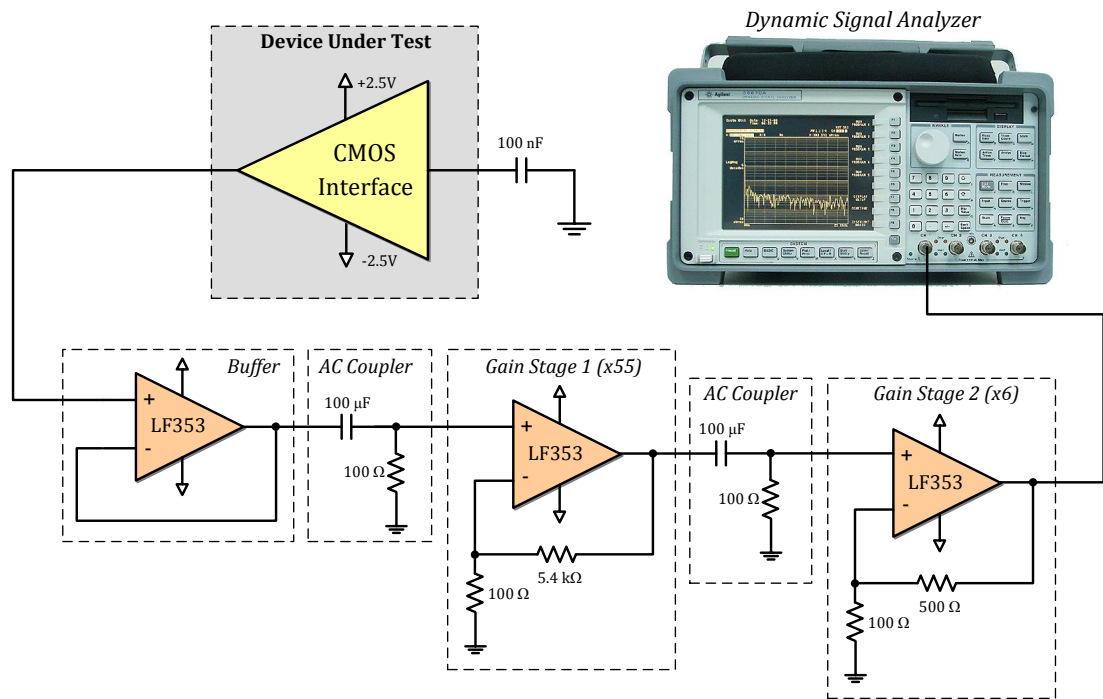


Figure 4.21: Block diagram of the test setup used in the noise tests of the UGB type resistive and capacitive interfaces.

4.2.1.1. UGB type Resistive Interface

The UGB type resistive interface is composed of a differential UGB and 200 k Ω of high-impedance node biasing resistors implemented with low-doped polysilicon. The resistance values of the high-impedance node biasing resistors are measured as 216 k Ω , showing almost 10% deviation from the designed value due to process

variations. On the other hand, it is measured that both differential resistors have exactly the same value owing to the fully-symmetric layout design.

Figure 4.22 shows the measured differential signals at the high-impedance nodes and differential outputs of the UGB type resistive interface when sinusoidal signals having $1 V_{p-p}$ amplitude and 500 mV offset are applied through coupling capacitors. Since the effective impedance of the oscilloscope probe disturbs the biasing, the high-impedance nodes are measured through external buffers. It is observed that the high-impedance node biasing resistors properly DC-bias the high-impedance nodes to the ground potential. However, there is an unexpected offset at the differential outputs of the UGB. Remembering the result of post-layout Monte Carlo simulation for the process variations and the transistor mismatches, the output offset should be within ± 3 mV range. This large difference between the simulated and the measured offset values implies that the process variations and the transistor mismatches are not properly modeled by the CMOS foundry.

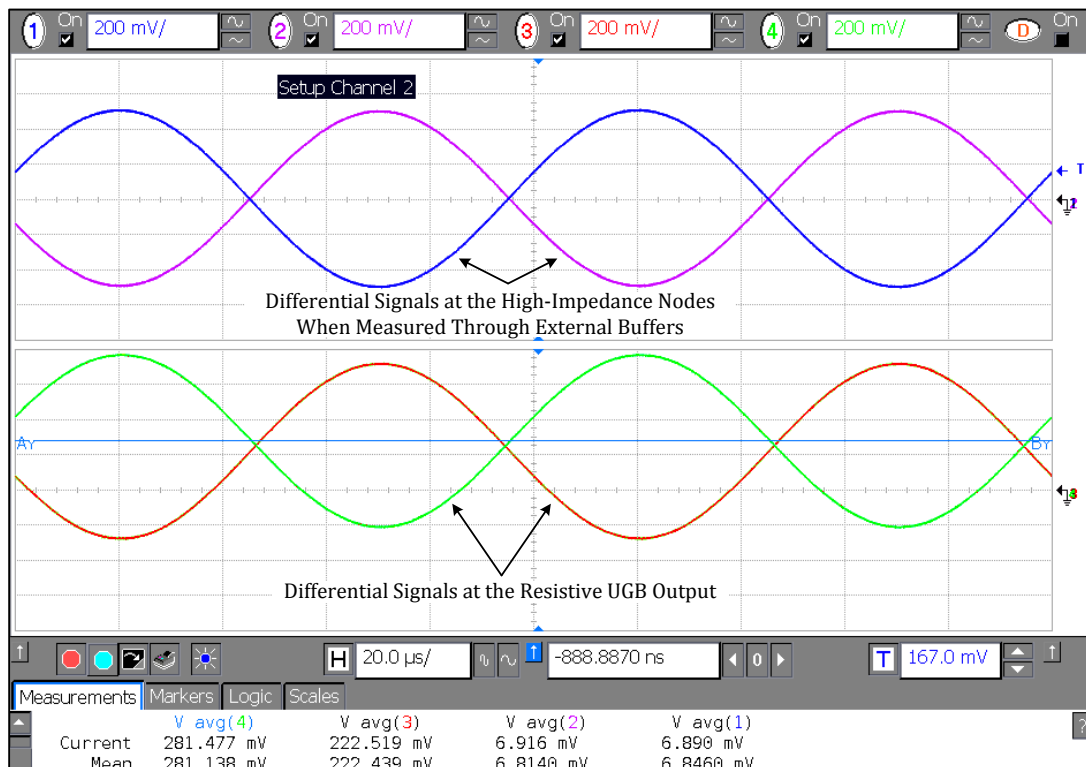


Figure 4.22: Measured differential signals at the high-impedance nodes and differential outputs of the UGB type resistive interface when sinusoidal signals having $1 V_{p-p}$ amplitude and 500 mV offset are applied through coupling capacitors.

Figure 4.23 shows the measured gain and phase characteristics of the differential UGB type resistive interface for the (a) first branch, and the (b) second branch. It is seen that both branches give almost the same gain and phase responses. Gain of the buffer is measured to be 0.96, while the introduced phase error is around -0.66° , which are both very close to the simulated values.

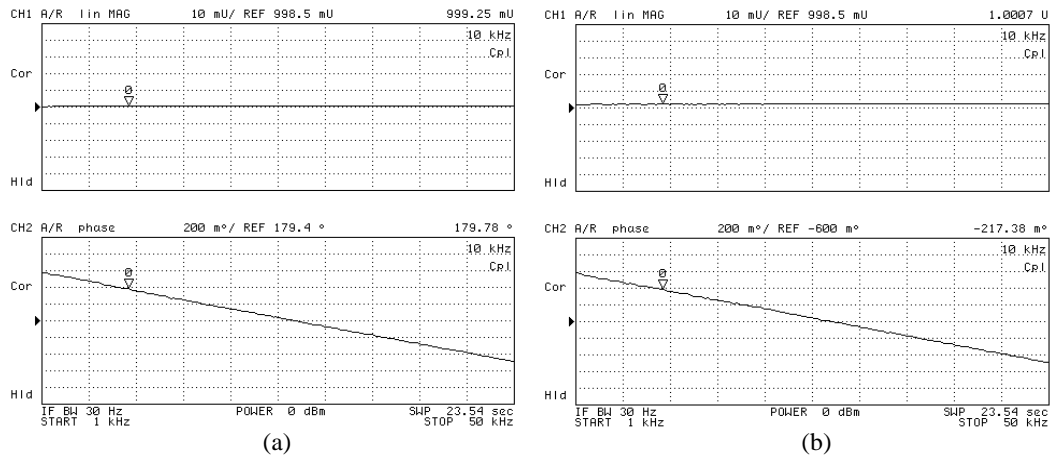


Figure 4.23: Measured gain and phase characteristics of the differential UGB type resistive interface for the (a) first branch, and the (b) second branch.

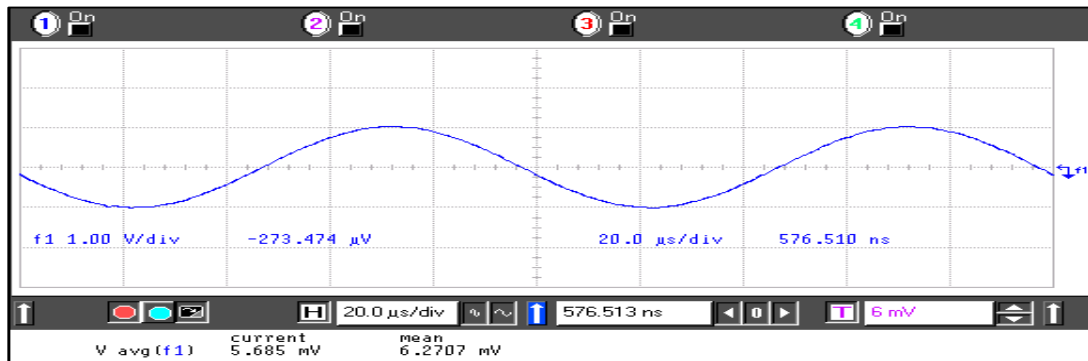


Figure 4.24: Difference of the differential output nodes of the UGB type resistive interface, illustrating that the output offset is cancelled out after the subtraction operation.

In order to observe the deviation of test results from die to die, same tests are performed for a number of UGB type resistive interface chips. Although tested chips demonstrate very similar gain and phase characteristics, it is observed that the offset

values vary for different chips. On the other hand, majority of the differential UGB circuits give almost the same offset values for each differential branch, implying that the offset can be cancelled out after the subtraction operation. Figure 4.24 shows the difference of the differential output nodes of the UGB type resistive interface, illustrating that the output offset is cancelled out after the subtraction operation.

Figure 4.25 shows the measured noise characteristics of the differential UGB type resistive interface for both differential branches. It is clearly seen that both branches give almost the same noise characteristics. The level of the thermal noise is found as $60 \text{ nV}/\sqrt{\text{Hz}}$, which is very close to the simulated value, $58 \text{ nV}/\sqrt{\text{Hz}}$.

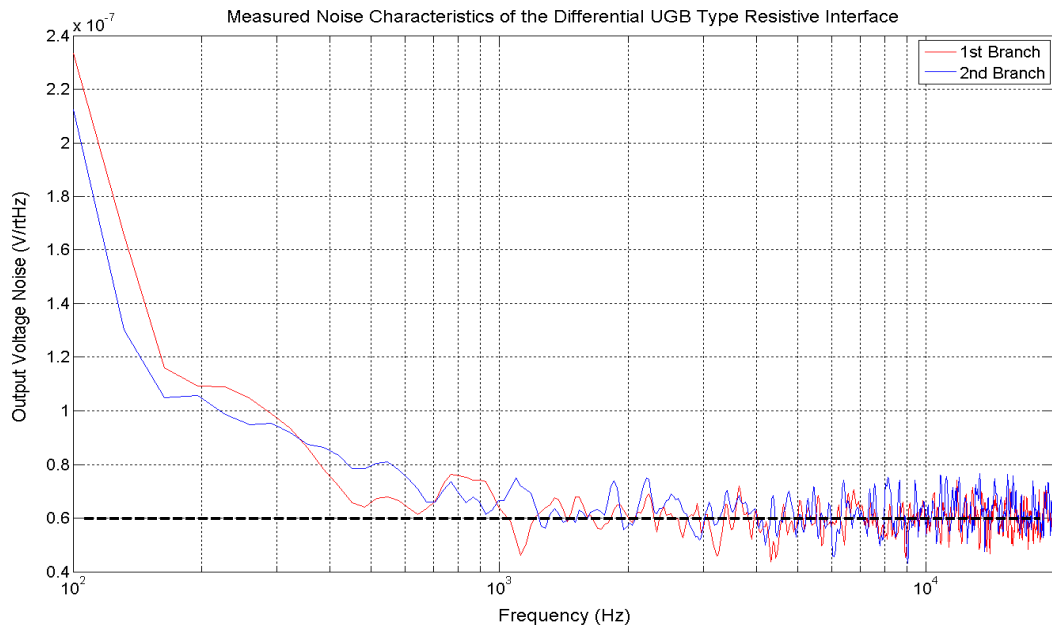


Figure 4.25: Measured noise characteristics of the differential UGB type resistive interface for both differential branches.

According to the characterization tests performed on the UGB type resistive interfaces, it is concluded that the fabricated chips demonstrate consistent performance values with the transistor-level simulations, except the unpredictable offset at the differential output nodes. Although this offset can be cancelled out by a differential to single-ended conversion operation or by employing AC couplers at the output nodes, the cause of this offset is still under detailed investigation.

4.2.1.2. UGB Type Capacitive Interface

UGB Type capacitive interface employs an NMOS-PMOS transistor pair operating in subthreshold region for realizing sufficiently large channel resistance to DC-bias the high-impedance nodes. Figure 4.26 shows the measured transient response of the differential outputs of the UGB type capacitive interface when $\pm 500\text{ mV}$ of step functions are applied to the differential inputs of the interface through 10 nF coupling capacitors. It is seen that the biasing mechanism properly biases the differential high-impedance nodes to the ground potential. From the simple RC time-constant calculation, the effective resistances of two NMOS-PMOS transistor pairs biasing each differential high-impedance node are found as $2.48\text{ G}\Omega$ and $2.56\text{ G}\Omega$. These values are larger than the simulated ones since the channel resistance of a subthreshold transistor highly depends on the process parameters. On the other hand, the measured values are still good enough for the high-impedance node biasing without causing significant decrease in the response speed.

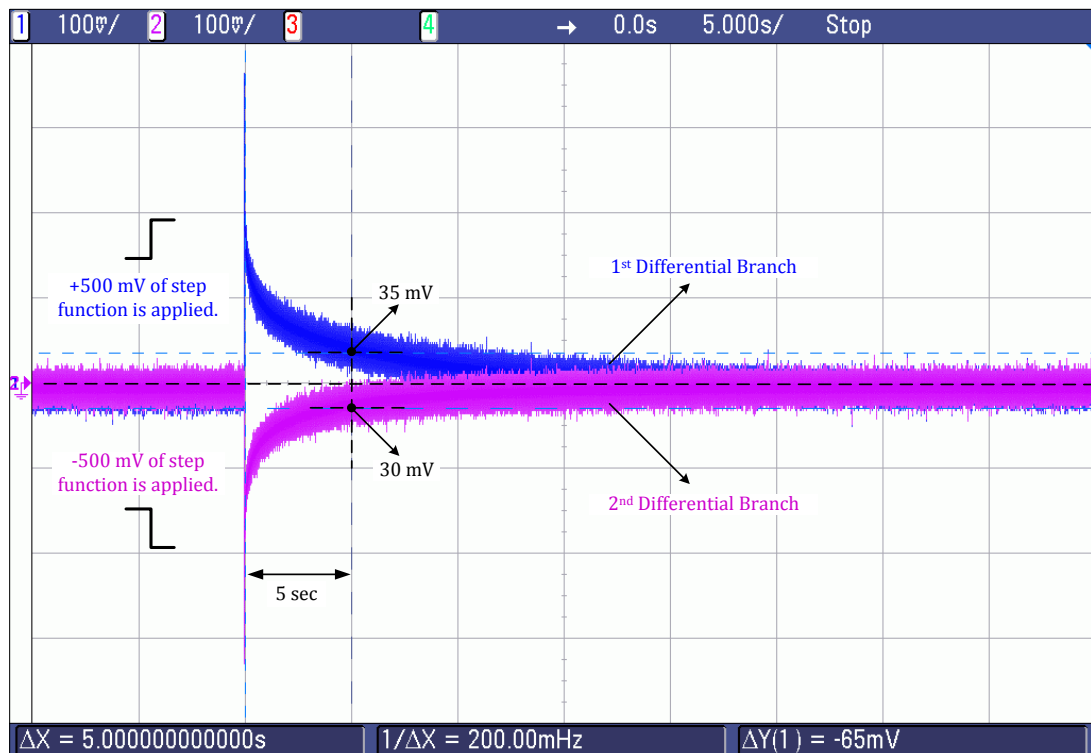


Figure 4.26: Measured transient response of the differential outputs of the UGB type capacitive interface when $\pm 500\text{ mV}$ of step functions are applied to the differential inputs of the interface through 10 nF coupling capacitors.

Figure 4.27 shows the measured differential signals at the capacitive UGB output when differential sinusoidal signals having 1 V_{p-p} amplitude and 500 mV offset are applied through coupling capacitors. The output offset values introduced by the capacitive interface are consistent with the expected values, and both branches have almost the same offset. On the other hand, as in the case of UGB type resistive interfaces, the offset at the UGB type capacitive interface output show variations from chip to chip.

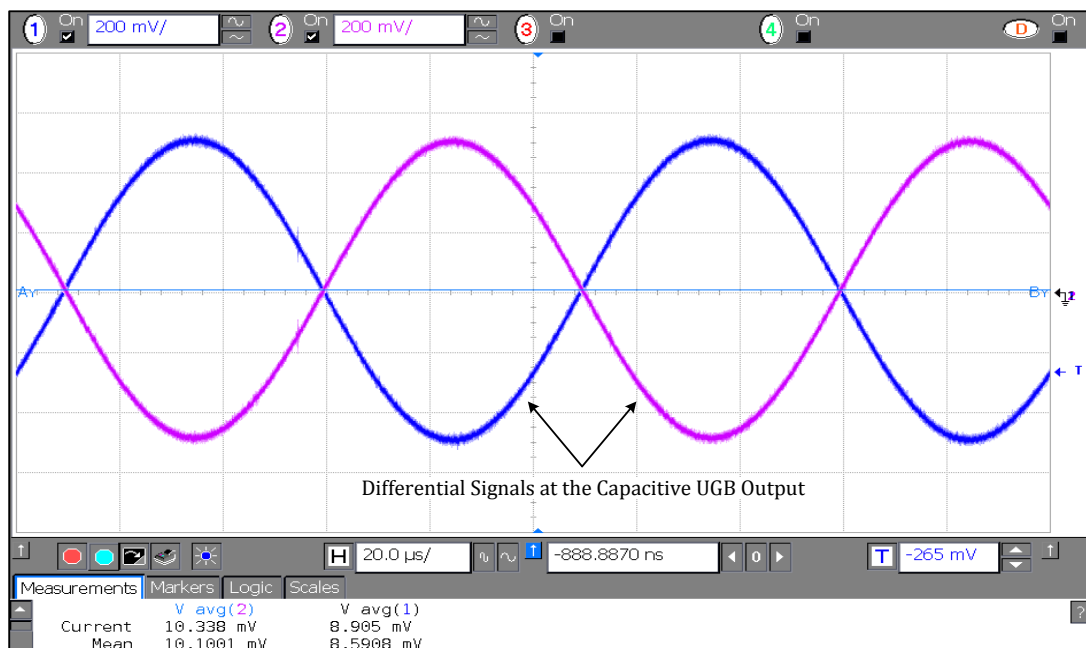


Figure 4.27: Measured differential signals at the capacitive UGB output when differential sinusoidal signals having 1 V_{p-p} amplitude and 500 mV offset are applied through coupling capacitors.

Figure 4.28 shows the measured noise characteristics of the differential UGB type capacitive interface for both differential branches. It is observed that both branches demonstrate very similar noise characteristics. The level of the output thermal noise is calculated as $62\text{ nV}/\sqrt{\text{Hz}}$, which is quite higher than the simulated value. The possible reason for this difference is that the CADENCE model of the transistor noise is not good enough to fully-model the subthreshold effects.

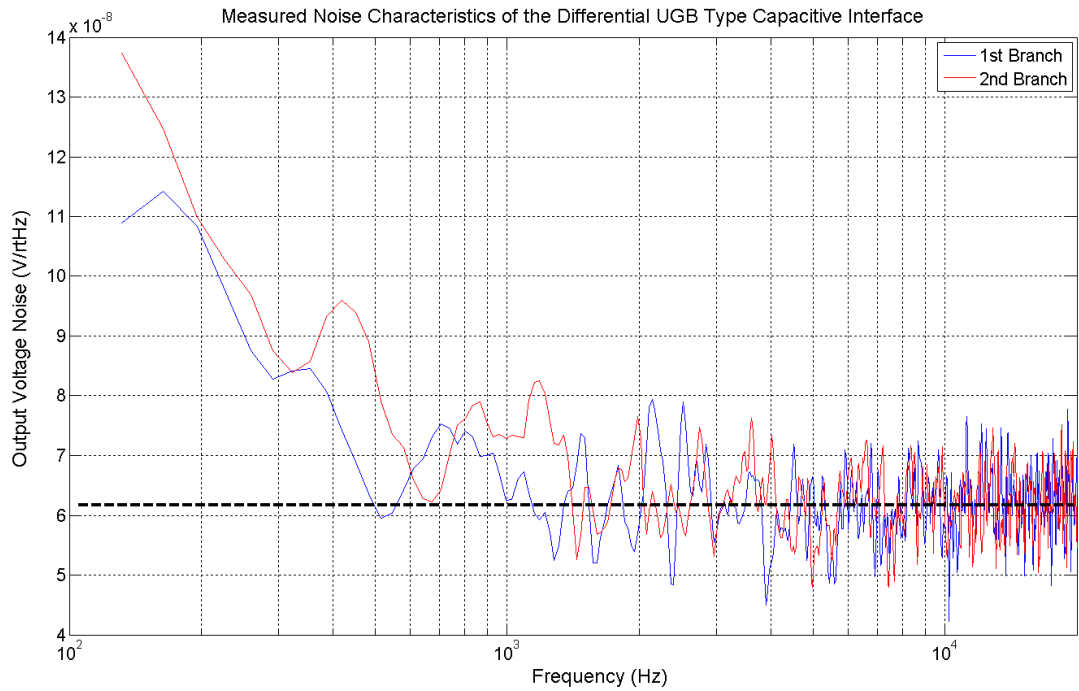


Figure 4.28: Measured noise characteristics of the differential UGB type capacitive interface for both differential branches.

Like UGB type resistive interfaces, the capacitive ones also demonstrate almost unity gain with phase error less than 1° according to the gain and phase characteristics measured by the network analyzer. Thus, it is verified that the proposed UGB type capacitive interfaces can be used in high-performance angular rate sensor systems as long as the offset problem is solved.

4.2.2. Characterization of TIA Type Resistive and Capacitive Interfaces

For the preliminary characterization tests, the differential TIA type interface chip including both the resistive interface for the drive-mode and the capacitive interface for the sense-mode is wire-bonded to a 24-pin ceramic package. Figure 4.29 shows the photograph of the differential TIA type capacitive and resistive interface chip wire-bonded to a ceramic package.

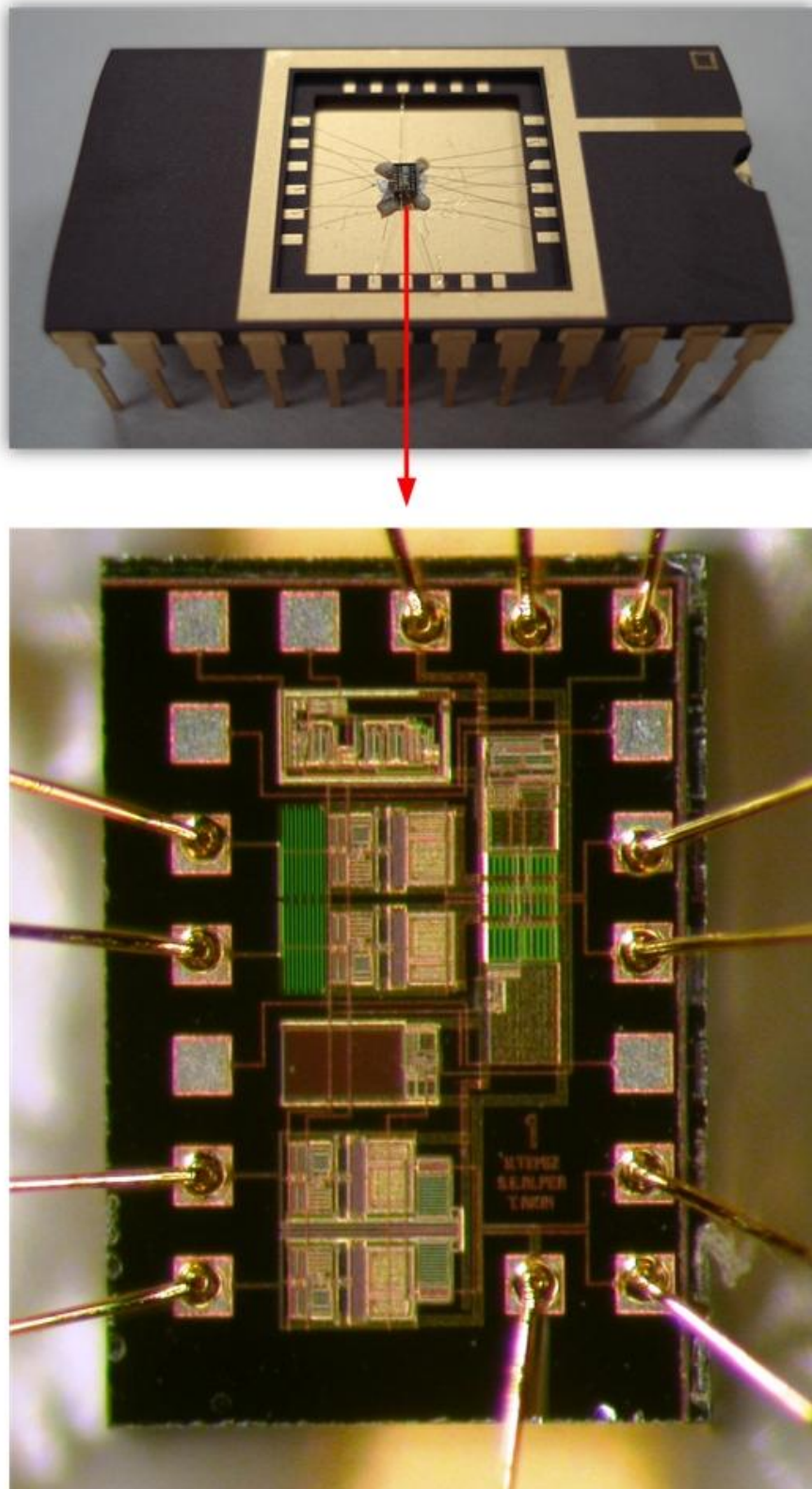


Figure 4.29: Photograph of the differential TIA type capacitive and resistive interface chip wire-bonded to a ceramic package.

Due to the absence of a current source supplying sinusoidal currents, the TIA type interfaces are tested by connecting external resistors in order to convert the TIA to an inverting voltage amplifier. Thus, the transient tests can be performed by simply applying sinusoidal voltages. Figure 4.30 shows the block diagram of the test setup used in the transient tests of the differential TIA type resistive and capacitive interfaces.

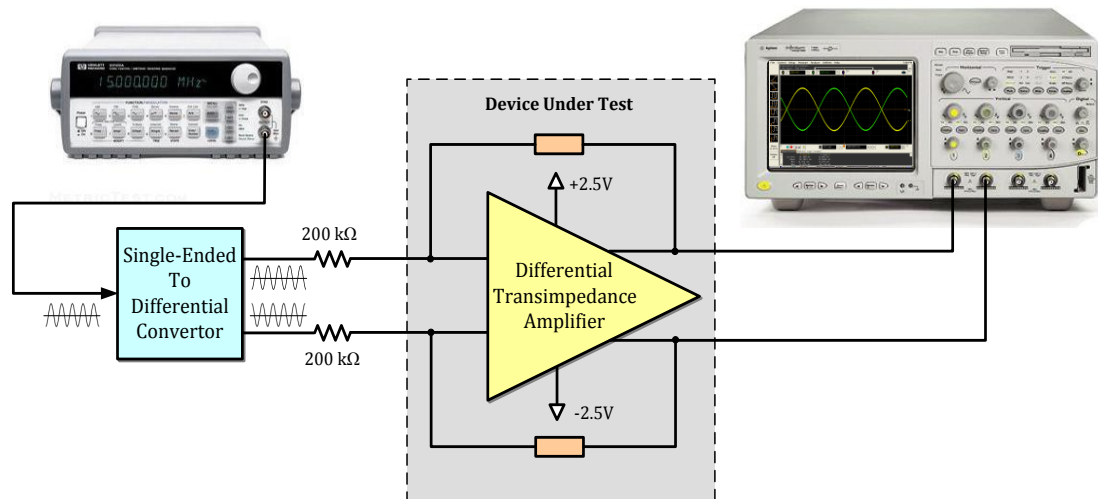


Figure 4.30: Block diagram of the test setup used in the transient tests of the differential TIA type resistive and capacitive interfaces.

4.2.2.1. TIA Type Resistive Interface

The TIA type resistive interface includes a feedback-connected OPAMP, where the feedback resistor designed to have 1 MΩ resistance. Then, current to voltage conversion is achieved on this resistor, ideally introducing 0° phase error. Feedback resistors in the fabricated chips are measured as 1.086 MΩ, showing a small difference from the designed value. Moreover, both feedback resistors in the differential branches have exactly the same value thanks to the compact and fully-symmetric layout design.

Figure 4.31 shows the measured transient response of the TIA type resistive interface when differential signals with $200\text{ mV}_{\text{p-p}}$ amplitude are applied through $200\text{ k}\Omega$ resistors. The circuit seems to have unequal and non-zero offset values at the differential outputs; however, this is completely due to the non-zero offset introduced by the applied differential signals. Thus, it is concluded that the feedback resistor properly DC-biases the OPAMP output to ground potential. It is also verified that the output offset is in tolerable ranges and consistent with the simulations.

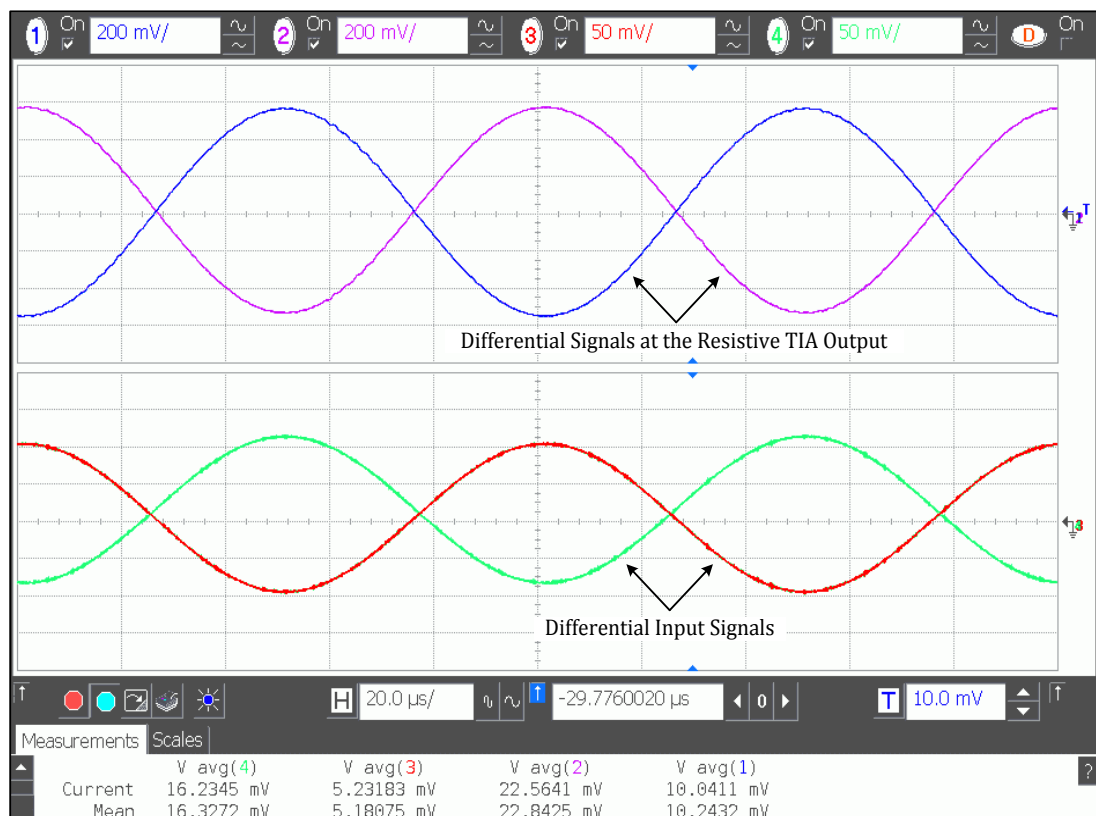


Figure 4.31: Measured transient response of the TIA type resistive interface when differential signals with $200\text{ mV}_{\text{p-p}}$ amplitude are applied through $200\text{ k}\Omega$ resistors.

Figure 4.32 shows the gain and phase characteristics of the TIA type resistive interface when the input signal is applied through a $200\text{ k}\Omega$ resistor. The gain is measured as 5.44, which corresponds to $1.088\text{ M}\Omega$ of feedback resistance, for a sufficiently large bandwidth. The phase error introduced by the circuit is only -0.7° at 10 kHz .

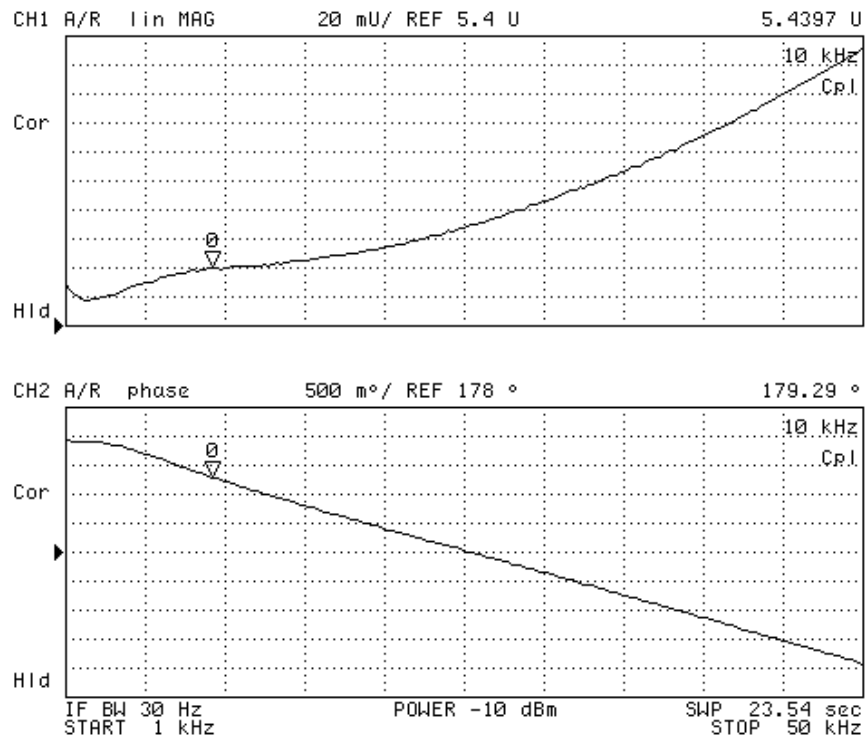


Figure 4.32: Gain and phase characteristics of the TIA type resistive interface when the input signal is applied through a 200 k Ω resistor.

Although the interface demonstrates very satisfactory results in transient and AC tests, an unexpected problem is observed. The fabricated differential interface is concluded to be very sensitive to the mismatches at the input nodes. For instance, even a small mismatch in the external 200 k Ω resistors may lead to instability at the differential outputs of the interface. On the other hand, it is expected that when the interfaces are connected to the dual-mass differential gyroscopes, which are currently in fabrication process, instability would not be a problem owing to full-symmetric structures of these gyroscopes.

4.2.2.2. TIA Type Capacitive Interface

The differential TIA type capacitive interface is composed of two OPAMPs having controlled-impedance FET biasing mechanisms to DC-bias the output nodes of the

interface. The effective resistance of the biasing mechanism is designed to be $1.2 \text{ G}\Omega$ in order to satisfy the capacitive interface condition. The current pumped by the gyroscope is then converted to voltage on the 2 pF capacitor feedback-connected to the OPAMP. In the transient tests, it is observed that the controlled-impedance FET biasing mechanism cannot properly bias the output node of the OPAMP. Thus, a dominant 50 Hz signal appears at the differential outputs of the interface, disturbing the regular operation.

In order to find the reason of the biasing problem, a test chip having the similar biasing mechanism with the TIA type capacitive interface is tested. This chip is a TIA type resistive interface where the feedback resistance is realized by a controlled-impedance FET having $1 \text{ M}\Omega$ of channel resistance. Figure 4.33 shows the output response of the test chip, when the $20 \text{ mV}_{\text{p-p}}$ input signal is applied by the function generator through a $200 \text{ k}\Omega$ resistor. It is verified that the FET biases the OPAMP output to a DC potential. The output signal has an amplitude of $170 \text{ mV}_{\text{p-p}}$, implying that the effective channel resistance is $1.7 \text{ M}\Omega$. This shows that the channel resistance is larger than the designed value due to process tolerances.

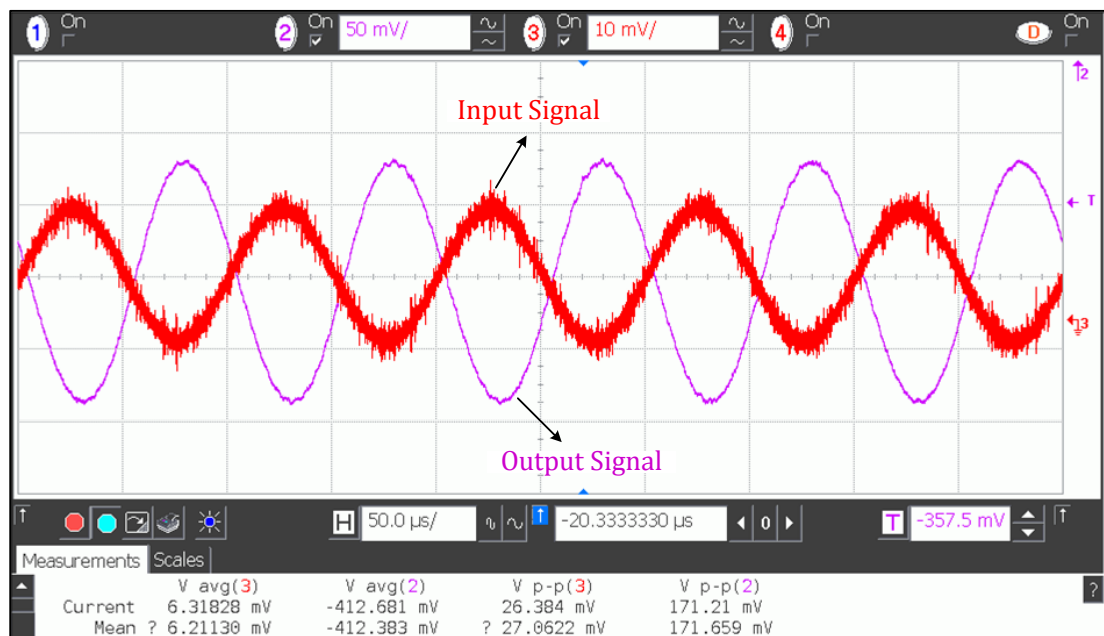


Figure 4.33: Output response of the test chip, when the $20 \text{ mV}_{\text{p-p}}$ input signal is applied by the function generator through a $200 \text{ k}\Omega$ resistor.

It is then concluded that the channel resistance of the biasing MOSFET in the fabricated TIA type capacitive interface is much larger than the designed value since the channel resistance of the MOSFET operating in its subthreshold region highly depends on the threshold voltage. Therefore, such large resistance cannot DC-bias the output of the OPAMP. For the future studies, biasing mechanisms having less dependency on process parameters should be developed.

4.2.3. Test Results of CMOS Fully-Differential Control Electronics

In this section, results of the tests performed on the CMOS single-ended to differential convertor and the fully-differential self-resonance excitation circuit with automatic amplitude control are presented.

4.2.3.1. Single-ended to Differential Convertor

This circuit aims to convert the single-ended driving signal generated by the external drive-mode electronics to differential signals for sustaining balanced and stable drive-mode vibrations. The proposed circuit is combined with TIA type resistive and capacitive interfaces on a single chip. Figure 4.34 shows photographs of the differential readout electronics and the single-ended to differential convertor wire-bonded to a 24-pin ceramic package. This single chip is an interconnection between the differential DWP gyroscope and the single-ended discrete signal processing electronics. Thus, all drive and sense mode signals connected to the gyroscope are differential while the signals associated with the external electronics are single-ended.

Figure 4.35 shows the measured differential output signals generated by the single-ended to differential convertor, when a $500 \text{ mV}_{\text{p-p}}$ sinusoidal signal is applied by the function generator. It is observed that the convertor properly generates differential signals with output offsets consistent with the expected values.

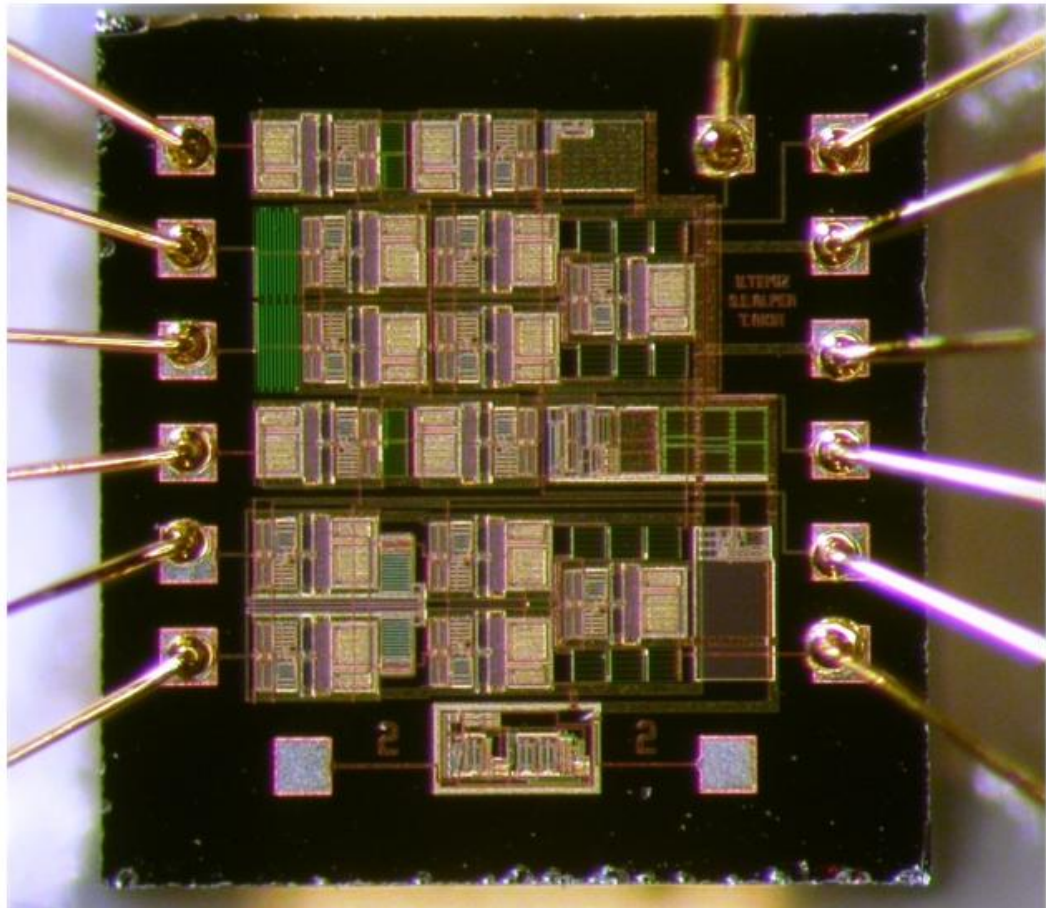
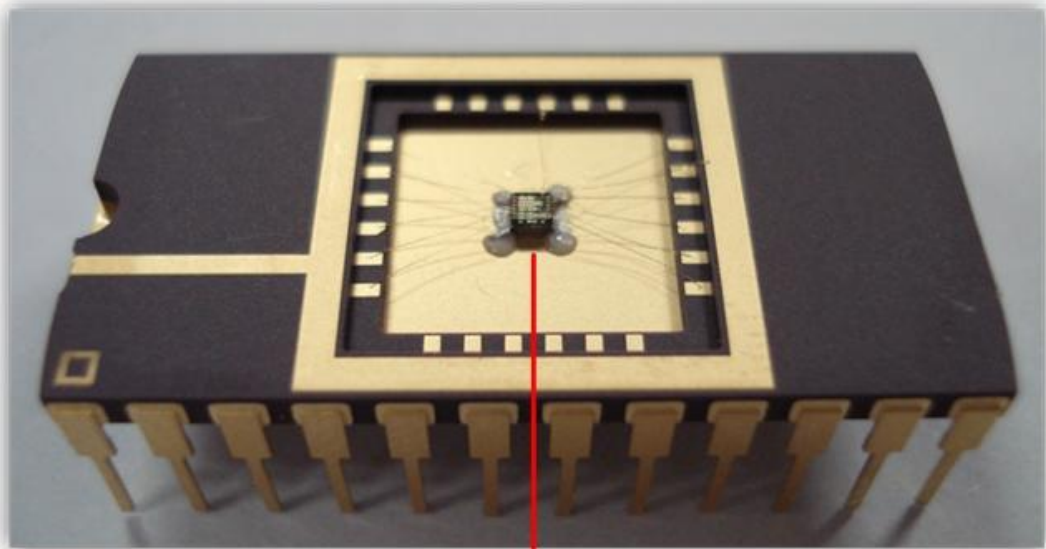


Figure 4.34: Photographs of the differential readout electronics and the single-ended to differential convertor wire-bonded to a 24-pin ceramic package.

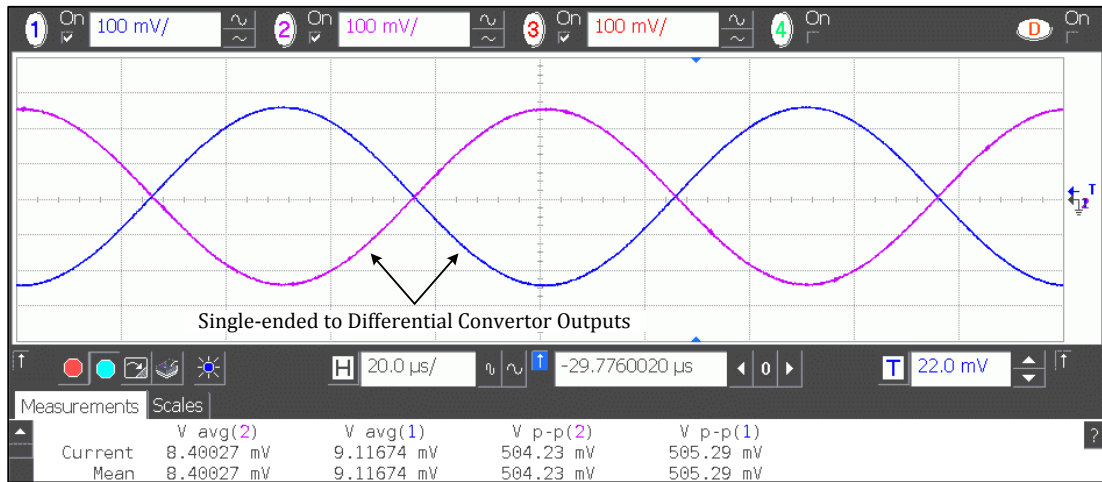


Figure 4.35: Measured differential output signals generated by the single-ended to differential convertor, when a 500 mV_{p-p} sinusoidal signal is applied by the function generator.

The most important issue in the single-ended to differential conversion is the phase error. Figure 4.36 shows the measured gain and phase characteristics of the single-ended to differential convertor for the inverting and the non-inverting outputs. Voltage gains introduced by each branch are measured to be unity. Moreover, phase errors are -220 mdeg and -217 mdeg for the inverting and the non-inverting outputs, respectively. This implies that the convertor generates almost exactly anti-phase differential signals.

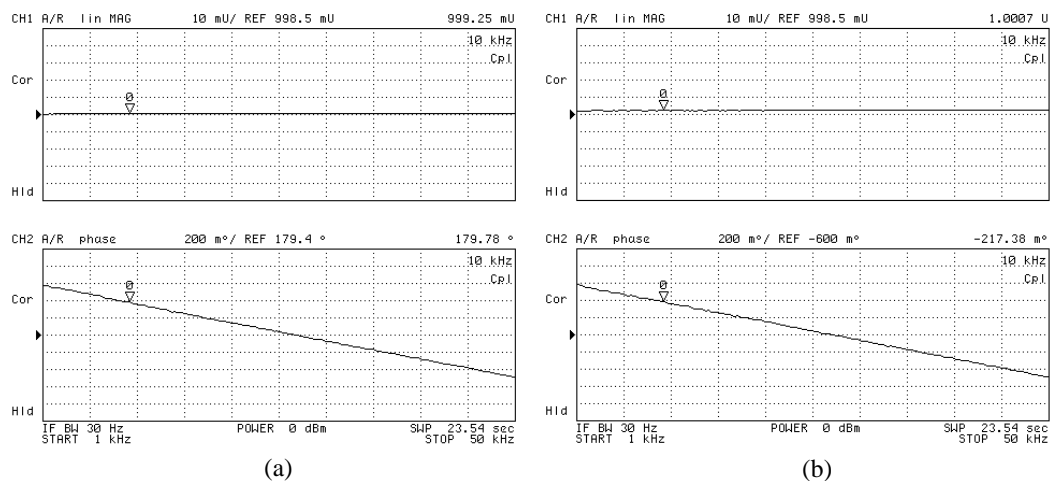


Figure 4.36: Measured gain and phase characteristics of the single-ended to differential convertor for (a) the inverting output and (b) non-inverting output.

4.2.3.2. Fully-Differential Self-Resonance Excitation Circuit with Automatic Amplitude Control

The fully-differential self-resonance excitation circuit with automatic amplitude control is designed to generate differential driving signals sustaining constant-amplitude vibrations at the drive-mode. This circuit is combined with TIA type interfaces and sense-mode demodulation electronics on a single chip having pad distribution compatible to the DWP gyroscope. Figure 4.37 shows the photographs of the complete angular rate system, the DWP gyroscope, and the CMOS fully-differential readout and control electronics.

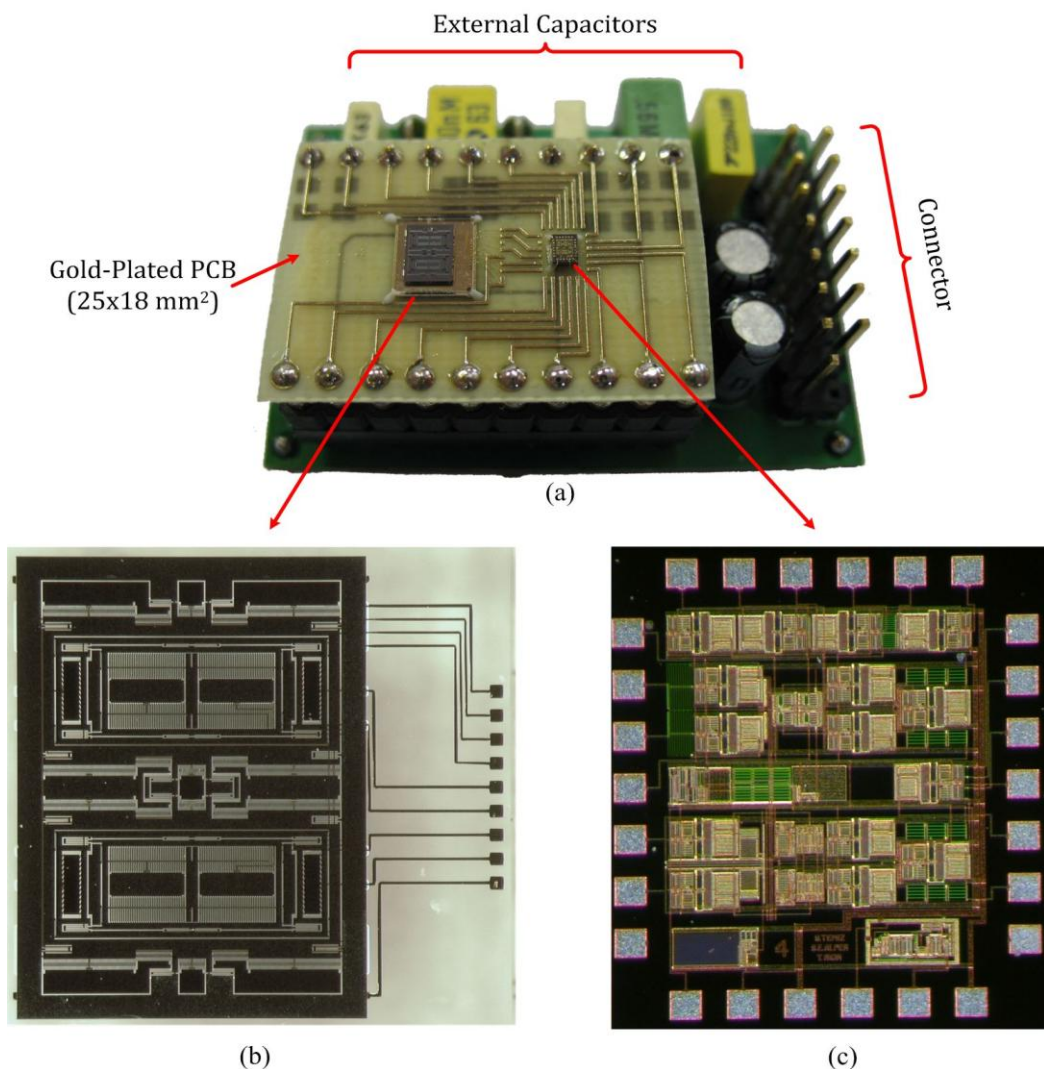


Figure 4.37: Photographs of (a) the complete angular rate system, (b) the DWP gyroscope, and (c) the CMOS fully-differential readout and control electronics.

However, this system cannot be properly tested due to a number of reasons. First, due to a problem associated with the dissolved-wafer process, most of the gyroscopes have short-circuited finger gaps. In addition to this, there measured to be resistive paths between the proof mass and stationary electrodes, resulting in permanent damages in the interface circuits because of the large DC polarization voltage applied to the proof-mass. Then, the gold-plated PCB fabricated in electroless gold electroplating process causes serious problems during the wire-bonding of the gyroscope and the CMOS chip. Moreover, the output offsets observed in the capacitive and resistive interfaces disturb the proper operation of the drive and sense mode electronics. Finally, because of the absence of a fully-functional vacuum-packaged DWP gyroscope, the tests are performed with uncapped gyroscopes in the vacuum chamber. However, the long cables coming from the chamber introduce considerable parasitics that affect the operation of the differential electronics. It is concluded that the overall system should be tested with vacuum packaged gyroscopes with a dedicated test setup.

4.2.4. Test Results of CMOS Fully-Differential Open-Loop Rate Sensing Electronics

The CMOS fully-differential open-loop rate sensing circuit aims to generate the full-wave rectified versions of the applied differential signals. Figure 4.38 shows the block diagram of the test setup used in the transient tests of the fully-differential full-wave rectifier.

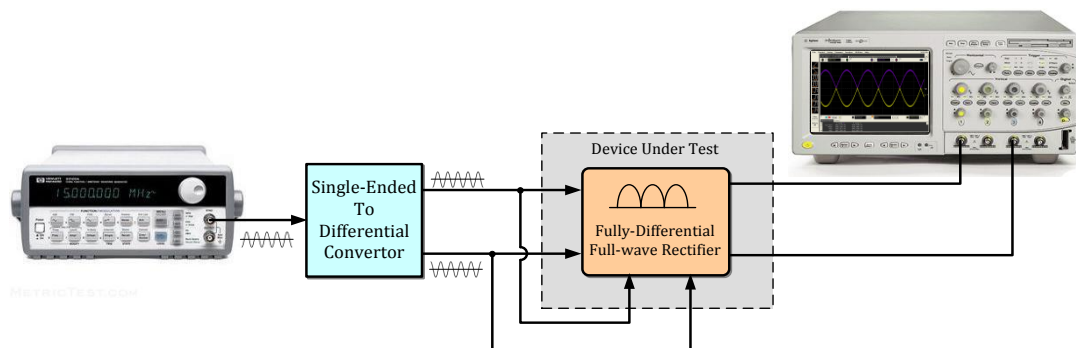


Figure 4.38: Block diagram of the test setup used in the transient tests of the fully-differential full-wave rectifier.

Figure 4.39 shows the measured differential output signals generated by the fully-differential full-wave rectifier when 1 V_{p-p} differential signals are applied. It is verified that the circuit properly generates the full-wave rectified differential signals.

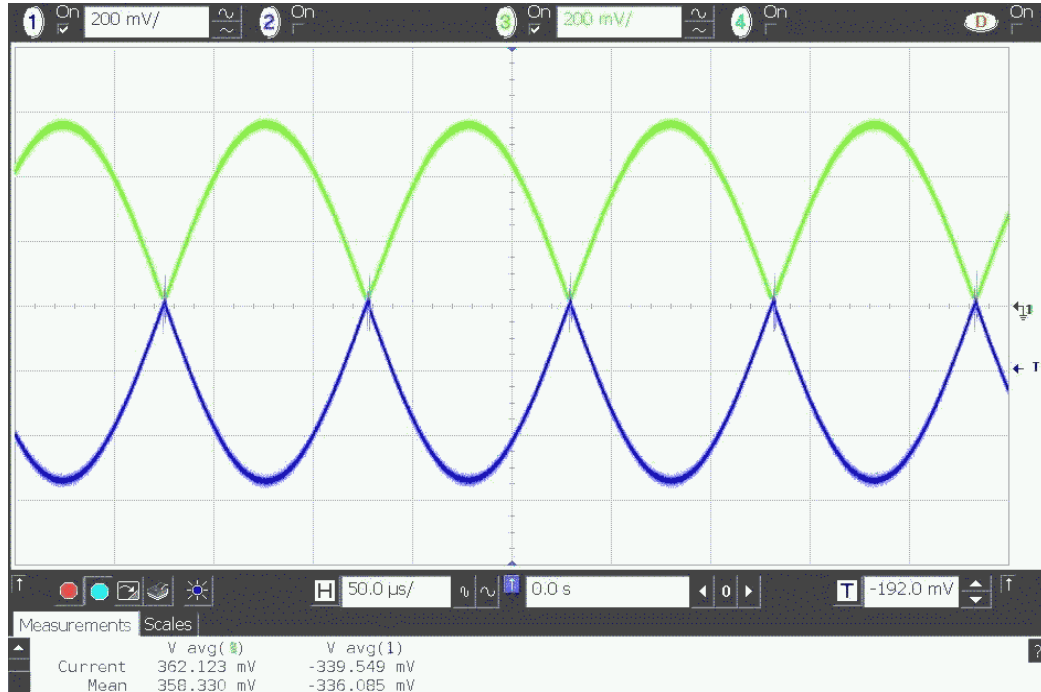


Figure 4.39: Measured differential output signals generated by the fully-differential full-wave rectifier when 1 V_{p-p} differential signals are applied.

4.3. Summary of the Tests

This chapter presented the results of the tests performed on the discrete and CMOS electronics designed for MEMS gyroscopes. Firstly, control and readout electronics implemented with commercial discrete components are tested with SOG, SOI, and DWP gyroscopes developed at METU. For the drive-mode, three different control electronics are tested: 1) single-ended self-oscillation loop with manual amplitude control, 2) single-ended self-oscillation loop with automatic amplitude control, and 3) differential self-oscillation loop with automatic amplitude control. Table 4.4 summarizes the drive-mode circuits tested with different types of gyroscopes.

Table 4.4: Drive-mode circuits tested with different types of gyroscopes.

Drive-Mode Circuit	SOG	SOI	DWP
Single-ended self-oscillation loop with manual amplitude control	✓ (1)	✓ (2)	-
Single-ended self-oscillation loop with automatic amplitude control	✓ (3)	-	-
Differential self-oscillation loop with automatic amplitude control	-	✓ (4)	✓

Table 4.5 gives the best performance results demonstrated by the angular rate systems given in Table 4.4. The third system which is composed of the SOG gyroscope and the single-ended self-oscillation loop with automatic amplitude control together with the differential sense-mode electronics demonstrates an impressive performance approaching tactical-grade. It is verified that this system can give even superior performance by employing closed-loop electronics in the sense-mode and by using a better test setup enabling constant vacuum ambient. Moreover, the differential amplitude control loop, which is tested with SOI gyroscopes, gives very promising results since it is the first time that a differential gyroscope is tested with differential electronics. In addition to this, although very satisfactory results are obtained in the drive mode of the DWP gyroscope, the performance tests of the angular rate system involving DWP gyroscope cannot be performed due to the pull-in problem in the sense-mode of the gyroscope.

Table 4.5: The best performance results demonstrated by the angular rate systems given in Table 4.4.

Parameter	1	2	3	4
Scale Factor (mV/(deg/sec))	1.97	8.9	22.2	11.4
R ² Nonlinearity (%)	0.001	0.04	0.01	0.03
Dynamic Range (deg/sec)	±100	±1000	±50	±50
Zero Rate Output (deg/sec)	-8.73	+39.7	-0.1	+31.9
Bias Instability (deg/hr)	124.7	106	14.3	102.4
Angle Random Walk (deg/√hr)	2.16	4.8	0.126	2.19
Bandwidth (Hz)	10	10	10	100

CMOS circuits are characterized through AC, transient, and noise tests. The unity-gain buffer (UGB) type resistive and capacitive interfaces demonstrate very satisfactory results in the characterization tests. The gain of the buffer circuits is measured as 0.96 while the phase error is only -0.66° . The thermal noise level is found as $60 \text{ nV}/\sqrt{\text{Hz}}$. Moreover, the effective resistances of the high-impedance node biasing subthreshold transistors are measured around $2.5 \text{ G}\Omega$, and it is verified that these biasing mechanisms properly DC-bias the high-impedance nodes to the ground potential. However, a non-zero output offset is observed in the UGB type interfaces, where the offset introduced by each differential branch measured to be equal. Therefore, it is concluded that output offsets can be cancelled out after converting the differential signals to a single-ended signal. Furthermore, transimpedance amplifier (TIA) type resistive and capacitive interfaces are also characterized by transient and AC tests. The TIA type resistive interface gives a phase error less than -1° in a sufficiently wide bandwidth. The output offset is measured to be almost 0 V in both differential branches. On the other hand, it is observed that the biasing mechanism used in the TIA type capacitive interface cannot properly bias the output node of the OPAMP. Then, the test chip employing a similar biasing mechanism is tested and it is verified that the channel resistance of the biasing transistor operating in its subthreshold region is much larger than the designed value due to process tolerances.

For the drive-mode of the dual-mass DWP gyroscopes, two different CMOS chips are tested: 1) single-ended to differential convertor and 2) fully-differential self-resonance excitation circuit with automatic amplitude control. The single-ended to differential convertor demonstrate a phase error less than -220 mdeg for both inverting and non-inverting branches. It is verified that this convertor generates almost perfectly anti-phase driving signals when connected to the external single-ended self-oscillation loops. However, the fully-differential self-resonance excitation circuit with automatic amplitude control circuit cannot be properly tested due to several reasons: 1) pull-in problems associated with DWP gyroscopes, 2) the difficulty of wire-bonding the gyroscope and the CMOS chip to the electroless gold-plated PCB, 3) parasitics introduced by the long cables coming from the

vacuum chamber. Thus, it is concluded that the overall system should be tested with vacuum packaged gyroscopes with a better test setup. Finally, the fully-differential full-wave rectifier circuit is tested and very satisfactory results are obtained.

In conclusion, advanced readout and control electronics implemented with both discrete components and the CMOS technology are characterized and tested with micromachined vibratory gyroscopes. Angular rate systems implemented with commercial discrete components demonstrate performances far superior than that of the best performance achieved at METU. These systems give performances very close to the tactical-grade requirements. Results of the tests performed on the CMOS circuits are mostly consistent with the simulated ones, although some discrepancies are observed due to the tolerances in CMOS fabrication process. It is concluded that improving the test setup and employing more reliable vacuum-packaged gyroscopes would yield even better performances.

CHAPTER 5

CONCLUSIONS AND FUTURE WORK

The research presented in this thesis involves the development of advanced readout and control electronics for realizing fully-functional and high-performance angular rate sensor systems employing MEMS gyroscopes developed at METU. Gyroscope electronics designed within the framework of this study includes resistive and capacitive type interfaces, single-ended and differential self-oscillation loops, and open-loop rate sensing mechanisms. The designed circuits are first implemented with commercial discrete components on dedicated printed circuit boards in order to verify the functionality of the proposed ideas. Different versions of discrete gyroscope electronics are tested for silicon-on-glass (SOG), silicon-on-insulator (SOI), and dissolved-wafer process (DWP) gyroscopes, and then the overall system performances are evaluated by a series of measurements. In addition, two different CMOS capacitive and resistive interface circuits, fully-differential automatic oscillation amplitude control loops, and sense-mode demodulators are designed for DWP gyroscopes in the standard 0.6 μm CMOS process. Operations of the fabricated chips are characterized by using special test setups enabling AC, transient, and noise tests of differential circuits.

Based on the results obtained from this study, following conclusions can be made:

1. The generalized electrical equivalent models of the micromachined vibratory gyroscopes are constructed by analyzing the mechanical dynamics and the transduction mechanisms of the gyroscopes. The obtained models are then used in the system-level and the transistor-level simulations of the proposed electronic circuits in order to characterize the overall angular rate sensor systems.

2. New approaches for the drive-mode self-oscillation loop with manual amplitude control and the sense-mode rate extraction circuit are developed. These circuits are implemented with commercial surface mount devices on a very compact and reliable PCB having $5.4 \times 2.4 \text{ cm}^2$ area. It is verified that the proposed circuit solves the phase error problem present in the previous self-oscillation loops developed at METU. According to the network analyzer tests, the circuit introduces only 0.5° of phase error, implying that the drive-mode vibrations are sustained almost exactly at the mechanical resonance frequency of the gyroscope. Rate tests of silicon-on-insulator (SOI) and silicon-on-glass (SOG) gyroscopes are performed with this circuit. SOI gyroscopes demonstrate angle random walk and bias instability values as low as $4.8 \text{ }^\circ/\sqrt{\text{hr}}$ and $106 \text{ }^\circ/\text{hr}$, respectively, with a scale factor of $8.9 \text{ mV}/(^\circ/\text{sec})$. Moreover, SOG gyroscopes hybrid-connected to CMOS source-follower interfaces and operated with the circuit developed in this research give angle random walk of $2.158 \text{ }^\circ/\sqrt{\text{hr}}$, and bias instability of $124.7 \text{ }^\circ/\text{hr}$. It is observed that although the proposed electronics provide satisfactory results for initial performance tests, amplitude of the drive-mode oscillations are dependent to the supply voltages, proof mass voltage, vacuum level, and other parameters. Moreover, the generated square wave driving signal creates a risk of exciting the higher modes of the gyroscope, resulting in instable operation. Thus, it is concluded that much complicated drive-mode control loops are required for achieving tactical-grade performance levels.

3. An advanced control mechanism sustaining self-triggered constant amplitude drive-mode oscillations at the mechanical resonance frequency of the gyroscope is developed. The linearized model of the control loop is constructed for optimizing the controller parameters according to the design specifications. The unknown parameters are calculated by a powerful optimization tool provided by SIMULINK. Together with the transresistance amplifier type interfaces and the sense-mode demodulation electronics, the proposed oscillation amplitude control circuit is connected to the SOG gyroscope, realizing a fully-functional angular rate sensor. The overall

system is implemented with discrete components on a two-layer PCB having $5.4 \times 2.4 \text{ cm}^2$ area. According to the initial performance tests, it is verified that the control loop generates an amplitude-controlled sinusoidal signal sustaining constant amplitude oscillations independent of external parameters. Then, a series of angular rate measurements are performed for determining scale-factor, linearity, dynamic range, angle random walk, bias instability, and zero-rate output. The overall system demonstrates impressive performance values with scale factor of $22.2 \text{ mV}/(\text{°}/\text{sec})$, zero rate output of $0.1 \text{ °}/\text{sec}$, angle random walk of $0.126 \text{ °}/\sqrt{\text{hr}}$, and bias instability of $14.3 \text{ °}/\text{hr}$, owing to its high-sensitive electronics integrated on a dedicated PCB. It is concluded that operating the gyroscope near to the matched-mode and using larger feedback resistors for sense-mode TRA interfaces increase the performance significantly. The gyroscope is also operated in exact matched-mode. Although, it demonstrates exceptional performance values with scale factor larger than $100 \text{ mV}/(\text{°}/\text{sec})$, and bias instability lower than $10 \text{ °}/\text{hr}$, the dynamic range is limited with the sense-mode finger gaps due to open-loop rate sensing electronics. Furthermore, it is verified that bias instability values can be further improved by using a vacuum chamber enabling precise control on the vacuum level. Even smaller noise levels can be achieved with a better test setup providing less parasitics introduced by the rate table slip-rings and interconnection cables.

4. An improved and differential version of the self-oscillation loop with automatic amplitude control mechanism is designed for dual-mass DWP gyroscopes. After optimizing the system parameters with SIMULINK, the overall system, also including the differential interfaces and sense-mode electronics, is implemented on a six-layer PCB with $4.4 \times 2.1 \text{ cm}^2$ area, which is extremely small for such a complex system. Tests are performed with a vacuum packaged DWP gyroscope prototype. According to the tests performed on the differential amplitude control circuit, the system gives constant amplitude oscillations for large deviations in the proof mass and amplitude set voltages as well as supply voltages. Moreover, it is verified

that the system overshoot in response to step transitions in the external parameters are in tolerable ranges and consistent with the simulation results. Although high-sensitive sense-mode electronics are also available in the system, the rate test cannot be performed due to problems associated with the gyroscope itself. It is observed that when the DC polarization voltage is applied to the proof mass, sense-mode fingers get short-circuited due to some unexpected problems seen during the fabrication process. These problems are being investigated by mechanical and process engineers, and it is expected that when fully-functional gyroscopes are produced, they would demonstrate tactical-grade performances owing to high-performance electronics developed in this research. Then, the same circuit is tested with differential SOI gyroscopes designed at METU and fabricated by MEMSCAP[®] Inc. The system demonstrates a scale-factor of 11.4 mV/(deg/sec) with 0.03% nonlinearity and 363.5 mV zero-rate output. The bias instability and angle random walk values are measured as 102.4 deg/hr and 2.19 deg/ $\sqrt{\text{hr}}$, respectively, where the bandwidth is 100 Hz.

5. Two types of CMOS differential interfaces are designed for the high-SNR capacitance change to voltage conversion in DWP gyroscopes. The post-layout simulations of the designed unity-gain buffer (UGB) and transimpedance amplifier (TIA) type resistive and capacitive interfaces are performed in CADENCE Analog Environment. Fabricated interfaces are then characterized through AC, transient, and noise tests by using special test setups. UGB interfaces properly bias the high-impedance nodes to the ground potential. However, these interfaces introduce non-zero output offset which show variations for different chips. According to the AC tests, UGB interfaces have phase error less than 1°. On the other hand, TIA type interfaces demonstrate lower performance compared to the UGB type interfaces due to the biasing problem. It is concluded that the controlled impedance FET biasing strategy used in these interfaces cannot bias the output of the OPAMP when the channel resistance is too large.

6. A complete angular rate system composed of DWP gyroscope and CMOS readout and control electronics is designed. A novel fully-differential self-oscillation loop with automatic amplitude control mechanism is developed for sustaining balanced and stable vibrations in the drive-mode of the dual-mass DWP gyroscope. The complete system is placed on a gold-plated PCB and the characterization tests are performed.
7. CMOS fully-differential switching type full-wave rectifier is developed and very promising results are obtained. According to the transient tests, it is verified that the fabricated chip gives the full-wave rectified version of the differential input signals.

Although major research objectives are accomplished by realizing fully-functional angular rate systems demonstrating tactical-grade performances, there is still need for further research for improving the overall performances of the gyroscopes and the CMOS electronics. Some of the possible future studies can be listed as follows:

1. Angular rate systems implemented with commercial discrete components demonstrate impressive performance in spite of the some disadvantages introduced by the test setup. It is concluded that the proposed systems would give even superior performance by using a vacuum chamber enabling precise control on the vacuum level since the bias instability increases as the vacuum level varies. Moreover, rate output signal should be converted to a digital signal before passing through the slip-rings of the rate table because these slip-rings introduce significant noise when the rate table servo motor is active.
2. The future research should consider employing closed-loop rate sensing electronics instead of open-loop AM demodulators. Closed-loop rate sensing mechanism allows the gyroscope to be easily operated in the matched-mode with a wider bandwidth and more linear response within a sufficiently large dynamic range. In addition to force-feedback mechanism, control loops automatically generating the necessary proof

mass voltage for the matched-mode operation should be researched. Another necessary control circuit that should be considered for the future work is the quadrature cancellation circuit, which applies an electrostatic force to the quadrature cancellation electrodes to minimize the mechanical crosstalk.

3. Offset problem associated with the CMOS interfaces must be investigated in detail. It is necessary to implement capacitive and resistive interfaces having less dependency on the process variations. Moreover, controlled impedance FET biasing strategy used in the TIA type capacitive interfaces should be improved by analyzing the behavior of subthreshold MOS transistors.
4. Pull-in problem observed in the dual-mass DWP gyroscopes must be solved by optimizing the fabrication process. Then, fully-differential sense and drive mode electronics designed within the framework of this research should be tested with these gyroscopes. Furthermore, future research should also consider using vacuum-packaged DWP gyroscopes in order to operate the gyroscopes in a constant-vacuum ambient. Then, the CMOS electronics designed for DWP gyroscopes should be tested.
5. For further studies, the mechanical sensor and the CMOS electronics should be integrated on a single chip. This monolithic solution would certainly increase the performance of the system since the parasitics coming from the interconnections are eliminated.

In conclusion, the major achievement of this research is the development of advanced readout and control electronics for MEMS gyroscopes. Designed angular rate systems show impressive performances required for tactical-grade applications. It is believed that the results demonstrated throughout this study will be helpful for the future research on high-performance MEMS gyroscopes for industrial, commercial and military applications.

REFERENCES

- [1] N. Yazdi, F. Ayazi, and K. Najafi, "Micromachined Inertial Sensors," *Proc. of the IEEE*, Vol. 86, No. 8, pp. 1640-1659, August 1998.
- [2] J. Marek, "Microsystems for Automotive Applications," *Proc. 13th Eur. Conf. Solid-State Transducers (Euroensors XIII)*, Hague, Netherlands, pp. 1-8, September 1999.
- [3] H. Kuisma, "Inertial Sensors for Automotive Applications," *Tech. Dig. 11th Int. Conf. Solid-State Sensors and Actuators (Transducers'01)*, Munich, Germany, pp. 430-433, June 2001.
- [4] R. Neul, U. Gómez, K. Kehr, W. Bauer, J. Classen, C. Döring, E. Esch, S. Götz, J. Hauer, B. Kuhlmann, C. Lang, M. Veith, and R. Willig, "Micromachined Angular Rate Sensors for Automotive Applications," *IEEE Sensors Journal*, Vol. 7, No. 2, pp. 302-309, February 2007.
- [5] Analog Devices, "ADXL50 – Monolithic Accelerometer with Signal Conditioning," *Datasheet*, 1996.
- [6] N. Yazdi, K. Najafi, "An All-Silicon Single-Wafer Micro-g Accelerometer with a Combined Surface and Bulk Micromachining Process," *Journal of Microelectromechanical Systems*, Vol. 9, No.4, pp. 544-550, December 2000.
- [7] J. Chae, H. Kulah, and K. Najafi, "A Monolithic Three-Axis Micro-g Micromachined Silicon Capacitive Accelerometer," *Journal of Microelectromechanical Systems*, Vol. 14, No. 2, pp. 235-242, April 2005.
- [8] S. E. Alper, "MEMS Gyroscopes for Tactical-Grade Inertial Measurement Applications," *Ph.D. Dissertation*, Middle East Technical University, September 2005.

- [9] P. Greiff, B. Boxenhorn, T. King, and L. Niles, "Silicon Monolithic Micromechanical Gyroscope," *Tech. Dig. 6th Int. Conf. Solid-State Sensors and Actuators (Transducers '91)*, San Francisco, CA, pp. 966-968, June 1991.
- [10] J. Bernstein, S. Cho, A. T. King, A. Kourepenis, P. Maciel, and M. Weinberg, "A Micromachined Comb-Drive Tuning Fork Rate Gyroscope," *Proc. IEEE Micro Electro Mechanical Systems Workshop (MEMS'93)*, Fort Lauderdale, FL, pp. 143-148, February 1993.
- [11] M. W. Putty, "A Micromachined Vibrating Ring Gyroscope," *Ph.D. Dissertation*, The University of Michigan, 1995.
- [12] G. He and K. Najafi, "A Single-Crystal Silicon Vibrating Ring Gyroscope," *Proc. IEEE Micro Electro Mechanical Systems Workshop (MEMS'02)*, Las Vegas, CA, pp. 718-721, January 2002.
- [13] X. Huikai and G. K. Fedder, "A CMOS-MEMS Latera-Axis Gyroscope," *Proc. IEEE Micro Electro Mechanical Systems Workshop (MEMS'01)*, Interlaken, Switzerland, pp. 162-165, January 2001.
- [14] H. Luo, X. Zhu, H. Lakdawala, L. R. Carley, and G. Fedder, "A Copper CMOS-MEMS Z-Axis Gyroscope," *Proc. IEEE Micro Electro Mechanical Systems Workshop (MEMS'02)*, Las Vegas, CA, pp. 631-634, January 2002.
- [15] T. Juneau, A. P. Pisano, and J. H. Smith, "Dual Axis Operation of a Micromachined Rate Gyroscope," *Tech. Dig. 9th Int. Conf. Solid-State Sensors and Actuators (Transducers '97)*, Chicago, IL, pp. 887-890, June 1997.
- [16] J. A. Geen, S. J. Sherman, J. F. Chang, and S. R. Lewis, "Single-Chip Surface Micromachined Integrated Gyroscope with 50 °/hr Allan Deviation," *J. Solid State Cct.*, Vol. 37, No. 12, pp. 1860-1866, December 2002.
- [17] M. F. Zaman, A. Sharma, and F. Ayazi, "High-Performance Matched-Mode Tuning Fork Gyroscope," *19th IEEE Int. Conf. on Micro Electro Mechanical Systems (MEMS 2006)*, Istanbul, Turkey, pp. 598-601, January 2006.

- [18] S. E. Alper and T. Akin, "A Single-Crystal Silicon Symmetrical and Decoupled MEMS Gyroscope on an Insulating Substrate," *Journal of Microelectromechanical Systems*, Vol. 14, No. 4, pp. 707-717, August 2005.
- [19] S. E. Alper and T. Akin, "A Symmetrical and Decoupled Nickel Microgyroscope on Insulating Substrate," *Sensors Actuators A*, Vol. 115/2-3, pp. 336-350, September 2004.
- [20] S. E. Alper, K. M. Silay, and T. Akin, "A Low-Cost Rate-Grade Nickel Microgyroscope," *Sensors Actuators A*, Vol. 132, Issue 1, pp. 171-181, November 2006.
- [21] S. E. Alper, K. Azgin, and T. Akin, "High-Performance SOI-MEMS Gyroscope with Decoupled Oscillation Modes," *19th IEEE Int. Conf. on Micro Electro Mechanical Systems (MEMS 2006)*, Istanbul, Turkey, pp. 70-73, January 2006.
- [22] K. Azgin, Y. Temiz, and T. Akin, "An SOI-MEMS Tuning Fork Gyroscope with Linearly Coupled Drive Mechanism," *20th IEEE Int. Conf. on Micro Electro Mechanical Systems (MEMS 2007)*, Kobe, Japan, pp. 607-610, January 2007.
- [23] S. E. Alper, K. M. Silay, and T. Akin, "Tactical-Grade Silicon-on-Glass Gyroscope with Very-Small Quadrature Coupling," *Proc. of the 20th European Conf. on Solid-State Transducers (Euroensors XX)*, Gothenburg, Sweden, September 2006.
- [24] N. Yazdi, H. Kulah, and K. Najafi, "Precision Readout Circuits for Capacitive Microaccelerometers," *Proc. IEEE Sensors 2004*, Vol. 1, pp. 28-31, October 2004.
- [25] B. E. Boser, "Electronics for Micromachined Inertial Sensors," *Tech. Dig. 9th Int. Conf. Solid-State Sensors and Actuators (Transducers '97)*, Chicago, IL, pp. 1169-1172, June 1997.

- [26] D. Fang and H. Xie, "A Low-Noise Low-Power Preamplifier for Capacitive CMOS-MEMS Gyroscopes," *49th IEEE Int. Midwest Symposium on Circuits and Systems (MWSCAS'06)*, San Juan, Puerto Rico, Vol. 1, pp. 270-274, August 2006.
- [27] J. Wu, G. K. Fedder, and L. R. Carley, "A Low-Noise Low-Offset Chopper-Stabilized Capacitive-Readout Amplifier for CMOS MEMS Accelerometers," *Tech. Dig. IEEE Int. Solid-State Circuits Conf.*, Vol. 1, February 2002.
- [28] T. Singh and T. Ytterdal, "A Single-Ended to Differential Capacitive Sensor Interface Circuit Designed in CMOS Technology," *Proc. IEEE Int. Symp. on Circuits and Systems 2004 (ISCAS'04)*, Vol. 1, pp. 948-951, May 2004.
- [29] M. Saukoski, L. Aaltonen, K. Halonen, and T. Salo, "Fully Integrated Charge Sensitive Amplifier for Readout of Micromechanical Capacitive Sensors," *Proc. IEEE Int. Symp. on Circuits and Systems 2005 (ISCAS'05)*, Vol. 6, pp. 5377-5380, May 2005.
- [30] A. Sharma, M. F. Zaman, and F. Ayazi, "A 104-dB Dynamic Range Transimpedance-Based CMOS ASIC for Tuning Fork Microgyroscopes," *IEEE J. of Solid-State Circuits*, Vol. 42, No.8, August 2007.
- [31] N. Wongkomet and B. E. Boser, "Correlated Double Sampling in Capacitive Position Sensing Circuits for Micromachined Applications," *IEEE Asia-Pasific Conf. on Circuits and Systems*, pp. 723-726, November 1998.
- [32] H. Kulah, J. Chae, N. Yazdi, and K. Najafi, "A Multi-Step Electromechanical Sigma-Delta Converter for Micro-g Capacitive Accelerometers," *IEEE Int. Solid-State Circuits Conf.*, pp. 202-203, February 2003.
- [33] G. K. Fedder, "Simulation of Microelectromechanical Systems," *Ph.D. Dissertation*, University of Michigan, 1995.

- [34] R. T. M'Closkey and A. Vakakis, "Analysis of a Microsensor Automatic Gain Control Loop," *Proc. of the American Control Conf.*, San Diego, CA, pp. 1229-1234, June 1999.
- [35] C. Acar, S. Eler, and A. M. Shkel, "Concept, Implementation, and Control of Wide Bandwidth MEMS Gyroscopes," *Proc. of the American Control Conf.*, Arlington, VA, pp. 3307-3311, June 2001.
- [36] R. Oboe, R. Antonello, E. Lasalandra, G. Spinola, and L. Prandi, "Control of a Z-axis MEMS vibrational gyroscope," *8th Int. Workshop on Advanced Motion Control (AMC'04)*, pp. 153-158, March 2004.
- [37] J. Raman, E. Cretu, P. Rombouts, and L. Weyten, "A Digitally Controlled MEMS Gyroscope with Unconstrained Sigma-Delta Force-Feedback Architecture," *19th IEEE Int. Conf. on Micro Electro Mechanical Systems (MEMS 2006)*, Istanbul, Turkey, pp. 710-713, January 2006.
- [38] S. An, Y.S. Oh, B.L. Lee, K.Y. Park, S.J. Kang, S.O. Choi, Y.I. Go, and C.M. Song, "Dual-Axis Microgyroscope with Closed-Loop Detection," *Proc. 11th Int. Workshop on Micro Electro Mechanical Systems (MEMS'98)*, pp. 328-333, January 1998.
- [39] X. Jiang, J. I. Seeger, M. Kraft, and B. E. Boser, "A Monolithic Surface Micromachined Z-Axis Gyroscope with Digital Output," *Tech. Dig. Symposium on VLSI Circuits*, pp. 16-19, June 2000.
- [40] Y. Dong, M. Kraft, and W. Redman-White, "Micromachined Vibratory Gyroscopes Controlled by a High-Order Bandpass Sigma-Delta Modulator," *IEEE Sensors Journal*, Vol. 7, No. 1, January 2007.
- [41] J. Jiwei, H. Ming, W. Xiangli, C. Yong, and W. Yuelin, "A Digital Demodulation Solution to Achieve Stable Driving for a Micro-machined Gyroscope with an AGC Mechanism," *Proc. IEEE Sensors*, Vol. 1, pp. 429-432, October 2004.

- [42] H. Rodie, D. Sandstrom, P. Pelin, N. Hedenstierna, D. Eckerbert, and G. I. Andersson, "A Digitally Controlled MEMS Gyroscope with 3.2 deg/hr Stability," *Tech. Dig. 13th IEEE Conf. on. Solid-State Sensors, Actuators and Microsystems (Transducers '05)*, Vol. 1, pp. 535-538, June 2005.
- [43] A. M. Shkel, R. Horowitz, A. A. Seshia, S. Park, and R. T. Howe, "Dynamics and Control of Micromachined Gyroscopes," *Proc. of the American Control Conf.*, San Diego, CA, Vol. 3, pp. 2119-2124, June 1999.
- [44] S. Park and R. Horowitz, "Adaptive Control for the Conventional Mode of Operation of MEMS Gyroscopes," *J. of Microelectromechanical Systems*, Vol. 12, No. 1 , pp. 101-108, February 2003.
- [45] R. P. Leland, "Lyapunov Based Adaptive Control of a MEMS Gyroscope," *Proc. of the American Control Conf.*, Anchorage, AK, pp. 3765-3770, May 2002.
- [46] L. Dong and R. P. Leland, "The Adaptive Control System of a MEMS Gyroscope with Time-varying Rotation Rate," *Proc. of the American Control Conf.*, Portland, OR, pp. 3592-3597, June 2005.
- [47] Robert P. Leland, "Adaptive Control of a MEMS Gyroscope Using Lyapunov Methods," *IEEE Transactions on Control Systems Technology*, Vol. 14, No. 2, pp. 278-283, March 2006.
- [48] S. E. Alper, "Silicon Surface Micromachined Gyroscopes Using MEMS Technology," *M.Sc Thesis*, Middle East Technical University, September 2000.
- [49] R. F. Yazicioglu, "Surface Micromachined Capacitive Accelerometers using MEMS Technology," *M.Sc. Thesis*, Middle East Technical University, August 2003.
- [50] K. M. Silay, "High-Performance CMOS Capacitive Interface Circuits for MEMS Gyroscopes," *M.Sc. Thesis*, Middle East Technical University, September 2006.

- [51] K. Azgin, "High-Performance MEMS Gyroscopes," *M.Sc. Thesis*, Middle East Technical University, February 2007.
- [52] B. Razavi, "Design of Analog CMOS Integrated Circuits," McGraw-Hill, 2001.
- [53] B. Linares-Barranco, T. Serrano-Gotarredona, "A Loss Control Feedback Loop for VCO Stable Amplitude Tuning of RF Integrated Filters," *IEEE Int. Symposium on Circuits and Systems (ISCAS'02)*, Vol. 1, pp. 521-524, May 2002.
- [54] F. Bahmani and E. Sánchez-Sinencio, "A Stable Loss Control Feedback Loop for VCO Amplitude Tuning," *IEEE Transactions on Circuits and Systems*, Vol. 53, No. 12, pp. 2498-2506, December 2006.
- [55] Analog Devices, "AD630, Balanced Modulator/Demodulator," *Datasheet*, 2004.
- [56] Analog Devices, "AD600/AD602, Dual, Low-Noise, Wideband Variable Gain Amplifiers," *Datasheet*, 2006.
- [57] Y. Zheng, J. Yan, and Y. P. Xu, "A CMOS dB-linear VGA with pre-distortion compensation for wireless communication applications," *Proc. of the Int. Symposium on Circuits and Systems (ISCAS'04)*, Vol. 1, pp. 813-816, May 2004.
- [58] E. Alpman, "Development of Low-Cost Uncooled Infrared Detector Arrays in Standard CMOS and SOI-CMOS Processes," *M.Sc. Thesis*, Middle East Technical University, September 2005.
- [59] IEEE Standard Specification Format Guide and Test Procedure for Single-Axis Interferometric Fiber Optic Gyros, *IEEE Std 952-1997*, pp. 65, September 1997.